BEHAVIOUR OF PARTIALLY GROUTED REINFORCED MASONRY SHEAR WALLS UNDER CYCLIC REVERSED LOADING

By

MAJID MALEKI
B.Sc., M.Sc.

A Thesis

Submitted to the School of Graduate Studies in Partial

Fulfillment of the Requirements

for the Degree

Doctor of Philosophy

McMaster University

DOCTOR OF PHILOSOPHY (2008)   McMaster University

(Civil Engineering)   Hamilton Ontario

TITLE: Behaviour of Partially Grouted Reinforced Masonry
                    Shear Walls under Cyclic Reversed Loading

AUTHOR: Majid Maleki, B.Sc., M.Sc. (Sharif University of Technology)

SUPERVISOR: Professor R. G. Drysdale

NUMBER OF PAGES: xxiv, 276

ABSTRACT

The existing gap between minimum reinforcing requirements specified in the current Canadian masonry design standard (CSA S304.1 2004) and the provision for unreinforced masonry limits engineers to use the same minimum requirements for regions with low or moderate seismic demands. As a result, this restricts the use of reinforced masonry construction as a cost-efficient building system in regions with moderate seismic risks. In this research program, the performance of partially grouted reinforced masonry (PG-RM) shear walls, having larger reinforcement spacing than specified as minimum seismic requirements, has been evaluated to help in future efforts to offer some relief from the code's limitation.

As the first phase of this research study, a computationally efficient numerical tool (finite element model) capable of predicting the pre- and post-peak response of PG-RM shear walls under in-plane loading was developed. The performance of the numerical model was evaluated by simulating available shear wall tests from other studies as well as the shear wall tests done as part of experimental program of this work. In general, acceptable accuracy was observed in numerically predicting both the pre- and post-peak behaviour of the shear wall specimens and the model was shown to be a reliable tool for further studies.

The experimental program was intended to document the effects of reinforcement spacing and aspect ratio on the response of PG-RM shear wall under cyclic reversed loading. Direct small scale modelling using half-scale model concrete masonry units was chosen for the experiments. Two stages of testing were

conducted. The first stage was designed to investigate the performance of masonry wallettes (panels) under the action of diagonal compression loading. Various patterns of grouting and reinforcing were studied by testing nine diagonal compression specimens. The second stage of the experimental research focused on the response of PG-RM shear walls under constant axial load and fully reversed cyclic lateral loading. The test matrix consisted of five masonry shear walls with nearly the same reinforcement ratios. The walls included three aspect ratios and three reinforcement spacings. Visual observations, loading, displacements, and crack pattern were recorded throughout the tests.

The developed numerical model was used to expand the scope of the study to include the effects of level of axial load and amounts of horizontal and vertical reinforcement on the behaviour of PG-RM shear walls. In addition, the effect of reinforcing two cells at the ends of a PG-RM shear wall was also simulated.

Close agreement was observed between the shear resistance estimated based on the Canadian masonry design standard (CSA 2004) and the experimental results of the PG-RM shear walls dominated by the shear failure mode. However, it was shown that the seismic load reduction factor, R value, suggested by CSA (2004) underestimates the energy dissipation ability of PG-RM shear walls despite the shear dominated behaviour observed for the test walls.

The finding of this research study indicates a relatively ductile behaviour with satisfactory energy dissipation capability for PG-RM shear walls. This emphasises potential application of this type of wall as a more cost-efficient alternative in the future of masonry construction.

DEDICATIONS

To my Beloved Mother and Father

To my Sincere Brother

ACKNOWLEDGMENTS

TABLE OF CONTENTS

LIST OF FIGURES

xix

LIST OF TABLES

CHAPTER 1

INTRODUCTION

1.1 GENERAL

In modern masonry construction, reinforced masonry shear walls act as the main structural element to carry the gravity loads to the foundation and resist lateral in-plane loads due to seismic or wind forces without the addition of frames or columns. As shown in Figure 1.1, shear walls are usually arranged to correspond with the two major axes of the building and, for multi-storey buildings, to support a concrete floor which provides a rigid diaphragms to distribute the shear forces to walls in proportion to their stiffnesses. To ensure sufficient ductility to permit redistribution of lateral load and to provide good energy dissipation characteristics during seismic excitation, it is important to obtain an accurate understanding of the in-plane behaviour of masonry shear walls.

Depending on the aspect ratio, loading conditions, and amounts of vertical and horizontal reinforcement, two distinct inelastic load-deformation mechanisms can be identified with shear wall panels subjected to simultaneous axial and lateral

Shear walls resisting
lateral loads in the
transverse direction

Corridor loadbearing wall
resisting lateral loads in the
longitudinal direction

Wall-floor connection
to transfer loads from
floor to shear walls

Concrete floor acting as a
rigid diaphragm to transfer
loads to shear walls
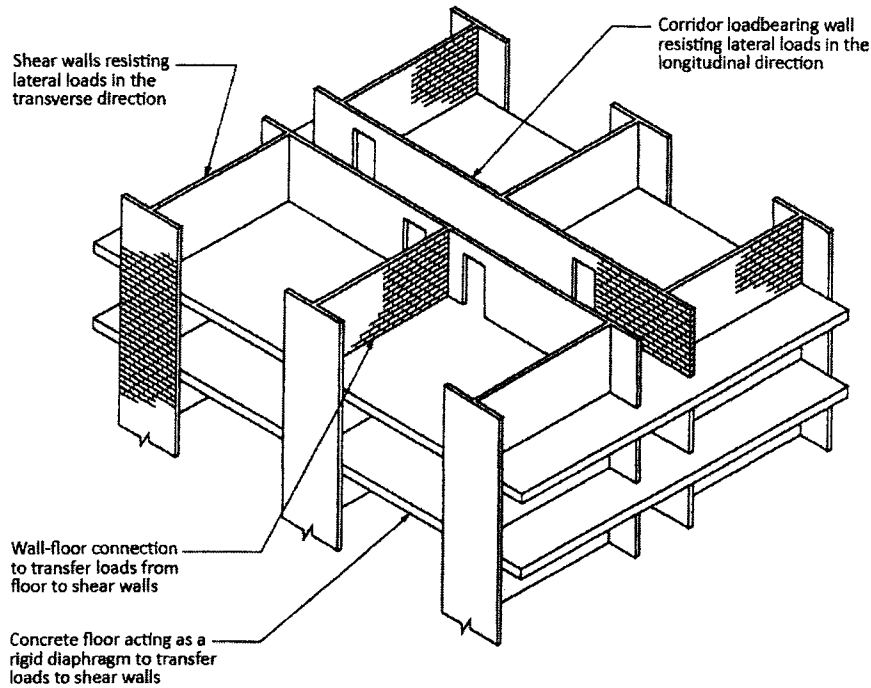
Figure 1.1 – *Masonry wall-type loadbearing building system (from Drysdale et al. 1999)*

loads. One is the flexural mechanism characterized by tensile yielding of the vertical reinforcement followed by compressive crushing of masonry at critical wall sections. The other is the shear mechanism characterized by diagonal tensile cracking (Shing et al. 1989). Figure 1.2 illustrates the described load-deformation behaviours of typical masonry shear walls. Masonry shear walls dominated by the shear failure mechanism tend to exhibit a more brittle behaviour than the ductile flexural failure mechanism which is more effective in dissipating energy by yielding of reinforcement. However, special circumstances such as low aspect ratio (the so-called squat walls), relatively high level of axial load, inadequate vertical or horizontal reinforcement, and/or large reinforcement spacing can lead to shear dominated failure modes.

In the following section, a current problem of the Canadian masonry standard

and other international design codes (CSA 2004, NZS 1990) which inspired the main

focus of this study is discussed. The significance and objectives of the research

program are then presented followed by a brief description of the scope of the

project. Finally a review of the previous research on masonry shear walls with an

emphasis on partially grouted reinforced masonry shear walls is presented.

(a) Ductile Flexural Failure Mechanism

(b) Shear Failure Mechanism
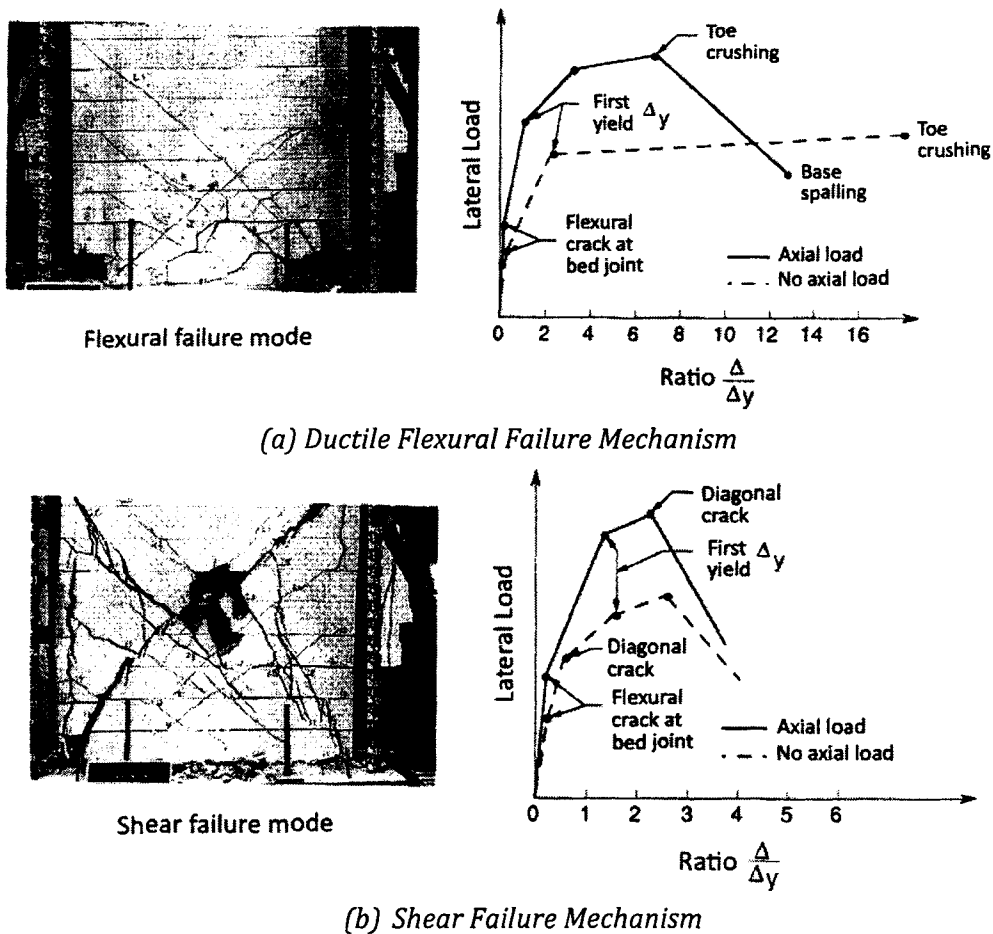
Figure 1.2 – *Failure mechanisms of masonry shear walls (from Shing et al. 1989)*

1.2 PROBLEM STATEMENT

Based on whether steel is present or not, masonry structures are typically categorized in two major groups as Reinforced Masonry (RM) and Unreinforced Masonry (URM). Unreinforced masonry structures are composed of brittle materials such as stone, clay brick, calcium silicate or concrete units joined together at the joints by a layer of cementitious mix known as mortar. Owing to the ease of construction, the high compressive strength and durability, URM is one of the oldest forms of construction. Nowadays URM is commonly used in low-rise buildings where low levels of lateral excitation are expected. To improve on the brittle characteristics and the low tensile strength of URM structures, reinforcing steel bars have been introduced in modern masonry construction. The improved tensile and compressive strength and, indeed, ductility characteristics of reinforced masonry resulted in development of this economical form of construction even in areas of high seismic demand.

To ensure satisfactory response under a minimum level of earthquake excitation, masonry codes require designers to comply with a set of minimum requirements for the amount and distribution of reinforcement within the concrete masonry units. In the current Canadian masonry standard (CSA S304.1 2004), there is a gap between these minimum reinforcing requirements for fully reinforced masonry and provisions of unreinforced masonry. CSA S304.1 (2004) specifies that at sites where the seismic hazard index is equal to or greater than 0.35 (areas with seismic activity ranging from medium to high), loadbearing walls, including shear

walls, must be reinforced horizontally and vertically with steel having a minimum total area of $0.002A_g$. (A_g corresponds to the gross area of the wall; that is thickness times length) This reinforcement is distributed with a minimum area of $0.00067A_g$ in any direction. Regarding spacing between horizontal and vertical seismic reinforcement, the standard mandates engineers not to exceed 6 times the nominal thickness of the wall or 1200 mm whichever is less.

A current problem is that these prescriptive provisions for reinforcement details are overly conservative compared to the similar provision specified in the American masonry standard (MSJC 2008) which allows engineers to use up to 3000 mm bar spacing for regions with low earthquake excitations. Thus, Canadian code limits engineers to use the same minimum requirements for regions with both low and moderate seismic demands. Consequently this restricts the use of reinforced masonry construction as a cost-efficient building system in Canada which is mainly located in regions with low seismic risks. Although larger spacing (up to maximum 2400 mm) is permitted in zones with less than seismic hazard index of 0.35, there is very little data available to confirm satisfactory shear wall behaviour at spacing up to the permitted 2400mm. Thus, designers have trended not to utilize spacing of more than 1200mm in any seismic design of reinforced masonry.

1.3   RESEARCH SIGNIFICANCE AND OBJECTIVES

The main goal of this research project is to address the performance of partially grouted reinforced masonry (PG-RM) shear walls, having less steel or larger spacing than specified as minimum seismic requirements. The performance

will be judged in terms of in-plane lateral load carrying capacity, stiffness, and post failure characteristics such as energy dissipation and displacement ductility. The primary objective of this research study is to document the effects of reinforcement spacing and aspect ratio on the behaviour of PG-RM shear wall under cyclic reversed loading. The outcomes of the study are intended to provide a step forward towards modifying the current prescriptive provision of the Canadian masonry code concerning minimum reinforcement requirements and load reduction factors for masonry structures in low or moderate seismic regions.

In addition, development of a numerical tool capable of predicting the pre- and post-peak behaviour of PG-RM shear walls subject to in-plane axial and lateral loading is another significant objective of this study. The numerical model is intended to be used in prediction of behaviour and in design of partially grouted masonry shear walls.

This research is intended to help in future efforts to introduce another type of masonry construction entitled Partially (or Nominally) Reinforced Masonry which can offer some relief from the code's limitation by creating an intermediate category between unreinforced and reinforced masonry structures.

1.4   SCOPE OF THE RESEARCH

To achieve the research objectives, a two phase study was planned for this research program. Phase one was intended to develop and evaluate a reliable and computationally efficient numerical tool (finite element model) capable of predicting the pre- and post-peak response of partially grouted reinforced masonry

shear walls under in-plane loading. In phase two, the effort was focused on an experimental study of the effects of aspect ratio and reinforcement spacing on cyclic response of partially grouted reinforced masonry shear walls. It was decided that the test program should consist of five partially grouted reinforced masonry shear walls with different bar spacing and aspect ratio while percentages of steel in both the vertical and horizontal directions remain relatively unchanged. The experimental data also was intended to be used to verify the numerical model.

Because partially grouted masonry testing, due to larger reinforcement spacing, involves large specimens and also because there is limited actuator capacity, full scale testing was not feasible in the available laboratory at McMaster University. Therefore, direct small scale modelling using half-scale model concrete masonry units was chosen for the experimental research. The half-scale allows the available smaller commercial deformed bars to be used as the half-scale model of the prototype bars.

1.5 LITERATURE REVIEW

Although masonry structures have been built since the earliest days of man, it has only been in relatively recent times that masonry structures have been designed based on engineering principles. The following sections present a brief review of the available studies focusing on different aspect related to the current research including previous works on numerical modelling of masonry composites, small-scale modelling techniques in masonry, and testing related to behaviour of masonry shear walls.

1.5.1   Review of Previous Studies on Numerical Modelling of Masonry Composites

The majority of existing numerical models for masonry composites can be classified in two categories (Giambanco et al. 2001):

- A one-phase material model treating masonry as an idealized homogeneous material with constitutive equations that differ from those of the components, and

- A multi-phase material model where the components are considered separately taking into account the interaction between them.

The constitutive models in the first category are relatively simple to utilize and require less input data and the failure criteria normally have a simple form. On the other hand, the derivation of constitutive equations is very complicated. These models are generally suitable for the study of global behaviour of masonry. The multi-phase material models are relatively costly to use as they deal with a greater number of the degrees of freedom. However, the constitutive equations of the component materials have normally a simple form. This type of model is generally suitable for the study of local behaviour for masonry structures/assemblages.

Many researchers have considered masonry as an assemblage of masonry units and mortar with average properties. Early investigations date back to 1965 when isotropic elastic behaviour of brick and mortar assemblages was assumed in order to simplify the problem (Rosenhaupt and Sokal 1965). Such linear analyses may be considered satisfactory in predicting deformations at low stress levels in the

elastic stress range, but are not expected to be adequate at higher stress levels when extensive stress redistribution occurs. This redistribution is caused by the nonlinear behaviour of the materials, cracking, and localized failure due to loss of bond between mortar, grout, reinforcement and units.

A method that accounts for the nonlinear behaviour of masonry was developed and applied to solid masonry by Page (1978) from the analogy of the behaviour of masonry assemblages and jointed rocks. In this study, masonry was considered as a two-phase material consisting of elastic bricks set in an inelastic mortar matrix modeled as spring joint elements. Failure in the joints was assumed to occur if a tensile or shear bond strength criterion was violated. These characteristics were incorporated into an incremental finite element program that modelled the nonlinear joint properties and allowed progressive joint failure to occur.

Hegemier and Arya (1982) extended this approach to grouted and hollow concrete masonry. The proposed model considered masonry as a discontinuous system along the mortar joints. In addition to separate modelling of mortar and masonry units, the physical behaviour of the interfaces was added by introducing pairs of double node elements. The interconnection between double nodes was specified to simulate the interface behaviour.

Use of spring interface elements in modelling of mortar joint modes of in-plane failure was also investigated by Saadeghvaziri and Mehta (1993) and Manos et al. (2003). In these studies, performance of various combinations of mortar and

spring element to represent mortar joints and its bond properties with masonry units was evaluated.

Since modelling of reinforced masonry structures with a discrete finite element model was not found to be computationally efficient, a smeared crack approach was implemented by many researchers including Ewing et al. (1987 and 1988), Lotfi and Shing (1991 and 1994), Shing et al. (1993a, 1993b), Mehrabi and Shing (1997), Lourenco (1996), Lourenco and Rots (1997), Khattab (1993), Maleki et al. (2005 and 2007), El-Dakhakhni et al. (2006), and there are many others. In this approach, the masonry and reinforcement are modeled separately using plane stress overlay elements and the effects of cracking are smeared over the masonry elements. The stress-strain relations of this model included tension stiffening, compression softening and strain softening as well as a degrading unloading rule which were essentially adopted from concrete studies (e.g. Kwak and Kim, 2004a and 2004b). Since, in fully grouted masonry walls, the bulk of the masonry consists of grout and concrete, mortar joints were not regarded as planes of weakness.

Lotfi and Shing (1991) assessed the capability of the smeared crack model in capturing the strength and various failure mechanisms of reinforced masonry shear walls. The results showed that while good agreement with respect to flexure dominated behaviour was observed, the prediction of brittle shear behaviour of lightly reinforced wall panels had major drawbacks due to an unrealistic kinematic constraints introduced by the imposed assumptions. In order to overcome this problem, Shing et al. (1993a and 1993b), Lotfi and Shing (1994), Cerioni and Donida

(1994), Mehrabi and Shing (1997), Shing and Cao (1997) and Maleki et al. (2007) integrated mortar joints into the foregoing model to account for the inherent inhomogeneity and anisotropy introduced by mortar joints. A constitutive model in a framework of plasticity was proposed to simulate the initiation and propagation of interface fracture as well as the experimentally observed dilatancy under combined shear and normal stresses. Adding the compressive failure of masonry to the constitutive model of unit-mortar interface, Lourenco (1996) and Lourenco and Rots (1997) developed a multi surface interface model capable of predicting cracking, slip, and crushing of the masonry components.

Khattab (1993) and El-Dakhakhni et al. (2006) also developed a multilaminate macro model in which the masonry assemblage was replaced by an equivalent material consisting of a homogenous medium intersected by two sets of planes of weakness along the head and bed joints. In this model, each masonry component was treated separately by establishing its own failure criterion. The overall response of the masonry assemblage was achieved by enforcing compatibility conditions and allowing for stress redistribution between components after failure of an individual component. This enabled the model to distinguish between different modes of failure for both reinforced and unreinforced masonry wall panels.

Due to great complexity in defining hysteretic stress-strain relations for concrete masonry and steel, only a small number of analytical studies, mostly adopted from reinforced concrete research, are attributed to the in-plane reversed

cyclic response of reinforced masonry walls. Seible et al. (1990) developed a numerical model to predict the complete nonlinear in-plane response of reinforced concrete masonry walls. The model followed a smeared crack approach and accounted for crack rotation. Reinforcement was treated as a smeared overlay. A cyclic stress-strain curve based on experimental work in concrete by Reinhardt (1987) was assumed for the masonry and steel was assumed to follow an elasto-plastic material law with strain hardening behaviour.

While it was not sensible to try to include all of the relevant previous numerical modelling in the above literature review, the referenced research was chosen to provide sufficient background on the current status of such modelling. This background served as the base for developing the numerical model presented in Chapter 2.

1.5.2   Review of Previous Studies on Testing of Small-Scale Models of Masonry Structures

1.5.2.1   Background

A comprehensive study of diverse type of structural modelling techniques and their applications to real structures has been addressed by Harris and Sabnis (1999). Among various classifications of structural models, direct models and strength models are most relevant for the purpose of this study and will be first discussed in this section.

In a **Direct Model,** geometry and loading are similar to the prototype in all respects. In this type of model, strains, deformations and stresses for each loading

condition are representative of similar quantities in the prototype for the corresponding loading condition (Harris and Sabnis 1999).

A **Strength Model**, also called a *realistic model* is a direct model that is made of materials that are identical or similar to the prototype materials such that the model will predict both elastic and inelastic behaviour of the prototype for all loads up to failure. This type of modelling is very restrictive in terms of choice of model materials and methods of fabrication (Harris and Sabnis 1999).

In order to achieve complete similarity (a true model) of the structural behaviour of masonry structures subjected to static and dynamic loading, each constituent material (block, mortar, grout and reinforcement) must satisfy each and every similitude requirements generated by dimensional analysis (Harris and Sabnis 1999). Under the assumption that there are no time dependent effect in the loading which influence the structural behaviour, such as the inelastic effects of cracking and yielding, the variables for the modelling of reinforced masonry structures are presented in Table 1.1 (Harris and Sabnis 1999).

The FLT system is used for dimensional analysis where the dimensions force of (F), length (L), and time (T) describe each quantity. In Table 1.1, the independent scale factors chosen for a true model approach are those for stress, S_σ, and length, S_l. All remaining scale factors are either unity or functions of S_σ and S_l. If it is assumed that the stresses caused by the self-weight of the structure are not significant, as may be the case in many reinforced masonry buildings, the scale factors given in Table 1.1 as a "practical true model", will be adequate for modelling

Table 1.1 – *Summary of dimension analysis for masonry under static or quasi-static loading (from Harris and Sabnis 1999)*

Group	Quantity	Dimension	True Model	Practical True Model
Loading	Concentrated load	F	$S_\sigma S_l^2$	S_l^2
	Line load	FL^{-1}	$S_\sigma S_l$	S_l
	Pressure	FL^{-2}	S_σ	1
	Moment	FL	$S_\sigma S_l^3$	S_l^3
Geometry	Linear dimension	L	S_l	S_l
	Displacement	L	S_l	S_l
	Area	L^2	S_l^2	S_l^2
Material Properties	Stress	FL^{-2}	S_σ	1
	Strain		1	1
	Modulus of elasticity	FL^{-2}	S_σ	1
	Poisson's Ratio		1	1
	Specific mass	FL^{-3}	S_σ/S_l	$1/S_l$

masonry structures. As indicated in Table 1.1, using a practical true model requires using the same stress-strain curves of both the model and the prototype masonry which is a very difficult challenge in small-scale modelling.

The approach taken in this study is to attempt to satisfy the practical true model requirements at the selected half-scale because of the availability of the model masonry blocks at this scale.

1.5.2.2 Size Effect in Small Scale Modelling

The effect of reducing size is one of the oldest scaling problems addressed by many researchers and inventors as cited in Bazant and Chen (1997):

> *"Among cords of equal thickness, the longest is the least strong"*
> *Leonardo da Vinci (1500s)*

This rule points out the commonly observed size effect in small scale modelling of structures where specimens of smaller size generally exhibit higher

strength with a greater scatter of data compared to the prototype specimens. Bazant and Chen (1997) and Harris and Sabnis (1999) addressed a large number of theoretical studies available in the literature on modelling. Although the size effect in structural modelling has been well accepted by experimentalists, this phenomenon is not yet fully understood. As addressed by Harris and Sabnis (1999) and Bazant and Chen (1997), one of the widely accepted statistical theories is the weakest-link concept which basically relates failure of the total assemblage to a single severe defect in any of the constituent elements (weakest-link). Consequently, the larger volume of full-size specimen results in a greater probability of material flaws likely to reduce strength.

Long (2006) summarized the results of numerous studies on the effect of small-scale modeling of structures with a main focus on the behaviour of qausi-brittle materials such as concrete and masonry. As a summary, the following key findings from various studies are cited:

- Shear strength at failure decreases with larger specimen size and smaller maximum aggregate size (Lubell et al. 2004).

- Higher concrete and steel strains are sustained in small-scale model of reinforced concrete beams prior to reaching the failure state. As a result, higher strain gradient/curvature is expected in smaller specimen. This also, in part, could explain the higher strength of reduced scale models compared to the prototype structure (Swamy and Qureshi 1971).

- Model structures exhibit fewer cracks than do prototype structures. This is

due to difficulties of modelling tensile strength of concrete. Moreover, relative crack spacing and crack width has been found to be higher in the model structures than the prototypes when aggregates are not scaled and reinforcing bond characteristics are the same as in the prototype (Swamy and Qureshi 1971).

- The bond strength between reinforcing steel bars and concrete is affected by the size of the bars. Results of pull out test of bars with different sizes and scaled embedment length indicate higher bond strength for smaller bars (Bazant and Sener 1968). The aggregate size was not altered in the forgoing test program, however, higher bond strength and stiffer bond behaviour have been reported for deformed wires cast in concrete containing coarse aggregate than in concrete with only fine aggregate (Harris and Sabnis 1999).

1.5.2.3 Small-Scale Modelling of Masonry

In the past, the high cost of full-scale testing of masonry structures has promoted small-scale modelling as a technique to provide an economical alternative to study both reinforced and unreinforced masonry structures. Although masonry is known to be one of the oldest and most classical types of construction in the history of mankind, the concept of using scaled models to study the behaviour of masonry is relatively new. An early engineered attempt to model masonry structure dates back to mid 1950s and was limited to research modelling of brick assemblages. The modelling of concrete masonry structures had less attention than brickwork until

the mid 1970s. The methodology and techniques for one-quarter-scale modelling of hollow concrete block masonry were developed by Harris and Becica (1978) at Drexel University. Their basic strength evaluation tests for compressive, flexural bond and shear strengths exhibited satisfactory correlation between model and prototype test results. A follow-up study was conducted by Hamid and Abboud (1986) and Abboud et al. (1990) using the same model units as Harris and Becica (1978). The behavioural characteristics of model ungrouted and grouted concrete masonry assemblages were investigated under shear and in-plane tension. Comparisons between model and prototype tests indicated excellent correlation and validated the feasibility of using the direct modelling technique for concrete block masonry at the assemblage level. Some deviations from prototype results were also observed. These deviations were believed to be attributed to size effect of aggregate size, imperfections in unit geometry and higher strength masonry blocks.

The feasibility of using the direct modelling technique in shear wall testing was assessed by Long (2005 and 2006) at McMaster University using half-scale concrete masonry units to model the behaviour of full-scale masonry shear walls under in-plane loading. Models of full-scale walls previously tested at McMaster University (Miller 2005 and Shedid 2005 and 2006) were constructed and loaded with attention paid to maintaining similarity. Based on the test results, small-scale shear walls designed to exhibit flexural load-deformation mechanisms were more similar to full-scale specimens than were walls designed to exhibit shear-dominated failure. Long (2005 and 2006) suggested that this was due to size-effects related to

cracking that more significantly affected the behaviour of walls failing primarily by diagonal cracking. Size effects, particularly related to the strain gradient effect, were shown to be more pronounced in the post-yielding region of behaviour of small-scale reinforced block walls. The half-scale walls were shown to have higher ductility and exhibited less damage at high displacement levels compared to corresponding full-scale walls. The blocks used in Long's (2006) research are the same as those used in this study.

1.5.3   Previous Studies on behaviour of Partially Grouted Reinforced Masonry Shear Walls

The in-plane behaviour of reinforced masonry shear walls under different combinations of axial load and lateral shear forces has been the main focus of many experimental investigations since the late 1950s. Early research programs were conducted by Schneider (1956 and 1959) and Scrivener (1966) on the effect of amount of horizontal and vertical reinforcement on the shear capacity of brick and concrete block reinforced masonry shear walls.

In Japan, Matsumura (1985, 1987, and 1990) conducted a comprehensive test program on full scale reinforced masonry shear walls. The main purpose of this research was to study the effect of shear reinforcement ratio, shear span ratio, axial compressive stress, and strength of materials as well as extent of grouting, (partial grouting and full grouting). A total of 57 concrete masonry walls and 23 brick walls were tested under two kinds of loading conditions, namely, "beam type" and "wall type". In the wall type loading method, walls with a fixed base and the top free to
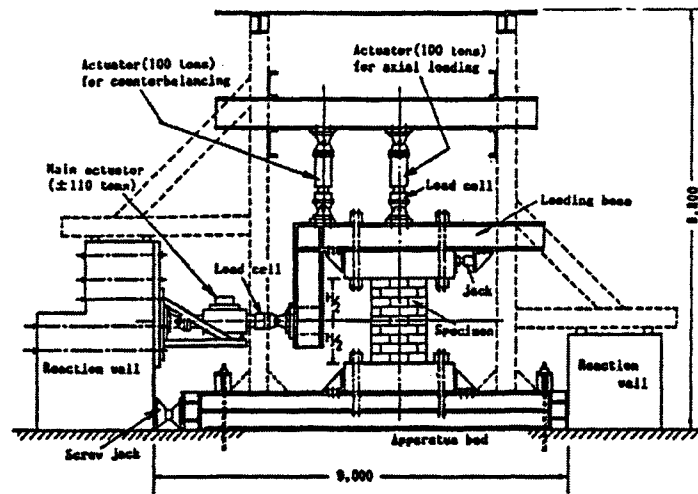
(a) Wall Type Loading
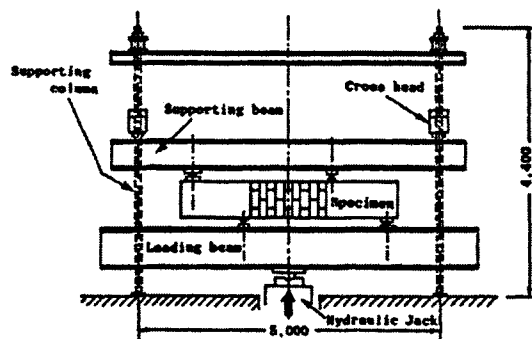
(b) Beam Type Loading

Figure 1.3 – *Outline of test setup used by Matsumura (1985)*

move horizontally, as shown in Figure 1.3-a, were subjected to horizontal shear

loads. In the beam type loading method, walls were laid horizontally and subjected

to vertical shear loads like the loading of a deep beam as illustrated in Figure 1.3-b.

Matsumura (1987) concluded that horizontal shear reinforcement enhanced the

truss effect within the walls by restraining the in-plane expansion of the walls due to

shear cracks. He also proposed a formula to predict the shear strength of ordinary

reinforced masonry walls (fully grouted), for different wall dimensions, uniaxial

compressive strength of grouted masonry, applied axial load, horizontal reinforcement ratio, and aspect ratio.

Shing et al. (1989, 1990a, 1990b, 1990c) performed another comprehensive study on the in-plane resistance of reinforced masonry shear walls by testing twenty two single storey reinforced masonry wall panels. The main purpose of this research was to investigate the flexural and shear behaviour of squat reinforced masonry wall panels under both monotonic and cyclic lateral loads. The effects of various design parameters were evaluated including the amounts of horizontal and vertical reinforcement and the level of applied axial load. Shing et al. (1990a) concluded that the flexural strength of a square wall panels can be predicted accurately using simple flexure theory based on simple plane-section assumption. It was also shown that the Uniform Building Code (UBC 1988) specifications appeared to be oversimplistic and very conservative for squat walls despite overestimating the added shear resistance provided by the horizontal reinforcement. Shing et al. (1990a and 1990b) proposed a new empirical shear formula taking into account the influence of axial stress and flexural reinforcement. It was also observed that changes in the overall shear stiffness prior to major diagonal cracking tended to be proportional to the axial compressive stress. The ductility of shear-dominated walls was found to be relatively low unless a large quantity of shear steel was introduced.

Adding to the previous study, the effect of aspect ratio of reinforced masonry shear walls was examined by Brunner and Shing (1996) though testing of three walls with low aspect ratios ranging from 0.60 to 0.96. With the additional data

along with the previous studies by Shing et al. (1990a and 1990b), a general analytical method was developed for walls having any aspect ratio. Based on the test results, Shing (1990a) classified the shear modes of failure into two different types depending on geometry. The first type, which occurs in walls with an aspect ratio slightly less than unity, is characterized by a major diagonal crack intersecting the base within the compression zone. This indicates that only part of the vertical force is transferred directly from the wall to the base at the compression toe. The remaining portion of the vertical force is transmitted across the diagonal crack which may rely on aggregate-interlock forces and perhaps some dowel action of vertical steel as well as tension in the horizontal reinforcement crossing the crack. The second classification is for a wall that is sufficiently squat that the diagonal crack originating at the upper corner of the wall panel falls outside the compression zone at the base. In this case, Brunner and Shing (1996) suggested that the entire area bounded by the compression block is effective in providing shear resistance at the compression toe. Since the normal compression across the diagonal crack is expected to be small, the aggregate-interlock forces were neglected in this case.

Fattal and Todd (1993) and Fattal (1993a and 1993b) evaluated the accuracy of four equations proposed by Matsumura (1987), Okamoto et al. (1987), Shing et al. (1990a and 1990b) and UBC (1988) in predicting the ultimate shear capacity of reinforced masonry shear walls. The shear equations were assessed using the experimental results of 62 reinforced masonry shear wall tests done by previous researchers. Two of the equations, Matsumura (1987) and UBC (1988) were found

to be inadequate for the prediction of ultimate shear strength of masonry walls. The equation proposed by Shing et al. (1990a) was found to predict shear strength well for a limited range of variables. It was suggested that the problem with the shear strength predictions was primarily due to excessive weight being given to the contribution of horizontal reinforcement to strength. The equation proposed by Matsumura (1987) was the closest predictor of ultimate strength although it showed some inconsistency. Correlation provided by the Matsumura (1987) equation was close for high strength walls but could not closely predict the shear strength of low strength walls, horizontally reinforced walls, unreinforced masonry walls and partially grouted reinforced masonry shear walls.

Schultz (1996) proposed a rational equation for the minimum horizontal reinforcement limits for seismic design of shear-critical masonry shear walls. The proposed formula, which agreed reasonably well with previous shear walls tests (Shing et al. 1990a and 1990b), was based on strength and energy criteria and was simplified for design applications. The strength criterion was influenced by material strengths such as masonry strength and yield strength of horizontal reinforcement, while the energy criterion was based on wall geometry.

Seible et al. (1993, 1994a, and 1994b) conducted a full-scale test of a five-storey building under simulated seismic loads at the University of California, San Diego (Figure 1.4). This remarkable project consisted of a total of 75 tests on a full-scale reinforced masonry research building constructed with coupled, flanged, fully grouted masonry walls and precast prestressed concrete hollow-core plank
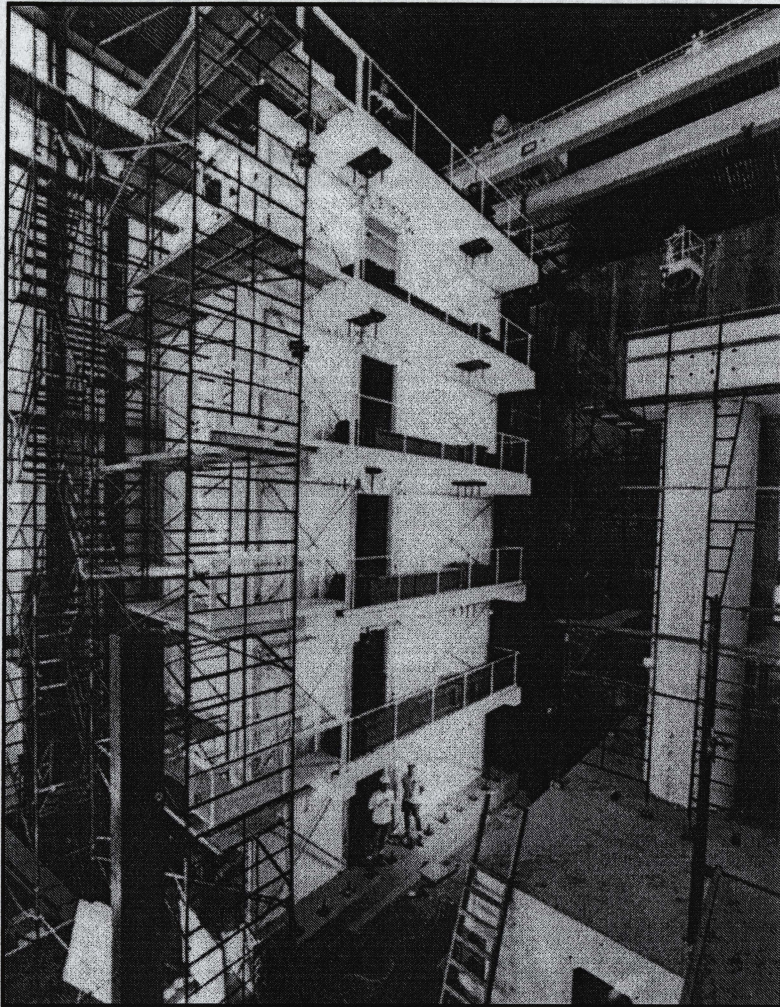
Figure 1.4 – *Full-scale five-story reinforced masonry research building (from Seible et. al. 1994)*

floors with reinforced concrete topping. The simulated seismic loads obtained from

selected earthquake ground acceleration records were applied to the building using

a new testing procedure called "Ground Sequential Displacement (GSD) Procedure"

(Seible et al. 1994a). This testing procedure is directly based on pseudodynamic

testing principles and can be applied in cases where full-scale shake-table testing is

not feasible or where response studies in pseudotime are advantageous to obtain

data at rates that allow in-test modifications. The overall displacement ductilities achieved for the building during the seismic load simulation tests were approximately 6 and 9 in the pull and push loading directions, respectively, corresponding to building drift levels of 1.0% and 1.5%, respectively. Overall, the test results indicated that, with appropriate design considerations, even stiff-structure-wall-type masonry buildings can exhibit a very ductile response well beyond the required design specifications.

Moon et al. (2003a, 2003b, and 2004) also tested a full-scale two-storey unreinforced masonry research building under cyclic reversed lateral loads at Georgia Institute of Technology. Several analytical methods were evaluated through direct comparison between the predictions and experimental results. The series of analyses included 3D finite element elastic analysis, dynamic analysis based on a simplified conceptual model, nonlinear finite element analysis employing contact elements, and nonlinear pushover analysis employing nonlinear spring elements (Moon et al. 2003a). It was shown that correct prediction of the maximum strength is not achieved unless the influence of flanges is considered. The overall behaviour of walls in the building, relevance between individual component tests and the overall structural performance as well as effectiveness of several retrofit techniques were also investigated through this study (Moon et al. 2003b).

Despite the attention paid to the behaviour of reinforced masonry (RM) shear walls, comparatively little effort has been dedicated to understanding the in-plane response of partially grouted-reinforced masonry (PG-RM) shear walls

characterized by large spacing between vertical and horizontal reinforcement. One of the early attempts to study the effect of partial grouting of reinforced masonry shear walls dates back to the mid 1980s when Matsumura (1987) conducted tests on numerous large and small-sized wall specimens. The walls were made of hollow units including both partially and fully grouted cases. Based on the test results, it was concluded that, for concrete masonry walls, shear strength of partially grouted walls (using the horizontal net area of the walls) are generally lower than when fully grouted. He also concluded that shear reinforcement in partially grouted concrete masonry walls was less effective than in similar fully grouted walls.

Research on partially grouted partially reinforced masonry walls was carried out at Drexel University in the 1990's using the small-scale modelling technique (Hamid and Chandrakeerthy 1992, Ghanem et al. 1993 and Ghanem 1992). Hamid and Chandrakeerthy (1992) studied the effect of extent of grouting on the compressive strength of partially grouted concrete masonry. The test results indicated that ultimate compression load per unit length of partially grouted masonry walls increased and variability decreased as grout spacing decreased. Ghanem (1992) and Ghanem et al. (1993) tested fourteen one-third scale models of partially grouted reinforced masonry shear walls made of one-third scale model concrete masonry blocks. The main objective of this project was to investigate the effects of various design parameters and loading conditions, namely, axial load, block strength, and amount and spacing of horizontal and vertical reinforcing steel bars on the capacity and inelastic load resistance mechanisms of partially grouted

reinforced masonry shear walls subjected to in-plane monotonic and cyclic lateral loading. The test results showed that increasing axial load significantly increased the ultimate load carrying capacity of the test walls as well as the initial stiffness of the uncracked section. Also, increasing the axial stress resulted in reduced ductility, increased cracking strength and changed the failure mode from flexure to shear. It was also concluded that, to avoid brittle behaviour, the axial stress should be not more than five percent of the masonry compressive strength.

Fattal (1993a) modified the shear strength equation proposed by Matsumura (1987) to obtain a closer correlation with the test results of partially grouted as well as fully grouted reinforced masonry shear walls. The proposed equation was then evaluated by conducting a critical parameter study on lateral-load response characteristics of partially grouted reinforced masonry shear walls (Fattal 1993b). The critical parameters were axial stress, compressive strength of masonry, aspect ratio of wall, and horizontal and vertical reinforcement ratios. The experimental database was selected from partially grouted shear wall tests reported in Fattal (1993a). The results of the study indicated a need for additional experimental and analytical/numerical research to develop an adequate basis for design of masonry shear walls.

Ingham et al. (2001) reported on studies conducted in New Zealand to evaluate the reinforcement requirements specified in New Zealand's masonry design standard (Code of Practice for the Design of Masonry Structures, NZS 4230:1990, 1990). The results of 16 concrete masonry shear wall tests having a maximum spacing of vertical reinforcement of 800 mm indicated sufficient inelastic

deformation capacity to satisfactorily develop a displacement ductility ratio greater than two. Based on the results of testing partially grouted masonry walls with an opening, they also concluded that considering frame action to occur due to the presence of the bond beam at the top of an opening may lead to considerable over-estimation of wall strength. Instead, it was recommended that masonry piers on either side of a penetration should be treated as separate vertical cantilevers.

Elshafie et al. (2002) also studied the effect of openings on lateral loading response of shear walls through testing thirteen one-third scale reinforced concrete masonry shear walls designed to exhibit a flexure-dominated failure mode. Based on the test results, the performance of a proposed simple analytical approach employing plastic hinge failure mechanisms for single-storey shear walls with openings was assessed. Comparison of the prediction results with experimental measurements showed very good agreement in terms of the walls' ultimate lateral load capacities and failure mechanisms. Elshafie et al. also concluded that the effects of openings on reduction of wall strength and stiffness were proportional (per cent reduction in stiffness because of openings is similar to the per cent reduction in strength).

At the University of Auckland, Voon and Ingham (2005) and Voon (2007) evaluated the effect of openings on the performance of partially grouted reinforced masonry shear walls (with maximum 800 mm bar spacing) under seismic loading conditions. The test program consisted of eight PG-RM shear walls with variations in lintel reinforcement detailing and a range of opening geometries. The test results

showed good accuracy for the strut-and-tie analytical method proposed to evaluate the strength of partially grouted reinforced masonry shear walls.

1.6   CLOSING REMARKS

Previous studies on partially grouted reinforced masonry shear walls, though very limited, indicated that shear walls with widely spaced reinforcing bars can provide adequate ductile behaviour with proper design. However, a better understanding of the response of this type of masonry shear walls under cyclic in-plane lateral loading is required in order to promote larger bar spacing and adjusted force modification factors compared to the current minimum requirements of the Canadian masonry standard (CSA S304.1 2004).

In addition, no numerical effort was found to be exclusively dedicated to modelling partially grouted reinforced masonry shear walls. Due to the special characteristics of PG-RM walls, such as sudden changes in material and geometric properties close to the reinforced grouted cells, particular attention needs to be paid to the numerical simulation of the behaviour of this type of wall.

In general, study of the previous research on the response of shear walls under lateral loading showed that a better evaluation of predictor equations for the ultimate lateral load capacity, energy dissipation (load modification factor) and wall stiffness estimation requires more experimental evidence as well as reliable numerical simulation.

CHAPTER 2

A TWO-PHASE MATERIAL MODEL FOR MASONRY

2.1 INTRODUCTION

Masonry, with the significant heterogeneity and anisotropy resulting from the presence of clay or concrete units, mortar, grout and steel bars, has been recognized as one of the most challenging composite materials for numerical simulation. In addition to the variety of the constituent components, their highly nonlinear and asymmetric stress-strain relationships as well as great complexity of the interaction effects has increased the difficulties in developing an accurate modelling method that can adequately predict the behaviour of this system of construction. Nevertheless, to date, various types of numerical techniques have been developed to enhance the basic understanding of the pre- and post-peak responses of masonry components with particular emphasis paid to shear walls as the main lateral loadbearing elements in modern masonry structures.

29

In this chapter, building on previous work in reinforced concrete and reinforced/unreinforced masonry, a numerical model is proposed to simulate the in-plane behaviour of partially grouted reinforced masonry shear walls subjected to axial and in-plane lateral loading. The material model and related constitutive relations are described after this introduction. The nonlinear finite element program developed for this study and the applied solution algorithm are then reviewed. The performance of the model is evaluated in two sections by direct comparison between available experimental data and the numerical results obtained from the proposed model. First, the model employed for masonry is evaluated based on the results of reinforced masonry shear wall tests done by Shing (1989 also cited in Ewing et al. 1990). Then, the accuracy of the unit-mortar interface model is assessed through direct comparison between the experimental observations of partially grouted reinforced masonry shear wall tests done by Ghanem et al. (1993) and the predictions of the finite element model. A brief discussion on the results follows each evaluation.

2.2   MATERIAL MODEL AND CONSTITUTIVE RELATIONS

In the proposed numerical model of this study, each concrete masonry block is represented by two individual continuum elements for unreinforced masonry or by two multi-layered continuum elements for reinforced masonry. In this approach, the effect of cracking in masonry is smeared over the entire element by modifying the material properties of the masonry in the principal directions. As illustrated in Figure 2.1, the contribution of horizontal and/or vertical steel reinforcement is included using an adjoining overlaid element assuming perfect bond between the
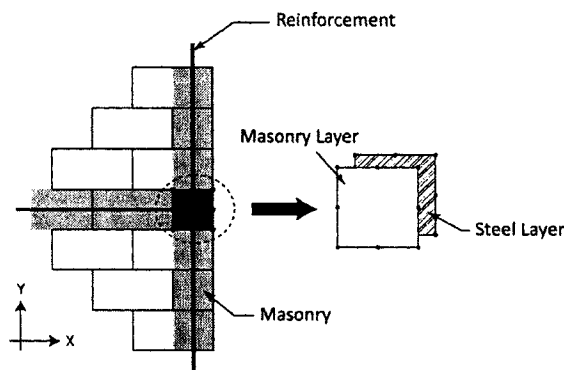
Figure 2.1 – Layered element employed for reinforced masonry model

layers of masonry and steel. Despite the assumption of perfect bond, the interaction

between grout and steel bar is implicitly considered in the tension stiffening model

of the masonry.

Previous studies on fully grouted masonry shear walls under in-plane loading

(Lotfi and Shing 1991, Ewing et al. 1990 and Maleki 2005) have shown that using a

smeared crack model with no distinction between masonry units and mortar joints

can produce reliable numerical results. This is mainly because of the effect of

grouting which reduces the anisotropy generated by mortar joints to a negligible

level. In contrast, debonding and shear-slip at the interface of masonry units and

mortar joints, in the form of continuous or stepped-pattern cracking, has been one

of the dominant local failure modes observed in unreinforced ungrouted masonry

shear wall tests (Lotfi and Shing 1994, Lourenco 1996). This emphasizes the

necessity of considering mortar joints as planes of weakness in numerical

simulation of this type of shear wall. Since partially grouted reinforced masonry

shear walls consist of both reinforced and unreinforced sections, mortar joints are

separately introduced in the model as a secondary material phase. The above

mentioned material models are described next.

2.2.1 PHASE ONE: Model for Grouted Masonry

2.2.1.1 Stress-Strain Relationship for Masonry

Masonry units are represented by an orthotropic smeared crack approach with similar but modified constitutive relations along the axes of orthotropy following cracking. These axes coincide with the principal directions of total strain and are continuously updated during analysis. Once the principal tensile stress exceeds the uniaxial tensile strength of masonry in one direction, cracking initiates in the normal direction and the constitutive relations along the existing principal axes are updated (Figure 2.2). This technique, the so-called rotating crack model, has been shown by Lotfi and Shing (1991) and Maleki et al. (2005) to be in good agreement with experimental results while the alternative approach, the fixed crack model, due to the constrain of crack direction underestimates the post-peak strength degradation compared to the experimental data.
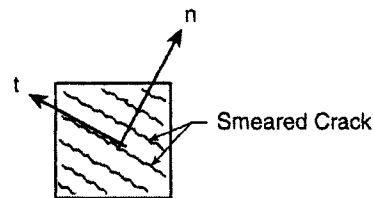
Figure 2.2 – Orientation of the axes of orthotropy

Due to the Poisson's effect and microcrack confinement, combinations of different biaxial stresses alter the strength and constitutive characteristics of masonry compared to those for uniaxial loading. In order to include this behaviour, the masonry strength in each principal direction is modified using the following equations (see Figure 2.3):

$$f_p = \lambda f'_m \tag{2.1}$$

$$\varepsilon_p = \lambda \varepsilon_o \tag{2.2}$$

where f'_m is the uniaxial compressive strength of masonry and ε_o is the strain at f'_m.

The parameter f_p is the equivalent compressive strength of biaxially loaded

masonry and ε_p is the corresponding strain at f_p. The modification factor, λ, is

defined based on the ratio of principal stresses or principal strains at each point.

According to the model originally proposed by Kupfer et al. (1969), for a

compression-compression biaxial state of stress, λ acts as an amplification factor

increasing the uniaxial compressive strength of masonry based on the following

equation:

$$\lambda = \frac{1 + A_0 \sigma_1 / \sigma_2}{\left(1 + \sigma_1 / \sigma_2\right)^2} \qquad 0 \le \sigma_1 / \sigma_2 \le 1 \tag{2.3}$$
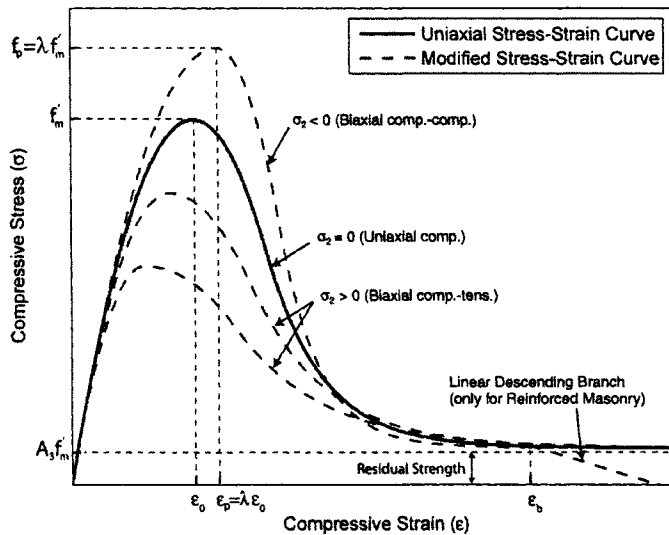
Figure 2.3 – *Modified stress-strain curve for masonry under biaxial state of stress*

where σ_1 and σ_2 are the principal stresses. The parameter A_0 is used to adjust the

model for different material properties and a value of 3.65 is suggested by Kupfer et

al. (1969) for concrete applications. Although this value is employed here, further

studies need to be conducted for masonry applications. This model exhibits a

maximum increase of 26% in compressive strength when the stress ratio σ_1 / σ_2 is

about 0.5.

Under a *tension-compression* state of stress, the compressive strength of

masonry decreases. Tests on reinforced concrete panels (Vecchio and Collins 1986)

have shown that, at the onset of cracking, this reduction is a function of lateral

tensile strain rather than tensile stress. In this case, λ defines a reduction factor

based on the following set of equations (Ewing et al. 1990):

$$\lambda = \begin{cases} 1.0 & \varepsilon_1 / \varepsilon_2 \geq -0.56 \\ \left[0.85 - 0.27 \left(\varepsilon_1 / \varepsilon_2 \right) \right]^{-1} & -0.56 > \varepsilon_1 / \varepsilon_2 \geq -20.0 \\ 0.16 & \varepsilon_1 / \varepsilon_2 < -20.0 \end{cases} \qquad (2.4)$$

where ε_1 and ε_2 are the principal strains considering positive values in tension and

negative values in compression. The same sign convention applies for stress values

throughout the proposed model

In the *tension-tension* biaxial combination of stress, the tensile strength

remains equal to the uniaxial properties in both directions of principal strain.

The uniaxial stress-strain relation of masonry in compression is presented in

Figure 2.4-a. This relation has been used in concrete and masonry by many

researches (for example, Lotfi and Shing 1991, Kwak and Kim 2004, Darwin and
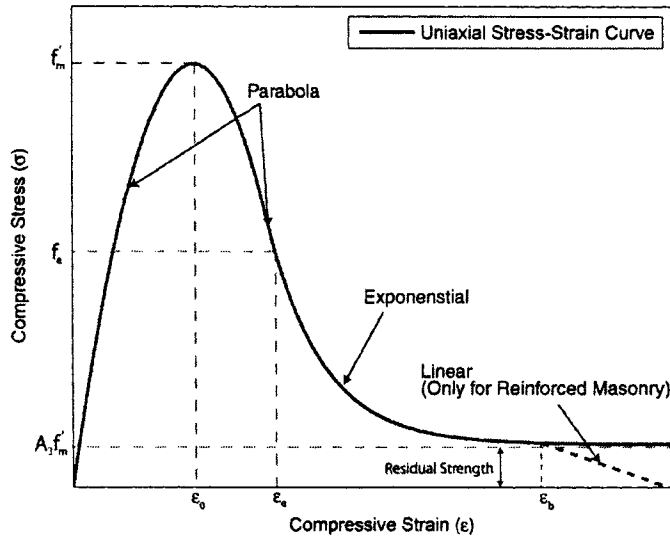
(a) Compression
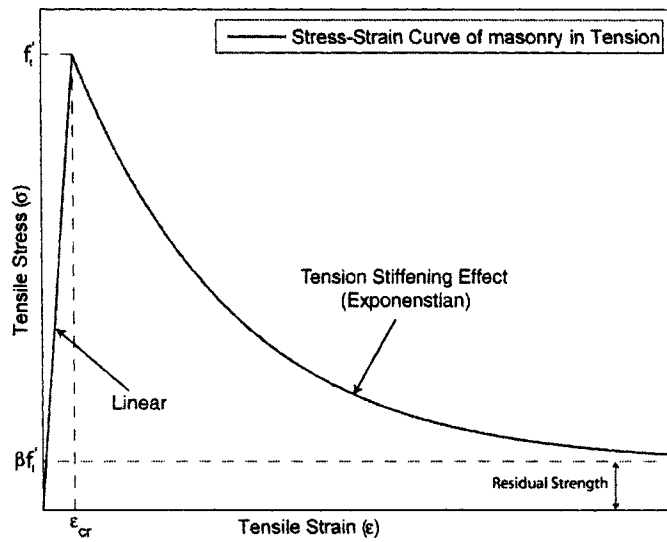
(b) Tension

Figure 2.4 – Uniaxial stress-strain relation for masonry

Pecknold 1977) and is expressed by the following equations (Ewing et al. 1990):

$$\sigma(\varepsilon) = \begin{cases} f_m' \left[A_1 (\varepsilon/\varepsilon_\circ) - (A_1 - 1)(\varepsilon/\varepsilon_\circ)^2 / \lambda \right] & 0 \geq \varepsilon \geq \varepsilon_p & (2.5) \\ f_p \left[1 - \left((\varepsilon - \varepsilon_p)/(A_2 \varepsilon_\circ - \varepsilon_p) \right)^2 \right] & \varepsilon_p > \varepsilon \geq \varepsilon_e & (2.6) \\ f_e \left[A_3 (f_m / f_e) + (1 - A_3 (f_m / f_e)) \exp(-\gamma(\varepsilon - \varepsilon_e)/\varepsilon_e) \right] & \varepsilon < \varepsilon_e & (2.7) \end{cases}$$

The parameter A_1 controls the shape of the rising branch and its value ranges from 1.0 to 2.0 where $A_1 = 1.0$ defines a linear behaviour prior to the peak strength and $A_1 = 2.0$ gives a parabolic shape for the rising branch of the curve. The parameter A_2 controls the shape of the initial falling branch and its value can be greater or equal to one. The parameter A_3 alters the lower limit of the exponential falling branch and its value can vary from zero to one. Equation (2.7) defines the exponential tail of the curve. The point (ε_e, f_e) indicates the transition from the curve defined by Equation (2.6) and the one defined by Equation (2.7) where ε_e is the point of tangency calculated based on the following equation:

$$\varepsilon_e = \varepsilon_\circ \left(1 + \lambda A_4 (A_2 - 1) \right) \tag{2.8}$$

Parameter f_e in Equation (2.7) is the corresponding compressive stress to ε_e and A_4 adjusts the initial point of the exponential tail. The parameter, γ, is determined such that Equation (2.7) becomes tangent to Equation (2.6) at ε_e and is defined by the following equation:

$$\gamma = 2\lambda \frac{f_m}{f_e} \times \frac{\varepsilon_e}{1 - A_3\left(f_m / f_e\right)} \times \frac{\left(\varepsilon_e - \varepsilon_p\right)}{\left(A_2\varepsilon_\circ - \varepsilon_p\right)^2} \qquad (2.9)$$

It is documented that the failure of a masonry shear wall is mainly initiated by crushing of the compressed toe followed by the degradation of the wall's load resistance (Drysdale et al. 1999, Shing et al. 1989, 1990a and 1990b). The onset of crushing exposes the embedded vertical reinforcing steel bars to large out-of-plane deformation due to inelastic buckling and consequently rapid degradation of strength at the toe of the wall. For a partially grouted reinforced masonry shear wall with large spacing between columns of grouted cells, this effect becomes more critical since the loss of a grouted-reinforced cell represents a large component of the compression capacity. This effect can play a key role in defining the softening response of this type of masonry shear wall after reaching the peak load. Thus, for an accurate simulation of post-peak response of a partially grouted reinforced masonry shear wall, it is necessary to include the effect of buckling of compressive steel reinforcement in the material model of reinforced masonry.

To investigate the behaviour of the compression toe of a partially grouted reinforced masonry shear wall after buckling of embedded vertical reinforcement, a series of uniaxial compressive tests, as described in detail in Section 2.4, were carried out on reinforced and unreinforced masonry prisms filled with grout. The prisms were three-blocks high and a half-block long simulating the exterior column

of grouted cells in the extreme compression zone of a partially grouted reinforced

masonry shear wall as shown in Figure 2.5. The comparison between the stress-strain relation of the reinforced and unreinforced grouted specimens, as presented in Section 2.4, indicates almost linear strength degradation associated with buckling of vertical reinforcement. Accordingly, to reflect this behaviour in the material model used for reinforced masonry, a linear descending branch is added to the end of the stress-strain relation of both masonry and steel within a specified strain range. This behaviour, illustrated in Figure 2.4-a (also see Figure 2.6), is defined by the following equation:

$$\sigma(\varepsilon) = \sigma_{bm} - A_5(\varepsilon - \varepsilon_b) \le 0 \qquad \varepsilon < \varepsilon_b \tag{2.10}$$

In this equation, ε_b defines the strain at which buckling starts and σ_{bm} is the corresponding stress value determined by Equation (2.7) (note that compression is negative in the equations). The parameter A_5 defines the strength degradation rate due to buckling of a compressive steel bar. According to this model, once strain in masonry reaches the bar buckling limit specified by ε_b, the compressive strength of masonry reduces to zero in a strain interval approximately equal to:

$$\Delta \varepsilon_b = A_3 f_m / A_5 \tag{2.11}$$

In this equation, the small exponential terms of Equation (2.7) are neglected. As described in Section 2.2.1.2, similar linear degradation within the same strain interval is assumed for axial resistance of the vertical steel bar at the compressed toe.
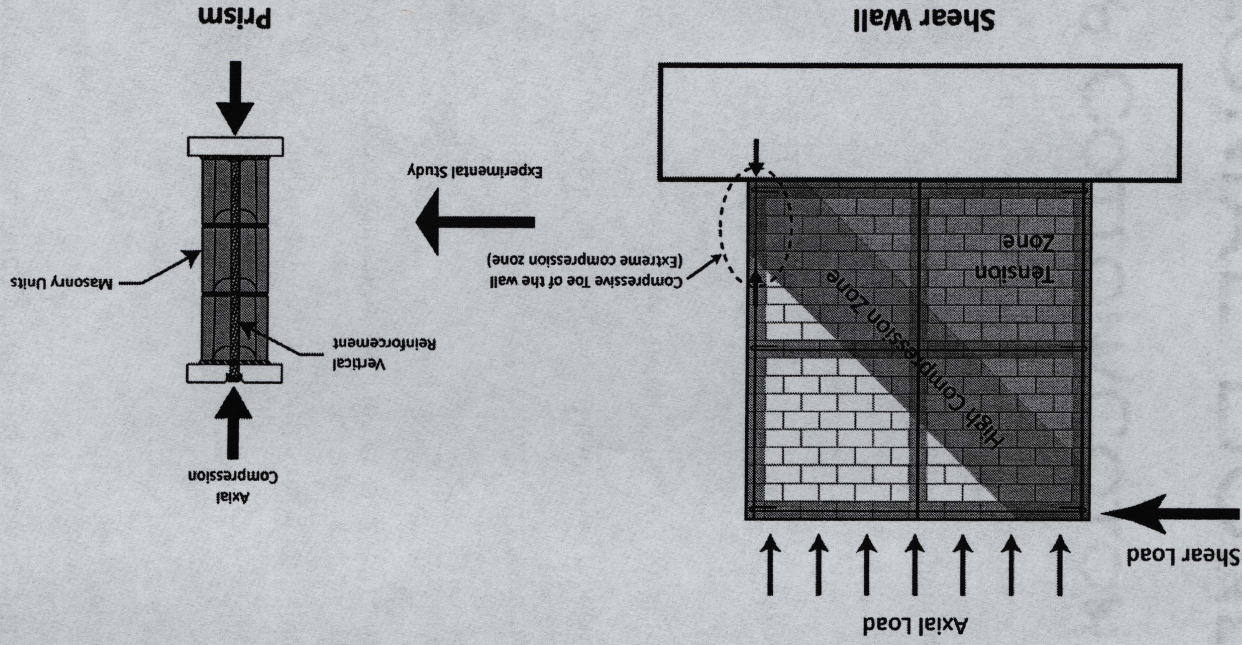
The stress-strain relation of masonry in tension is assumed to be independent of lateral compressive stress and is defined by a linear behaviour prior to cracking followed by an exponentially descending branch (Figure 2.4-b). This relation is defined by the following equations:

$$\sigma(\varepsilon) = \begin{cases} E_t \varepsilon & 0 < \varepsilon \le \varepsilon_{cr} \\ f_t' \left[\beta + (1-\beta)\exp\left(-\alpha(\varepsilon - \varepsilon_{cr})/\varepsilon_{cr}\right) \right] & \varepsilon > \varepsilon_{cr} \end{cases} \quad (2.12)$$

The parameter β controls the lower limit of the exponential branch and α incorporates the effect of tension stiffening (Kupfer et al. 1969) where ε_{cr} is the strain at which masonry cracks.

The constitutive model used for masonry is comprised of two stages. The first stage is applicable prior to tensile cracking and follows the model presented by Darwin and Pecknold (1977) which is defined by the following constitutive matrix:

$$\mathbf{D_m} = \frac{1}{1-\nu^2} \begin{bmatrix} E_1 & \nu(E_1 E_2)^{1/2} & 0 \\ \nu(E_1 E_2)^{1/2} & E_2 & 0 \\ 0 & 0 & (1-\nu^2)G \end{bmatrix} \quad (2.13)$$

where E_1 and E_2 can be either the secant or the tangent moduli of elasticity in the directions of the principal axes of total strains. The parameter ν indicates the Poisson's ratio and G is the shear modulus. Since the shear strain vanishes in the principal directions, the shear modulus will not provide any contribution to the constitutive model of masonry. Nevertheless, from the invariance condition under general transformation of the reference axes, the following relation for G is derived:

$$G = \frac{E_1 + E_2 - 2v\sqrt{E_1 E_2}}{4(1-v^2)} \qquad (2.14)$$

After tensile cracking, the constitutive matrix is changed to:

$$D_m = \frac{1}{1-v^2}\begin{bmatrix} E_1 & 0 & 0 \\ 0 & E_2 & 0 \\ 0 & 0 & (1-v^2)G \end{bmatrix} \qquad (2.15)$$

where, $G = (E_1 + E_2)/4(1-v^2)$. The constitutive matrix of masonry is transformed from the local principal directions to the global coordinate system using the following transformation relation:

$$\bar{D}_m = T^T D_m T \qquad (2.16)$$

where

$$T = \begin{bmatrix} \cos^2\theta & \sin^2\theta & \cos\theta\sin\theta \\ \sin^2\theta & \cos^2\theta & -\cos\theta\sin\theta \\ -2\cos\theta\sin\theta & 2\cos\theta\sin\theta & \cos^2\theta - \sin^2\theta \end{bmatrix} \qquad (2.17)$$

and θ is the inclination of the axes of orthotropy with respect to the global coordinate axes.

2.2.1.2 Stress-Strain Relationship for Steel

As shown in Figure 2.6, the stress-strain relationship for steel before and after yielding is represented by an idealized bilinear strain hardening behaviour which is assumed to be identical in tension and compression. Rupture of the steel is considered in the model by limiting the tensile strain to the ultimate strain of steel in tension. Similar to the masonry model, the effect of buckling of the reinforcing steel bar is simply represented by a linear descending branch attached to the stress-
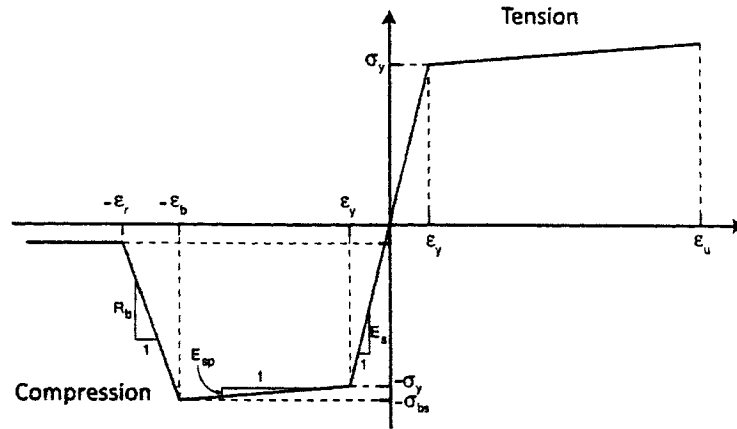
Figure 2.6 – *Uniaxial stress-strain relation for steel*

strain curve of steel in compression. This behaviour is consistent with the experimental evidence provided by the uniaxial compression tests on reinforced masonry prisms (see Section 2.4 for details). Strength degradation due to buckling of the reinforcement starts at ε_b which is the same buckling strain as defined in the masonry model. The residual strength of steel, σ_r, is assumed to be $0.1\sigma_y$ in which σ_y is the yielding strength of steel. The degradation rate of the reinforcing steel bar is defined by the following equation:

$$R_b = \frac{\sigma_{bs} - \sigma_r}{\Delta_b} \qquad (2.18)$$

where σ_{bs} is the stress corresponding to ε_b at which point buckling initiates. Δ_b was previously defined by Equation (2.11).

The constitutive matrix for steel is defined by:

$$\mathbf{D}_s = \begin{bmatrix} \rho_h E_{sx} & 0 & 0 \\ 0 & \rho_v E_{sy} & 0 \\ 0 & 0 & 0 \end{bmatrix} \qquad (2.19)$$

where E_{sx} and E_{sy} are the secant or tangent moduli of steel in the x- and y-directions

depending on the stress integration scheme. The parameters ρ_h and ρ_v are local

reinforcement ratios in the x- and y- directions, respectively. A dummy zero value is

assigned in the absence of steel reinforcement. The constitutive matrix of steel is

added to the constitutive matrix of masonry in the global coordinate system.

2.2.2 PHASE TWO: Model for Unit-Mortar Interface

The behaviour of a mortar joint and its interface with a masonry unit is

simulated using a plasticity based technique. The model, adopted from Lotfi and

Shing (1994), comprises the initiation and propagation of fracture of the unit-

mortar interface under combined normal and shear stresses and includes joint

dilatancy due to the roughness of the fracture surface.

2.2.2.1 Yield Criterion

The yield criterion, as the elastic limit, is described by a three-parameter

hyperbolic surface, which offers a smooth evolution between Mohr-Coulomb and

tension cut-off yield criteria. This surface, shown in Figure 2.7, is expressed by:

$$F(\mathbf{\sigma},\mathbf{q}) = \tau^2 - \mu^2 (\sigma - s)^2 + 2r(\sigma - s) \qquad (2.20)$$

in which $\mathbf{\sigma} = \{\tau \ \sigma\}^T$, where τ and σ are shear and normal stresses. In this

equation, the internal variables $\mathbf{q} = \{s, r, \mu\}^T$ represent the mechanical properties of

the contact surface which contribute in defining the shape of the yield surface. The

parameter s defines the tensile resistance, μ is the slope of the asymptotes of the

hyperbola corresponding to the friction coefficient between a masonry unit and mortar joint and $r = (c^2 - \mu^2 s^2)/2s$ defines the radius of curvature of the yield surface at the vertex of the hyperbola in which c is the cohesion value. As shown in Figure 2.7, $\mathbf{q}_o = \{s_o, r_o, \mu_o\}^T$ indicates the initial intact interface and $\mathbf{q}_r = \{0, r_r, \mu_r\}^T$ shows the residual values corresponding to the final state of interface where the tensile resistance of the unit-mortar interface becomes zero.
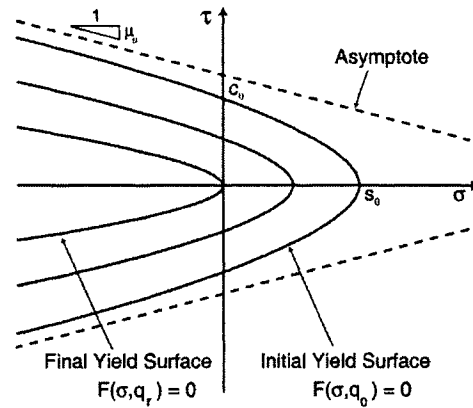
Figure 2.7 – *Hyperbolic yield surface for unit-mortar interface model (Lotfi and Shing 1994)*

2.2.2.2   Plastic Potential Surface

A nonassociated flow rule is employed (Lotfi and Shing 1994) to model the dilation of the contact area due to the roughness of the fractured surface. Accordingly, the plastic potential surface is defined by:

$$Q(\boldsymbol{\sigma}, \mathbf{q}) = \eta \tau^2 + (r - r_r)(\sigma - s) \tag{2.21}$$

$$\dot{\mathbf{d}}^p = \lambda \frac{\partial Q}{\partial \boldsymbol{\sigma}} \tag{2.22}$$

in which η adjusts the dilatancy of the interface model by controlling the direction

of plastic flow, $\mathbf{d}^p = \{\dot{d}_t^p \quad \dot{d}_n^p\}^T$ is the rate of plastic deformation in the transverse and

normal directions, and λ is the plastic multiplier. As shown in Figure 2.8, consistent

with experimental evidence (Pluijm 1994), the dilatancy in the interface model

decreases when the compressive (normal) stress increases. Furthermore, for a given

compressive stress, the rate of dilatancy decreases with increasing cumulative

relative tangential displacements (Lotfi and Shing 1994).

2.2.2.3 Softening Behaviour

The softening behaviour of the unit-mortar interface is governed by

preserving the Mode-I (pure tensile) and Mode-II (pure shear) fracture energies per

unit volume during the strength degradation. It is assumed that in the shear-tension

region, the tensile strength, s, decreases while the shear strength produced by r

and μ remains unchanged. However, in the shear-compression zone, both tensile

and shear strength decrease due to the progression of plastic flow (Lotfi and Shing

1994). The internal parameters describing the yield surface are controlled by the
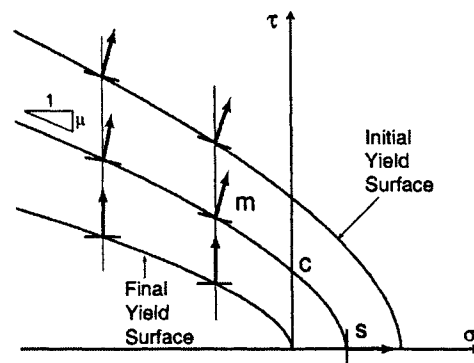
Figure 2.8 – Evolution of plastic potential surface during plastic flow (Lotfi and Shing 1994)

following softening relations proposed by Stankowski (1992):

$$s = s_o \left(1 - \frac{\kappa_1}{G_f^I} - \frac{\kappa_2}{G_f^{II}} \right) \tag{2.23}$$

$$r = r_r + (r_o - r_r) e^{-\beta \kappa_3} \tag{2.24}$$

$$\mu = \mu_r + (\mu_o - \mu_r) e^{-\alpha \kappa_3} \tag{2.25}$$

where G_f^I and G_f^{II} are the fracture energies corresponding to Mode-I and Mode-II conditions. The α and β terms adjust the rate of softening. The tensile strength degradation is controlled by κ_1 and κ_2 while frictional shear strength degradation is controlled by κ_3 given the following plastic flow equations (Lotfi and Shing 1994):

$$\dot{\kappa}_1 = \sigma \dot{d}_n^p \quad if \quad \sigma \geq 0 \tag{2.26}$$

$$\dot{\kappa}_2 = \left[\tau - \tau_{r1} \text{sign}(\tau) \right] \dot{d}_t^p \tag{2.27}$$

$$\dot{\kappa}_3 = (\tau_{r1} - \tau_{r2}) \text{sign}(\tau) \dot{d}_t^p \tag{2.28}$$

in which $\tau_{r1} = \mu^2 \sigma^2 - 2r\sigma$ and $\tau_{r2} = \mu_r^2 \sigma^2 - 2r_r \sigma$. It is assumed that τ_{r1} and τ_{r2} are zero in the tension-shear region.

2.2.2.4 Integration of the Constitutive Equations

To update the stress state based on the described plasticity equations, an explicit strain-driven return-mapping algorithm is employed. Even though the implicit backward Euler scheme has been shown to be more stable (Ortiz and Popov 1985), the explicit forward Euler scheme is used to simplify the correction step since the yield surface is defined by a single smooth hyperbolic curve. In this method, for a given incremental relative displacement, $\Delta \mathbf{d}_n$, the following system of

nonlinear equations is solved for σ_{n+1}, q_{n+1} and $\Delta\lambda_n$:

$$\sigma_{n+1} = \sigma_{n+1}^e - \Delta\lambda_n D^e m_n \qquad (2.29)$$

$$q_{n+1} = q_n + \frac{\partial q}{\partial \kappa}\Delta\kappa \qquad (2.30)$$

$$F\left(\sigma_{n+1}, q_{n+1}\right) = 0 \qquad (2.31)$$

where $\Delta\kappa = \left\{\Delta\kappa_1, \Delta\kappa_2, \Delta\kappa_3\right\}^T$ is the incremental change in the softening parameters

defined by Equations (2.26) to (2.28).

2.3 FINITE ELEMENT PROGRAM AND SOLUTION ALGORITHM

The described nonlinear constitutive relations are implemented in a

displacement-driven finite element program developed as part of this study. Plane

stress, isoparametric, eight-noded elements are used for the masonry blocks and

plane stress, six-noded contact elements are used for the unit-mortar interface. The

elastic behaviour of the joints is considered in the stiffness matrix of interface

elements. Using zero thickness for interface elements representing mortar joints can

lead to the appearance of an unrealistic interpenetration of adjacent block elements.

This is simply an indication of shortening in mortar joints under compressive

normal stress.

Since the conventional or modified Newton-Raphson iteration scheme fails to

converge in the vicinity of the peak load, the arc-length incremental algorithm

(Criesfield 1997) is employed as the solution strategy and a convergence criterion

based on the norm of nodal displacement vectors is used. To prevent numerical

instabilities and achieve adequate accuracy, the convergence tolerance was set to 0.001 which has been recommended by other researchers (Lotfi and Shing 1991 and Hegemier and Arya 1982). A premature termination was enforced when slow convergence was observed during the iteration process.

2.4   AUXILIARY COMPRESSION TESTS

Although the effects of large elastic and inelastic deformation on the behaviour and load carrying capacity of individual steel bars or columns have been well documented (Bae et al. 2005), no experimental evidence has been documented regarding the effect of buckling of a steel bar on the behaviour of a reinforced masonry assemblage under compression loading. In order to study the effect of buckling of reinforcement on the post-peak response of masonry in compression, a series of uniaxial compressive tests were carried out on reinforced and unreinforced masonry prisms. Eight, fully grouted prisms, four reinforced and four unreinforced, were constructed using the half-scale model of 20-cm concrete masonry blocks. The test specimens were a half-block long and three-blocks high representing the exterior column of grouted cells of a partially grouted reinforced masonry shear wall located at the toe of the wall (Figure 2.5). The prisms were filled with fine grout after construction. Four 200-mm-high by 102-mm-diameter cylinders were cast as grout samples. The average uniaxial compressive strength obtained for the grout samples was 34.2 MPa (C.O.V. = 15.2%).

Type S portland cement-lime mortar with an average compressive strength of 23.0 MPa based on the 2-in. mortar cube tests (ASTM 2002a) was used for mortar

joints. The steel reinforcement was No. 10 bars ($A_s = 100$ mm^2) with 475 MPa yield

strength corresponding to approximately 0.0024 mm/mm tensile strain. The steel

bars of the reinforced specimens were welded to top and bottom bearing plates to

ensure uniform transfer of load to the masonry and the reinforcement. A sketch of

the test set up is shown in Figure 2.9-a. The prisms were tested under in-plane

displacement-controlled axial compression using a four loading screw Tenius Olsen

Machine driven by displacement rate (Figure 2.9-b). The axial deformation of the

prisms was monitored using four displacement potentiometers attached to the top

and the bottom bearing plates on each side of the prism (Figure 2.10). A constant

displacement rate of 0.05 mm/min was applied and displacement and loading

measurements were recorded at one second intervals.

The similar failure mode observed for both the reinforced and unreinforced

prisms was characterized by vertical and inclined cracking on the face shells of the
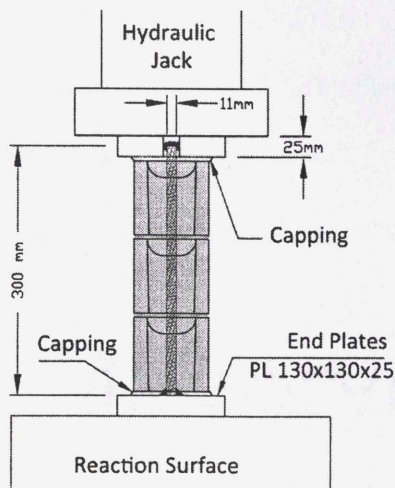
(a) Sketch of test setup   (b) Actual test setup

Figure 2.9 – Test setup used for auxiliary prism compression test
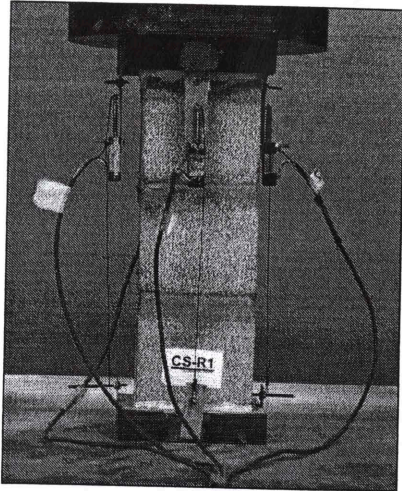
Figure 2.10 – *Instrumentation for auxiliary prism compression tests*
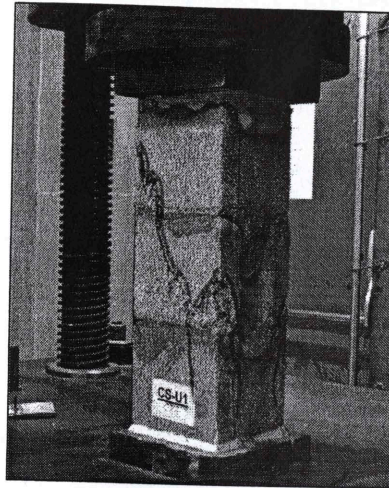
Figure 2.11 – *Vertical cracks on the face shells of the prisms*

blocks (Figure 2.11). At degradations of strength of down to 50% and 30% of the peak resistance of the reinforced and unreinforced prisms, respectively, the face shell of blocks in the cracked area, started to detach from the prism stripping the specimens to their interior grout core.

With further increases of the applied axial displacement, a few vertical cracks were observed on the column of grout inside the blocks after removing the crushed/loose face-shells. However, as seen in Figure 2.12-a, the integrity of the grout core in the unreinforced prism was preserved throughout the test which in turn provided the unreinforced specimens with about 30% residual strength. On the other hand, wide vertical and diagonal cracks initiated and developed in the column of grout inside the reinforced prisms which eventually led to crushing of the grout core as shown in Figure 2.12-b.

The average stress-strain curves obtained from the compression test of the

(a) Unreinforced   (b) Reinforced
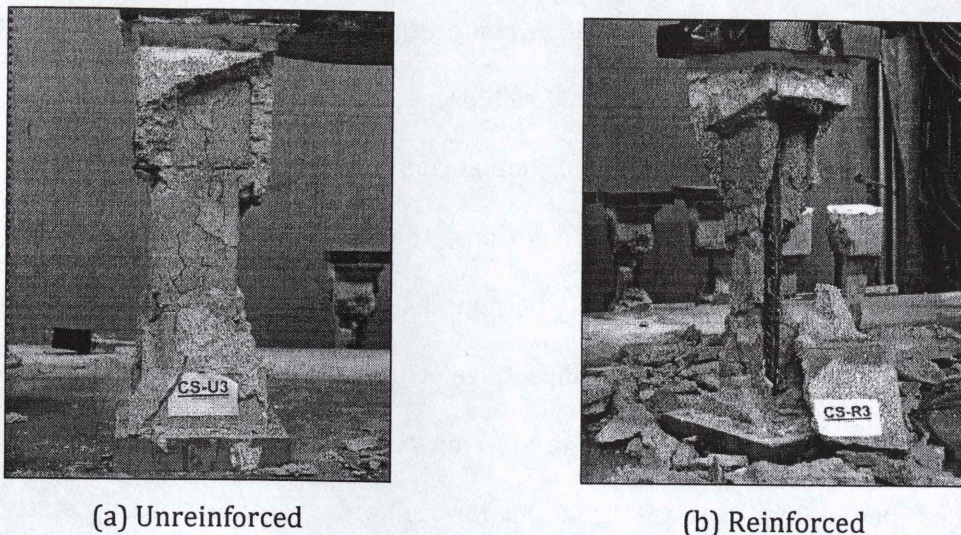
Figure 2.12 – *Unreinforced and reinforced compression prisms after testing*
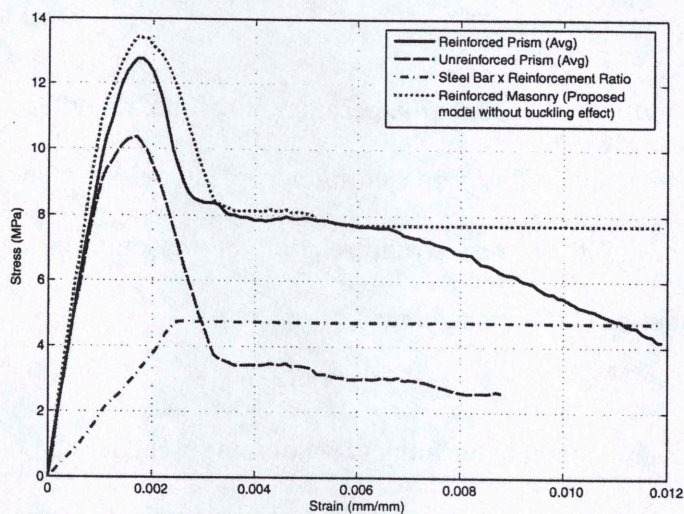
Figure 2.13 – *Average Stress-strain curve obtained from prism tests*

prisms are presented in Figure 2.13. As expected, the difference between the peak

compressive strength of the reinforced and unreinforced prisms was approximately

equal to the calculated steel resistance at the same strain level

(approximately $\varepsilon_{peak} = 0.0015$). This difference increased until the steel

reinforcement yielded at about a strain level of 0.0025. This continuing

contribution of the reinforcement in compression explains the larger difference between residual strength of the reinforced and of the unreinforced prisms compared to the difference at the maximum compressive strength. As can be seen in Figure 2.13, at high compression strains, the decreased residual compressive resistance of reinforced specimens became distinct from unreinforced specimens. The rapid loss of the residual compressive strength was thought to be associated with buckling of the embedded reinforcing bars. Based on the test results, the second descending part of the curve for reinforced grouted prisms started at approximately 2.5 times the yield strain of the steel bar with an average degradation rate of 650 MPa in the prism.

Consistent with the presented experimental results, the effect of buckling of steel bars was reflected in the proposed numerical model by a linear descending branch connected to the stress-strain relation of masonry in compression as described by Equation (2.10), assuming:

$$\varepsilon_b = 2.5\varepsilon_y \qquad A_s = 650 \text{ MPa} \qquad\qquad (2.32)$$

Only the overall effect of buckling of reinforcing steel bars on the compressive response of grouted masonry is studied through the auxiliary tests reported in this section. A more comprehensive test program would be required to investigate the potential effect of other parameters such as slenderness (unsupported length to bar diameter ratio), load eccentricity and masonry strength. Then these factors could be accounted for in the constitutive relations attributed to the compression behaviour of the combined masonry and steel section.

2.5 EVALUATION OF THE NUMERICAL MODEL

2.5.1 PHASE ONE: Evaluation of the Model for Grouted Masonry

The performance of the proposed model for masonry is evaluated in the following section. To exclude the interaction effect of masonry units and mortar joints, fully grouted reinforced masonry shear walls were selected as the experimental evidence. As discussed in Section 2.2, the anisotropy introduced by mortar joints essentially becomes negligible due to the effect of continuous grout in fully grouted reinforced masonry shear walls.

2.5.1.1 Experimental Evidence

Six reinforced masonry shear walls tested by Shing (1989 also cited in Ewing 1990) at University of Colorado were selected as the experimental data. The walls were 1800 mm long, 1800 mm high and 140 mm thick made of 6 in. (nominal) concrete block units. Knocked-out webs were used throughout, which allowed the grout to completely fill the head joints. The vertical and horizontal reinforcement were uniformly distributed in both directions and walls were filled with grout. The horizontal reinforcement was anchored to the extreme vertical reinforcement using 180-degree hooks. Each wall was fabricated on a reinforced concrete base that was subsequently fixed to the floor. The loading consisted of a constant vertical axial load and an in-plane lateral shear load controlled by displacement increments. The reinforcement ratios, reinforcement properties, and the axial load for each wall are shown in Table 2.1.

2.5.1.2 Finite Element Model

As shown in Figure 2.14, the wall was modelled using 36 eight-node quadrilateral elements. The model included the concrete base and top beam simulated as relatively rigid members using elastic plane stress elements with much higher elastic modulus compared to the value used for masonry (100 times higher than regular masonry units). The wall was restrained at the bottom in both the x- and y- directions. To simulate the boundary conditions of the top beam, all nodes at

Table 2.1 – *Properties of the walls selected for evaluation test (from Ewing et al. 1988)*

Wall No.	Vertical Reinforcement				Horizontal Reinforcement				Axial Load (MPa)
	Qty.*	ρ_v (%)	f_y (MPa)	f_u (MPa)	Qty.*	ρ_h (%)	f_y (MPa)	f_u (MPa)	
6	5#5	0.38	442	711	5#3	0.14	400	587	0
4	5#7	0.74	490	711	5#3	0.14	400	587	0
12	5#5	0.38	442	718	5#4	0.24	462	738	0.69
5	5#7	0.74	490	711	5#3	0.14	400	587	0.69
2	5#5	0.38	442	711	9#3	0.24	386	566	1.86
3	5#7	0.74	511	766	5#3	0.14	386	566	1.86

* *USA standard bar size*
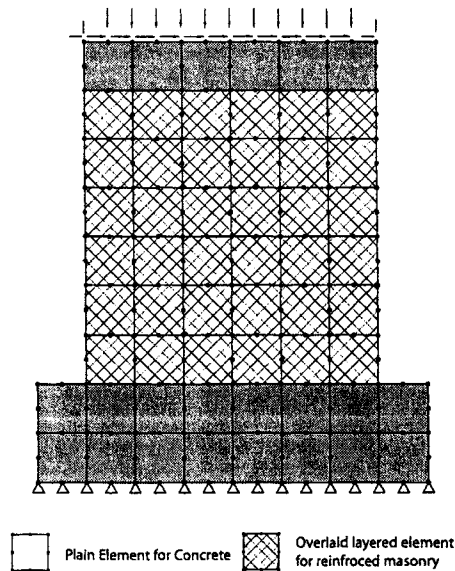
Figure 2.14 – *Finite element mesh for the reinforced wall model*

the top level were constrained to have equal displacements in the x-direction. The constant axial load was applied from the beginning of the analysis.

2.5.1.3 Material Properties

The masonry material properties adopted from the original study and used here in the analysis were as follows: Uniaxial compressive strength $f'_m = 20.1$ MPa, Strain at peak strength $\varepsilon_o = 0.0026$, Tensile cracking strength $f_{cr} = 0.7$ MPa, Elastic modulus of masonry $E_m = 20,000$ MPa, Poisson's ratio $v = 0.16$. The strain hardening parameter for reinforcement was $\zeta = 2\%$. The tension stiffening parameter accounting for the tension in the masonry between cracks was chosen to vary between 0.02 and 0.25 based on the steel ratio. Regarding the parameters describing the constitutive relation and failure envelope in Equations (2.5) to (2.9), the following values were used in the analysis (Ewing et al. 1990):

$$A_o = 3.65, \quad A_1 = 2.0, \quad A_2 = 2.0, \quad A_3 = 0.1, \quad A_4 = 0.6 \qquad (2.33)$$

2.5.1.4 Numerical versus Experimental Results

Figure 2.15 shows the load-deflection curves for monotonically applied loading obtained from the finite element analyses versus the cyclic response of Walls 6 and 3. Stable hysteresis loops and low degradation of stiffness in Wall 6 (Figure 2.15-a) correspond to a flexural failure which is closely predicted by the finite element analysis. On the other hand, the presence of the axial load and an increased amount of vertical steel changed the mode of deformation from a ductile flexural mode to a brittle shear mode in Wall 3 (Figure 2.15-b). Considering both
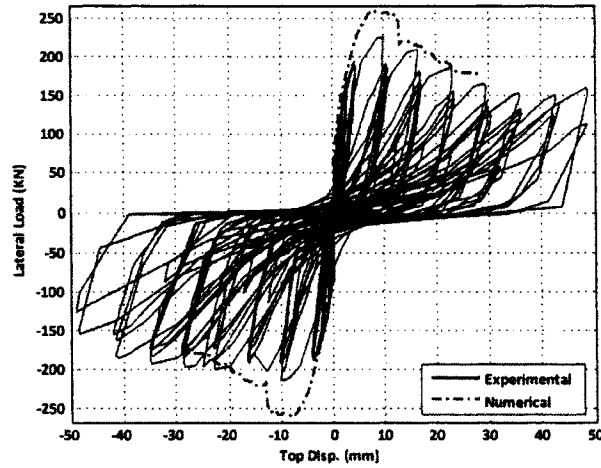
(a) Flexural failure mode (Wall 6)
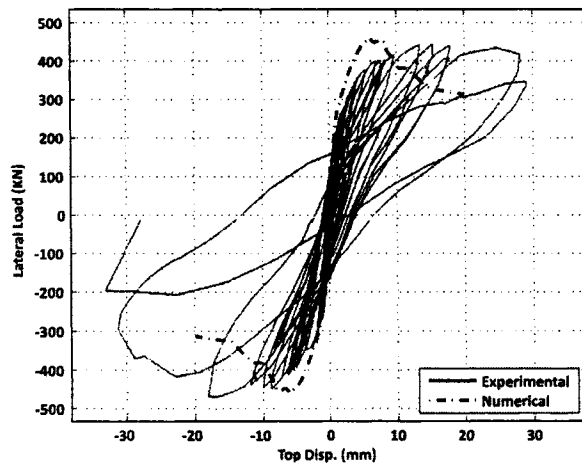
(b) Shear failure mode (Wall 3)

Figure 2.15 – Load-deflection path of analytical model and experimental results

halves of the hysteresis loops, the overall comparison indicates good agreement between experimental results and analytical predictions in terms of initial stiffness and ultimate strength especially for the flexural failure mode. The results showed some discrepancies which are thought to be due to the different loading histories (monotonic versus cyclic). Cyclic loading leads to gradual softening and degradation

of the masonry response. In monotonic loading, the integrity of the wall is not pre-damaged by reversing cycles and, therefore, higher strength and smaller deformations are expected. The overall results at the peak loads for the six test walls are presented in Table 2.2.

In general, the comparison between analytical and experimental results showed good agreement in prediction of initial stiffness and ultimate strength for the different failure modes. The pre- and post-peak predictions for flexural failures were more representative than for shear failure where post-peak response under monotonic loading predicted greater degradations of strength than the degradation rates observed under post-peak cyclic loading.

Table 2.2 – *Comparison of experimental (from Ewing et al. 1988) and analytical results in terms of the peak load*

Wall No.	Test Results		Numerical Result (kN)	Num./ Exp. (Avg.) Ratio	Failure Mode*
	Peak Load Push (kN)	Peak Load Pull (kN)			
6	231	214	262	1.17	F
4	320	387	390	1.10	F
12	316	316	311	0.98	F
5	396	374	412	1.07	F
2	369	436	385	0.96	SH
3	445	467	463	1.02	SH

*F: Flexure, SH: Shear

2.5.2   PHASE TWO: Evaluation of the Model for Unit-Mortar Interface

To evaluate the performance of the unit-mortar interface model, a direct comparison, described in the next section, was carried out between analytical and experimental results of the pre- and post-peak response of partially grouted-reinforced masonry shear walls under in-plane loading,.

2.5.2.1 Experimental Evidence

Two partially grouted-reinforced masonry shear walls tested by Ghanem et al. (1993) were selected as the experimental evidence. The single wythe wall specimens were constructed using one-third-scale model units of 140 mm thick concrete block. The walls were 940 mm long (7 blocks) by 920 mm high (13 courses), representing a 2.80 m × 2.77 m masonry shear wall at full-scale. The steel bars were placed around the perimeter and at midheight and midlength of the wall as shown in Figure 2.16. The reinforcement ratio for both the vertical and horizontal directions was 0.12% and the spacing between bars in both directions was about 400 mm (1.2 m spacing at full-scale). The wall panels were tested as cantilever walls under in-plane monotonically increasing lateral loading controlled by lateral displacement, with different level of constant axial load during each test. A reinforced concrete footing was used as a strong base at the bottom and a concrete beam was cast at the top to serve as a distribution beam for application of the vertical and lateral loads.

The behaviour of specimen SWA1 under 0.7 MPa axial stress was dominated by a mixed flexural and shear failure mode with flexural yielding of reinforcing steel bars, toe crushing as well as diagonal cracking as shown in Figure 2.17-a. Specimen SWA2 with 1.4MPa axial stress exhibited severe diagonal cracking with very little or no flexural deformation (Figure 2.17-b) which is an indication of a dominant shear failure mode.
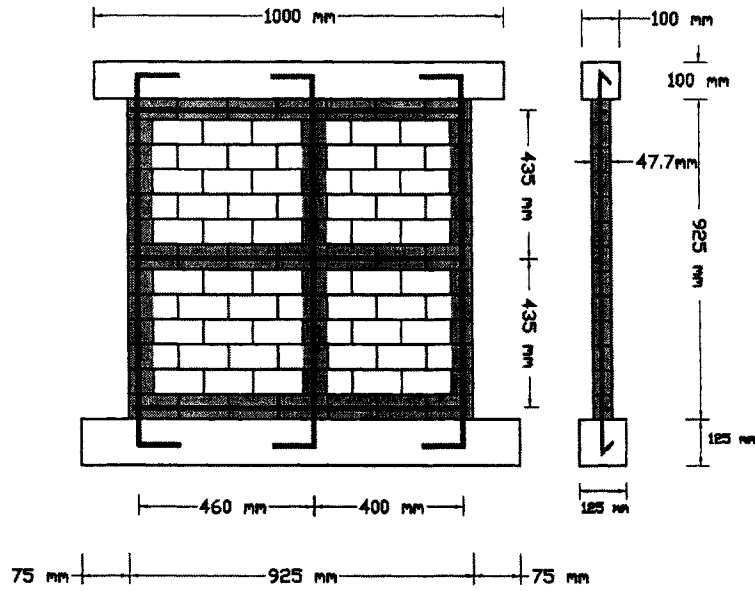
Figure 2.16 – *Sketch of the shear wall specimens used in the tests (Ghanem et al. 1993)*

(a) Wall SWA1   (b) Wall SWA2
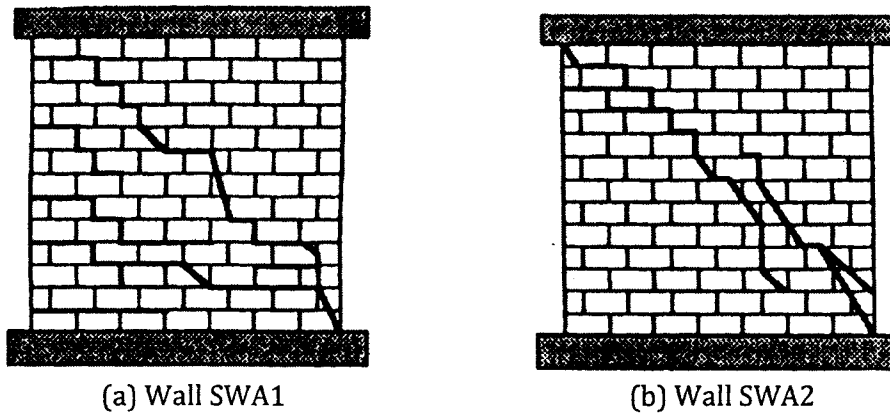
Figure 2.17 – *Crack pattern of the wall specimens tested by Ghanem et al. (1993)*

2.5.2.2 Finite Element Model

As illustrated in Figure 2.18, the wall specimens were modeled using 195 (15×13) quadrilateral eight-node elements with 3×3 Gauss-Quadrature points for numerical integrations. The model also included the concrete base and top beam which were simulated as relatively rigid members using elastic plane stress elements. The model was restrained at the bottom in both the x- and y- directions. The boundary conditions at the top were simulated by having all top nodes constrained to move equally in the x-direction. A total of 271 six-noded interface elements with 3×1 Gauss-Quadrature points were used to model the interfaces between masonry elements and mortar joints. A constant axial load representing the axial stress was applied at top of the wall from the beginning of the analysis. The first load increment was assigned to account for the initial deformation due to axial compression. Subsequently, the total axial load was maintained constant and lateral load were applied incrementally.
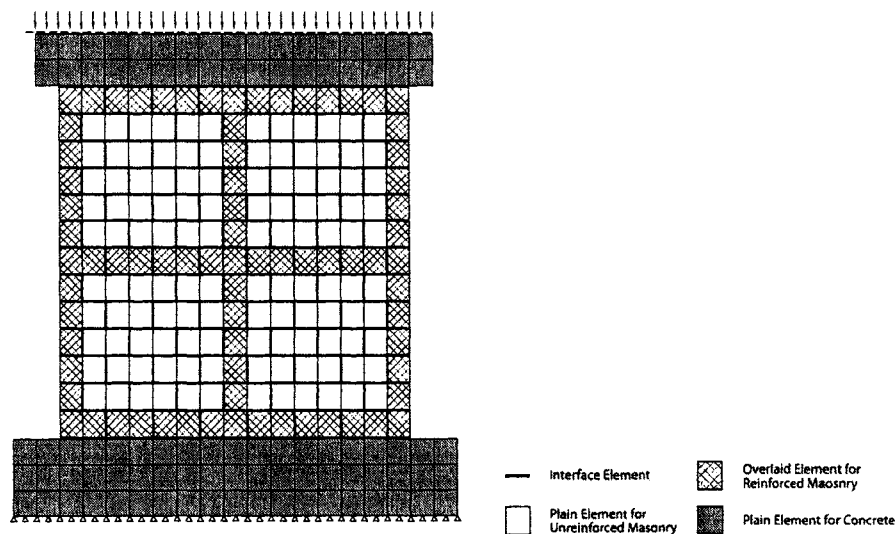
Figure 2.18 – *Finite element mesh for the partially grouted reinforced wall's model*

2.5.2.3 Material Properties

The material properties adopted from the original study and used here for the masonry were as follows: Uniaxial compressive strength $f'_m = 20.0$ MPa (grouted), $f'_m = 16.5$ MPa (hollow), Strain at peak strength $\varepsilon_o = 0.0025$ (grouted), $\varepsilon_o = 0.0020$ (ungrouted), Tensile cracking strength $f_{cr} = 1.40$ MPa, Elastic modulus of masonry $E_m = 20,000$ MPa and Poisson's ratio $v = 0.16$. The tension stiffening parameters were assumed equal to $\alpha = 0.02$ and $\beta = 0.10$. Similar to other studies (Ewing et al. 1990, Maleki 2005, Kupfer et al. 1969), the parameters describing the constitutive relation and failure envelope were assumed to be: $A_o = 3.65$, $A_1 = 2.0$, $A_2 = 2.0$, $A_3 = 0.1$ and $A_4 = 0.6$. Adopted from the results of the auxiliary tests carried out in this study, $\varepsilon_b = 2.5\varepsilon_y$ and $A_5 = 640$ MPa were the values set for the constitutive relation of grouted masonry in compression.

The mechanical and geometric properties of the reinforcing steel bars used in the wall specimens tested by Ghanem et al. (1993) are presented in Table 2.3. The slope of the linear strain-hardening behaviour of steel was assumed to be $E_{sp} = 0.02E_s$ in which E_s is the elastic modulus of steel.

Table 2.3 – Properties of Reinforcing Steel Bars (Ghanem et al. 1993)

Diameter (mm)	Area (mm²)	E_s (MPa)	σ_y (MPa)	ε_y (mm/mm)	σ_u (MPa)	ε_u (mm/mm)
4.90	18.85	186300	447.1	0.0024	489.9	0.039

Despite the significant effect of mortar joints and the bond characteristics of

the masonry unit-mortar interface on the global behaviour and failure mode of the

test specimens, no specific experiments were conducted on the joint properties.

Hence, the parameters of interface elements were adopted from other similar

studies (Lotfi and Shing 1994, and Mehrabi and Shing 1997). The constitutive

parameters used for the interface model are presented in Table 2.4. Some

adjustments of the normal and shear moduli were enforced in the numerical model

to match the initial stiffnesses of the experimental results. Thus, the normal and

shear stiffnesses for specimen SWA2 carrying 1.4 MPa axial stress were increased to

$D_{nn} = 18000$ MPa and $D_{tt} = 9000$ MPa, respectively. This indicates that the level of

Table 2.4 – Material properties for unit-mortar interface model

Material Model Parameter	Bed Joints	Head Joints
D_{nn} (MPa/m)	7,200	7,200
D_{tt} (MPa/m)	3,600	3,600
s_0 (MPa)	0.85	0.35
r_0 (MPa)	0.85	0.35
r_r (MPa)	0.03	0.03
μ_0	0.95	0.75
μ_r	0.60	0.45
α, β (mm/N)	11.4	11.4
η	0.1	0.2
G^f_{min} (N.m/m²)	50.2	8.51
G^f_I (N.m/m²)	250.9	42.6
G^f_{II} (N.m/m²)	501.7	85.1

axial load may effectively change the elastic stiffness of the mortar joints and, consequently, the overall stiffness of the wall. Deformation of the Interface elements between grouted reinforced masonry elements were ignored by assigning linear behaviour with relatively high normal and shear stiffnesses.

2.5.2.4 Numerical versus Experimental Results

The load-displacement curves generated by the numerical model along with the experimental data are shown in Figure 2.19. Onset of the first yield and rupture of the vertical reinforcing bars in addition to the toe crushing of masonry block elements are also indicated on the curves. In Figure 2.20, the post-peak pattern of mortar joint debonding, masonry tensile cracking, masonry crushing and incident of buckling of vertical reinforcing bars are shown on the deformed mesh of the finite element model at 85% of the ultimate load (after peak load). It should be noted that the mesh displacements shown in these figures are significantly exaggerated for a better presentation. Crushing is assumed to occur when the principal compressive strain exceeds the peak compressive strain of the masonry. Buckling is also assumed to happen when the compressive strain in vertical reinforcements exceeds the buckling strain, ε_b, defined in Section 2.2.1.1.

In both shear walls SWA1 and SWA2, the ultimate load was predicted reasonably well by the finite element model (within ±10% of the experimental results). In general, the load-deflection curves of both specimens SWA1 and SWA2 (Figure 2.19) were in very good agreement with the experimental results.
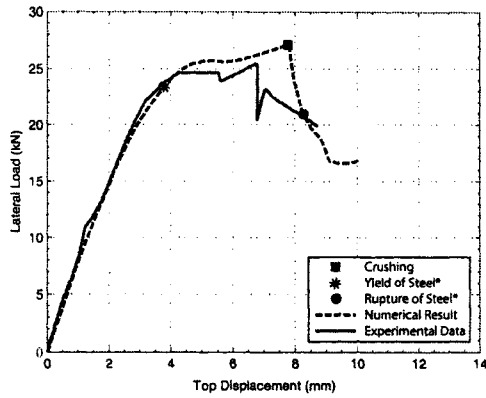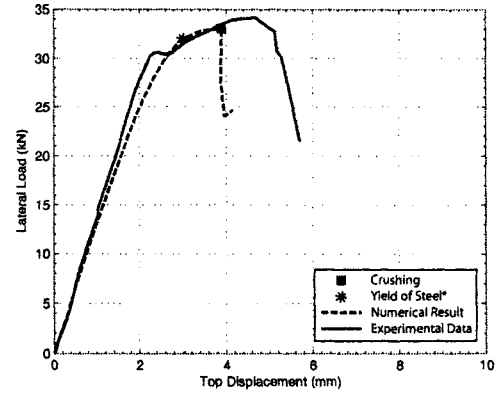
(a) Wall SWA1   (b) Wall SWA2

Figure 2.19 – *Numerical versus experimental load-displacement curves for walls (Ghanem et al. 1993)*
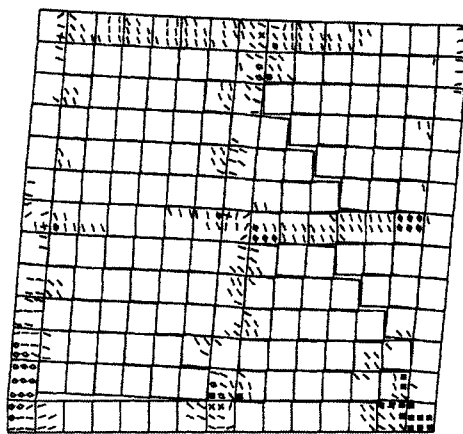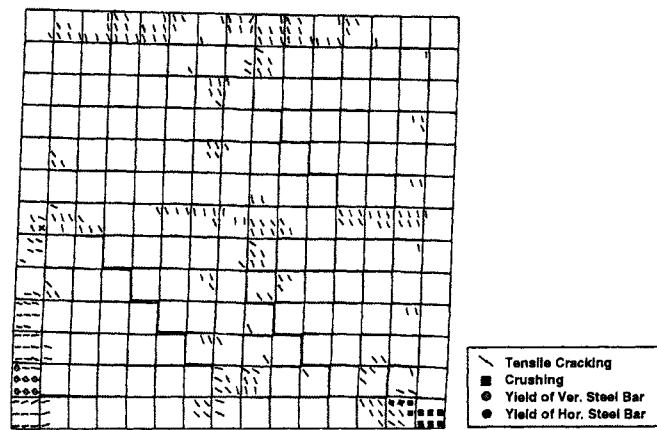
(a) Wall SWA1   (b) Wall SWA2

Figure 2.20 – *Crack pattern and other deformations for finite element model of Walls SWA1 and SWA2 at 85% of the ultimate load (after peak load)*

The failure of the finite element model for Wall SWA1 carrying (0.7MPa axial stress) was initiated by yielding of the outermost tensile reinforcement at about 80% of the ultimate load along with formation of step-pattern cracks in a combination of head joints and bed joints in the hollow (ungrouted) sections of the finite element model of the wall (Figure 2.20-a). Reaching the ultimate load carrying capacity of the wall was accompanied by extensive toe crushing in the compression zone and rupture of the extreme vertical reinforcing bar after nearly 20% strength degradation. This indicated that, consistent with the experimental observations, the finite element model predicted a mixed shear-flexure failure mode. Also, comparison between the numerical and experimental crack patterns (Figure 2.17-a versus Figure 2.21-a) indicated very good agreement.

The failure predicted by the finite element model for Wall SWA2, carrying 1.4 MPa axial stress, started by yielding of the outermost tensile reinforcement at about 90% of the ultimate load predicted by the numerical model. As shown in Figure 2.19-b, sudden degradation of strength down to about 75% of the ultimate load occurred soon after the wall reached its maximum lateral load resistance. At this point, crushing occurred in the compressed toe and stepped-pattern cracking developed along head joints and bed joints in the hollow (ungrouted) sections of the finite element model of the wall (Figure 2.20-b). This crack pattern agreed fairly well with the diagonal cracking observed in the experiment (Figure 2.17-b). No rupture of vertical or horizontal reinforcement was predicted even after 25% strength degradation.

2.6 Closing Remarks

In this chapter, a computationally efficient numerical technique was introduced for analysis of the behaviour of partially grouted reinforced masonry shear walls. Building on previous models developed in reinforced and unreinforced masonry studies, an orthotropic rotating smeared crack model with equivalent constitutive relations along the axes of orthotropy was adopted for concrete masonry. Steel was represented by using a separate overlaid element connected to the masonry elements at each node. The interface of the mortar joints and masonry units, as the planes of weakness in the structure, was modeled in a plasticity framework. The model was implemented in a displacement driven finite element code using eight-noded plane-stress elements for masonry and six-noded contact elements for the unit-mortar interface.

For an accurate simulation of post-peak response of a partially grouted reinforced masonry shear wall, it was decided to include the effect of buckling of the compressive steel reinforcement in the material model of grouted masonry and reinforcing steel bar. This effect was simply represented by a linear descending branch attached to the compressive stress-strain curves for both the steel and the masonry. A series of uniaxial compressive tests on reinforced and unreinforced masonry prisms was carried out to reasonably simulate the behaviour of the toe of a partially grouted reinforced masonry shear wall under high compressive stress.

The performance of the numerical model was evaluated by comparisons of available experimental data with the numerical predications for both fully grouted

and partially grouted reinforced masonry shear walls. In general, very good agreement was observed between the experimental results and finite element predictions in terms of the pre- and post-peak response, ultimate load carrying capacity and damage pattern. This indicated acceptable accuracy of the proposed numerical model for further studies on reinforced masonry shear walls with either close or widely spaced reinforcement.

CHAPTER 3

DESCRIPTION OF THE EXPERIMENTAL PROGRAM

3.1 INTRODUCTION

The experimental program presented in this chapter was designed to provide sufficient information to evaluate the performance of partially grouted reinforced concrete block shear walls under in-plane cyclic loading. As previously mentioned in Chapter 1, these walls are unique as the result of having less than the commonly used minimum amount of reinforcing steel and larger bar spacing than specified in the seismic requirement of the current Canadian masonry design standard, CSA S304.1-04 (CSA 2004) for regions with low and moderate seismic activities.

It is widely thought (Warner et al. 1999) that the load resisting mechanism of a squat shear wall with widely spaced reinforcement subjected to in-plane lateral loading could be represented by a simple strut and tie model as illustrated in Figure 3.1. This model implies that, in a partially grouted reinforced masonry shear wall, the unreinforced area enclosed by steel bars experiences a significant corner-to-

corner compressive stress prior to failure of the wall. In view of this concept, the first stage of the experimental study was designed to investigate the response of masonry panels (wallettes) with various grouting and reinforcing patterns under the action of diagonal compression loading. The results were also to be used to evaluate the performance of the numerical model proposed in Chapter 2 to simulate progression of stepped-pattern cracking in a masonry panel.

The second series of tests, pursuing the primary goal of this research program, was focused on the fully cyclic reversed loading response of partially grouted reinforced masonry shear walls subjected to in-plane axial and lateral loading. The experimental program was designed to investigate the effects of wall aspect ratio (at three levels) and reinforcement spacing (at three levels) within five shear wall specimens. These test results also offered direct experimental evidence to assess the accuracy of the numerical model.
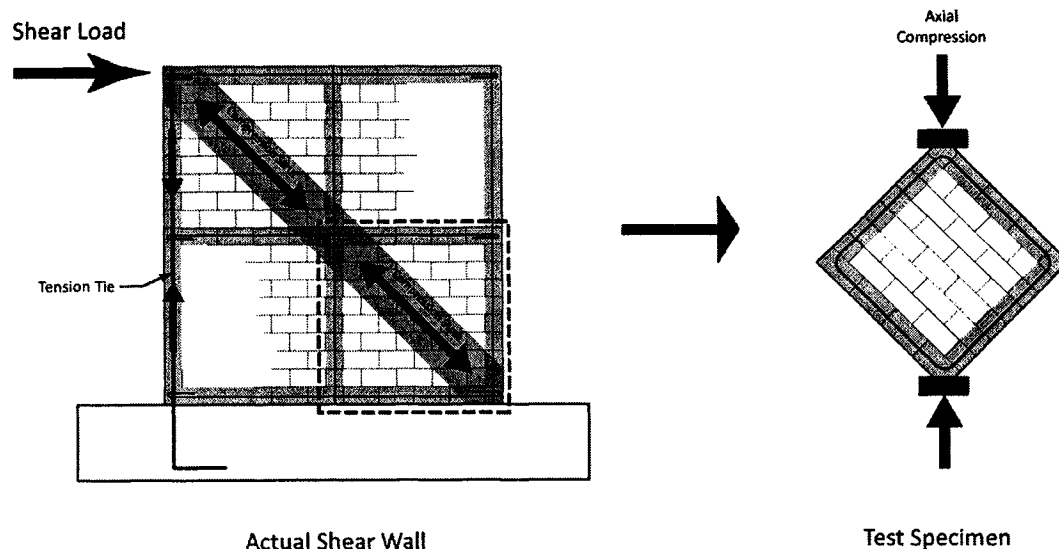
Figure 3.1 – *Strut and tie model for a partially grouted reinforced masonry shear wall*

Half-scale model units of hollow 20-cm concrete blocks (actually 47 percent scale) were used in construction of the test specimens. Scaled blocks were used because wide bar spacing made it difficult to test wall specimens at full-scale size and also there were limits to the capacity of the actuators available in the laboratory of McMaster University.

In the next two sections, the diagonal compression tests on wallette specimens and the tests of the partially grouted reinforced masonry shear walls are presented. In each section, the rationale for the experimental program and the applied test technique are first discussed. Then, details of construction and constituent material properties are presented followed by a description of the implemented test setup and instrumentation. Finally the loading procedure followed for testing is presented.

3.2 DIAGONAL COMPRESSION TEST

3.2.1 Rationale of the Experimental Program

The tests of this part of the experimental program were mainly intended to satisfy two objectives: the first was to study the effect of the extent of grouting and reinforcing on masonry panels subjected to diagonal compression loading. The second was to evaluate the capability of the numerical model proposed in Chapter 2 to simulate the propagation of diagonal stepped-pattern cracking along the mortar head and bed joints. Diagonal-stepped cracking was expected to dominate the failure mode of the unreinforced section within a partially grouted reinforced masonry shear wall.

The test specimens were designed to represent 1400 mm steel bar spacing at

full-scale which exceeds the maximum allowed spacing of 1200 mm specified in the

seismic requirement for zone 2 (seismic hazard index greater than 0.35) in the

current Canadian masonry design standard (CSA 2004). Hence, the experiments also

provided an evaluation of the effect of using bar spacing beyond the specified limit.

3.2.2 Description of the Wallette Specimens

Nine diagonal compression specimens were constructed using half-scale

model hollow 20-cm concrete blocks. The half-scale test specimens were 750-mm

square wallettes (four-block-long by eight-block-high). Three specimens (W-H1, 2

and 3) were hollow, three specimens were fully grouted but only reinforced along

the four sides (W-G1, 2 and 3) and three specimens were grouted and reinforced

only at the end cells and top and bottom courses along the four sides (W-PG1, 2 and

3). Sketches of the designed test specimens are presented in Figure 3.2.

3.2.3 Construction of the Wallettes

The specimens were constructed by a qualified mason and filled with grout at

Wallette Type W-H   Wallette Type W-G   Wallette Type W-PG
Hollow   Fully Gouted Reinforced   Partially Grouted Reinfroced
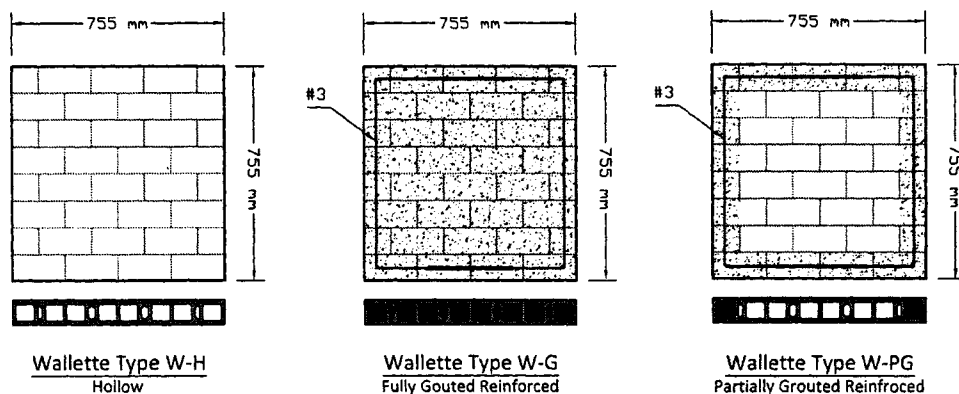
Figure 3.2 – Sketches of the wallette test specimens

24 hours after construction. Five millimetre mortar joints were used and no mortar was laid on the webs except at the ends of the grouted cells to prevent grout from flowing out into the inner cells intended to be ungrouted. The extension of the face-shell at the frogged-end shape of the blocks provided 48-mm-wide total head joints across the blocks which were fully buttered with 5-mm-thick mortar.

In partially grouted wallettes, to avoid flow of grout to the lower courses, a layer of plastic mesh was embedded in the bed joint located beneath the course to be grouted (Figure 3.3-a). A one-piece No. 3 (USA size) steel bar ($A_s = 71.3$ mm²) was used as reinforcement. As shown in Figure 3.3-b, the bar was bent to the designated profile before construction. This eliminated using hooks at the corners and provided a better representation of real steel distribution in a partially grouted-reinforced masonry shear wall. Before final grouting, the two ends of the steel bars were welded together at a point midway between a pair of adjacent corners. To ensure a strong connection, two extra 100-mm-long pieces of No. 3 (USA size) steel bar were also welded on each side of the connection. The specimens were air-cured in standard laboratory conditions for at least 28-days before testing.
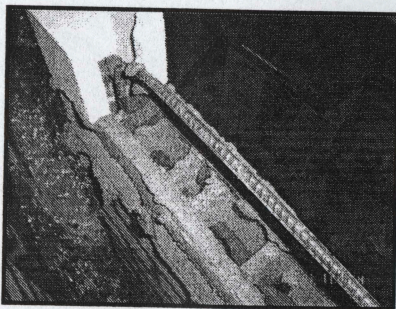
(a) Plastic mesh laid beneath the course to be grouted
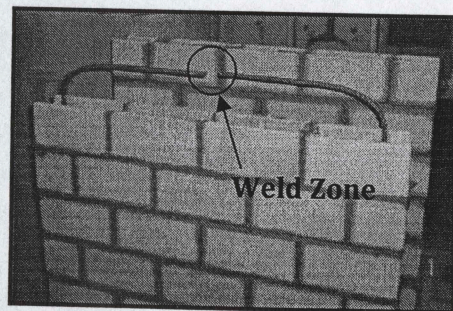
(b) One-piece reinforcement
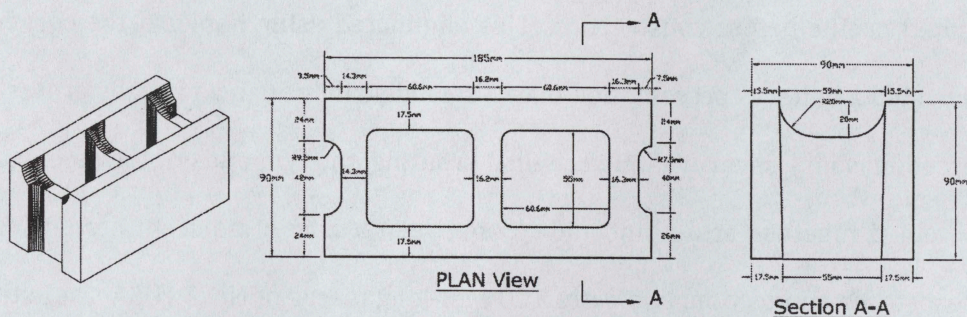
Figure 3.3 – Construction of wallette specimens

3.2.4   Description of Constituent Materials

3.2.4.1   Masonry Blocks

A half-scale model of 20-cm hollow concrete block was used for the construction of the test specimens. Geometric properties of the half-scale blocks used in the wall construction along with a photo comparing the half-scale model with its prototype are shown in Figure 3.4. Half-scale blocks were manufactured at the Newtonbrook block plant (Aurora, Ontario) using the same concrete mix as for full-scale block. Detail of the manufacturing process and the mechanical properties of the blocks were presented elsewhere by Long (2006).

(a) Details of the half-scale model of 20-cm concrete masonry block
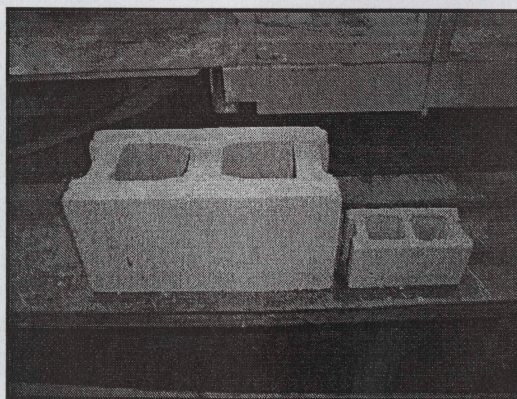
(b) Half-scale model versus the prototype masonry block

Figure 3.4 – Half-scale model block

3.2.4   Description of Constituent Materials

3.2.4.1   Masonry Blocks

A half-scale model of 20-cm hollow concrete block was used for the construction of the test specimens. Geometric properties of the half-scale blocks used in the wall construction along with a photo comparing the half-scale model with its prototype are shown in Figure 3.4. Half-scale blocks were manufactured at the Newtonbrook block plant (Aurora, Ontario) using the same concrete mix as for full-scale block. Detail of the manufacturing process and the mechanical properties of the blocks were presented elsewhere by Long (2006).

(a) Details of the half-scale model of 20-cm concrete masonry block
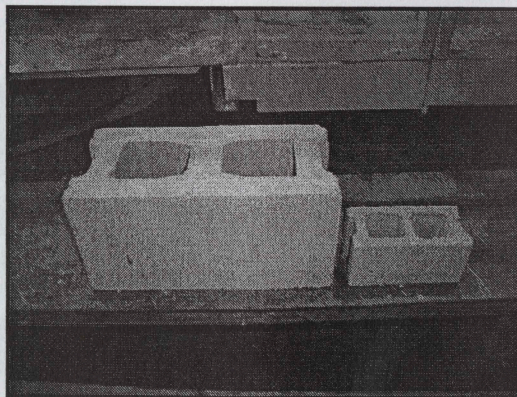
(b) Half-scale model versus the prototype masonry block

Figure 3.4 – Half-scale model block

3.2.4.2 Mortar

Standard type S mortar composed of type 10 normal portland cement, type S autoclaved mason's lime and dry masonry sand was used for construction of the wallette specimens. The mortar was mixed in the laboratory during the construction in proportions of 1.0:0.21:3.53 parts by weight (cement:lime:sand). Water was added to the dry mix at a ratio of 0.88 (water:cement) satisfying the workability requirements. Three 50mm mortar cubes were cast before using each batch of mortar in the construction. The cubes were air cured for at least 28 days under the same laboratory conditions as the wallette specimens. The mortar cubes were tested under uniaxial compression in accordance with ASTM C109/C109M-02 method (ASTM 2002a). The average compressive strength obtained for the 12 mortar cubes was 23.8 MPa (C.O.V. 6.3%) (See Appendix A for complete test data).

3.2.4.3 Grout

Fine grout was mixed for this experimental program using type 10 normal portland cement, type S autoclaved mason's lime and dry concrete sand with maximum aggregate size of five millimetres. The constituent materials were mixed in a wheelbarrow in two batches in the proportion of 1.0:0.04:2.4 parts by weight (cement:lime:sand). A water:cement ratio of 0.64 was used giving an average of 267 mm (10.5 in.) slump.

Three grout samples were cast for each batch of grout at the same time as wallettes was grouted. The samples were block-moulded prisms, as shown in Figure 3.5, with the approximate dimensions 90×90×185 mm prepared using the full scale
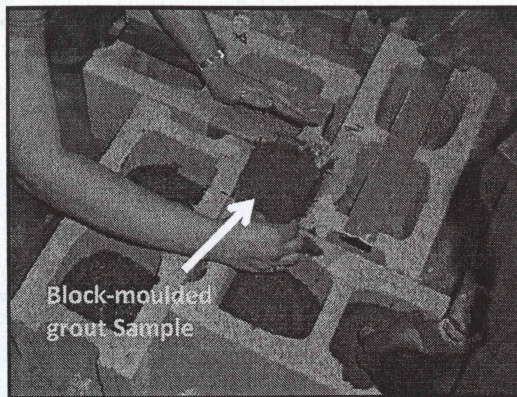
***Figure 3.5** – Block-moulded prisms used for grout sample*

blocks according to the method specified in ASTM C1019. All samples were hard capped using hydrostone and were tested under uniaxial compression. The average compressive strength obtained for the six grout prisms was 40.7 MPa with a coefficient of variation of 15.9% (See Appendix A for complete test data).

3.2.4.4   Reinforcement

The steel bars used in the reinforced specimens were No. 3 (USA size) with 71.3 mm² cross-section area. Three 600-mm-long coupon samples were randomly cut and tested under uniaxial tension. An extensometre with a gauge length of 50 mm was used to measure the tensile strain of the steel (Figure 3.6). The properties of the reinforcing bars are presented in Table 3.1. A typical stress-strain curve obtained from the bar tensile tests is shown in Figure 3.7.

3.2.4.5   Assemblage Tests

In order to determine the compressive strength as well as the ultimate strain of masonry in compression, four grouted and four hollow prisms were constructed

Figure 3.6 – *Uniaxial tensile test of reinforcement*

Table 3.1 – *Mechanical properties for No. 3 (USA standard size) reinforcing bar used in wallette tests*

Type	Sample No.	E_s (GPa)	f_y (MPa)	ε_y (mm/mm)
No. 3 (USA Size) A_s=71 mm²	1	203.1	487.3	0.0024
	2	196.2	481.7	0.0025
	3	204.8	485.9	0.0022
	Average (C.O.V.)	201.4 (2.26%)	485.0 (0.60%)	0.0024 (6.45%)
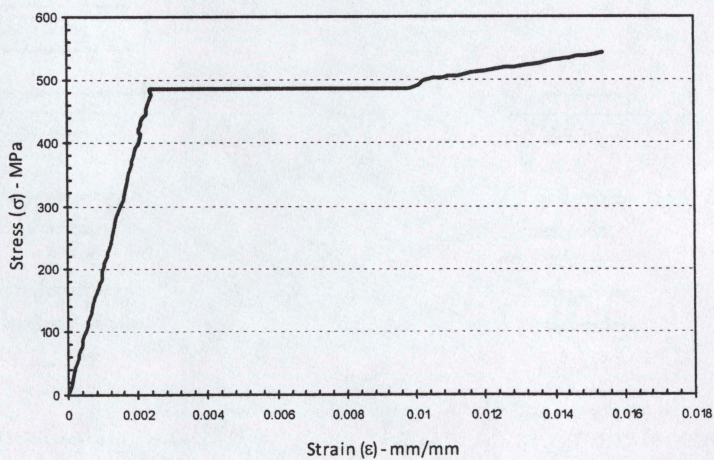
Figure 3.7 – *Stress-strain curve for a typical No. 3 (USA size) bar*

by the same qualified mason during the construction of wallette specimens. All of

the specimens were constructed in running bond pattern using ¼ and ¾ end blocks

as suggested by Halucha (2002) (Figure 3.8-a). The main merit of using ¼ and ¾

blocks, versus using full and half blocks in alternating courses, is that the deficiency

of filling frogged ends is eliminated. Moreover, using the same number of head joints

in each course reduces the variability over the height of the specimens and provides

a better representation of actual construction (Halucha 2002). Specimens were

cured in the same laboratory condition as the wallettes for at least 28 days before

testing.
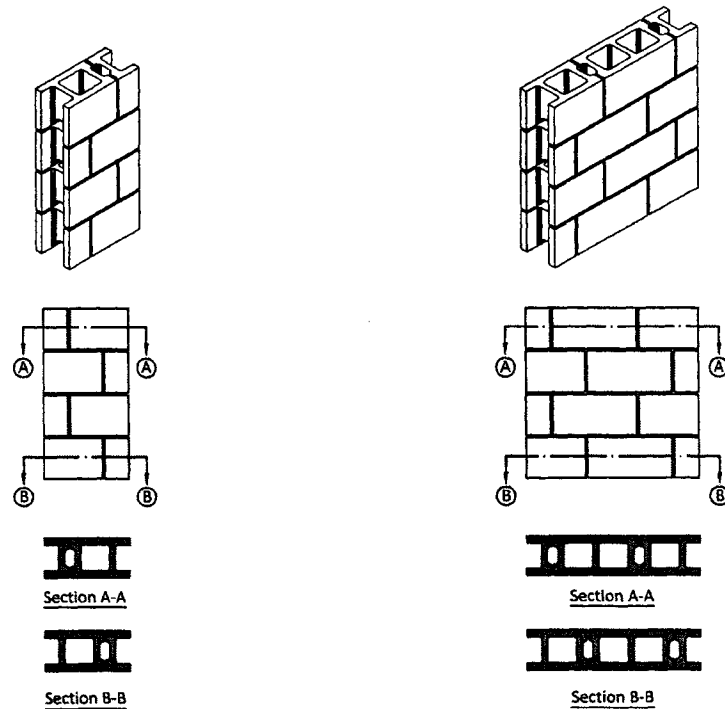
(a) Uniaxial compression prisms   (b) Diagonal tension specimens

Figure 3.8 – Control specimens used for auxiliary tests

Prisms were capped with hydrostone and tested under uniaxial compression using a 600 kN capacity Tenius Olsen machine according to ASTM C1314-03b (ASTM 2003b). Vertical strain was measured over a three block and three bed joint height by means of two 12-mm-stroke linear displacement potentiometer. The potentiometers were mounted on opposite faces of the prisms over a central gauge length of 300 mm (Figure 3.9). The results obtained from the prism tests are summarized in Table 3.2. Gross cross sectional area was used for strength calculation of grouted prisms while average effective mortared area along the 15.6 mm thick face shells of masonry blocks (total area of 2×15.6 mm×185 mm = 5772 mm²) was used for hollow prisms.
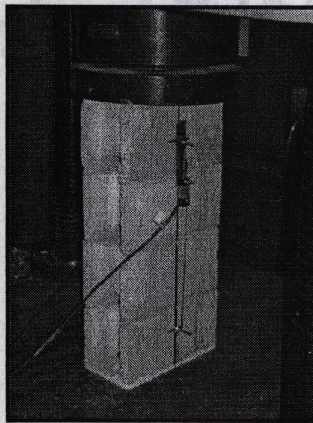
***Figure 3.9** – Uniaxial compression prism test*

Diagonal tension tests were conducted in accordance with ASTM E519-02 (2002b). Two-block-wide by four-block-high specimens (Figure 3.8-b) were prepared for diagonal testing at the same time as construction of the wallettes using ¼ and ¾ end blocks. Four hollow and four grouted specimens were made. The corners of the specimen were capped within half-scale models of the standard

Table 3.2 – Prism test results related to wallette tests

Type	Sample No.	f'_m (MPa)	ε_m (mm/mm)
Grouted	P-G1	14.7	0.0013
	P-G2	14.8	0.0012
	P-G3	13.7	0.0012
	P-G4	14.7	0.0015
	Average (C.O.V.)	14.5 (3.4%)	0.0013 (13.0%)
Hollow	P-H1	25.2	0.0015
	P-H2	25.1	N/A*
	P-H3	27.1	0.0014
	P-H4	25.2	0.0015
	Average (C.O.V.)	25.6 (3.7%)	0.0014 (3.3%)

* Displacement readings were found faulty due to LVDT malfunction

loading shoes specified in ASTM E519-02 (ASTM 2002b). Deformations along the diagonals of each specimen were recorded by two 12-mm stroke potentiometers over a gauge length of 360 mm on each face (Figure 3.10). The results of the diagonal tension tests are summarized in Table 3.3. Similar to the prism tests, gross cross-section area for grouted specimens and net area based on effective mortared area of a masonry block for hollow specimens were used in the calculations. This is 16657 mm² based on an effective average face shell thickness of 15.6 mm for hollow wallette specimens. The results of the diagonal tension tests for specimens DT-G3 and DT-H2 were found to be much lower than their other three companion specimens. It was believed that these samples were damaged during moving and handling prior to testing. Consequently, the test results concerning these specimens were not included in the averages and coefficients of variations.
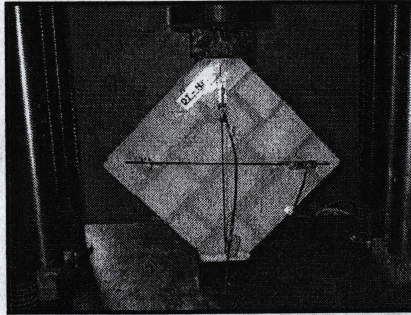
Figure 3.10 – *Diagonal tension test of control specimen*

Table 3.3 – *Diagonal tension test results related to wallette tests*

Type	Specimen No.	f'_m (MPa)	ε_m (mm/mm)
Grouted	DT-G1	2.19	0.00069
	DT-G2	2.14	0.00046
	DT-G3	1.76	0.00057
	DT-G4	2.22	0.00047
	Average* (C.O.V.)	2.18 (1.98%)	0.00054 (24.0%)
Hollow	DT-H1	2.24	0.00044
	DT-H2	1.62	0.00046
	DT-H3	2.50	0.00034
	DT-H4	2.27	0.00060
	Average** (C.O.V.)	2.33 (6.07%)	0.00046 (27.7%)

* Average values and C.O.V. values are based on the three similar results and exclude specimen DT-G3 and DT-H2

3.2.5   Test Setup and Instrumentation

The wallette specimens were tested under in-plane diagonal compression using a four screw Tenius Olsen Machine driven by displacement rate. The corners of the specimen were capped within the same loading shoes as the ones used for the auxiliary diagonal tension tests in accordance with ASTM E519-02 (ASTM 2002b). A typical test setup is shown in Figure 3.11. The horizontal and vertical deformations along the two diagonals were monitored using two 12-mm-stroke potentiometers
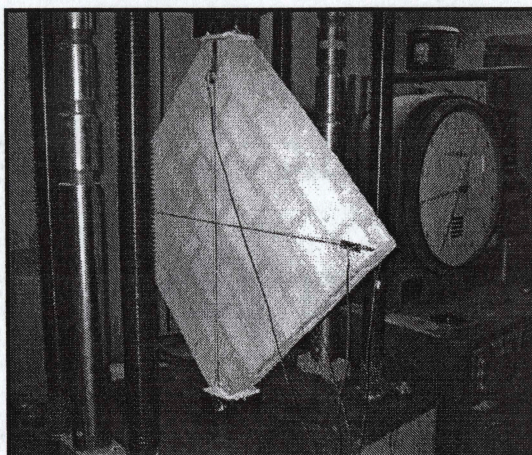
Figure 3.11 *– Test setup, loading and instrumentation for diagonal compression test of masonry wallette*

on each face of the wallettes. A gauge length of 900 mm was used to measure average strain. A constant displacement rate of 0.05 mm/min was applied and displacements and loading were recorded at one-second intervals. Failure was considered to occur when the load-deformation curve showed a steady decrease in load down to 60% or less of peak load.

3.3   SHEAR WALL TESTS

3.3.1   Rationale of the Experimental Program

The key parameter affecting the behaviour of a partially grouted reinforced masonry shear wall can be identified as (Drysdale et al. 1999):

- Aspect ratio (Wall Geometry)

- Amount of horizontal and vertical reinforcing steel

- Vertical and horizontal reinforcement spacing

- Level of axial load

- Extent of grouting (full or partial grouting)

To reach conclusions about how significantly the different levels of these factors would affect the response of a partially grouted reinforced masonry shear wall, one may suggest a comprehensive experimental program based on factorial design (Montgomery and Runger 1994). However, given the number of key parameters and their wide range of values, even a comparative design solution (one-factor-at-a-time), which ignores the interaction effects between the factors, would require a large number of tests. Because this was not a feasible choice within the limited time and budget available for this study, the experimental program was narrowed to only consider the effects of aspect ratio (3 levels) and reinforcement spacing (3 levels) using five shear wall specimens.

As previously discussed, larger reinforcement spacing requires large specimens. Due to this and limited actuator capacities, full scale testing was not feasible. Therefore, direct small scale modelling technique (half-scale modelling) complying with the similitude requirements for constituent materials was adopted for testing. Similar to the wallette tests, a half-scale model unit of 20-cm hollow concrete block was used in wall construction (Figure 3.4) and smaller commercial deformed bars and wires were used as the model bars to represent full scale prototypes.
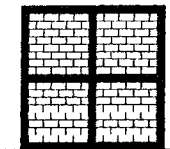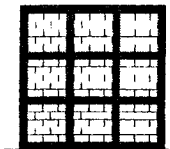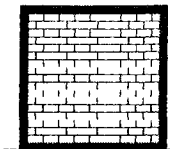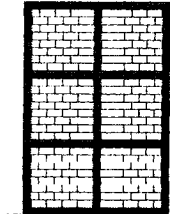
The initial correlation tests on properties of the half-scale and full-scale masonry units and assemblages were done in the Applied Dynamics Laboratory of McMaster University by Long (2006). These correlation tests include density, absorption, compressive strength and splitting tensile tests on masonry units as

well as compressive strength prism tests and diagonal tension tests on both hollow and fully grouted masonry assemblages. The test results confirmed the similarity of half-scale and full-scale masonry with some differences in geometric and material properties which were not found to be significant in composite behaviour. Long (2006) also extended the correlation tests to compare the behaviour of full-scale and half-scale reinforced block shear walls characterized by both distinct shear and flexural failure modes. Although half-scale shear walls designed to exhibit shear dominated failure showed some discrepancies with their prototype wall, the results supported the feasibility of modelling full-scale masonry using half-scale units.

3.3.2   Description of the Shear Wall Specimens

The shear wall specimens were designed to exhibit the effect of aspect ratio and reinforcement spacing on the behaviour of partially grouted reinforced masonry shear walls. The test matrix of the test program is presented in Table 3.4 and sketches of the walls are shown in Figure 3.12. As can be seen, all wall specimens were 1800 mm long (3600 mm long at full scale) with approximately the same steel ratio in the vertical and horizontal directions. Walls 1, 2 and 3 were intended to study the effect of reinforcement pattern. Wall 1 with 855 mm (1710 mm at full scale) bar spacing represented a typical partially grouted reinforced masonry shear wall. Wall 2 with 570 mm (1140 mm at full scale) bar spacing was intended to represent the maximum spacing of 1200 mm allowed by the current Canadian standard in masonry construction. For Wall 3, bar spacing was set to 1710 mm (3420 mm at full scale) as an extreme value. Wall 4 and Wall 5 along with

Table 3.4 – *Test matrix for shear wall specimens*

Specimen Label	Wall 1	Wall 2	Wall 3	Wall 4	Wall 5
Reinforcing Pattern	Wall 1	Wall 2	Wall 3	Wall 4	Wall 5
Dimensions	L = 1800 mm H = 1800 mm T = 90 mm	L = 1800 mm H = 1800 mm T = 90 mm	L = 1800 mm H = 1800 mm T = 90 mm	L = 1800 mm H = 900 mm T = 90 mm	L = 1800 mm H = 2700 mm T = 90 mm
Number and Size* of Reinf.	3 × #10 (V) 3 × D4 (H)	4 × #3 (V) 4 × D3 (H)	2 × #4 (V) 2 × 2D3 (H)	3 × #10 (V) 2 × D3 (H)	3 × #10 (V) 4 × D4 (H)
Reinforcement Ratio**	$\rho_v = 0.19\%$ $\rho_h = 0.05\%$	$\rho_v = 0.18\%$ $\rho_h = 0.05\%$	$\rho_v = 0.16\%$ $\rho_h = 0.05\%$	$\rho_v = 0.19\%$ $\rho_h = 0.05\%$	$\rho_v = 0.18\%$ $\rho_h = 0.04\%$
Bar Spacing	855 mm	570 mm	1710 mm	855 mm	855 mm
Aspect Ratio (H / ℓ)	1.0	1.0	1.0	0.5	1.5
Axial Stress**	0.75 MPa	0.75 MPa	0.75 MPa	0.75 MPa	0.75 MPa

* #10 (CA, $A_s = 100\ mm^2$), #3 (US, $A_s = 71.3\ mm^2$), #4 (US, $A_s = 130\ mm^2$), D3 (US, $A_s = 19.4\ mm^2$), D4 (US, $A_s = 25.8\ mm^2$ – US: USA size, CA: Canadian size.

** Based on gross area

Figure 3.12 – *Sketches of the shear wall test specimens*

(a) Wall 1

(b) Wall 2

(c) Wall 3

(d) Wall 4

(e) Wall 5

Wall 1 were designed to investigate the effect of aspect ratio (height to length) at three levels of 0.5, 1.0 and 1.5. A constant superimposed axial load of 120 kN corresponding to a compressive stress of 0.75 MPa (based on gross area) was applied on each wall. The applied axial stress represents an axial loading likely to be resisted by a shear wall in a typical five-storey masonry building.

3.3.3 Predicted Strength of the Test Walls

The first yield and ultimate flexural capacities together with shear resistances of the test walls were estimated in the design stage of the experimental test program. The calculated values are presented in Table 3.5. Flexural strength of the test walls were predicated based on simple beam theory ignoring material resistance factors. Linear stress distribution was assumed for estimation of the first yield strength of the walls. The compression force in the masonry at ultimate limit state was calculated using the rectangular stress block approach with $0.85 f_m'$ height

Table 3.5 – Preliminary simple prediction of flexural capacity and shear capacity of shear wall specimens

Specimen No. Bar Spacing (Aspect Ratio)	Flexural Strength (kN)		Shear Strength (kN)	
	First Yield	Ultimate	60% Effective Horizontal Steel	100% Effective Horizontal Steel
Wall 1 855 mm (1.0)	101.4	121.1	84.6	94.7
Wall 2 570 mm (1.0)	94.2	115.8	86.0	93.5
Wall 3 1710 mm (1.0)	106.2	113.0	87.1	102.2
Wall 4 855 mm (0.5)	202.8	230.8	106.8	114.3
Wall 5 855 mm (1.5)	67.6	80.8	84.6	94.7

and depth of 80% of the distance to the neutral axis. The vertical reinforcement was considered to be fully involved in load resisting capacity of the walls. The ultimate load was assumed to occur when masonry strain at the extreme compression fibre reached 0.003. The compressive strength, f'_m, was assumed to be 15 MPa for the grouted masonry and 25 MPa for the hollow sections. These values were adopted from the prism test results of phase one (diagonal compression tests) of this experimental program. A total face shell thickness of 31.2 mm and full thickness of 90 mm were used for the hollow and grouted areas, respectively. Modulus of elasticity for masonry was set to 850 times the corresponding compressive strength of the masonry. Yield strength of 475 MPa with elastic modulus of 200 GPa were used for both the vertical and horizontal steel bars.

Two sets of calculations, reported in Table 3.5, were conducted for shear capacity of the walls based on the Canadian masonry standard CSA S304.1-04 (CSA 2004) ignoring material resistance factors. One assumed 100% and the other one 60% contribution from the horizontal reinforcement to shear resistance. Walls 1, 3 and 4 were expected to experience a shear failure mode before reaching the yield stress of the vertical reinforcement. Wall 2 showed 10% higher shear strength than the first yield strength considering 60% effectiveness for the horizontal steel bars whereas the ultimate load was controlled by shear capacity of the wall. The first yield of Wall 5 was predicted to occur at about 85% of its governing flexural strength which indicates a flexural dominated failure mode. The details of flexural and shear strength calculations are presented in Appendices B and C.

3.3.4 Construction of the Wall Specimens
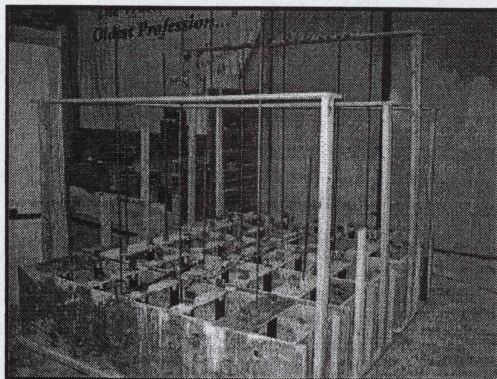
3.3.4.1 Reinforced Concrete Base

To simulate the effect of a relatively rigid foundation, each wall was constructed on a 500 mm wide by 400 mm high reinforced concrete base. Details of the reinforcement are presented in Figure 3.13. The vertical reinforcing bars of the wall specimens extended into the reinforcement cage of the base to provide adequate development length. As shown in Figure 3.14, the vertical bars were laterally braced by forms at their midheight to keep them vertically aligned during pouring of the concrete (Figure 3.14-a). The reinforcing cage of the base along with the vertical bars was placed inside a wooden form before pouring the concrete (Figure 3.14-b and c). Ten plastic tubes previously coated with grease were placed inside the formwork and removed when the concrete hardened. The resulting vertical holes were required to prestress the wall base onto the laboratory floor. The bases were poured with ready mix concrete with an average compressive strength of 35.2 MPa at the time of the first test. Figure 3.14-d shows the completed concrete based after prestressing onto the test platform.
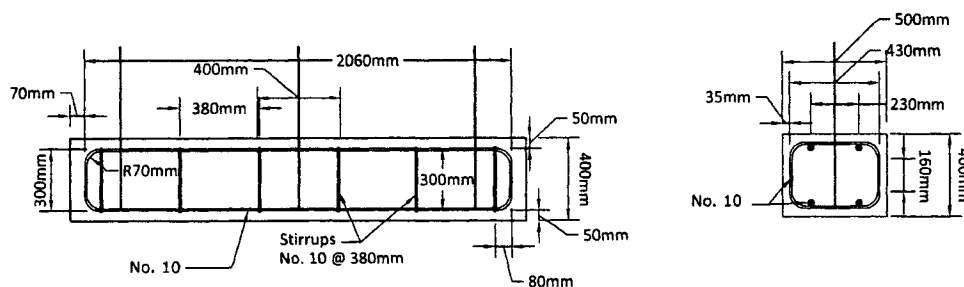
Figure 3.13 – *Reinforced concrete base used for shear wall tests*
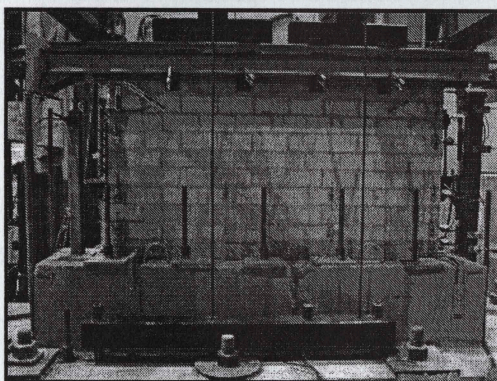
(a) Position of vertical reinforcing bars before pouring RC base

(b) Framework for vertical bars and tubes to accommodate prestressing rod

(c) Configuration of reinforcing bars inside the RC base

(d) Final RC base

***Figure 3.14** – Framework for reinforced concrete base of the shear wall specimens*

(a) Position of vertical reinforcing bars before pouring RC base

(b) Framework for vertical bars and tubes to accommodate prestressing rod

(c) Configuration of reinforcing bars inside the RC base

(d) Final RC base

Figure 3.14 – *Framework for reinforced concrete base of the shear wall specimens*

3.3.4.2 Wall Specimens

Wall specimens were constructed on the disposable concrete bases by a qualified mason. Using half-scale hollow concrete blocks required the mason to reduce the thickness of mortar joints to 5 mm. The height of the finished courses was controlled during the construction to size the mortar joints as precisely as possible. Based on the overall dimensions of the finished walls, the average thickness of the joints was approximately 5.72 mm indicating 14.4% greater thickness than the desired value.

Since the wall specimens were partially grouted, special consideration was required to prevent the grout from flowing into the adjacent blocks. Extra mortar on the block webs was used to fill the gap between the upper and lower blocks where only a continuous column of cells was to be grouted. To prevent the grout from flowing into the lower courses at the locations of horizontal reinforcement, a layer of plastic mesh (typical window screen with approximately 35% solid area) was placed on top of the course of block just below the course to be grouted. Figure 3.15-a shows this mesh prior to spreading the bed joint mortar and Figures 3.15-b and 3.15-c show the mesh after laying mortar and the corresponding course during grout pouring, respectively. A photograph of a grouted course exposed after destruction of one of the tested walls is also shown in Figure 3.16. As can be seen, the continuity of the grouted cells in the horizontal direction was satisfactorily achieved and the mesh prevented the flow of grout during pouring. Walls were grouted using fine grout mixed in the laboratory. Multiple lifts of grouting were done depending on the number of horizontally reinforced courses in each wall.
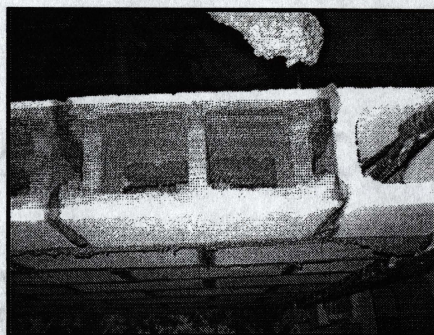
(a) Placement of plastic mesh before laying mortar

(b) Laying mortar bed joints

(c) Grout pouring

***Figure 3.15** – Construction of horizontally reinforced course in the middle of a shear wall*

***Figure 3.16** – Effectiveness of the plastic mesh in preventing grout flow to the lower courses (picture taken after demolishing the tested shear wall specimen)*

3.3.5 Description of Constituent Materials

3.3.5.1 Masonry Blocks

Similar to phase one tests (diagonal compression tests) in this experimental program, the half-scale model of 20-cm concrete blocks were used in the construction of the wall specimens (Figure 3.4). The webs of the masonry blocks which were to be used in courses containing horizontal reinforcement were knocked out to half height to permit positioning of the horizontal reinforcing bar in the middle of the block course.

3.3.5.2 Mortar

Standard type S mortar was used for wall construction. The constituent material consisted of type 10 normal portland cement, type S autoclaved mason's lime and dry masonry sand. The above materials were mixed in 25 kg batches in proportions by weight of 1.0:0.21:3.53 parts for cement:lime:sand. A water:cement ratio of 0.88 was used to satisfy the workability requirements and each batch was used within 30 minutes of mixing and no retempering was allowed after mixing. Construction of all of the shear wall specimens and control specimens required a total of 28 batches.

The initial mortar flow was measured for each batch. The average initial flow was 127.4 mm with a coefficient of variation of 2.0% (see Appendix A for detail test results). Three 50-mm mortar cubes were also cast before using each batch of mortar. The cubes were air cured in the laboratory under the same conditions as the wall specimens. The mortar cubes were tested in compression in accordance with

ASTM C109/C109M-02 (ASTM 2002a). The average compressive strength of the hardened mortar was 21.4 MPa with a coefficient of variation of 15.7% (see Appendix A for detail test results).

3.3.5.3 Grout

Test walls were filled with fine grout at location of horizontal and vertical reinforcement. The grout was prepared using type 10 normal Portland cement, type S autoclaved mason's lime and dry concrete sand with a maximum aggregate size of 5 mm. The small amount of lime was added to increase workability of the mix. The mix design consisted of the proportion of 1.0:0.04:2.4 parts by weight of portland cement:lime:sand. A water:cement ratio of 0.64 by weight was used resulting in 267 mm (10.5 in.) slump.

Since the walls were partially grouted, each wall was grouted in multiple lifts during construction. To reduce the required number of grout mixes, all five walls were constructed up to the first course which needed to be grouted. The grout batch was then mixed and the cells containing horizontal and vertical reinforcement were filled with grout. This routine continued until construction of walls was complete.

Three 200-mm-high by 102-mm-diameter cylinders and three block-moulded prisms using half-scale blocks with the approximate prism dimension of 90 mm × 90 mm × 185 mm were cast as control specimens during each lift of grouting. All of the specimens were hard capped using hydrostone and were tested under uniaxial compression. The test results for the grout samples are presented in Table 3.6.

Table 3.6 *– Grout control compression test results related to shear wall tests*

Type	Sample No.	Strength (MPa)	Type	Sample No.	Strength (MPa)
Cylinder	G-C1-1	35.0	Block-Moulded Prism	G-P1-1	27.8
	G-C1-2	34.1		G-P1-2	41.1
	G-C1-3	33.1		G-P1-3	28.9
	G-C2-1	32.1		G-P2-1	35.0
	G-C2-2	34.3		G-P2-2	42.7
	G-C2-3	33.4		G-P2-3	36.4
	G-C3-1	31.3		G-P3-1	34.7
	G-C3-2	35.9		G-P3-2	37.9
	G-C3-3	37.5		G-P3-3	40.9
	G-C4-1	42.7		G-P4-1	34.8
	G-C4-2	39.6		G-P4-2	43.5
	G-C4-3	43.0		G-P5-3	46.4
	Average (C.O.V.)	36.0 (10.9%)		G-P5-1	41.7
				G-P5-2	39.4
				G-P5-3	32.9
				Average (C.O.V.)	37.6 (14.2%)

* *Cross sectional area = 8171.3 mm²*

* *Cross sectional area = 8100 mm²*

3.3.5.4 Reinforcement

The vertical reinforcement used in this experimental program include No. 10 (A_s = 100 mm²), No. 3 (USA size, A_s = 71.3 mm²) and No. 4 (USA size, A_s = 130 mm²) bars. Three randomly chosen 600-mm-long samples were tested under uniaxial tension for each bar size. The elongations of the bars were measured using an extensometer with a gauge length of 50 mm. The average stress-strain relationships of the bars are presented in Figure 3.17-a.

For horizontal reinforcement, D3 (A_s = 19.4 mm²) and D4 (A_s = 19.4 mm²) deformed wires were used. These wires were manufactured in compliance with ASTM A496/A496M-05 (ASTM 2005). Figure 3.17-b shows the stress-strain relationships of these deformed wires obtained using the same apparatus as for the

(a) Vertical Reinforcement　　　　　(b) Horizontal Reinforcement
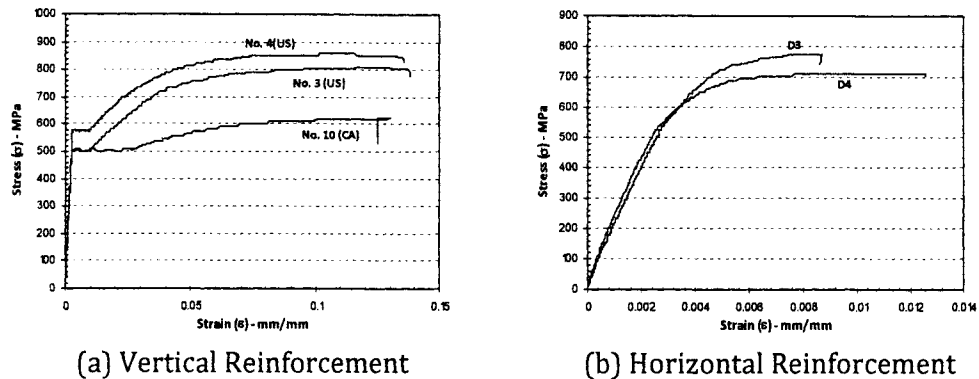
Figure 3.17 *– Average stress-strain curves for steel reinforcing bars*

vertical reinforcement. In contrast to the vertical bars, the deformed wires did not exhibit well defined yield points. Therefore, the yield strength was defined at 0.2% offset strain by finding the intersection of the stress-strain curve with a line parallel to the linear elastic part of the curve and which intercepts the abscissa at 0.002. The geometric and mechanical properties of the bars used in the construction of the shear wall specimens are listed in Table 3.7.

3.3.5.5 Assemblage Tests

Assemblage tests consisting of masonry prism, diagonal tension and splitting tests normal to the bed joints were carried out in order to identify material and assemblage properties. The prism and diagonal tension specimens were built during construction of the shear walls by the same experienced mason. Six hollow specimens and six grouted specimens were fabricated for each test. All of the specimens were constructed in running bond using full unit and half-unit masonry blocks cut from a full block as illustrated in Figure 3.18. This arrangement of units was found to provide a better representation of actual condition at the compression

Table 3.7 – *Geometric and mechanical properties for reinforcing steel bars related to shear wall tests*

Type	Sample No.	E_s (GPa)	f_y (MPa)	ε_y (mm/mm)
No. 10 (CA Size) $A_s=100$ mm²	1	201.8	497	0.0025
	2	201.1	489	0.0024
	3	202.1	489	0.0024
	Average (C.O.V.)	201.6 (0.23%)	491.7 (0.94%)	0.0024 (0.92%)
No. 3 (US Size) $A_s=71$ mm²	1	201.9	500.0	0.0025
	2	192.3	507.4	0.0026
	3	208.9	501.5	0.0024
	Average (C.O.V.)	201.0 (4.15%)	502.9 (0.77%)	0.0025 (4.85%)
No. 4 (US Size) $A_s=126$ mm²	1	200.7	563.6	0.0028
	2	203.3	565.3	0.0028
	3	201.5	565.3	0.0028
	Average (C.O.V.)	201.8 (0.65%)	564.7 (0.17%)	0.0028 (0.53%)
D3 (US Size) $A_s=19.4$ mm²	1	155.6	744.0	0.0048
	2	185.8	743.1	0.0040
	3	209.6	744.1	0.0036
	Average (C.O.V.)	183.6 (14.7%)	743.7 (0.07%)	0.0041 (15.2%)
D4 (US Size) $A_s=25.8$ mm²	1	206.1	688.8	0.0033
	2	184.5	695.0	0.0038
	3	204.0	688.4	0.0034
	Average (C.O.V.)	198.2 (6.01%)	690.7 (0.53%)	0.0035 (6.77%)

toe of a partially grouted reinforced masonry shear wall where the compression one ends in full and half unit masonry blocks. As shown in Figure 3.18, to represent actual construction, the frogged-ends of half blocks were positioned towards the inside the specimens. The control specimens were grouted with the same batch of grout as used for the shear walls. Two prisms and two diagonal tension samples were grouted from each of three different lift of grout during construction of the shear walls.

<table>
<tr><td>(a) Uniaxial
compression prisms</td><td>(b) Diagonal tension and normal to
bed joints splitting test specimens</td></tr>
</table>
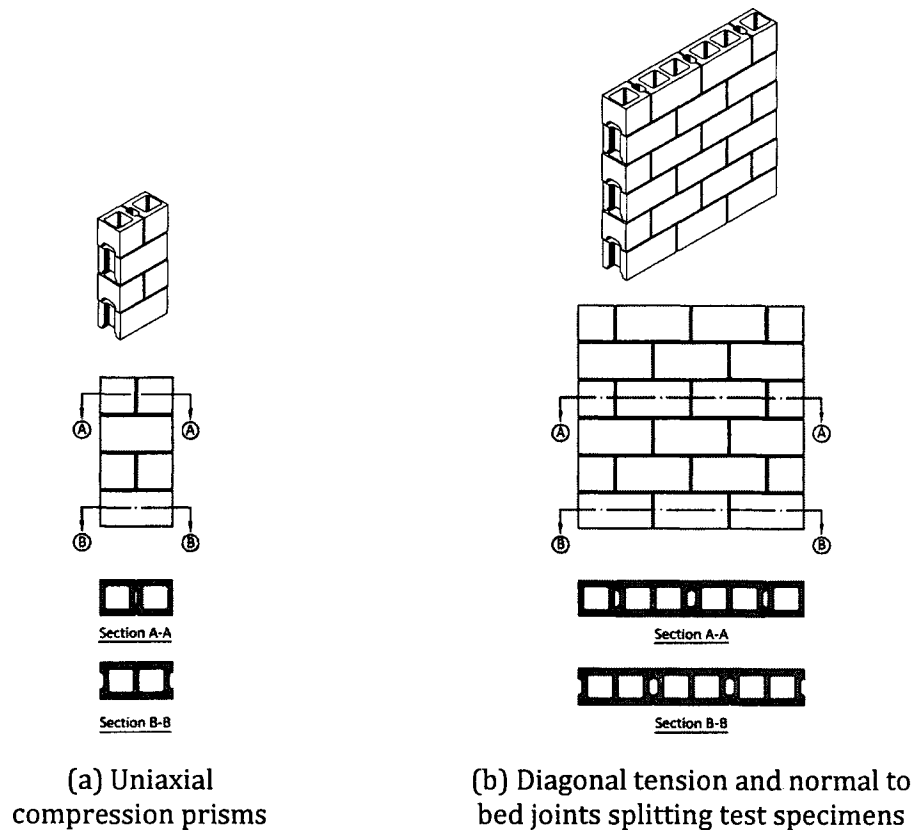
Figure 3.18 – Control specimens for shear wall tests

The masonry prisms were capped with hydrostone and were tested under uniaxial compression according to ASTM C1314-03b (ASTM 2003). Test setup, instrumentation and calculation scheme were the same as for the prism test related to diagonal tension tests of the wallettes as described in Section 3.2.4.5. The test results are presented in Table 3.8. The average uniaxial compressive strength of grouted prisms was 12.4 MPa (C.O.V. = 6.8%) corresponding to an average strain of 0.0013 (C.O.V. = 15.1%). An average uniaxial compressive strength of 21.6 MPa (C.O.V. = 4.7%) was also obtained for hollow prisms with an average strain of 0.0013 (C.O.V. = 18.6%) at maximum stress.

Table 3.8 – *Prism test results related to shear wall tests*

Type	Sample No.	f'_m (MPa)	ε_m (mm/mm)
Grouted	P-G1-W	12.83	0.0011
	P-G2-W	13.25	0.0015
	P-G3-W	11.63	0.0011
	P-G4-W	11.88	0.0012
	P-G5-W	13.43	0.0016
	P-G6-W	11.56	0.0013
	Average (C.O.V.)	12.43 (6.76%)	0.0013 (15.1%)
Hollow	P-H1-W	20.18	0.0011
	P-H2-W	21.95	0.0014
	P-H3-W	20.98	0.0010
	P-H4-W	22.48	0.0013
	P-H5-W	21.18	0.0013
	P-H6-W	22.92	0.0017
	Average (C.O.V.)	21.61 (4.73%)	0.0013 (18.6%)

The diagonal tension tests were conducted in accordance with ASTM E519-02 (ASTM 2002b). The results of the tests are summarized in Table 3.9. The specimens for diagonal tension testing were increased in size to three-block-wide by six-block-high samples (see Figure 3.18-b) compared to the ones used for diagonal tension tests related to the wallette tests as described in Section 3.2.4.5 (see Figure 3.8-b). This larger specimen was chosen to reduce the effect of boundary conditions and forced loading path which are key deficiencies of the diagonal tension test. Test specimens were capped and tested using a test procedure similar to that described in Section 3.2.4.5. The average diagonal tensile strength of grouted specimens was 1.9 MPa (C.O.V. = 7.7%) corresponding to an average tensile strain of 0.00044 (C.O.V. = 21.6%). For hollow specimens, an average diagonal tensile strength of

1.9 MPa (C.O.V. = 10.7%) was measured with an average tensile strain of 0.00024 (C.O.V. = 15.4%).

To provide an estimation of the bond strength of mortar bed joints, five hollow three-block-wide by six-block-high specimens (Figure 3.18-b) were constructed and tested under uniaxial compression along the middle bed joint to create splitting tension normal to the bed joint. Details of the test setup are presented in Figure 3.19. A strip of 20-mm-thick plywood along with a 20-mm-thick steel plate provided the top and bottom bearing surfaces. The strips were 50 mm wide which distributed the applied load over a width equal to 0.087 of the height of the specimen. This ratio gives a deviation of tensile stresses from those calculated on the basis of line loads, $f_t = 2P/\pi dt$, of less than 3% (Hamid 1978) which is not

Table 3.9 – Diagonal tension test results related to shear wall tests

Type	Sample No.	f_t (MPa)	ε_m (mm/m m)
Grouted	DT-G1-W	2.22	0.00045
	DT-G2-W	1.96	0.00047
	DT-G3-W	1.90	0.00050
	DT-G4-W	1.86	0.00054
	DT-G5-W	1.84	0.00043
	DT-G6-W	1.83	0.00027
	Average (C.O.V.)	1.93 (7.71%)	0.00044 (21.6%)
Hollow	DT-H1-W	1.65	0.00029
	DT-H2-W	1.93	0.00020
	DT-H3-W	1.91	0.00025
	DT-H4-W	1.94	0.00021
	DT-H5-W	N/A*	N/A
	DT-H6-W	2.23	0.00023
	Average (C.O.V.)	1.93 (10.7%)	0.00024 (15.4%)

* *Specimen was damaged during moving and handling*
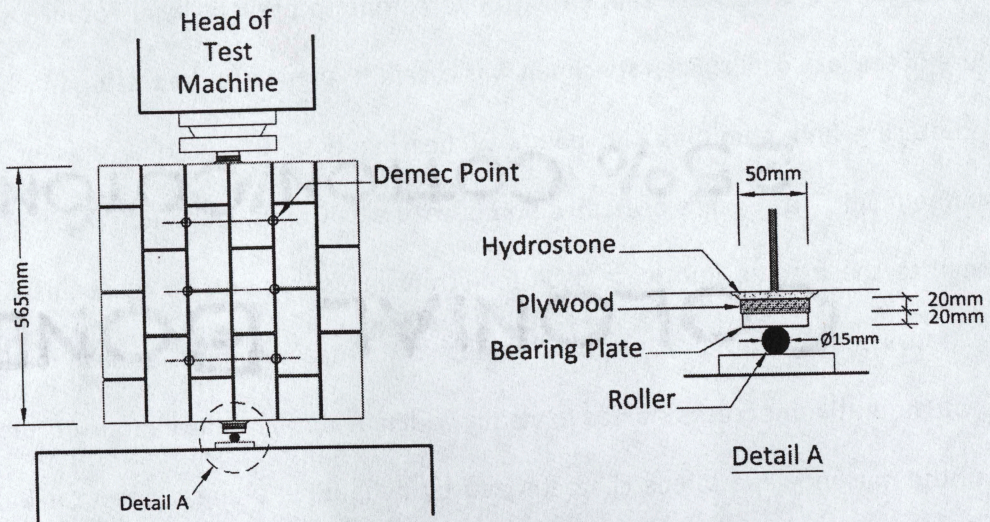
(a) Sketch of the test setup
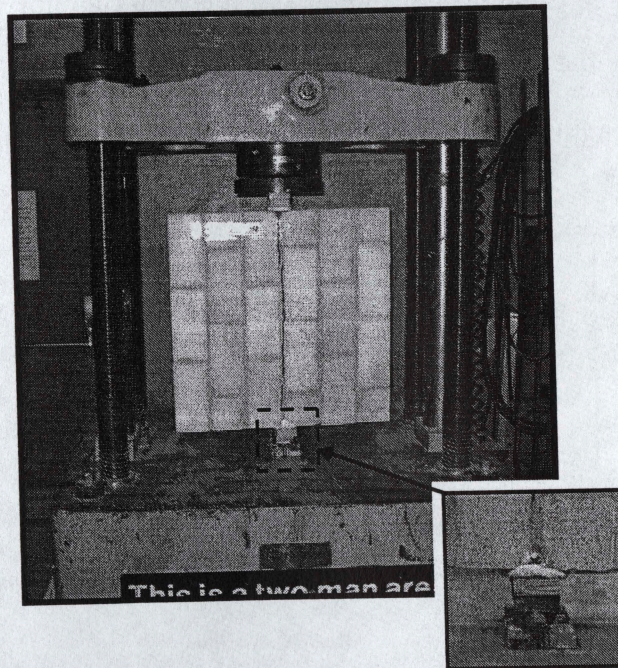
(b) Actual test setup

Figure 3.19 – *Test setup used for splitting test normal to bed joints*

significant compared to the variation in test results. The surfaces of the bearing

blocks under the load were capped with hydrostone to prevent local compression

failure of the face shells. Each specimen was carefully aligned in the testing machine

by centering and plumbing the points of bearing with the vertical axis of the

machine head. Three pairs of Demec points with a 200 mm gauge length oriented

normal to the loading line were used for strain measurements in the transverse

direction. The load was slowly applied taking strain measurements at each loading

increment until joint cracks started to visibly widen. A similar failure mode occurred

in all the masonry specimens characterized by debonding along the mortar-block

interface in the vicinity of the loaded plane. The stress-strain results of the tensile

splitting tests are presented in Figure 3.20. Table 3.10 contains a listing of the bond

strengths where the first change in the stiffness of stress-strain curve indicates the

initial bond strength of the mortar bed joints. The hardening behaviour beyond this
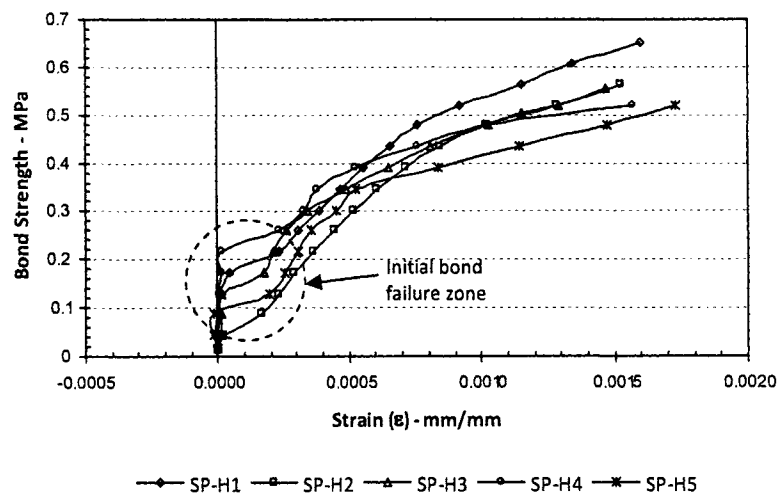
Figure 3.20 – Stress-strain relation from splitting test normal to bed joints

Table 3.10 – *Results of splitting test normal to bed joint related to shear wall tests*

Type	Sample No.	Bond Strength (MPa)
Hollow	ST-H1-W	0.217
	ST-H2-W	0.087
	ST-H3-W	0.173
	ST-H4-W	0.260
	ST-H5-W	0.130
	Average (C.O.V.)	0.173 (39.5%)

point is believed to be due to the fact that close to the loading points, the specimen experienced a biaxial compression-compression state of stress. This, in turn, resisted penetration of vertical cracks into this zone and enabled vertical compression paths to continue to exist and resist increasing load on both sides of the crack (Figure 3.20). Therefore, only the initial bond strength up to cracking was considered as the bond strength of the mortar-block interface.

3.3.6   Test Setup

A sketch of the entire setup used for the shear wall tests is illustrated in Figure 3.21. The setup was intended to provide lateral and axial in-plane loading with the optimal possible accuracy. Technical details of the main elements of this setup are provided in this section.

A 600-mm-deep reusable concrete slab which had been prestressed down to the 600-mm-thick strong floor of the laboratory was used as a relatively rigid platform for testing. To facilitate the vertical and horizontal plumbing of the test wall and also precise alignment of the wall's plane with the axis of the loading actuator, an approximately 20-mm-deep layer of mortar was spread between the
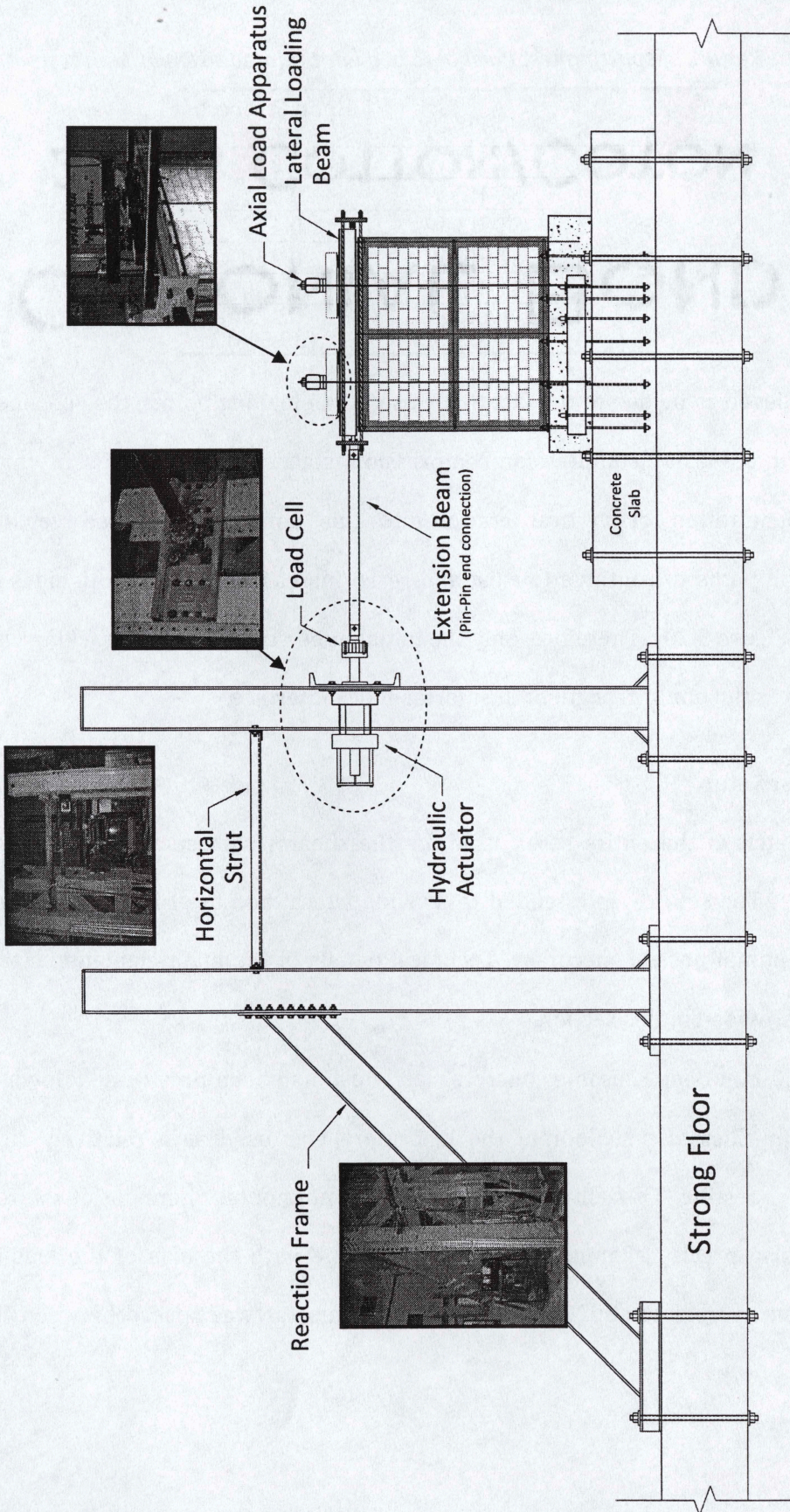
Figure 3.21 – Front view of the shear wall test setup

disposable base of the wall specimens and the permanent concrete platform. The base of the wall specimen was prestressed down onto the testing platform using five 25.4 mm diameter steel prestressing steel bars on each side of the wall. These prestressing bars were anchored in the reusable concrete slab and spaced at 400 mm in the longitudinal direction and at 320 mm in the transverse direction. After positioning the test wall, the prestressing bars were post-tensioned to clamp the disposable base of the specimen onto the reusable testing platform (Figure 3.22).

As shown in Figure 3.21, the hydraulic actuator used to apply the lateral load on the wall specimens was mounted between two wide flange shape columns which had been prestressed down to the main laboratory floor along their strong axis. The actuator was bolted to a relatively stiff beam spanning between the two columns. To

(a) Front View (b) Side View
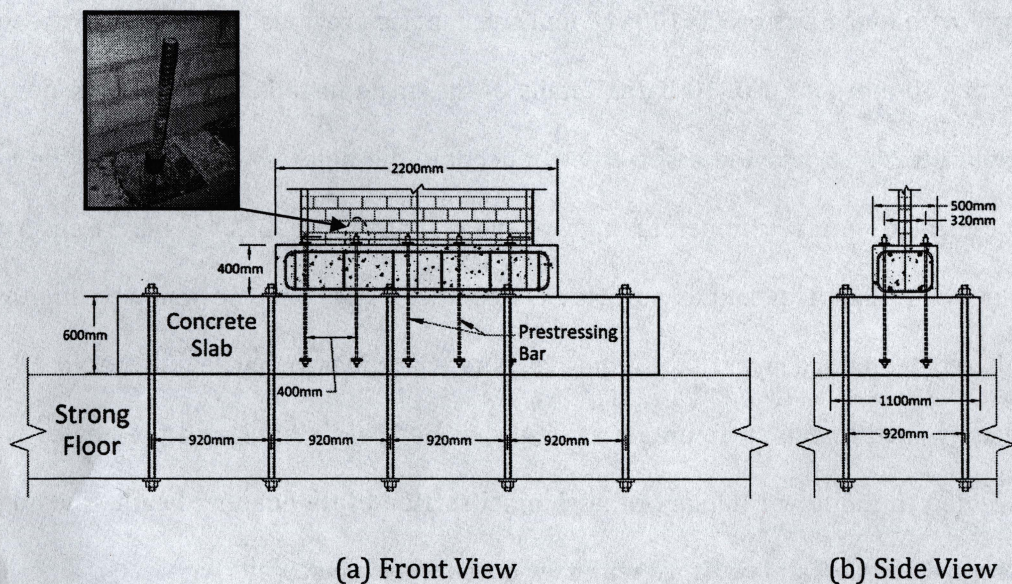
Figure 3.22 – Prestressing testing platform onto the strong floor and the disposable base onto the testing platform

reduce the deflection at the level of the actuator, the columns were connected to another reaction frame by horizontal struts.

A steel beam, shown in Figure 3.23, was attached to the top of the wall and used to transfer the applied lateral load uniformly along the top of the wall. The beam was composed of a 200-mm-wide by 19-mm-thick steel plate welded to two C150×19 channels along its length. The steel plate had pre-drilled holes positioned to coincide with the vertical reinforcing and additional doweling bars extending above the top of the wall. A layer of mortar (approximately 10 mm thick) was laid between the loading beam and the top of the wall to provide a soft surface for levelling. The vertical bars were welded to 13-mm-thick steel washer plates which had been previously welded to the 19-mm-thick loading beam plate. To help ensure uniform shear transfer from the loading beam to the wall, it was also attached to the wall with four pairs of 75×100×10 mm steel angles previously anchored to the wall with 150-mm-long No. 10 bars. Details of the angle installations are presented in Figure 3.24. To provide a slip free connection, the holes drilled through the wall were filled with a commercial high strength structural adhesive[1] before inserting the No. 10 bar. The contact surface between the angles and the wall specimen was also coated with a layer of the adhesive. When the adhesive hardened, the No. 10 bar was welded to the structural steel angles at both of its ends and the angles were welded to the lower flange of the channel section of the loading beam. The angles were ground off and replaced with new ones for each test wall.

---

[1] AC100 PLUS – Epoxy Acrylate adhesive designed for use in anchoring threaded rods and reinforcing bars into concrete and masonry base materials

Top View

Front View

Section A-A
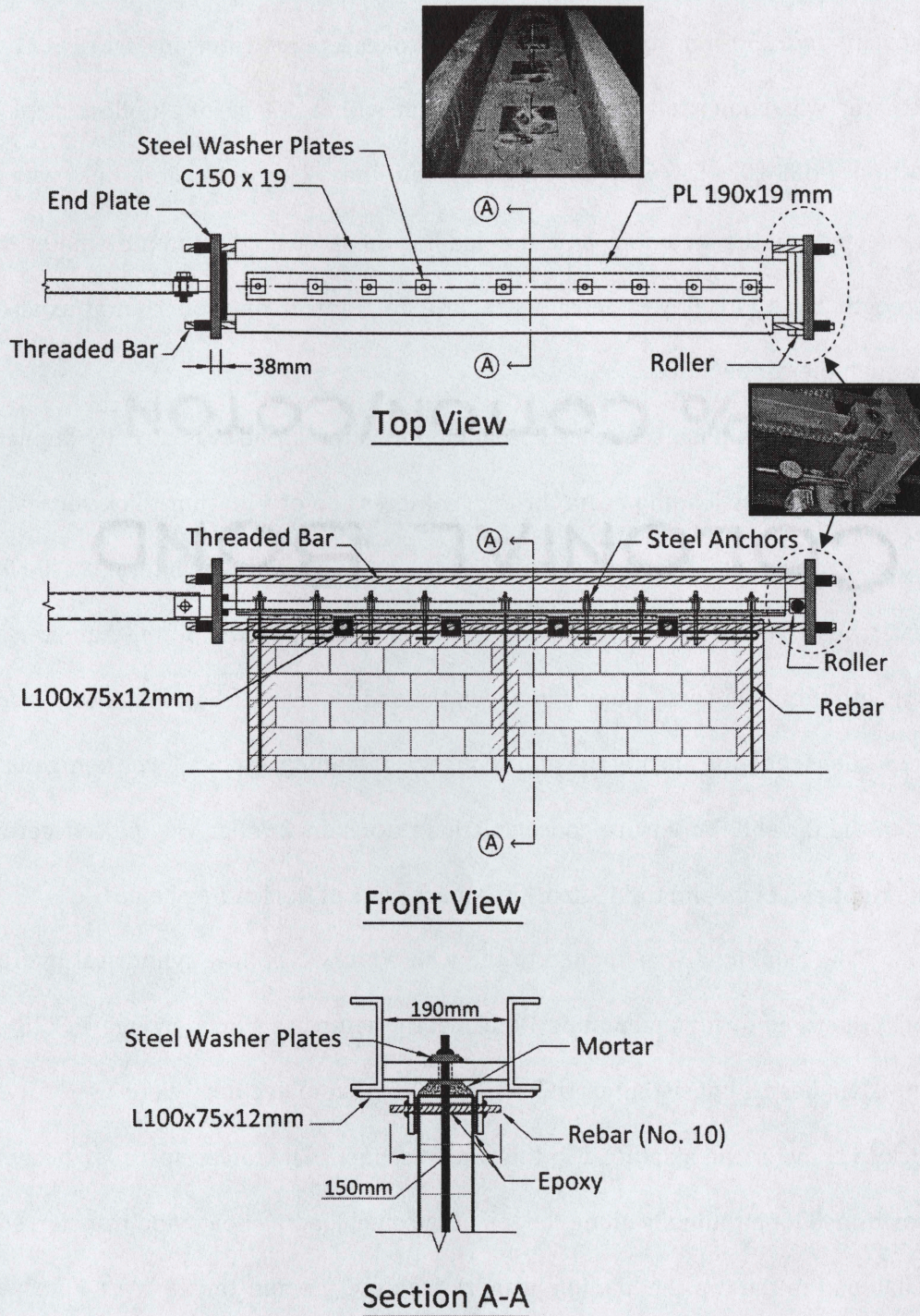
Figure 3.23 – *Details of loading beam for shear wall tests*

Lateral load was applied using a MTS 204.71 hydraulic actuator with 250 kN capacity and 150 mm total displacement stroke. As illustrated in Figure 3.21, the actuator was connected to the loading beam with a 1.4-m-long hollow steel box section (HSS 102×51×6.2) as an extension link. The extension link was pin connected to the actuator and the loading beam using 20-mm-diameter high strength bolts (1100 MPa tensile strength) to transfer only horizontal axial load through the connection.

During the push sequence of loading, the lateral load was directly applied to the left end of the loading beam through compression of a 38-mm-thick vertical end plate. However, when load was applied in the pull direction, the lateral tensile force was transferred to the right end of the wall by pulling four 25-mm-diameter high strength threaded bars fastened between the end plates of the loading beam (Figure 3.23). Consequently, during the pull sequence of loading, the wall was being pushed from the far end. To ensure concentric load transfer, a roller was placed between the right end plate and the 19-mm-thick base plate of the loading beam.

The axial load was applied to the wall with two hollow cylindrical hydraulic jacks operated by manual pumps. Details of the setup are shown in Figure 3.25. Two spreader beams consisting of HSS 127×127×6.35 mm sections were used for each jack to transfer the axial load to the wall specimen. The lower spreader beam was positioned longitudinally along the top of the steel loading beam and transferred the axial load to the top the loading beam though two 19-mm-thick plates. Four plates were used for each wall (two for each jack) positioned at one-fifth points along the
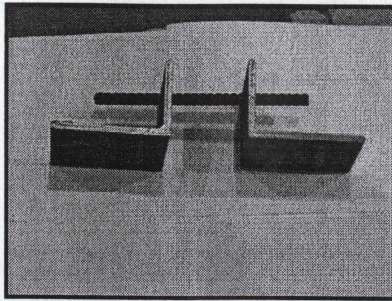
(a) Angles and rebar before installation
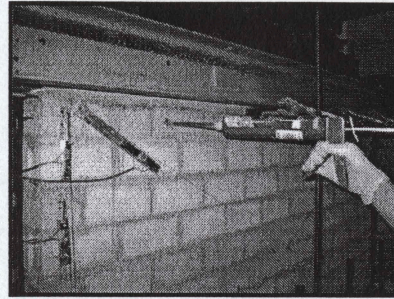
(b) Injection of adhesive into drilled holes
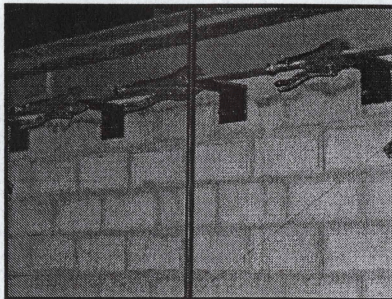
(c) Temporary fasteners after adhesive injection
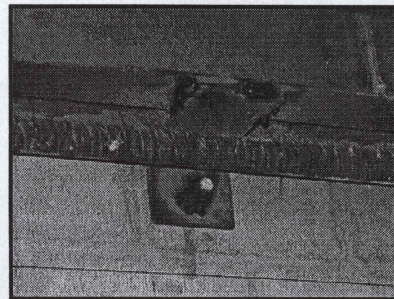
(f) Welded angle to the loading beam and to the rebar

Figure 3.24 – Installation of auxiliary shear transfer angles

length of the wall to ensure uniform distribution of axial load. The upper spreader beam through which the high strength rods were attached was placed transversely on top of the lower spreader beam and separated with a 38-mm-diameter roller to provide a moment free connection. Each hydraulic jack was hung from the transverse spreader beam by 10-mm-diameter high strength threaded rods. A similar rod was used on the other side of the spreader beam to counteract the applied axial load and maintain equilibrium. The high strength rods were bolted down to a HSS 127×127×6.35 mm beam that was attached to the permanent concrete slab and laboratory floor using the large bolts that also anchored the concrete slab onto the laboratory floor.

Concrete
Slab

Load Cell

Lower
Spreader
Beam

Hydraulic Jack
(Hollow and Cylindrical)

Upper Spreader
Beam

Roller

Bearing
Plate

High Strength
Threaded Rod

Anchoring Beam

Strong
Floor
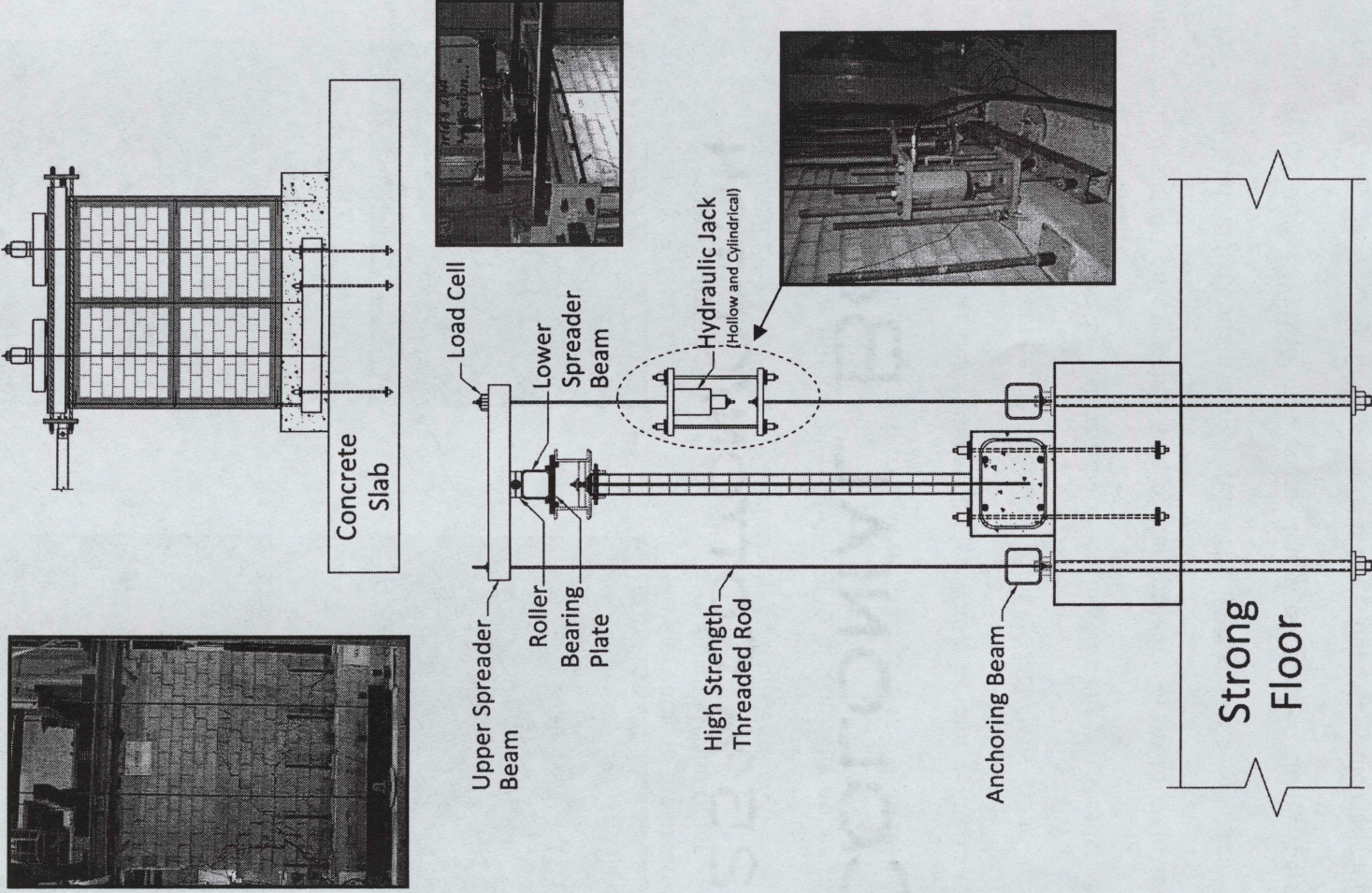
Figure 3.25 – Axial load application setup

An out-of-plane bracing system consisting of two hollow steel box sections attached to steel columns was used to prevent movement of the loading beam (and the wall) in the out-of-plane direction. To minimize resistance to the in-plane displacement of the loading beam, two rollers attached to the bracing members were positioned between the two channel-sections of the loading beam with approximately 5 mm space between each roller and the adjacent channel-section. Details of the out-of-plane bracing system are presented in Figure 3.26.
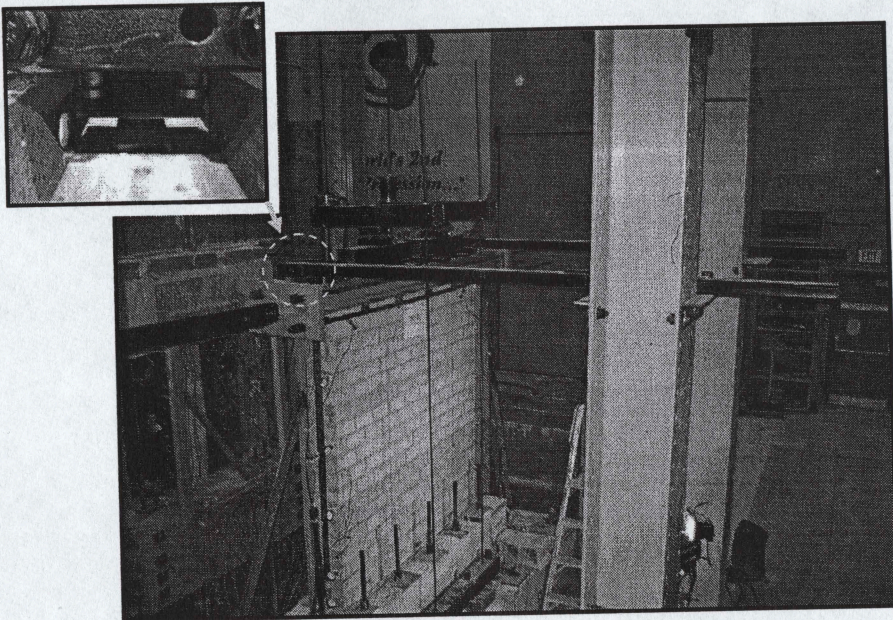
Figure 3.26 – Out-of-plane bracing system

3.3.7 Instrumentation

Lateral displacements of the walls were monitored during the tests using dial gauges mounted at designated heights along both the right and left ends of the walls. The dial gauges at each end were attached to a relatively stiff reference frame which

was laterally braced to prevent any movement. The typical arrangement of instrumentation devices used for the wall specimens with aspect ratio of one is shown in Figure 3.27.

Pairs of Demec points spaced at 200 mm were used to monitor the average flexural curvature of the wall at various levels over the height of the wall. Since larger changes in lateral displacement and flexural curvature were expected at lower levels, spacing between dial gauges and pairs of Demec points was reduced

External Instrumentation

Internal Instrumentation
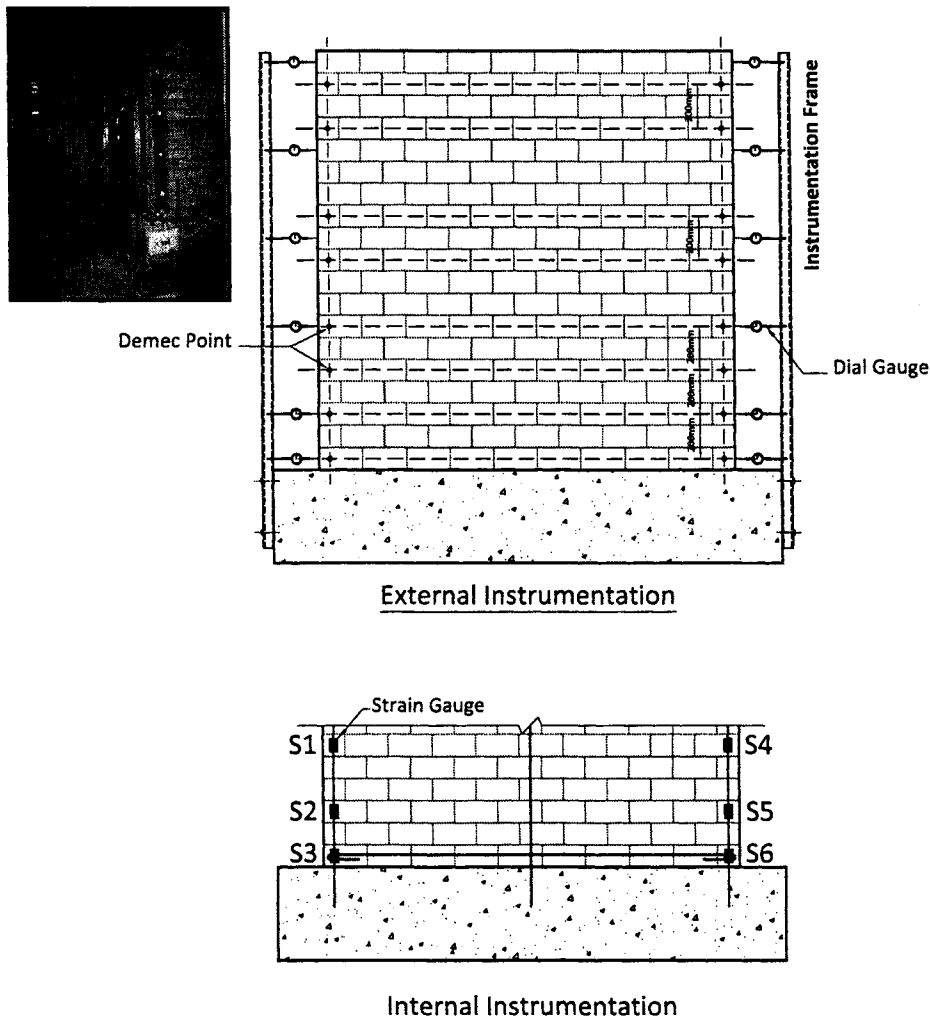
Figure 3.27 – Typical instrumentation for square shear wall specimens

near the base. Six electrical strain gauges were also attached to vertical reinforcing bars at the ends of the walls to monitor the strain history of these outermost steel bars during the test.

The displacements of the upper right and upper left corners of the wall measured by the top dial gauges were recorded simultaneously by two technicians throughout each loading cycle. The time interval between the readings was decided by the test operator based on the displacement rate assigned to the actuator for each loading cycle. To provide an accurate load-displacement hysteresis loop, at least 75 readings were taken during each push and pull loading cycle. The in-plane lateral displacements of the wall measured by dial gauges along with the Demec point readings were recorded at the extreme displacement intended for each loading cycle. [It should be noted that electronic measurements were not found to be sufficiently accurate for very small displacements.]

3.3.8 Loading Procedure

All test walls were subjected to fully reversed cyclic loading controlled by displacements measured in the push and pull directions. Loading started with a displacement amplitude corresponding to approximately 0.01% storey drift and then was increased to between 130% and 150% of the previous cycle depending on the damage progression observed during each cycle. Each loading cycle was repeated twice and testing continued until the remaining resistance had degraded by more than 50% of the ultimate strength of the test specimen. A typical loading cycle employed for Wall 1 is illustrated in Figure 3.28.
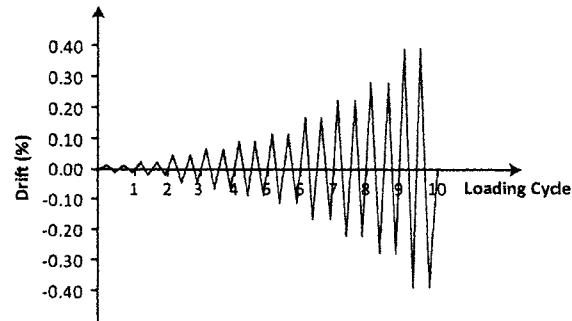
Figure 3.28 – *Typical loading cycle used for Wall 1*

3.4   CLOSING REMARKS

The experimental test program of this study consisting of two phases has been presented in this chapter. The test program was designed to provide a body of test data to evaluate the performance of partially grouted reinforced concrete block shear walls under the action of in-plane cyclic loading. The rationale for the designed experimental program and selection of specimens were discussed followed by descriptions of the construction stage and properties of constituent materials. The implemented test setup was then described and illustrated in detail. Finally, the loading procedure adopted for the shear wall tests was presented. The results of the shear wall tests are discussed in Chapter 4.

CHAPTER 4

EXPERIMENTAL RESULTS AND ANALYSIS

4.1 INTRODUCTION

The results of the experimental program are presented and discussed in the two sections after this introduction. The first section documents the experimental observations of the preliminary tests on diagonal behaviour of masonry panels followed by a discussion on the significance of the results. In the next section, the results of five shear wall tests intended to investigate the cyclic response of partially grouted reinforced masonry shear walls under in-plane axial and lateral loading are presented. The general observations recorded during each test including the overall wall behaviour, crack pattern and sequence of failure are first described. The wall load-displacement hysteresis loops are then reviewed followed by a discussion of measured lateral in-plane deformation and average curvature along the wall height. Finally, a detailed analysis of the experimental data is provided highlighting key behavioral characteristics of masonry shear walls such as lateral load resistance, stiffness, displacement ductility and evaluated seismic load reduction factor.

115

4.2 DIAGONAL COMPRESSION TESTS – WALLETTE TESTS

Nine diagonal compression tests were carried out to investigate the effect of peripheral confinement provided by the reinforced masonry blocks along the four sides of the masonry wallettes. The results of the diagonal tension tests including ultimate load, ultimate shear stress and corresponding shear strain as well as failure mode are summarized in Table 4.1. Further details regarding test observations for each type of wallette specimen are discussed in the following subsections.

4.2.1 Fully Grouted Reinforced Wallettes (W-G Series)

The compression load vs. deformation along the vertical diagonal (average of the two faces) is presented in Figure 4.1-a. The wallettes did not exhibit any visible

Table 4.1 – Test results for wallette tests

Specimen		Area (mm²)	Ultimate Strength				Failure Mode
			Load (kN)	Vertical Deformation (mm)	Shear Stress (MPa)	Shear Strain (mm/mm)	
Fully Grouted Reinforced	W-G1	67950*	164.9	0.49	1.72	0.00116	Vertical / Diagonal Stepped Pattern Crack
	W-G2		167.7	0.49	1.74	0.00056	
	W-G3		181.6	0.41	1.89	0.00046	
	Average (C.O.V.)		171.4 (5.2%)	0.46 (10.0%)	1.78 (5.2%)	0.00073 (52.1%)	
Partially Grouted Reinforced	W-PG1	45105**	64.68	0.24	1.65	0.00044	Diagonal Stepped Pattern Crack
	W- PG2		77.59	0.26	1.34	0.00029	
	W- PG3		79.74	0.96	1.61	0.00194	
	Average (C.O.V.)		74.0 (11.0%)	0.49 (84.3%)	1.53 (11.0%)	0.00089 (102.5%)	
Hollow	W-H1	37495***	46.0	0.23	1.38	0.00027	Shear-Slip
	W-H2		49.2	0.20	1.48	0.00025	
	W-H3		50.5	0.31	1.52	0.00033	
	Average (C.O.V.)		48.6 (4.8%)	0.25 (23.1%)	1.46 (4.8%)	0.00028 (14.7%)	

* Based on gross area
** Based on two half blocks fully grouted and face-shell area for remainder of wall length
*** Based on face-shell mortared area
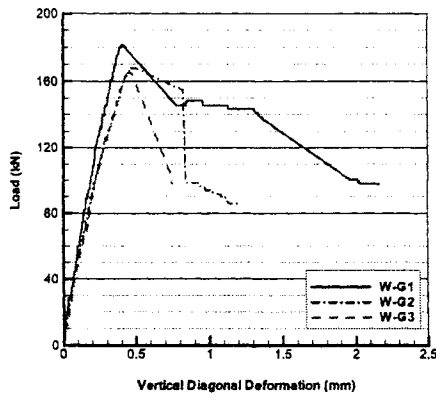
(a) L-D Curve: W-G Series

(b) Typical Crack Pattern: W-G Series

(c) L-D Curve: W-PG Series
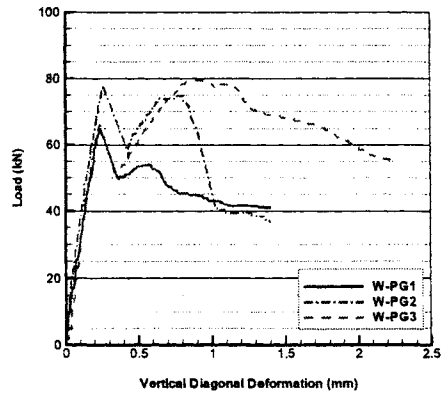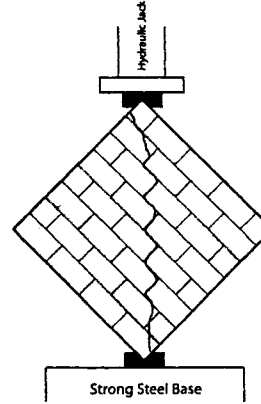
(d) Typical Crack Pattern: W-PG Series

(e) L-D Curve: W-H Series
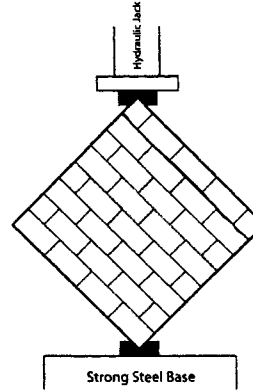
(f) Typical Crack Pattern: W-H Series

Figure 4.1 – *Load-deformation curves and general crack patterns for wallette tests*

crack before peak load. Upon reaching the maximum strength, a mixed crack pattern through the joints and the masonry units suddenly appeared on the specimens and widened while the test progressed (Figure 4.1-b). The crack pattern followed an essentially straight vertical line near the corners and a distinct stepped-pattern over the midheight. Continuation of the post-peak loading even down to 30% of the peak load did not affect the integrity of specimens. However, some signs of spalling close to the loading shoes were observed.

4.2.2   Partially Grouted Reinforced Wallettes (W-PG Series)

Failure was dominated by a distinct stepped-pattern crack along the loading path (Figure 4.1-d). As expected, due to the confinement provided by the peripherally grouted and reinforced cells, wallettes maintained their integrity after diagonal cracking. The compression load vs. deformation along the vertical diagonal (average of the two faces) is shown in Figure 4.1-c. Although different in magnitude, all three specimens showed some residual post-peak strength after cracking until the diagonal cracks penetrated to and led to crush of the grouted reinforced blocks at the corners. Wallette W-PG1 experienced 21% higher strength after the first peak load while wallettes W-PG2 and W-PG3, only reached 95% and 85% of the initial cracking strength, respectively.

4.2.3   Hollow/Ungrouted Wallettes (W-H Series)

To avoid any damage due to moving and handling, the specimens had been lightly prestressed before testing. A vertical precompression was applied using two 12 mm diameter threaded rods tightened at both ends on two 50 mm thick wooden

bearing blocks. Unlike the other types of specimens, the hollow wallettes showed a distinct shear-sliding failure along the top bed joint followed by a sudden drop in strength (Figure 4.1-f). The compression load vs. deformation results along the vertical diagonal (average of the two faces) are presented in Figure 4.1-e. Domination of the shear-sliding failure mode rather than stepped-pattern cracking could be explained by the longer failure path length for a head joints-bed joints stepped-crack pattern. In the partially grouted specimens, the shear-sliding failure mode did not occur because of strengthening by continuous columns of grout around the perimeter of the specimen.

4.2.4 Significance of Experimental Observations

As expected in partially grouted reinforced wallettes, due to the peripheral constraint provided by the continuous reinforcing steel bar, the crack path followed the maximum compressive loading path on the vertical diagonal. The lower shear-sliding resistance of the hollow portion did not affect the response. As shown in Figure 4.2, slightly higher strength was observed in the partially grouted reinforced wallettes compared to the hollow specimens. However, this difference is significantly increased in the fully grouted reinforced wallettes where the central initial diagonal tension region benefited from the strengthening effect of grout. The shape of the load-deformation curves beyond the ultimate load varied with the extent of grouting. The hollow specimens showed a steep descending branch whereas the fully grouted wallettes showed a more gradual degradation of strength under post-peak loading conditions. The post-peak response of the partially grouted
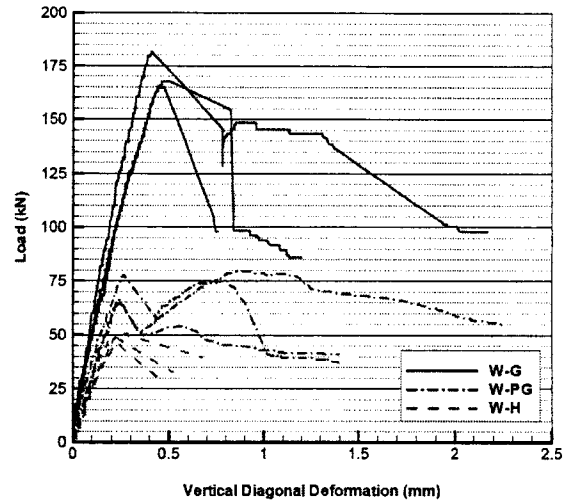
Figure 4.2 – *Load-deformation curve comparisons for wallette tests*

reinforced wallettes is unique as a result of having a reserved strength after reaching the first peak load in the curve corresponding with initial cracking. In addition, a more gradual loss of load resistance after reaching ultimate load indicated a relatively ductile behaviour of these wallettes. In terms of ultimate load, the fully grouted wallettes, obviously due to greater effective area, had a much higher resistance compared to the partially grouted and hollow wallettes. Ultimate shear strength was calculated using net area of wallette specimens (gross area for grouted cells and face shell mortared area for hollow cells). As shown in Figure 4.3, the ultimate shear strength decreased with reduced extent of grouting. Although three tests is a small statistical sample, the coefficients of variation are relatively small (see Table 4.1). Thus, the large differences in behaviour of the W-PG specimens (Figure 4.1-c) after reaching the peak strength at initial cracking are considered to be a good indication of post-cracking behaviour. Residual bond and frictional strength are likely to be highly dependent on cracking pattern and have
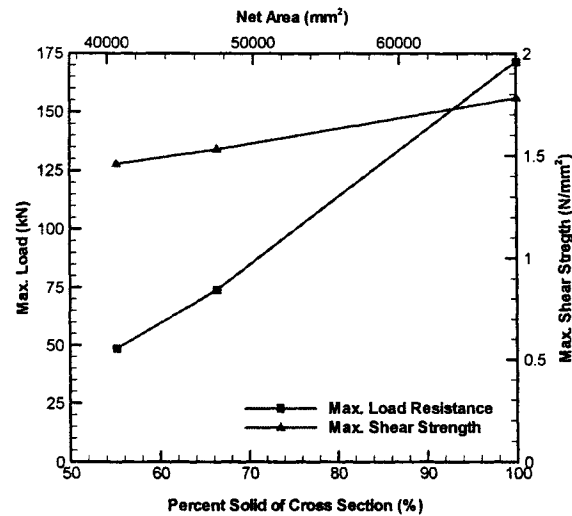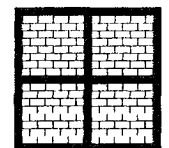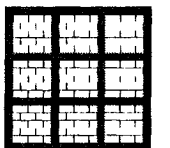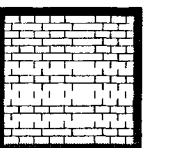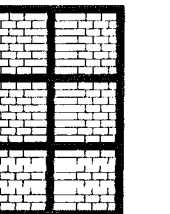
Figure 4.3 *– Average maximum load resistance and maximum shear strength vs.*
extent of grouting

significant effects on post-cracking strength and deformation behaviour. Except that

the partially grouted results show potential for post-cracking strength to increase,

the variability of post-cracking behaviour is similar for both the hollow and fully

grouted specimens.

4.3 PARTIALLY GROUTED-REINFORCED MASONRY SHEAR WALL TESTS

Five shear wall tests were carried out to document the cyclic response of

partially grouted reinforced masonry shear walls under in-plane axial and lateral

loading. The aspect ratio and spacing between reinforcing steel bars were altered in

each test specimens maintaining nearly the same vertical and horizontal

reinforcement ratios. Walls were tested in displacement controlled cyclic reversed

loading using the test setup described in Chapter 3. The test matrix of the

experimental program describing reinforcement spacing, number of bars, aspect

ratios, axial stress and steel ratios for each wall is presented in Table 4.2.

Table 4.2 – Description of test matrix for shear wall tests (Reproduction of Table 3.4)

Specimen Label	Wall 1	Wall 2	Wall 3	Wall 4	Wall 5
Reinforcing Pattern	Wall 1	Wall 2	Wall 3	Wall 4	Wall 5
Dimensions	L = 1800 mm H = 1800 mm T = 90 mm	L = 1800 mm H = 1800 mm T = 90 mm	L = 1800 mm H = 1800 mm T = 90 mm	L = 1800 mm H = 900 mm T = 90 mm	L = 1800 mm H = 2700 mm T = 90 mm
Number and Size* of Reinf.	3 × #10 (V) 3 × D4 (H)	4 × #3 (V) 4 × D3 (H)	2 × #4 (V) 2 × 2D3 (H)	3 × #10 (V) 2 × D3 (H)	3 × #10 (V) 4 × D4 (H)
Reinforcement Ratio**	$\rho_v = 0.19\%$ $\rho_h = 0.05\%$	$\rho_v = 0.18\%$ $\rho_h = 0.05\%$	$\rho_v = 0.16\%$ $\rho_h = 0.05\%$	$\rho_v = 0.19\%$ $\rho_h = 0.05\%$	$\rho_v = 0.18\%$ $\rho_h = 0.04\%$
Bar Spacing	855 mm	570 mm	1710 mm	855 mm	855 mm
Aspect Ratio (H / ℓ)	1.0	1.0	1.0	0.5	1.5
Axial Stress**	0.75 MPa	0.75 MPa	0.75 MPa	0.75 MPa	0.75 MPa

* #10 (CA, A_s = 100 mm²), #3 (US, A_s = 71.3 mm²), #4 (US, A_s = 130 mm²), D3 (US, A_s = 19.4 mm²), D4 (US, A_s = 25.8 mm² – US: USA size, CA: Canadian size.

** Based on gross area

4.3.1 Wall 1

Wall 1 was 1800 mm long and 1825 mm high with average 5.8 mm thick mortar bed joints (Figure 4.4). The wall was reinforced vertically using three No. 10 bars ($A_s = 100$ mm^2) with 855 mm spacing ($\rho_v = 0.19\%$) located at the ends and mid-length of the wall. Three D4 deformed wires ($A_s = 25.8$ mm^2) was used as horizontal reinforcement with 855 mm spacing ($\rho_h = 0.05\%$) at the top, midheight and bottom of the wall. The horizontal reinforcing bars were anchored around the extreme vertical bars with a 180° hook. The wall was subjected to a superimposed axial load of 120 kN giving a compressive stress of 0.75 MPa based on the gross cross section area of the wall.
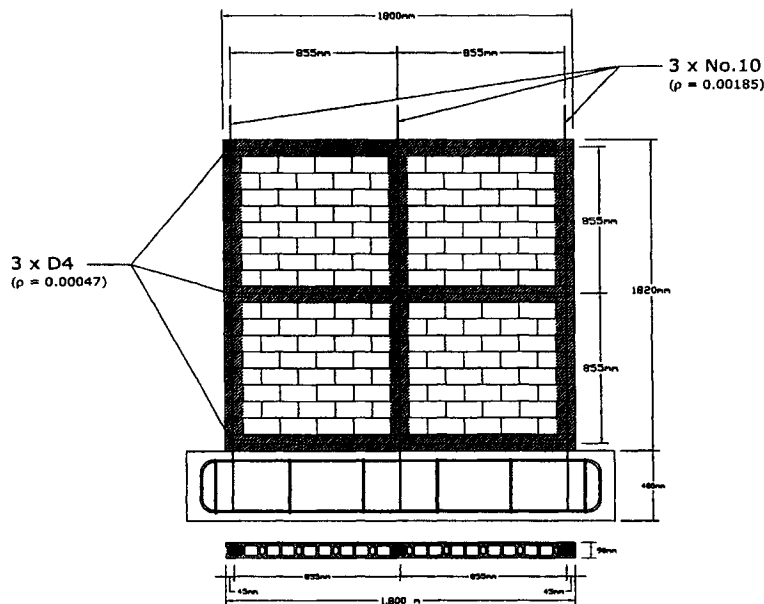
Figure 4.4 – Schematic view of Wall 1

4.3.1.1 General Observations

The load-displacement hysteresis curves for Wall 1 are shown in Figure 4.5 for the full range of loading history. Displacements at top-right and top-left corners of the wall were monitored by two dial gauges mounted on the instrumentation column. The consistency between the readings of dial gauges was lost once a diagonal crack initiated and developed close to the top-right corner of the wall during the 4.0 mm pull displacement cycle corresponding to 0.22% drift (see Figure 4.6). The width of the diagonal crack created the difference. Consequently, the readings from this corner were believed not to represent overall wall deflection and, for the rest of the test, top displacement readings relied on the dial gauge connected
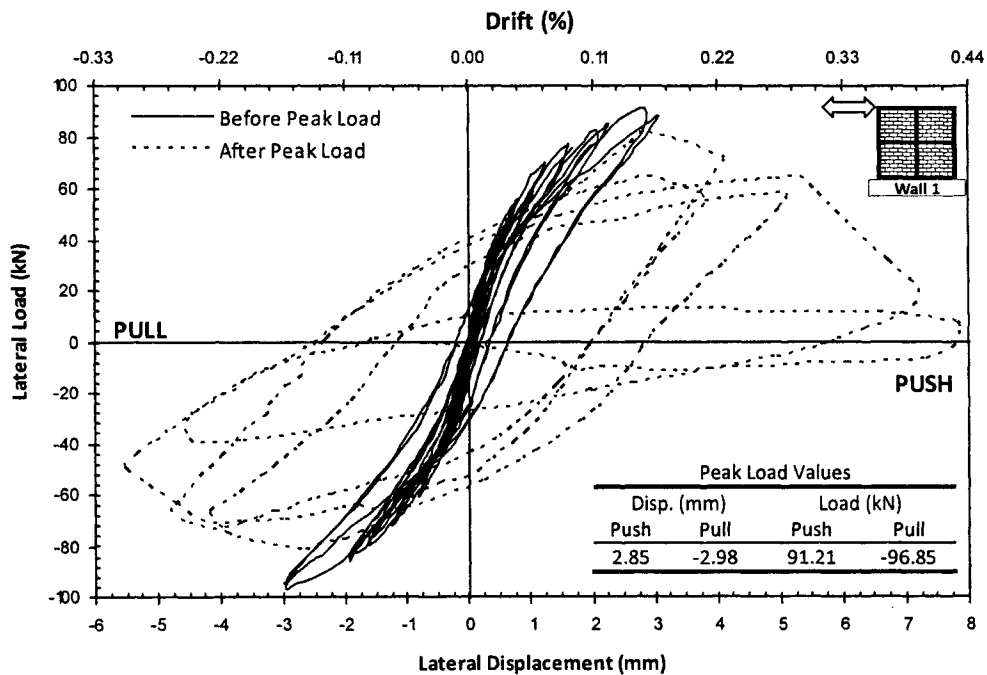
Figure 4.5 - Hysteresis loops for Wall 1

Figure 4.6 – *Cracking at top- right corner at 4.00 mm pull displacement (pull displacement is toward left)*

to the top-left corner. Loading started at 0.20 mm displacement (0.01% drift) in the push and pull sequences. The amplitude of the cycles was then increased to ±0.40, ±0.80, ±1.20, ±1.60, ±2.00, ±3.00, ±4.00, ±5.00 and ±7.00 mm and each cycle was repeated twice throughout the test. The latter amplitude corresponds to the loading cycle in which the test terminated due to extensive strength degradation of the wall.

Symmetric horizontal bed joint cracks were observed in both left and right ends of the wall during the ±1.60 mm displacement cycle corresponding to 0.09% drift. The horizontal cracks propagated toward the centre of the wall as the test progressed. The first stepped-pattern crack along the contiguous mortar bed and head joints appeared on the left half of the wall at the ninth course during the 2.00 mm push displacement (0.11% drift) cycle (Figure 4.7-a).

As shown in Figure 4.7-b, diagonal stepped-cracks extended and penetrated into the blocks located at the right compression toe during the 3.00 mm push displacement (0.17% drift) cycle. The maximum lateral load carrying capacity of the wall in the push direction occurred when the wall reached +2.85 mm displacement

Figure 4.6 – *Cracking at top- right corner at 4.00 mm pull displacement (pull displacement is toward left)*

to the top-left corner. Loading started at 0.20 mm displacement (0.01% drift) in the push and pull sequences. The amplitude of the cycles was then increased to ±0.40, ±0.80, ±1.20, ±1.60, ±2.00, ±3.00, ±4.00, ±5.00 and ±7.00 mm and each cycle was repeated twice throughout the test. The latter amplitude corresponds to the loading cycle in which the test terminated due to extensive strength degradation of the wall.

Symmetric horizontal bed joint cracks were observed in both left and right ends of the wall during the ±1.60 mm displacement cycle corresponding to 0.09% drift. The horizontal cracks propagated toward the centre of the wall as the test progressed. The first stepped-pattern crack along the contiguous mortar bed and head joints appeared on the left half of the wall at the ninth course during the 2.00 mm push displacement (0.11% drift) cycle (Figure 4.7-a).

As shown in Figure 4.7-b, diagonal stepped-cracks extended and penetrated into the blocks located at the right compression toe during the 3.00 mm push displacement (0.17% drift) cycle. The maximum lateral load carrying capacity of the wall in the push direction occurred when the wall reached +2.85 mm displacement

(a) Crack pattern during
2.00 mm displacement cycle
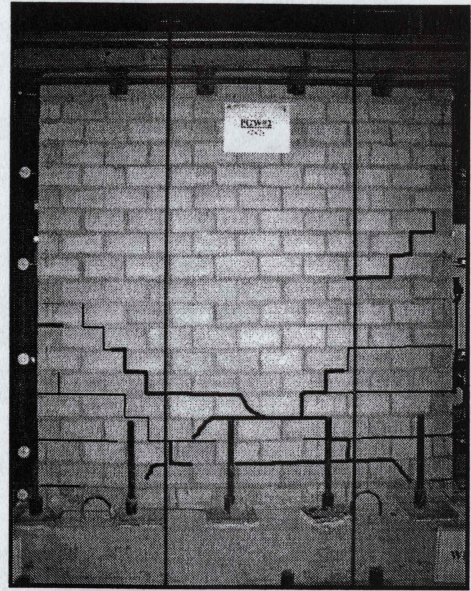
(b) New cracks during
3.00 mm displacement cycle
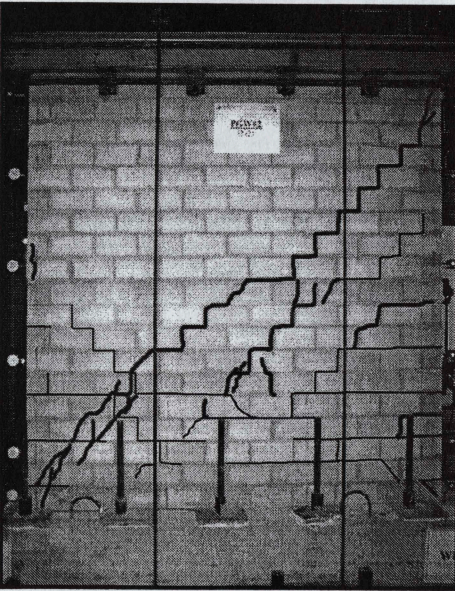
(c) New cracks during
4.00 mm top displacement
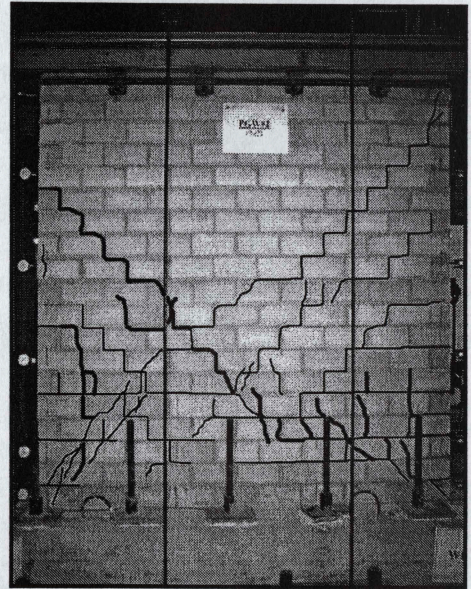
(d) New cracks during
5.00 mm displacement cycle

Figure 4.7 - *Crack pattern for Wall 1 at selected displacement levels (Photos enhanced for crack pattern - darker lines indicate new cracks during the specified displacement cycle)*

corresponding to 0.16% drift. In the pull direction, the ultimate load resistance of the wall was recorded at 2.98 mm displacement corresponding to 0.22% drift while no major penetration of stepped-pattern cracks into the blocks was observed.

During the 4.00 mm push displacement (0.22% drift) cycle, once the wall reached 90% of the ultimate load recorded during the previous push sequence, the load suddenly decreased to about 80% of the peak load. A vertical crack was observed at the outermost bottom right (compression) corner block (Figure 4.8) and the previous face cracks widened but their length didn't change. At the peak load of the 4.00 mm (0.22% drift) cycle in the pull direction, a long continuous stepped-pattern crack started from the top-right corner of the wall and joined together a series of diagonal cracks and penetrated into blocks in the left compression corner (Figure 4.7-c). At this displacement level, the diagonal cracks had visibly widened and light could pass through the wall blocks. Limited spalling of the compression toes began by losing the face shells of the bottom-right corner compression toe block (Figure 4.9).
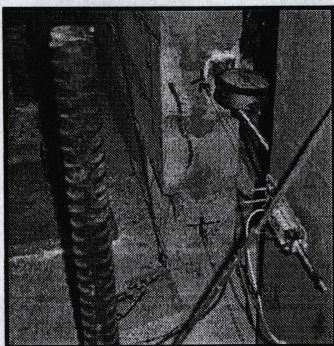
Figure 4.8 - *Vertical crack at right toe at 4.00 mm displacement (push)*
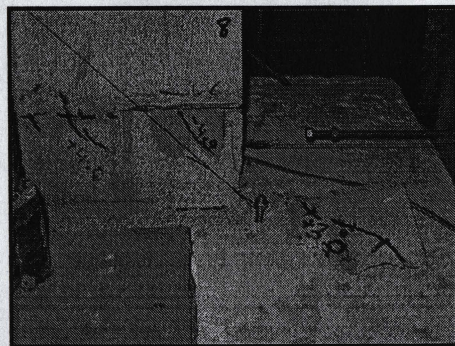
Figure 4.9 - *Spalling of face shell at 4.00 mm displacement (push)*

Severe toe crushing at the bottom-left corner of the wall occurred during the 5.00 mm pull displacement (0.28% drift) where the vertical reinforcement at the left end buckled out and the surrounding grout cell crumbled up to the second course (Figure 4.10). At this point, due to onset of a vertical crack connecting to an existing diagonal crack, the left end of the wall was significantly damaged and almost separated from the remainder of the wall with high out-of-plane displacement over the bottom six courses (Figure 4.11). As a result the adjacent cracks also opened up and this led to an extra 0.50 mm displacement in the pull direction. Toe crushing at the right end of the wall occurred during the second push sequence of this displacement but a lower level of damage was observed compared to the left toe. However, several vertical and diagonal cracks were observed through blocks around the right toe by the end of this cycle. Similar to what happened during loading in the pull direction, a 2.0 mm displacement overshoot occurred due to sudden opening of a crack upon reaching the peak strength of the wall during this loading cycle.

Figure 4.10 - Crushing at left toe at 5.00 mm pull displacement
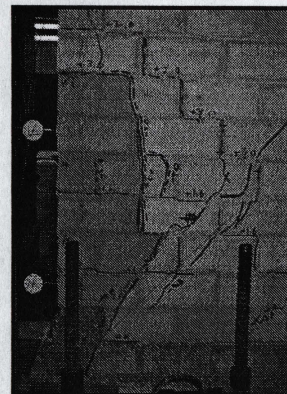
Figure 4.11 - Connection of vertical and diagonal cracks at 5.00 mm pull disp. (Photo enhanced for presentation)

The diagonal cracks that developed through blocks in the left compression zone of the wall were wide but were limited to a few cracks whereas the diagonal cracks that developed in the right compression zone were more numerous and scattered rather than wide (Figure 4.12).

As shown in Figure 4.13, continuous face shell crushing and spalling was observed at both the front and the back faces of the wall at the fifth course along previously cracked bed joints. This occurred in the region where Wall 1 had the least cross sectional area after losing a significant portion of the left half of the wall (see Figure 4.11) due to severe cracking. It is thought that the observed face shell crushing could be a result of high level of the normal stress due to redistribution of the axial load along with the normal stress due to overturning moment.

The ultimate load carrying capacities of the wall recorded during the test were 91.21 kN in the push direction (at +2.85 mm top displacement, 0.16% drift) and 96.82 kN in the pull direction (at -2.98 mm top displacement, 0.17% drift).
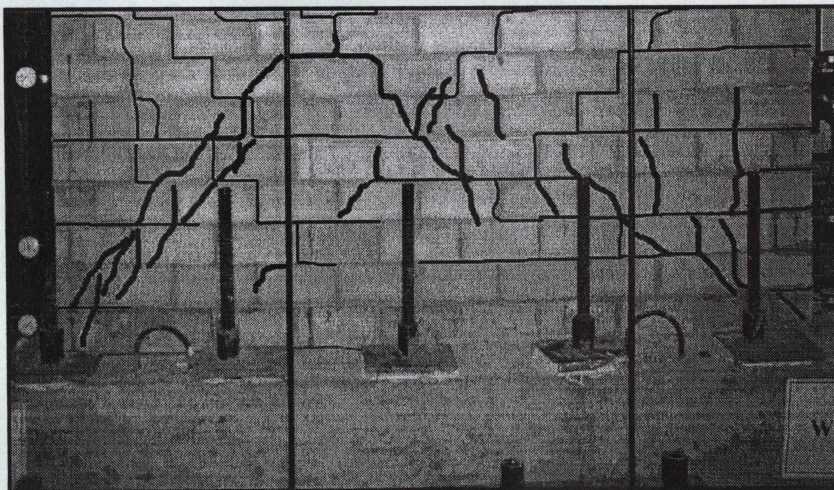
Figure 4.12 – Diagonal cracking into blocks (Photo enhanced for crack pattern)
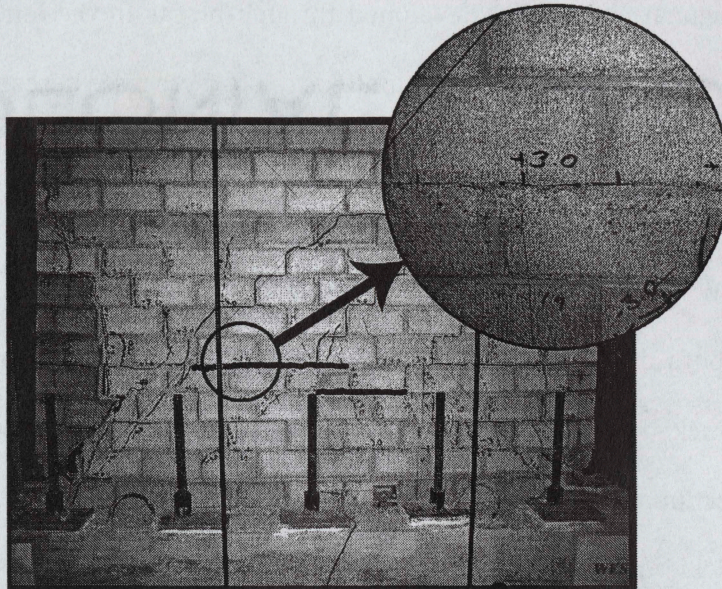
Figure 4.13 - *Face shell crushing at the forth and fifth course*
(Photos enhanced for crack pattern)

In general, the diagonal stepped-pattern cracks were concentrated mostly within the hollow sections of the wall surrounded by the grouted-reinforced cells. Propagation of horizontal bed joint cracks progressed only up to the 3.00 mm displacement (0.17% drift) cycle when the ultimate load capacity was achieved. Afterwards, diagonal and stepped-pattern cracks propagated and widened until complete crushing of the compression toes occurred.

4.3.1.2   Load-Displacement Response

The load-displacement hysteresis loops for Wall 1 (Figure 4.5) show fairly symmetric response prior to reaching the ultimate load resisted by the wall. The post-peak response follows the same pattern of strength degradation in both the push and the pull directions but a more rapid loss of strength is evident in the push direction. Earlier formation and penetration of diagonal stepped-cracks into the

compression toe during the push cycles would be one of the possible reasons for this difference. The differences are also attributable in part to the large displacement associated with the sudden cracks which appeared close to the end of loading cycles that led to overshooting the top displacements. Very similar ultimate load resistances and corresponding displacements were observed in the push and in the pull directions.

Despite of the presence of horizontal tensile cracks along mortar bed joints, further inspection of strain profiles recorded by three strain gauges attached to the vertical reinforcing steel bars showed no tensile yielding on either extreme left or right end bar. In addition, fairly brittle failure of the wall along with formation of wide diagonal cracks followed by complete toe crushing indicates domination of a shear failure mode in this test.

The wall was removed after testing to assess the continuity of hardened grout in the designated cells. Inspection of the dismantled wall showed well compact grout in the designated horizontal and vertical cells. Some grout leakage was also discovered next to the grouted cells at the bottom of the wall. Since these areas were limited to a one-cell-wide by two block-high zone and they were only partially filled with noncompacted grout, this was thought to be insignificant to the overall behaviour of the wall.

4.3.1.3 Wall Deformation and Drift

The in-plane lateral displacement of the wall was measured using six dial gauges over the height of the wall at both ends. Figure 4.14 shows the lateral

displacement profile of the wall at the end of the second sequence of loading for selected cycles for both the push and pull directions. For comparison purposes, deformations at both the left and right end of the wall are shown in the same plot. The overall lateral displacement profile of the wall indicates a fairly linear response along the entire height up to the 2.00 mm displacement (0.11% drift) cycle. During the 2.00 mm (0.11% drift) and 3.00 mm (0.17% drift) displacement cycles, the shapes of the curves for the edge of the wall under compression (right end during

(a) Pull   (b) Push
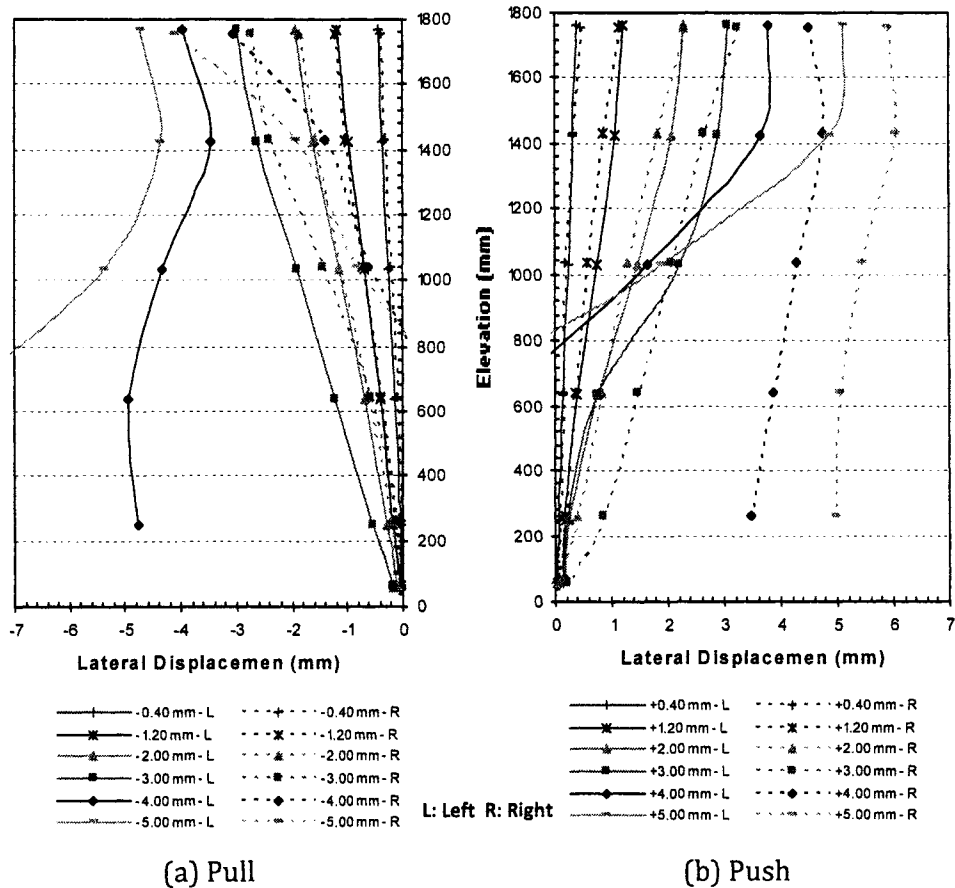
Figure 4.14 - *Lateral displacement profiles for Wall 1 at selected displacement levels*

push and left end during pull) are fairly consistent with the displacement profile expected for a cantilever wall. However, the opposite edge of the wall under tension (left end during push and right end during pull) follows the deformation profile more representative of a fixed-fixed end type of shear wall. The latter could be explained by the opening of the horizontal and diagonal cracks in the tension zone (lower left side of the wall during push and lower right side of the wall during pull). Due to the severe cracking that occurred in the lower half of the wall during the 4.00 mm (0.22% drift) and higher displacement cycles, the profiles indicate that the displacements at the bottom of the wall were highly affected by opening and closing of adjacent cracks; the recorded data was affected by the side of the crack from which displacement was measured.

4.3.1.4   Wall Curvature

Average curvature was monitored at eight elevations along the height of the wall. Details of the method used for curvature measurement and calculation of curvature are presented in Appendix E. The curvature profiles of the wall for both the pull and push directions of loading, shown in Figure 4.15, indicate a very small amount of flexural deformation over the height of the wall. This is consistent with expected behaviour since shear deformation was predicted to dominate the lateral displacement of the wall without significant curvature.

4.3.2   Wall 2

Wall 2 was 1806 mm long and 1825 mm high with average 5.8 mm thick mortar bed joints (Figure 4.16). The wall was reinforced vertically with four No. 3

(a) Pull   (b) Push
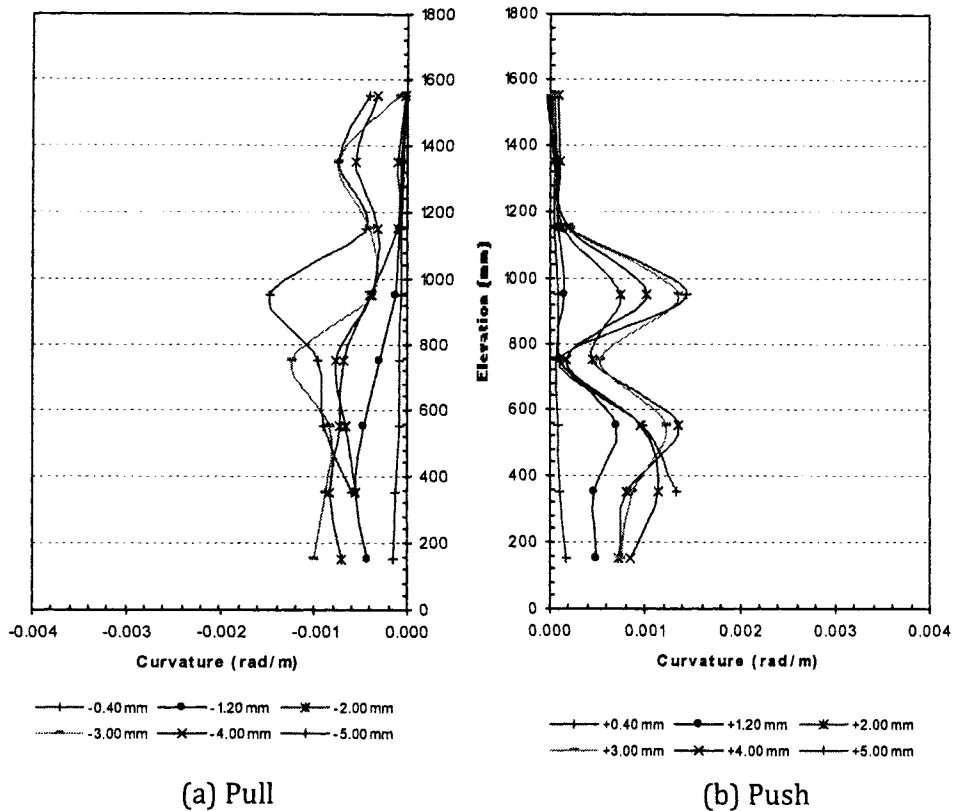
Figure 4.15 – *Average curvature profiles for Wall 1 at selected displacement levels*

bars (US Size - $A_s = 71.3$ mm^2) at 570 mm spacing ($\rho_v = 0.18\%$). Four D3 deformed wires ($A_s = 19.4$ mm^2) was used as horizontal reinforcement with 570 mm spacing ($\rho_h = 0.05\%$). The horizontal reinforcing bars were anchored around the extreme vertical bars with a 180° hook. The wall was subjected to a superimposed axial load of 120 kN giving a compressive stress of 0.75 MPa based on gross area.

During installation of the load application members, the wall accidentally suffered from a severe lateral impact in the pull (left) direction. Due to this accident, a visible stepped-pattern cracking in the compressive diagonal zone (Figure 4.17)

appeared on the wall. However, the compressive diagonal zone in the opposite direction (the push direction) remained intact. The cause of the accident and the resulting crack pattern are described in the following section.
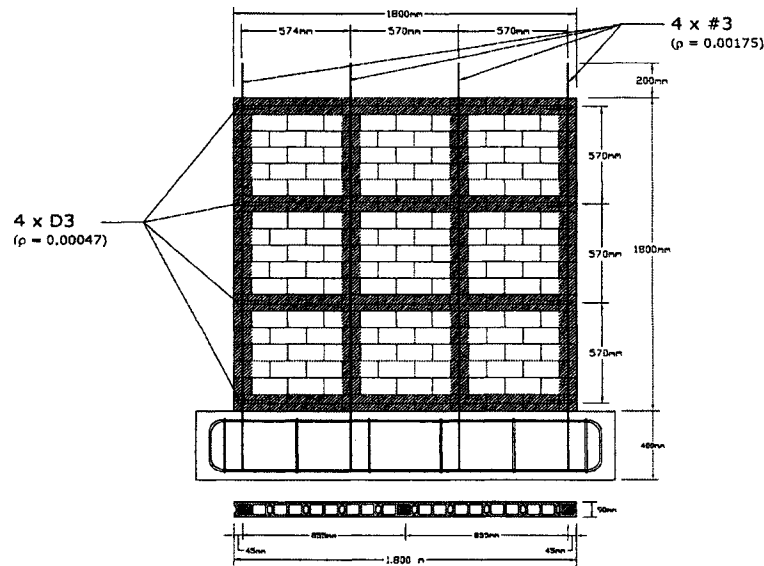
Figure 4.16 - *Schematic view of Wall 2 (correct the blocks configuration)*

4.3.2.1 Accidental Cracks

As discussed in describing in the test setup (see Section 3.3.6), in order to connect the actuator to the loading beam of the wall specimen, a 1.4-m-long hollow steel box section was used as an extension link. The extension link was attached to the actuator and the loading beam with two pins to create a moment free connection. The extension link, as shown in Figures 3.21 and 3.23, was free to slide over the connecting pieces extending from the loading beam and from the actuator. During positioning of the extension link for testing of Wall 2, while the left-end pin (facing the actuator) was in place, the pin holes of the connecting members at the
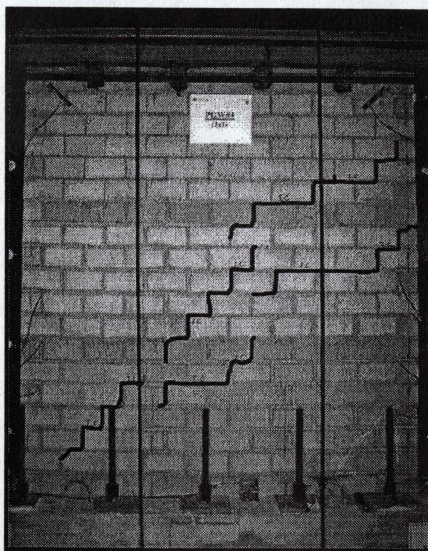
Figure 4.17 - *Initial Cracks prior to testing*
(Photo enhanced for presentation)

opposite end (the end facing the wall) were being manually lined up by slowly moving the actuator and eye-balling the holes' positions.

The accident resulted from a slight misalignment of the actuator's axis with the loading beam's axis which resulted in mechanical interlock between the two connecting pieces. Consequently, the axial degree of freedom was constrained and the applied displacements were directly transferred to the wall rather than sliding between the two connecting members. Owing to the fact that the applied displacements at this stage were well beyond the displacement corresponding the cracking point of the wall, when the actuator and subsequently the wall were being pulled toward the left direction, a visible diagonal stepped-pattern crack formed along the compressive diagonal (Figure 4.17).

Upon noticing the crack, the process was immediately stopped and the wall's loading beam was manually disconnected from the extension link. It should be

pointed out that no axial load had been applied at the time of the incident. The accidental cracks were in the form of horizontal and stepped-pattern joint cracks and were limited only to the compressive diagonal zone in the pull direction. Some of the cracks located over the midheight of the wall were approximately 1 mm wide. No cracking was observed along the opposite diagonal indicating that the wall's behaviour in the push direction could be considered not to be significantly affected by the accidental damage.

4.3.2.2   General Observations

The load-displacement hysteresis loops for Wall 2 are shown in Figure 4.18 for the full loading history. The load displacement curves for the smaller range of
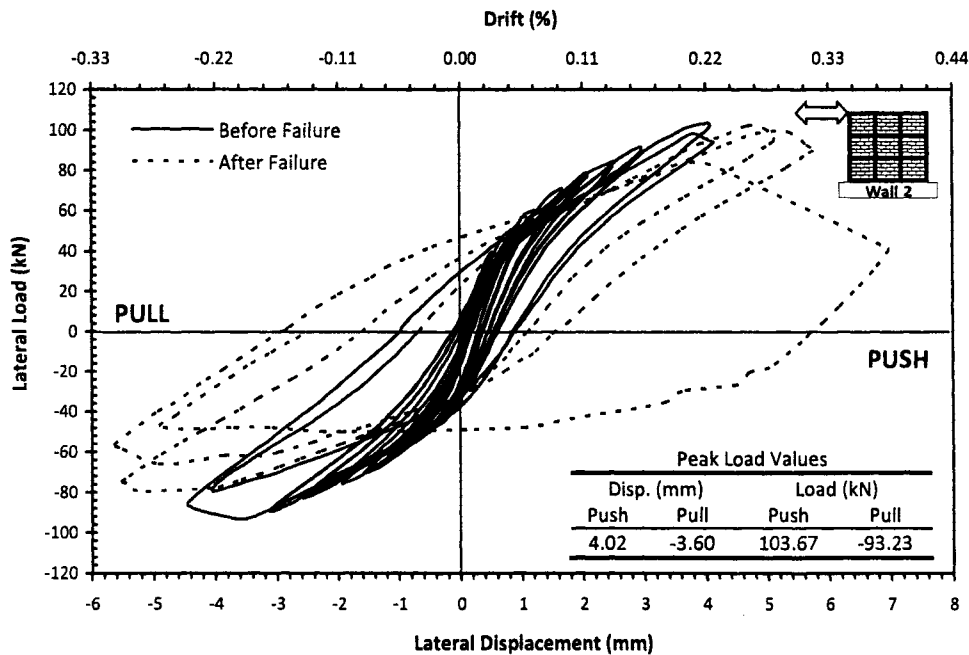
Figure 4.18 - *Hysteresis loops for Wall 2*

displacements are presented at a larger scale in Figure 4.19 for study of pre-peak

behaviour. Displacement was monitored using two dial gauges connected to the top-

right and the top-left corners of the wall. The fairy consistent readings between the

pair of dial gauges were lost during the 4.00 mm displacement (0.22% drift) cycle

when a significant diagonal crack occurred and developed close to the top-left

corner (Figure 4.20). From this point on, readings of the top-left dial gauge were

believed to be unrepresentative of overall wall deflection and the rest of the test was

conducted based on the readings from the top-right dial gauge as being

representative of the wall's top displacement. This corner of the wall remained

undamaged to the end of the test. Loading was started using a 0.20 mm top

displacement (0.01% drift) in the push direction. Then, the amplitude of the cycles
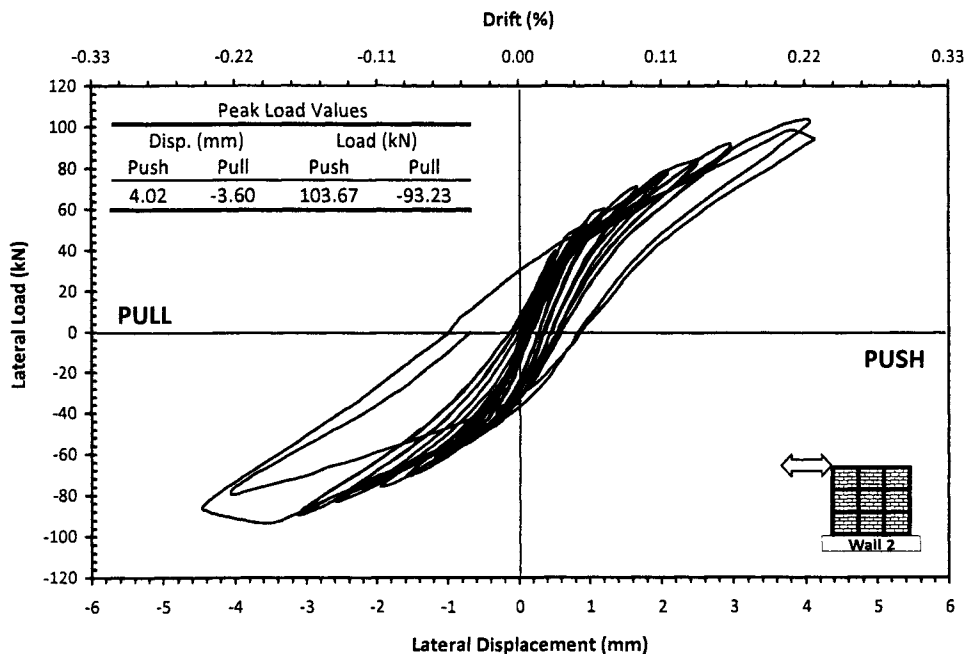
Figure 4.19 - *Hysteresis loops at low range of displacement for Wall 2*
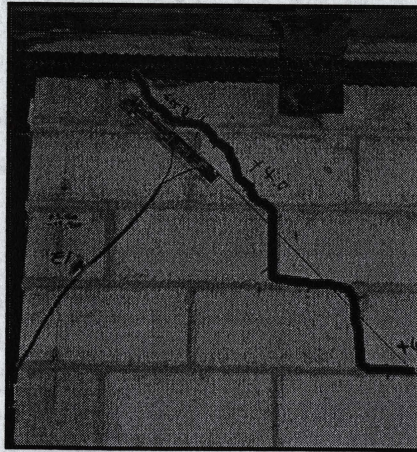
Figure 4.20 – *Cracking at top left corner of*
Wall 2 at 4.00 mm displacement (Push)

increased to ±0.40, ±0.60, ±0.80, ±1.00, ±1.20, ±1.60, ±2.00, ±2.50, ±3.00, ±4.00,

±5.50 and ±7.00 mm and each cycle was repeated twice throughout the test. The

final amplitude corresponds to the rupture of one of the horizontal reinforcing bars

and significant crack opening. At this point, due to stability concerns, continuation of

loading was believed to be unsafe and the test was terminated after the first cycle of

7.00 mm displacement (0.39% drift).

Aside from the accidental cracks, the first crack appeared in the right half of

the wall during the 1.00 mm pull displacement (0.06% drift) cycle (Figure 4.21-a).

The crack pattern was in the form of three horizontal cracks with the longest one

starting from the third course and extending to the second course close to the

middle of the wall. Similar horizontal cracks at the right end of the wall were also

observed during the next loading cycle with 1.20 mm top displacement amplitude

equal to 0.07% drift (Figure 4.21-a). More horizontal bed joint cracks with higher

concentration at the right end of the wall occurred during the 1.60 mm and 2.00 mm

(a) New cracks during 1.00 mm
and 1.20 mm displacement cycle
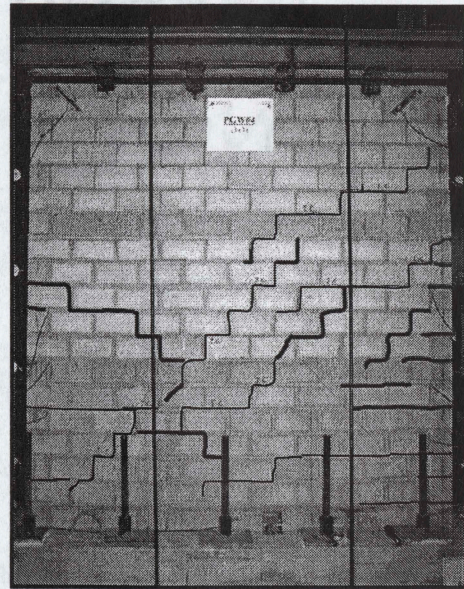
(b) New cracks during 1.60 mm,
2.00 mm and 2.50 mm disp. cycle
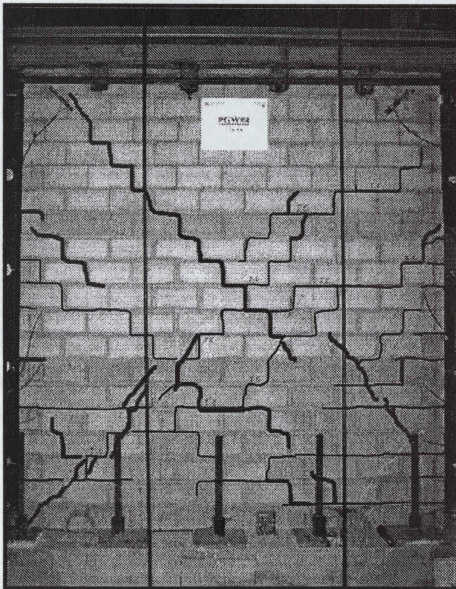
(c) New cracks during
4.00 mm displacement cycle
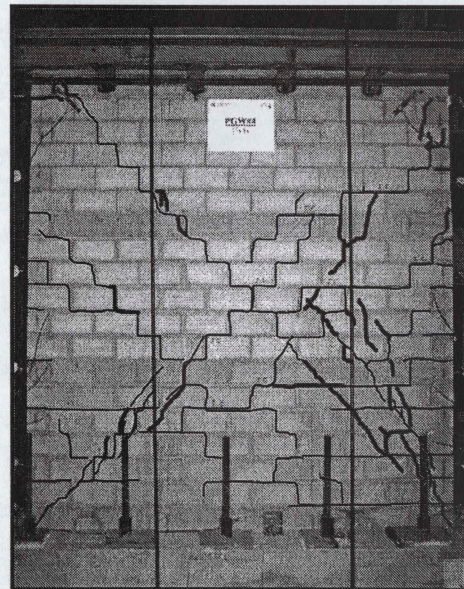
(d) New cracks during
5.50 mm displacement cycle

Figure 4.21 – Crack pattern for Wall 2 at selected displacement levels (Photos enhanced for crack pattern - darker lines indicate new cracks during the specified displacement cycle)

displacement cycles corresponding to 0.09% and 0.11% drift, respectively. Also two

short diagonal stepped-cracks through mortar joints were observed on the right half

of the wall during the 2.00 mm displacement (0.11% drift) cycle, as shown in Figure

4.21-b. The first major diagonal stepped-crack on the left half of the wall occurred

during the 2.50 mm displacement (0.14% drift) cycle in the push direction (Figure

4.21-b).

In the first push sequence of the 4.00 mm displacement loading giving 0.22%

drift, significant cracking in the form of stepped-pattern and diagonal cracks into

blocks occurred and the load resisted by the wall started to decrease (Figure 4.21-

c). The maximum load carried by the wall was +103.67 kN in the push loading

direction. In the pull direction, the maximum load carrying capacity of the wall was

recorded as -93.23 kN when the wall reached -3.60 mm top displacement equal to

0.20% drift. Then the applied load gradually decreased. The approximately 10%

lower strength observed in the pull direction could be related to the accidental

damage that occurred prior to testing. A three course high vertical crack through

webs of the bottom right corner blocks also initiated and progressed in this loading

cycle (Figure 4.22).

During the 5.50 mm push displacement (0.31% drift) cycle, the wall resisted

almost the same lateral load as in the previous cycle. At the end of the push cycle,

some of the existing head joint cracks closer to the center of the wall significantly

widened to approximately 5 mm. During the pull sequence of loading, the crack

pattern of the wall was limited to a few diagonal cracks around the bottom left

corner (see Figure 4.21-d). At this point, the face shell and the side web of the bottom left corner block were removed due to severe cracking and toe crushing (Figure 4.23).
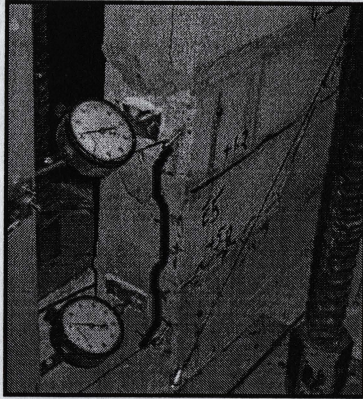
Figure 4.22 – Vertical crack at left toe of Wall 2 at 4.00 mm displacement (pull)
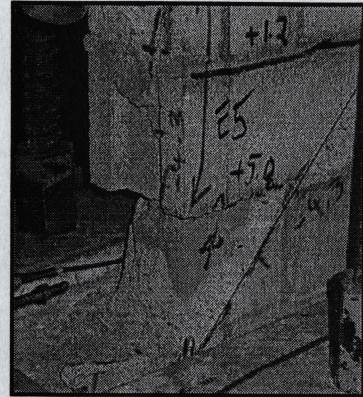
Figure 4.23 – Toe crushing at left toe of Wall 2 at 5.50 mm displacement (pull)

During the 7.00 mm displacement (0.39% drift) cycle, a sudden loud noise (bang) was heard when the wall reached +4.00 mm displacement (0.22% drift) in the push direction and the load dropped from +83.5 kN (80% of the peak load) to +41.47 kN (40% of the peak load). Further inspection after dismantling the wall, revealed that the loud noise was due to the rupture of at least one of the middle horizontal reinforcing bars (Figure 4.24). During the pull displacement cycle, the wall reached only -50.17 kN load and the existing cracks widened significantly. Toe crushing at the bottom left corner extended up to the third course (Figure 4.25) and some cracks located close to the centre of the wall opened up to approximately 7 mm (Figure 4.24). The test terminated at -4.90 mm displacement (0.27% drift) due to stability and safety concerns and the load was then returned to zero. An overall view of the final crack pattern of the wall is presented in Figure 4.26.
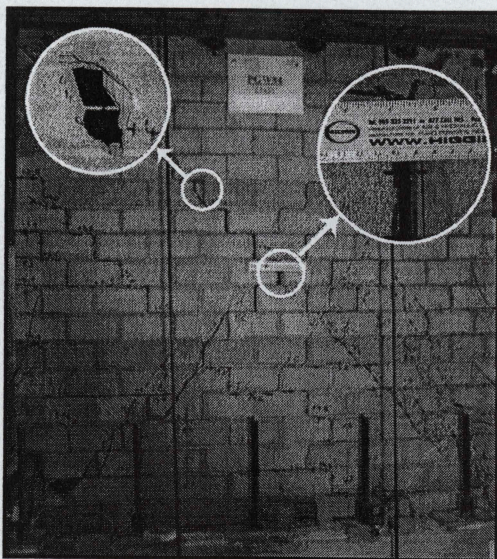
Figure 4.24 – *Widening of joint cracks and rupture of horizontal reinforcement of Wall 2*
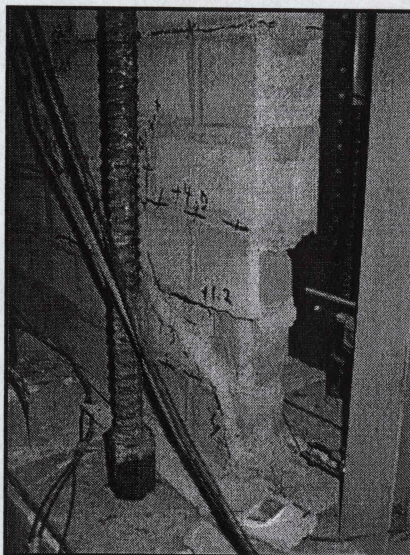
Figure 4.25 – *Toe crushing of Wall 2 at 5.50 disp. during 7.00 mm disp. cycle (pull)*
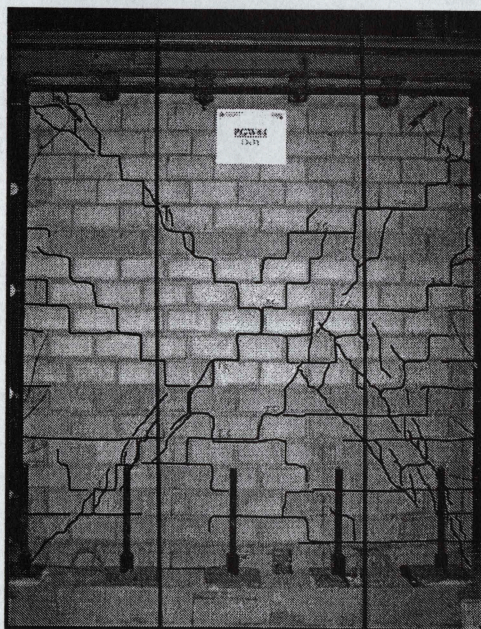
Figure 4.26 - *Crack pattern of Wall 2 at the end of the test (Photo enhanced for crack pattern)*

4.3.2.3 Load-Displacement Response

Since the cracks existing before starting the tests were judged to only affect the behaviour of the wall for loading in the pull direction, it is believed that the data related to the push direction are reasonably reliable in representing the actual behaviour of the undamaged wall. Despite the presence of the initial cracks, shown in Figure 4.19, the hysteresis loops for Wall 2 indicates very good symmetry between the push and pull directions before reaching the peak load. However, the 10% lower ultimate load in the pull compared to the push direction could be due to the presence of pre-fractured joints in the eventual failure region of the wall.

Linear elastic behaviour was observed at low displacement cycles (up to approximately 0.8 mm). The response of the wall gradually became bilinear with wider hysteresis hoops when the loading cycles approached the maximum load carrying capacity of the wall. The post failure response of the wall indicates more gradual degradation of strength in the pull direction than in the push direction. Despite the narrow pre-peak hysteresis loops, the fat loops in the post-peak response of the wall indicate good energy dissipation characteristics for this wall.

The data recorded by strain gauges attached to vertical steel reinforcement revealed that the extreme tension bars at both ends reached their yielding strength at load levels close to the peak load of the wall. In the push direction, the tension bar located at the left side of the wall yielded at 102.8 kN corresponding to 3.90 mm (0.22% drift). A force of 90.1 kN corresponding to -3.27 mm (0.18% drift) was recorded as the wall's yield strength in the pull direction. After inspection of the dismantled wall, it was noticed that each horizontal bar had ruptured at two points

where the reinforcement intercepted the stepped-pattern cracks along the diagonals of the wall. Thus, final failure was fairly brittle with formation of wide diagonal cracks being followed by complete toe crushing. Failure of the horizontal reinforcement indicated a shear dominated failure mode in this test.

4.3.2.4 Wall Deformation and Drift

The in-plane lateral displacement of the wall was monitored using six dial gauges over the height of the wall at the both ends. Figure 4.27 shows the displacement profile of the wall at the end of the second sequence of loading for selected displacement cycles. For comparison purposes, deformations at both the right and left ends of the wall are shown in the same plot. Comparison between the push and pull directions shows fairly linear response in the push direction on the right end of the wall (solid curves) even up to 3.00 mm top displacement(0.17% drift). However, during the pull sequence, due to opening of the accidental crack, especially the horizontal crack created in the midheight region of the wall, the upper half of the wall shows larger lateral displacement at the right end.

More consistent behaviour was observed on the left end of the wall, as shown in Figure 4.27 (dashed lines). Prior to the 4.00 mm displacement (0.22% drift) cycle, the deflection profiles on the left edge were quite symmetric and linear in both the push and the pull directions. Less horizontal cracking on the left half of the wall would explain this behaviour.

At the 4.00 mm displacement (0.22% drift) cycle and beyond which coincided with the post failure response of the wall, the dial gauge readings were locally

affected by the opening and closing of wide cracks. Consequently, erratic changes

are observed in the deflection profiles of the wall. The data regarding the 7.00 mm

displacement (0.39% drift) cycle were discarded due to the observed severe

damage.

(a) Pull   (b) Push
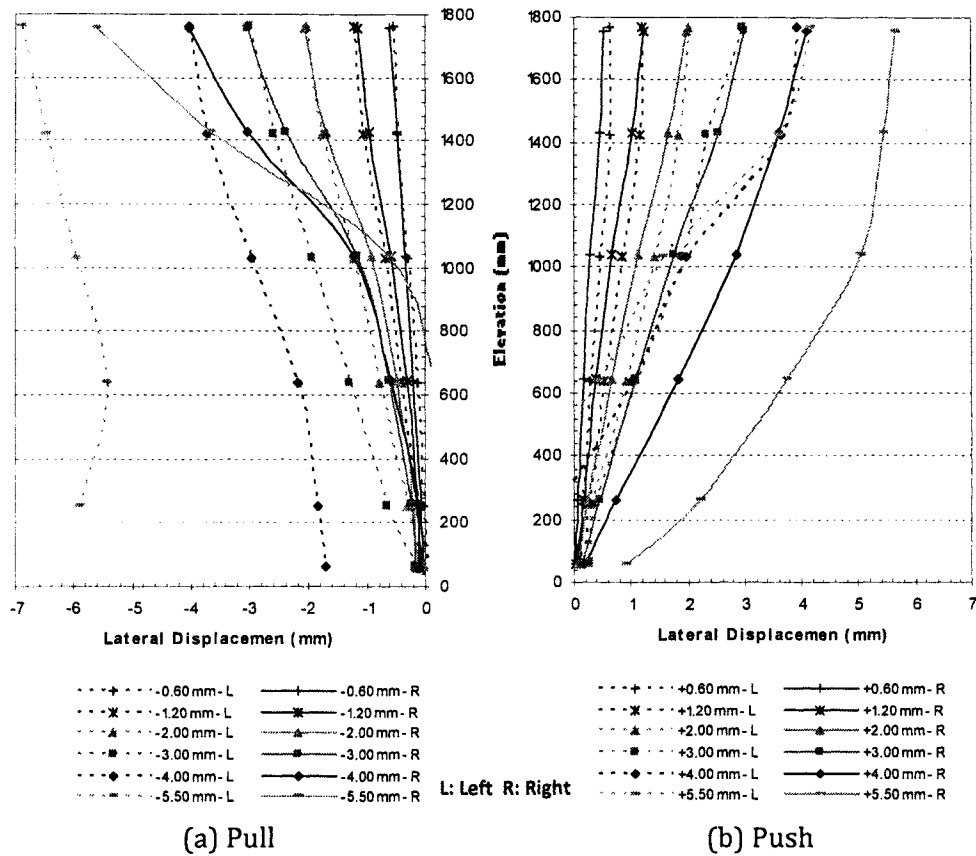
Figure 4.27 - *Lateral displacement profiles for Wall 2 at selected displacement levels*

4.3.2.5 Wall Curvature

Average curvature was calculated at five elevations over the height of the wall

(See Appendix E for details). The profiles at the end of the second loading sequence

for selected displacement cycles are shown in Figure 4.28. Very small flexural

deformation with slightly higher concentration near the base was observed in both the pull and the push directions of loading. The pinching shape close to the bottom of the wall which initiated at low displacement levels is believed to be a result of a local horizontal crack rather than flexural deformation. At the 5.50 mm displacement (0.31% drift) cycle, the bottom Demec points became detached and, therefore, no data point was available for the lowest segment of the wall. The curvature profile for the 7.00 mm displacement (0.39% drift) cycle was also not completed due to loss of multiple Demec points over the height of the wall.

(a) Pull   (b) Push
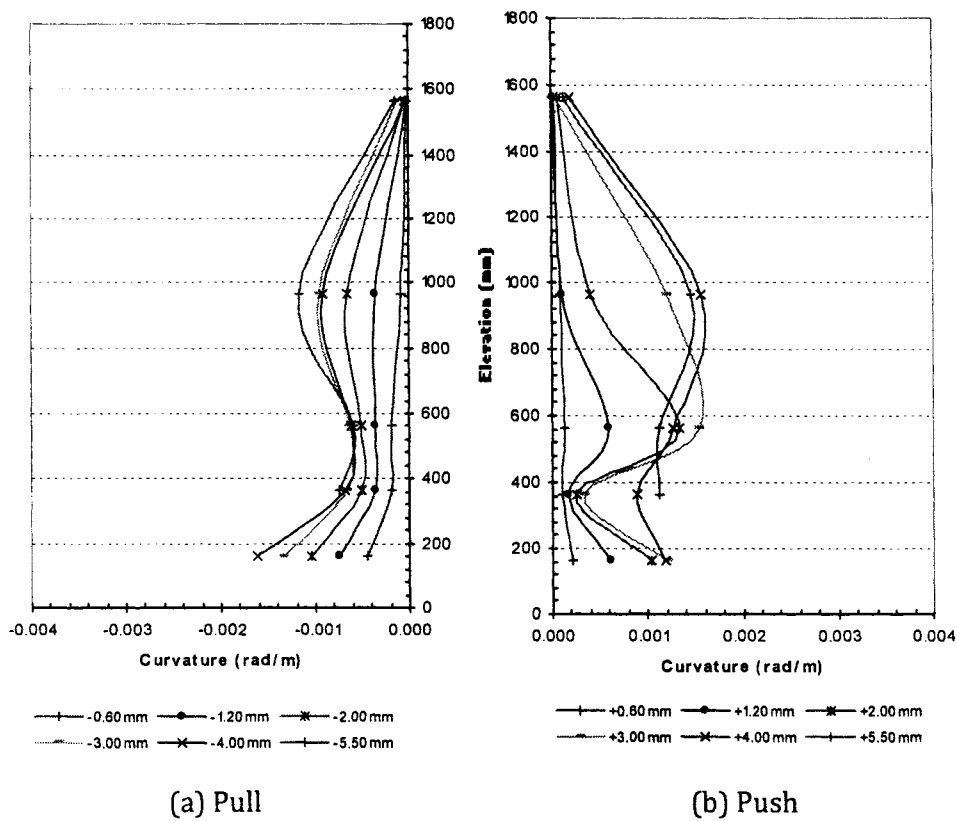
Figure 4.28 – Average curvature profiles for Wall 2 at selected displacement levels

4.3.3   Wall 3

Wall 3 was 1796 mm long and 1830 mm high with average 5.7 mm thick mortar bed joints (Figure 4.29). The wall was reinforced vertically using two No. 4 bars (USA Size - $A_s = 130$ mm^2) with 1710 mm spacing ($\rho_v = 0.16\%$) located in the end cells of the wall. Two pairs of D3 deformed wires ($A_s = 19.4$ mm^2) were used as horizontal reinforcement with 1710 mm spacing ($\rho_h = 0.05\%$) in the top and bottom courses of the wall. Each horizontal reinforcing bar was anchored around the extreme vertical bars with a 180° hook. The wall was subjected to a superimposed axial load of 120 kN resulting in a compressive stress of 0.75 MPa based on gross area.

4.3.3.1   General Observations

The load-displacement hysteresis loops for Wall 3 are shown in Figure 4.30
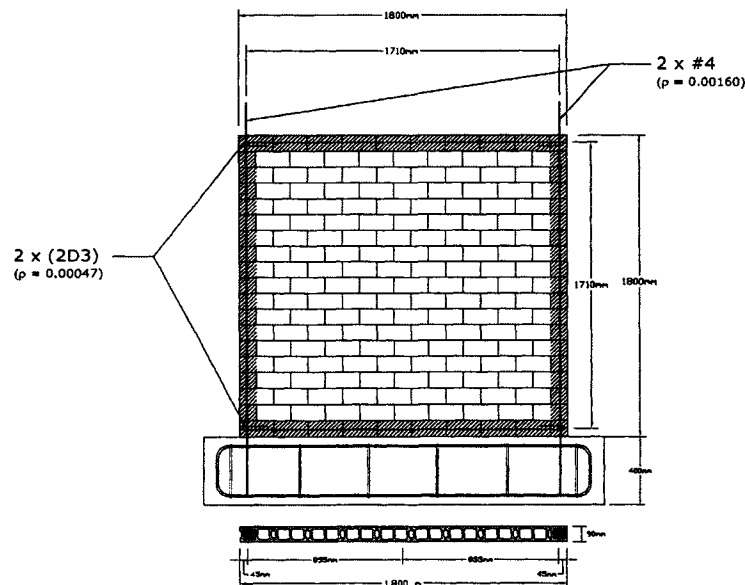
Figure 4.29 - *Schematic view of Wall 3*
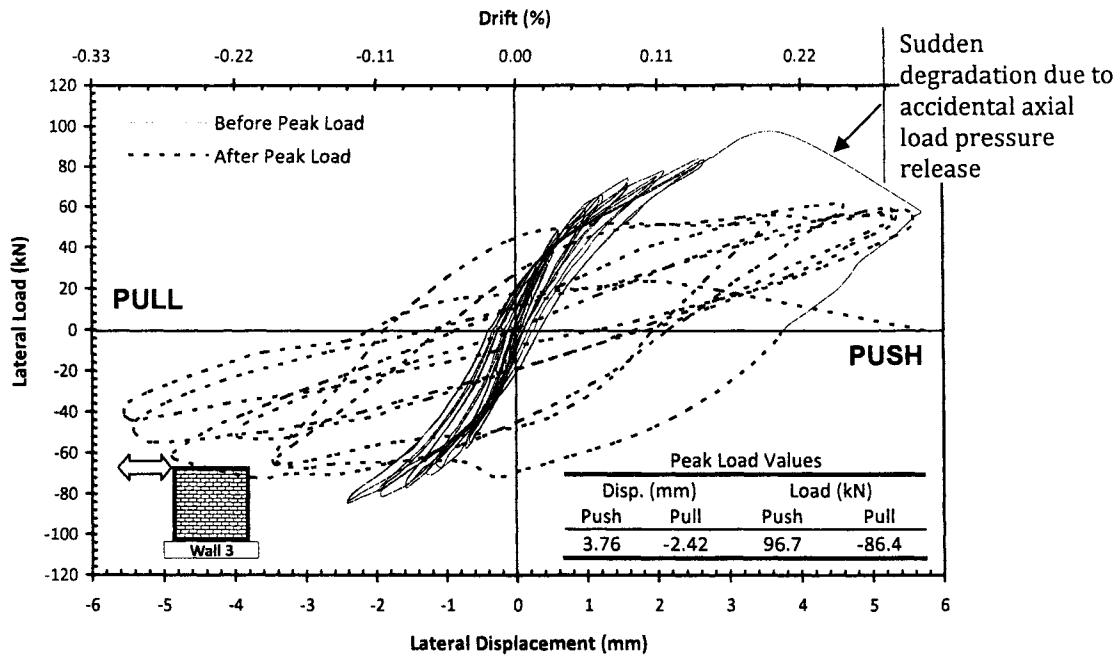
Figure 4.30 - Hysteresis loops for Wall 3

for the full loading history. The two dial gauges at the top-left and top right ends of the wall showed fairly consistent readings throughout the test. For the purpose of presentation, the readings from the dial gauge connected to the top-right corner of the wall were used. Loading started with a 0.20 mm displacement cycle at the top of the wall corresponding to 0.01% drift and then the amplitudes of the cycle were increased to ±0.40, ±0.60, ±0.80, ±1.25, ±1.50, ±2.00, ±2.50, ±3.60, ±4.60 and ±5.60 mm and each cycle was repeated twice throughout the test.

The first cracks appeared on the wall during the 1.25 mm displacement (0.07% drift) cycle. The cracks were in the form of short horizontal bed joint cracks starting from the far left and right sides of the wall. During the next 1.50 mm displacement cycles (0.08% drift), the horizontal crack on the right side of the wall

elongated to double the initial length and a stepped-pattern crack through contiguous mortar joints developed in the left half of the wall (Figure 4.31-a).

More stepped-pattern cracks formed on both the left and the right halves of wall during the 2.00 mm displacement (0.11% drift) cycle. In addition, the existing horizontal crack in the right half elongated up to the midlength of the wall (Figure 4.31-b). During the 2.50 mm displacement (0.14% drift) loading cycles, a diagonal stepped-crack appeared in the right half of the wall and the cracks formed a fairly symmetric pattern (Figure 4.31-c).

During the push sequence of the 3.60 mm displacement (0.20% drift) cycle, the wall reached its maximum load resistance at 95.65 kN corresponding to 3.58 mm displacement (0.20% drift). The displacement was slightly overshot to 3.75 mm (0.21% drift) due to sudden formation and opening of new cracks near the right toe of the wall. At this point, loading was stopped for crack inspection. It was also noticed that, due to flexural deformation of the wall and rotation of the top loading beam, the uniform distribution of axial load between the two hydraulic jacks was significantly altered resulting in 17% higher axial load on the left jack and 10% lower axial load on the right hydraulic jack. To restore the balance between applied axial loads, the servo valve of the left hydraulic jack needed to be manually opened and closed in a very short instant. This would let enough oil eject from the piston and consequently release the extra pressure. During the adjustment process, when the first few attempts to reduce the extra pressure failed, it was decided to open and close the servo valve slower. However, the next attempt resulted in a huge reduction
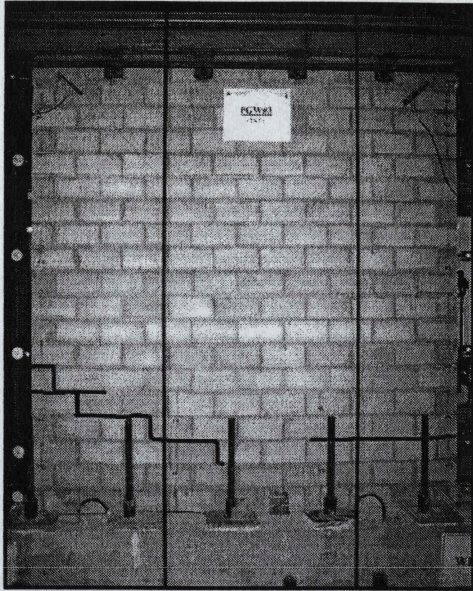
(a) Crack pattern during 1.25 mm
and 1.50 mm displacement cycle
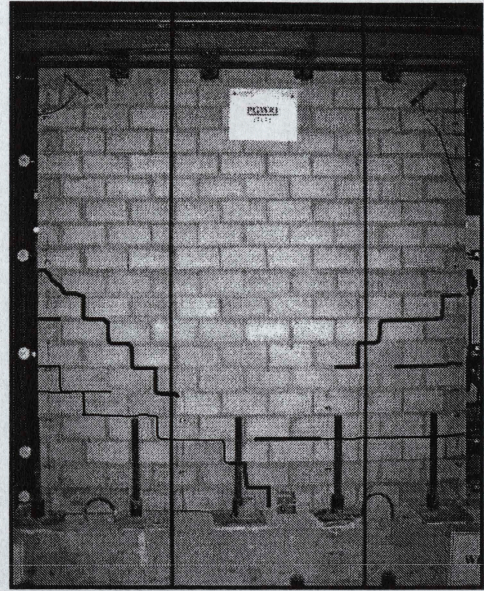
(b) New cracks during
2.00 mm displacement cycle
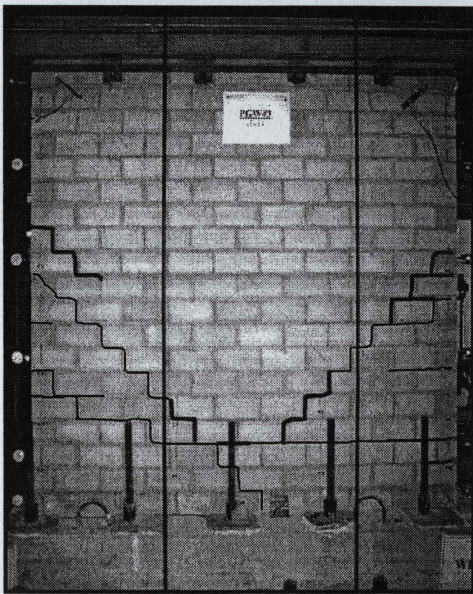
(c) New cracks during
2.50 mm displacement cycle
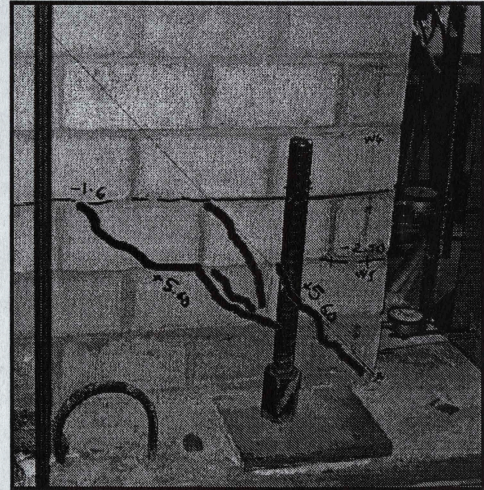
(d) New cracks at
5.60 mm displacement cycle

Figure 4.31 – *Crack pattern for Wall 3 at selected displacement levels (Photos enhanced for crack pattern - darker lines indicate new cracks during the specified displacement cycle) (to be continued)*
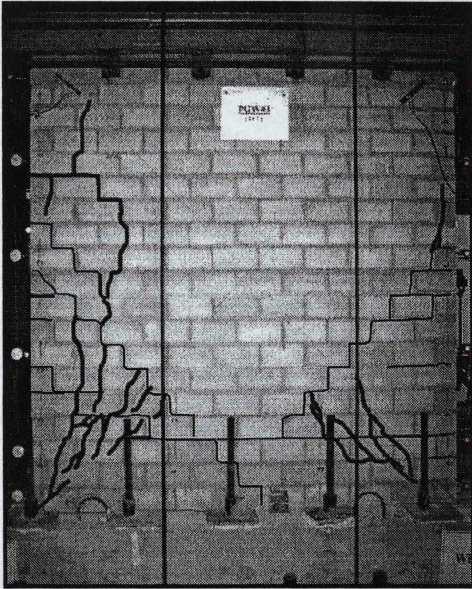
(e) New cracks during
3.60 mm displacement cycle
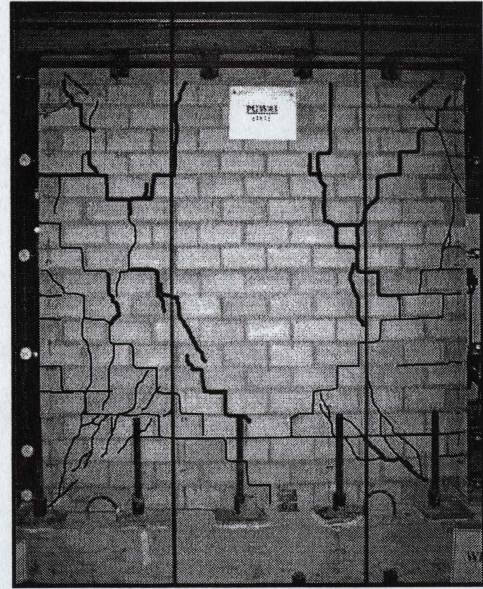
(f) New cracks during
4.60 mm displacement cycle
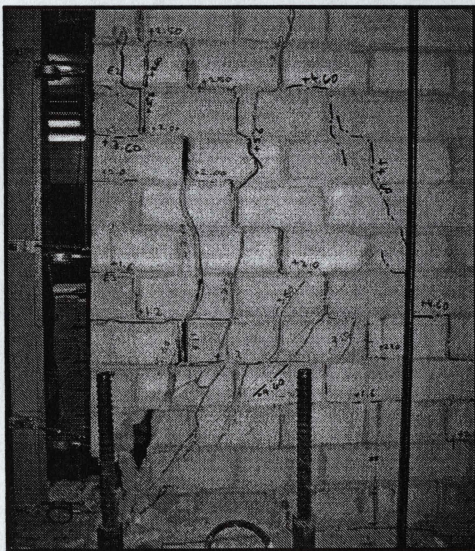
(g) Crack opening due to buckling
vertical reinforcement
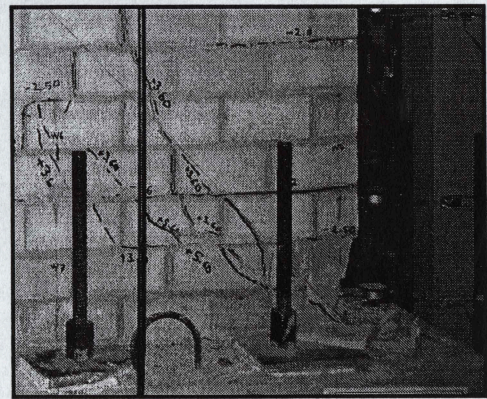
(h) Crushing of the right toe of
during the 5.60 mm disp. cycle

Figure 4.31– (Continued)

of pressure to approximately 33% of its original value. Although the released pressure was corrected, the incident led to a significant overshot displacement to 5.59 mm (0.31% drift) in the push direction (see Figure 4.30) and the diagonal cracks into the right toe of the wall widened to more than 3 mm (Figure 4.31-d).

It was decided to restore the axial load and continue the test based on the intended amplitudes. Thus, the wall was pulled to -3.60 mm top displacement (0.20% drift). Several diagonal cracks formed in the right and the left toes of the wall. Vertical cracks were also observed in both the right and left upper halves of the wall (Figure 4.31-e) and some diagonal stepped-cracks widened to approximately 5 mm (Figure 4.32). At this point, the face shell, outer web and part of the grout inside the bottom-left corner block were removable by hand due to severe crushing (Figure 4.33). After removing the crumbled portion of the left corner block, it was noticed that the vertical reinforcing bar inside the block was deformed (bent) which was an indication of onset of buckling.
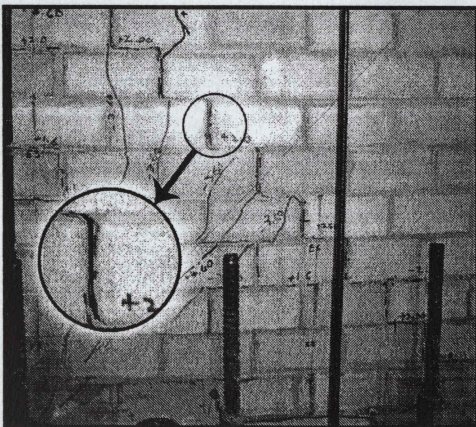
Figure 4.32 *- Five mm wide joint cracks for Wall 3 at 3.60 mm displacement (push)*
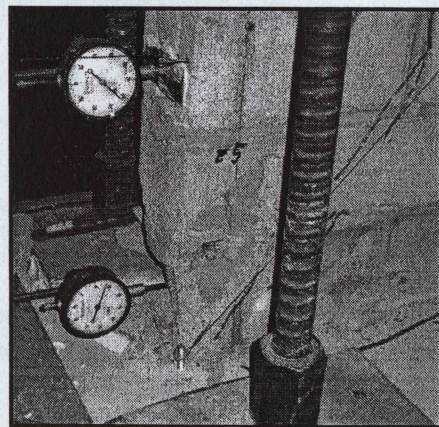
Figure 4.33 *- Crushing of the left toe of Wall 3 at 3.60 mm displacement (pull)*

The highest load resisted by Wall 3 in the pull sequence of this loading cycle was 71.60 kN which was 15% less than the 84.36 kN maximum strength recorded in the previous cycle. Also a lower degradation rate was observed during the first cycle of loading in the pull direction compared to the push direction after reaching the peak load. Although it was thought that this post-peak response of the wall would have been affected by the accidental 5.59 mm overshot displacement during the first loading cycle, the response of the wall in the second cycle showed a quite similar pattern in both the pull and push directions.

During the 4.60 mm displacement cycle (0.26% drift), several vertical and diagonal stepped-cracks appeared in the upper half of the wall and the existing cracks widened (Figure 4.31-f). Formation of the vertical cracks could be explained by buckling of vertical steel bars and reduced depth of the compression zone resulting in higher axial compressive strain leading to compression failure of the concrete blocks.

During the 5.60 mm displacement (0.31% drift) cycle, the vertical reinforcement at the left end of the wall buckled out resulting in large increases in width of adjacent vertical and diagonal cracks up to nine courses (Figure 4.31-g). Extensive crushing was also observed at the right toe of the wall and the face shell of the surrounding blocks spalled off (Figure 4.31-h). Despite wide open cracks and the severe damage observed on the wall, approximately 65% of the peak lateral load resistance was developed by the wall during this loading cycle.

During the next attempt to increase the amplitude of the displacement loading, the wall reached less than 25% of its maximum strength recorded during

the test. At this point, due to extensive strength degradation of the wall and stability

concerns regarding the test setup, loading was terminated and the test ended.

The tested wall was dismantled for further inspection to assess the quality of

grouting. Well compaction and continuous grouting was observed in the designated

horizontal and vertical cells. Only a very small amount of grout was found to have

leaked into the contiguous cells (up to two adjacent block cells) at the bottom of the

wall and this was thought to be insignificant to the overall behaviour of the wall.

4.3.3.2 Load-Displacement Response

The load-displacement response for Wall 3 indicates relatively symmetric and

narrow hysteresis loops for the push and the pull loading directions before reaching

the maximum resistance of the wall. The wall showed linear behaviour up to almost

1.25 mm top displacement (0.07% drift). After formation of the first horizontal bed

joint cracks, a fairly bilinear pattern was observed in the loading-unloading path of

the hysteresis loops resembling a rocking type of behaviour (Moon 2003b).

The ultimate lateral load resisted in the pull direction was about 12% lower

than in the push direction. More gradual strength degradation was observed in the

pull direction. The load-displacement hysteresis loops indicated approximately 35%

lower strength in the push direction during the following cycle after reaching the

ultimate resistance compared to only 15% strength degradation in the pull

direction. It is thought that the asymmetric strength degradation is attributable to

the damage that the wall experienced due to the significant displacement overshot

in the push direction as described in the previous section. Despite the asymmetric

post-peak response for Wall 3, the envelope of the load-displacement curves, shown

in Figure 4.34, indicates nearly the same slope for the descending branch in both the

push and pull directions of loading.

After inspection of the strain profile recorded by three strain gauges attached

to the vertical reinforcing steel bars, no tensile yielding was observed on either the

left or right end bars. The general behaviour of Wall 3 indicated a shear dominated

failure mode characterised by formation of wide diagonal cracks followed by

complete toe crushing. The fairly fat load-displacement hysteresis loops observed

after reaching the peak lateral load resistance of the wall indicated good energy

dissipation characteristics for Wall 3.
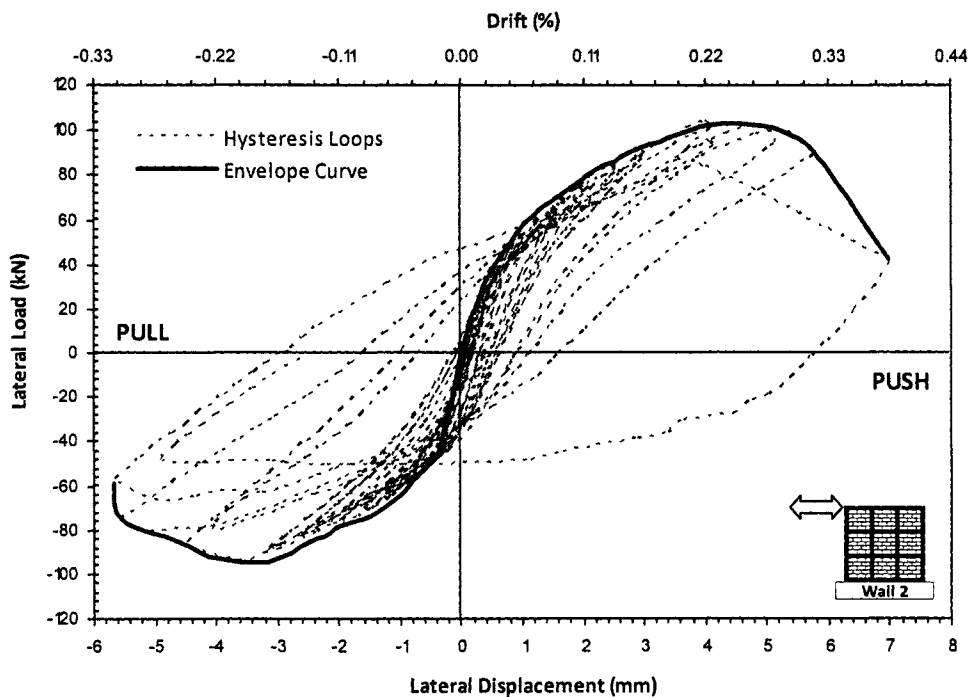
*Figure 4.34 - Envelope of load-displacement hysteresis loops for Wall 3*

4.3.3.3 Wall Deformation and Drift

The in-plane lateral displacement of the wall was measured using six dial gauges over the height of the wall at both the left and right ends. The lateral displacement profiles for selected loading cycles are presented in Figure 4.35. For comparison purposes, displacements at both ends are shown in the same plot. The displacement profiles were essentially linear up to the 2.50 mm displacement (0.14% drift) cycle which indicates domination of shear deformation. The overshot displacement due to the release of the axial load is reflected in the 5.60 mm top

(a) Pull   (b) Push
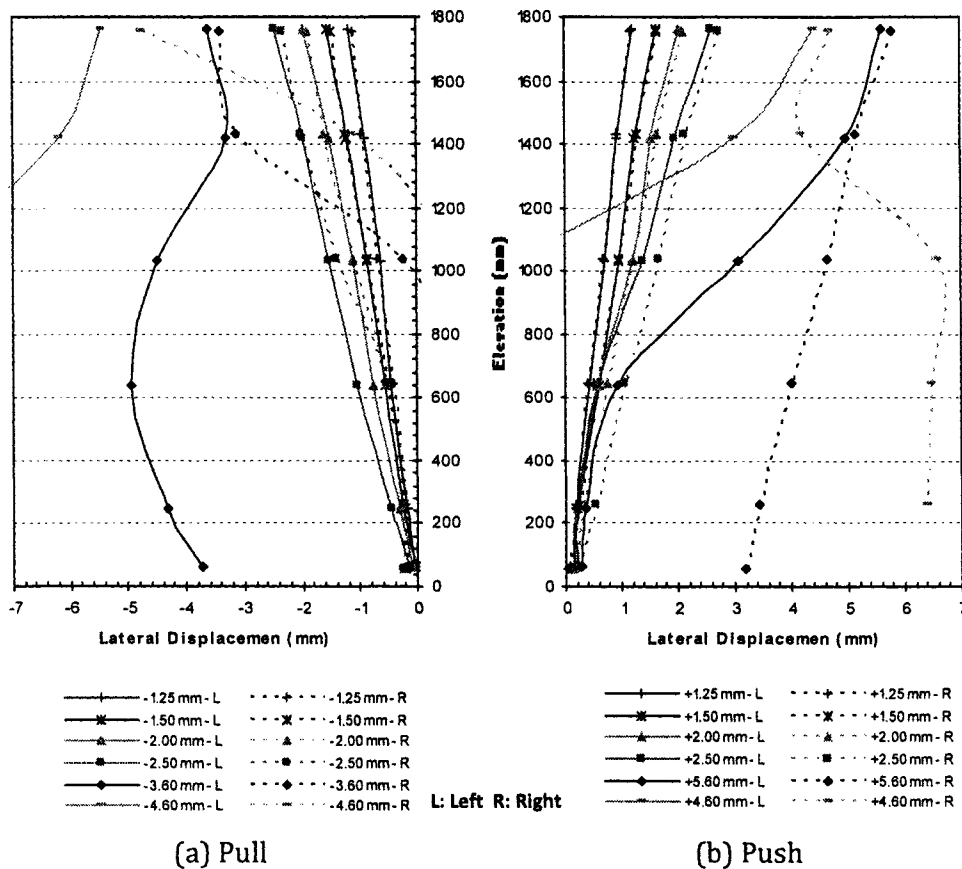
Figure 4.35 – *Lateral displacement profiles for Wall 3 at selected displacement levels*

displacement (0.31% drift) in the push direction. The large deformations observed at the bottom of the wall for the final cycles are believed to be due to permanent opening of the diagonal cracks at the left and right toes of the wall and does not necessary represent sliding at the base. This is because very small displacements were observed at the left toe of the wall compared to the right toe.

4.3.3.4 Wall Curvature

Average curvature was calculated at five elevations over the height of the wall as described in Appendix E. The average curvature curves, presented in Figure 4.36, correspond to the end of the second cycle of selected loading displacements. The relatively uniform curvature observed along the height of the wall is consistent with the expected behaviour since shear deformation dominated the lateral displacement of the wall. Slightly higher curvature near the base of the wall is due to the small flexural deformation that the wall experienced during the test.

4.3.4 Wall 4

Wall 4 was 1799 mm long and 960 mm high with average 5.6 mm thick mortar joints (see Figure 4.37). The wall was reinforced vertically with three No. 10 bars ($A_s = 100$ mm^2) with 855 mm spacing ($\rho_v = 0.19\%$) located at the ends and midlength of the wall. Two D3 deformed wires ($A_s = 19.4$ mm^2) were used as horizontal reinforcement ($\rho_h = 0.05\%$) with 855 mm spacing. The horizontal reinforcing bars were anchored around the extreme vertical bars with a 180° hook. The wall was subjected to a superimposed axial load of 120 kN corresponding to a compressive stress of 0.75 MPa based on gross area.

(a) Pull   (b) Push
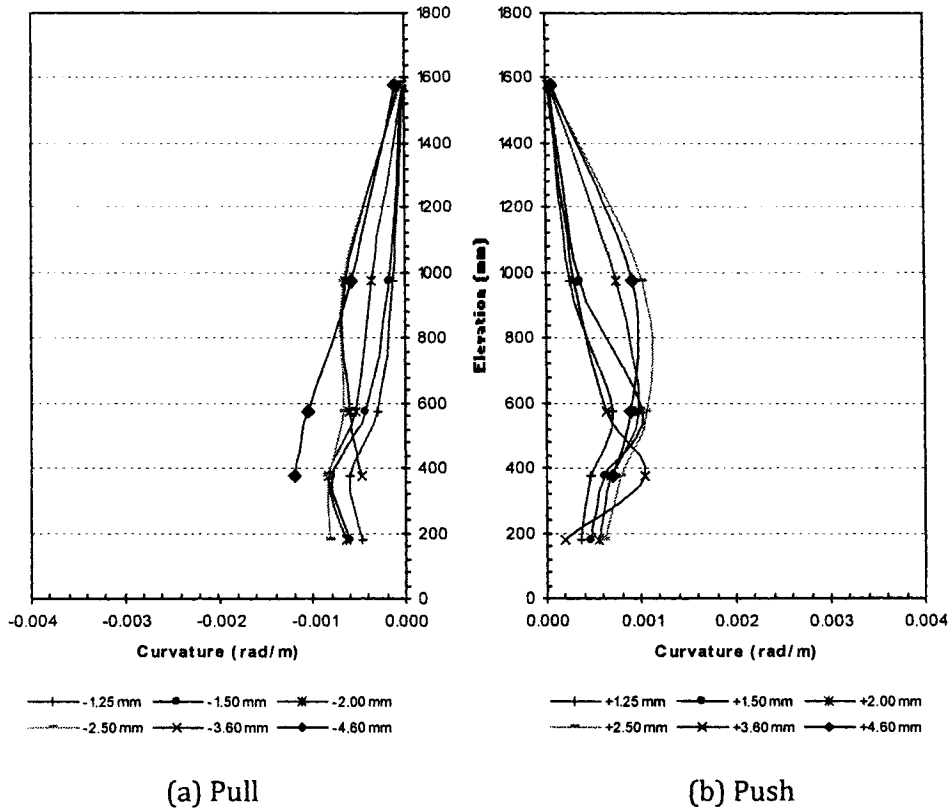
Figure 4.36 - *Average curvature profiles for Wall 3 at selected displacement levels*
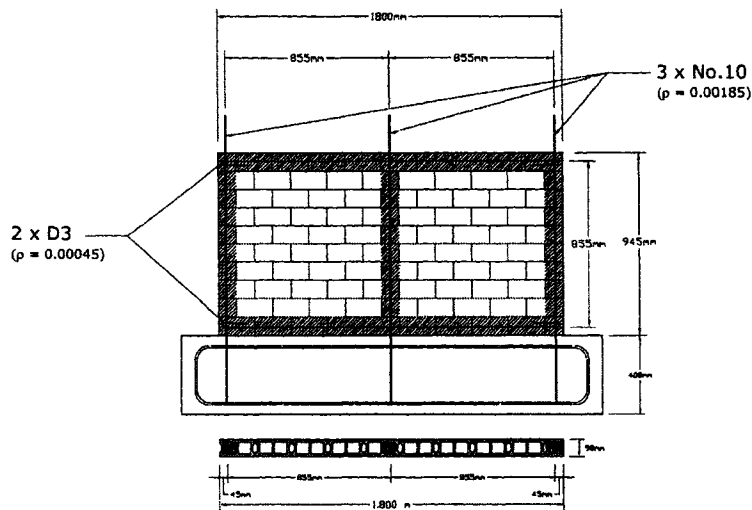
Figure 4.37 - *Schematic view of Wall 4*

4.3.4.1   General Observations

The load-displacement hysteresis loops for Wall 4 are presented in Figure

4.38 for the full loading history and in Figure 4.39 for a smaller displacement range.

Displacement was monitored by two dial gauges attached to the reference frame at

the top-right and at the top-left corners of the wall. The consistency between

reading from the two dial gauges was lost when a diagonal stepped-crack occurred

in the left half of the wall (Figure 4.40-a) during the 0.6 mm pull displacement

(0.07% drift). Subsequently, the readings of the top-left corner were believed to be

unrepresentative of overall wall deflection. Therefore, readings from the dial gauge

attached to the top-right corner of the wall were used as the top displacement of the
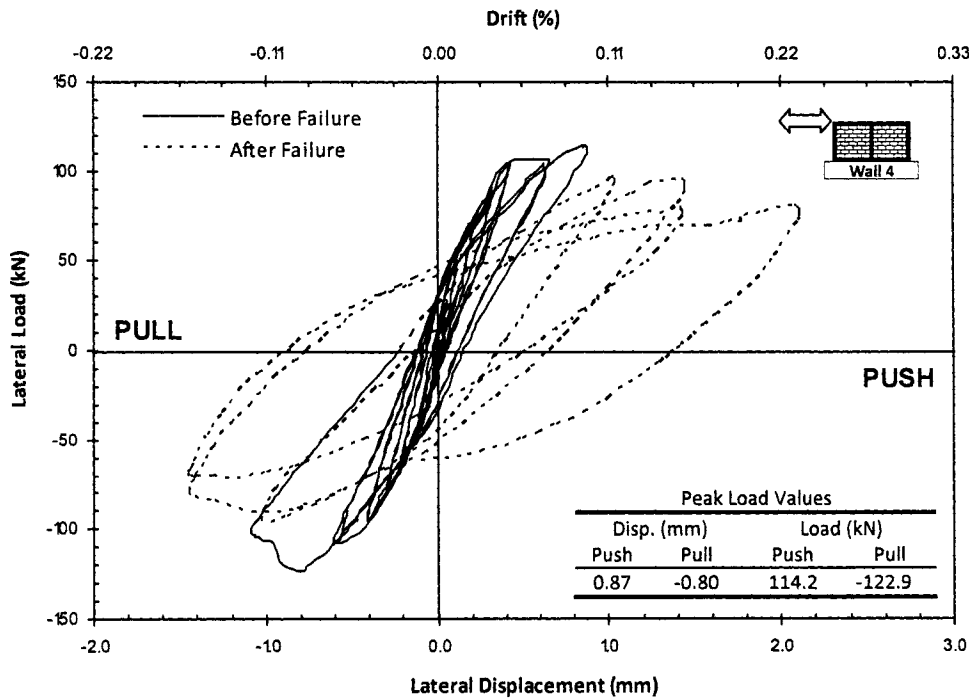
Figure 4.38 - Hysteresis loops for Wall 4
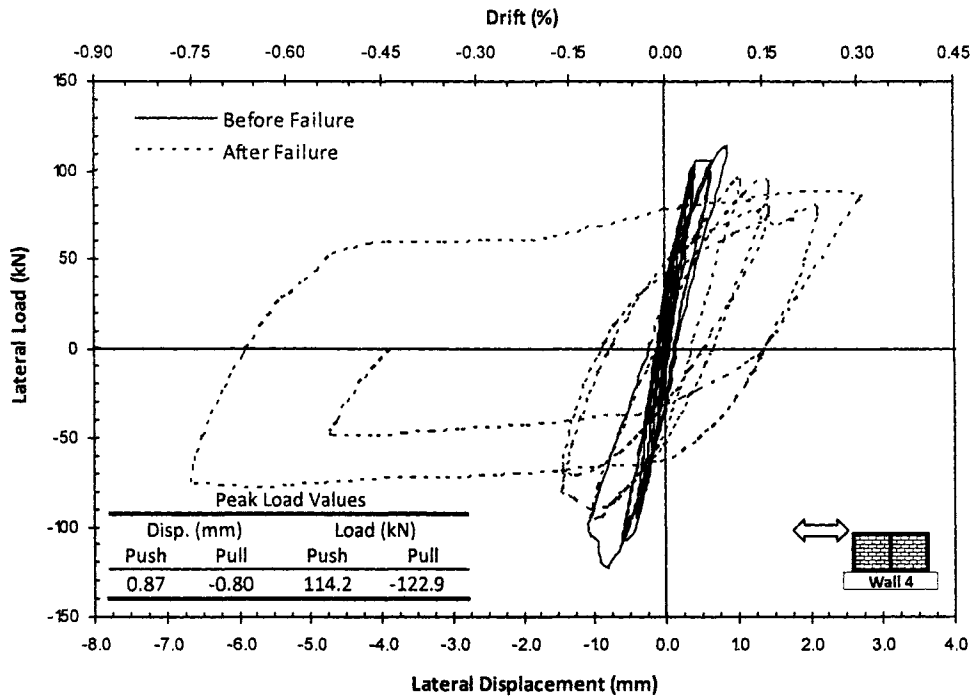
Figure 4.39 - *Hysteresis loops for small displacement level of Wall 4*

wall. Testing started at 0.10 mm displacement (0.01% drift) in the push and pull directions. The amplitude of the cycles was then increased to ±0.20, ±0.30, ±0.40, ±0.60, ±1.00, ±1.40 mm and each cycle was repeated twice throughout the test.

The first diagonal cracks occurred during the 0.60 mm displacement (0.07% drift) cycle inside the unreinforced area of the left half of the wall creating an X-shape pattern (Figure 4.40-a). During the 1.00 mm push displacement (0.11% drift) cycle, a new diagonal stepped-crack formed in the hollow part of the right half of the wall but unlike the left half, the X-shape pattern was not completed until near the end of the test. This may be explained by poor sealing of adjacent blocks of the middle cells resulting in leakage of wet grout into the wall at the right side of the
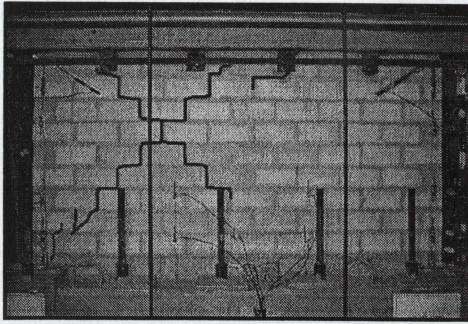
(a) Crack pattern at
0.60 mm top displacement
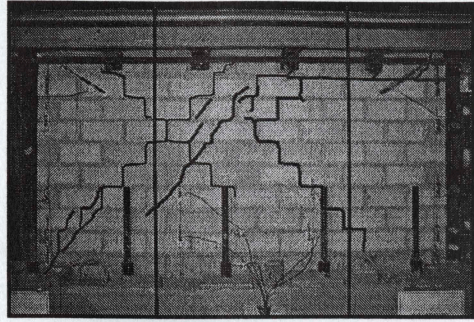
(b) New Cracks during
1.00 mm top displacement
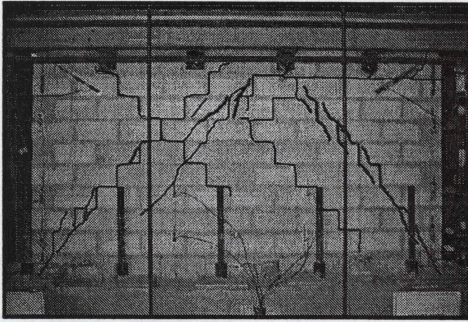
(c) New Cracks during
1.40 mm top displacement
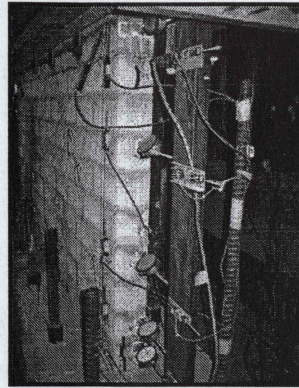
(d) New Cracks during
2.00 mm top displacement (push)
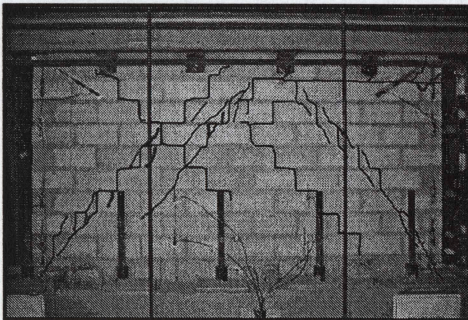
(e) New Cracks during
6.60 mm top displacement (pull)
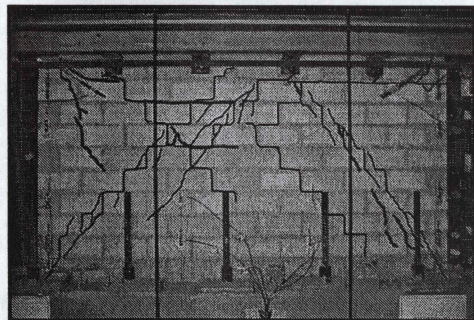
(f) New Cracks during
2.67 mm top displacement (push)

Figure 4.40 – Crack pattern for Wall 4 at selected displacement levels (Photos enhanced for crack pattern - darker lines indicate new cracks during the specified displacement cycle)
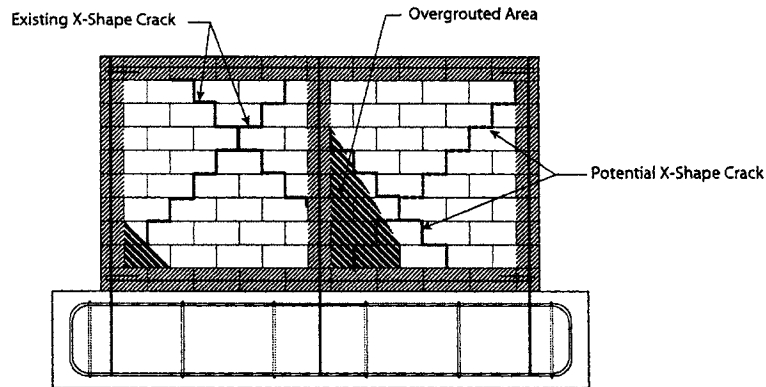
Figure 4.41 *- Schematic of grout leakage areas*

central column of grouted cells. The area filled with grout was exposed after dismantling the tested wall as shown in Figure 4.41. As can be seen, in the right half of the wall, grout leakage covered a significant portion of the wall and would be expected to provide higher resistance to formation of diagonal cracks intersecting the grouted area compared to the left half of the wall. During the pull sequence of the 1.00 mm displacement (0.11% drift) cycle, a new diagonal crack propagated through masonry blocks. As highlighted in Figure 4.40-b, it initiated in the left half of the wall and some of the existing diagonal stepped-pattern cracks on this half of the wall extended to the left corner toe. Also, a four-block long horizontal bed joint crack was observed along the uppermost bed joint of the wall starting from the right end. This crack turned to a diagonal stepped crack at its right end and stopped when it reached the middle grouted-reinforced part of the wall.

Cracking in the 1.00 mm displacement cycle also included a short diagonal crack that penetrated to the top-right corner of the wall where, in the next cycles, complete face shell spalling of the surrounding blocks occurred. A similar crushing pattern occurred at the top-left end during the push sequence of the next loading

cycle. This type of crushing is believed to be due to the effect of shear deformation constrained by the relatively rigid loading beam on top of the wall which consequently resulted in crushing of the top corner blocks due to excessive compressive stresses. [It should be noted that, considering shear deformation in beam theory, this effect is reduced to the power of three of the wall's aspect ratio (Timoshenko and Goodier 1970). This indicates less significant contributions of shear deformation in the other test walls having aspect ratios equal to or greater than 1.0].

The maximum lateral load carrying capacity of the wall in the push direction was recorded when the wall reached 0.87 mm top displacement (0.10% drift) in the push direction and 0.80 mm top displacement (0.09% drift) in the pull direction corresponding to 114.2 kN and 122.9 kN lateral load, respectively.

A continuous diagonal crack through masonry blocks was formed in the right half of the wall during the +1.40 mm push displacement equal to 0.16% drift (Figure 4.40-c). The existing cracks also noticeably widened and light could be seen though the cracks. These cracks were comprised of the ones close to the corners of the wall and some head joint cracks.

During the 2.00 mm displacement (0.22% drift) cycle in the push direction, some vertical cracks appeared on the webs of the top and bottom right corner blocks (Figure 4.40-d). Despite the intention to apply 2.00 mm top displacement toward the pull direction, the diagonal crack at the top-right corner block visibly widened to at least 5 mm and the expected 2.00 mm displacement was never completed according to the readings from the dial gauge attached to the top-right

corner of the wall. Hence, the wide cracks and the significant damage noticed on the

wall raised doubt concerning whether displacement readings from the top-right dial

gauge were still representative of overall wall deflection. Consequently, testing was

paused to assess the problem and determine the best option to continue.

Inspection of the crack pattern revealed less damage around the top-left

corner. Thus, it was decided to continue the test relying on the displacement reading

from the dial gauge attached to this corner. To evaluate the consistency of the

readings from the two corner dial gauges at this stage of testing, the hysteresis loops

recorded by the two dial gauges were plotted together (see Figure 4.42) starting

from the +2.00 mm displacement (0.22% drift) cycle having set the initial

displacement of the left dial gauge equal to the right one at the beginning of the

cycle. As can be seen in Figure 4.42, the fairly good agreement between the two
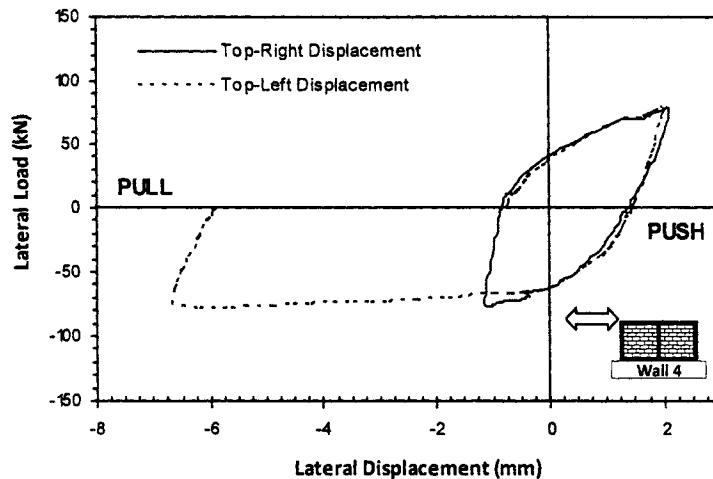
Figure 4.42 - *Inconsistency between top-right and top-left dial gauge readings for Wall 4 at the 2.00 mm pull displacement*

hysteresis loops ceased when the first sequence of loading in the pull direction (negative displacements) started. Then, while the right end of the wall was barely moving as a result of crack opening, the left end continued to move with the stiff loading beam along the top of the wall and resulted in approximately -6.60 mm pull displacement corresponding to 0.73% drift. This significant displacement led to visible widening of most of the existing diagonal cracks with limited extension to their length (see Figure 4.40-e). Therefore, it was decided to reverse the load and push the wall back to +2.00 mm top displacement based on the displacement readings from the dial gauge attached to the top-left corner of the wall. An excessive displacement of 0.67 mm (total displacement of 2.67 mm equal to 0.30% drift in the push direction) occurred during this sequence of loading due to a sudden crack opening. During this push cycle, a nearly vertical crack formed close to the top-left corner of the wall and extended down to the fifth course from the top (Figure 4.40-f). The face shells of the blocks in the right toe cracked and some diagonal cracks located around this area widened up to about 10 mm (Figure 4.43). At this point, the face shells of the top-right corner of the wall also spalled off (Figure 4.44).
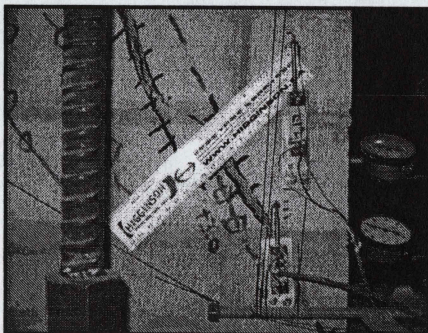
Figure 4.43 - Wide crack at the right toe of Wall 4 at 2.67 mm displacement (push)
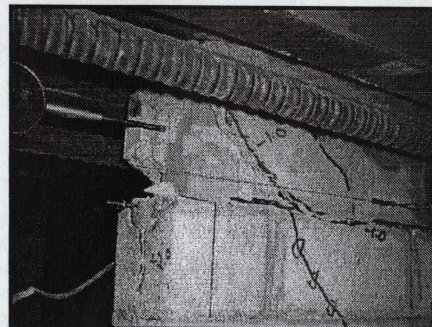
Figure 4.44 - Face shell spalling of the top right corner of Wall 4 at 2.67 mm displacement (push)

The final loading cycle was carried out in the pull direction and, once the wall reached -4.20 mm displacement (0.47% drift), the face shell of the top-left corner block, where the dial gauge was touching the wall, began to spall off. No new crack appeared in the wall at this loading cycle. Since more than 50% of the wall's strength had been lost at this stage, due to safety concerns, it was decided to stop recording any manual data readings and reverse the load until complete collapse of the wall. The behaviour of the wall was only recorded via a video camera. Collapse of the wall occurred at 37 kN during a push loading sequence. The incidence of collapse was initiated by out of plane instability after buckling of the middle vertical bar and was followed by loss of a large section of the hollow portion in the right half of the wall (Figure 4.45).
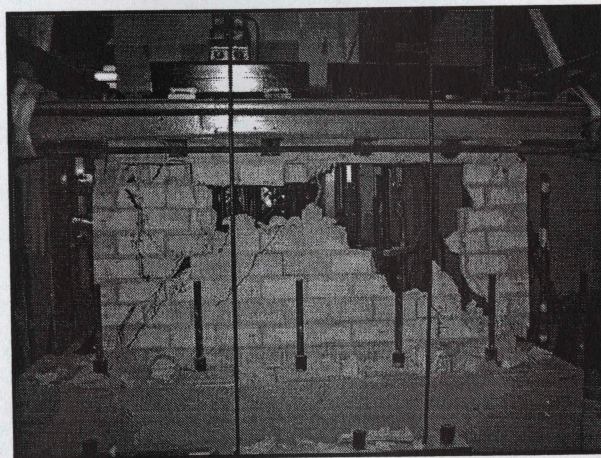
Figure 4.45 - Wall 4 after collapse

4.3.4.2   Load-Displacement Response

Only the behaviour of the wall prior to the significantly overshot displacement which occurred during the 2.00 mm (0.22% drift) loading cycle in pull direction is considered in the current discussion and later on in the analysis of the results

presented in Section 4.3.6. It should be noted that the overshot displacement results in almost 50% decrease in strength.

The overall behaviour of the wall indicated a shear dominated type of failure characterised by diagonal cracking and narrow hysteresis loops with fairly symmetric shape in the push and pull loading directions. The ultimate load in the push direction (114.2 kN) was about 8% lower than the measured value for the pull direction (122.9 kN). This may be explained by the contribution of areas overfilled with grout, shown in Figure 4.41, which increased the effective thickness of the diagonal compression strut resisting the load applied in the pull direction.

Significantly gradual strength degradation was observed upon reaching the ultimate load in either direction. However, slightly more rapid degradation was noticed during the loading in the pull direction. Further inspection of the strain profile recorded via three strain gauges attached to the vertical steel reinforcing bars showed no tensile yielding of either the left or right end bar.

4.3.4.3 Wall Deformation and Drift

The in-plane lateral displacements of the wall were measured using five dial gauges attached to the right edge of the wall. Figure 4.46 shows the lateral displacement profile of the wall at the end of the second sequence of loading for selected cycles in the push and pull directions.

The overall lateral displacement profile of the wall indicates a fairly linear response along the entire height up to the 1.00 mm displacement cycle in which the maximum strength of the wall was reached at about 0.8 mm (0.09% drift) in both

the pull and push directions. The shape of the lateral displacement profile for the

1.00 mm displacement cycle corresponding to 0.11% drift indicates a fairly large

value for the uppermost dial gauge reading while the bottom portion of the wall did

not moved as much. This may be due to shear sliding along the horizontal crack at

the uppermost bed joint that developed during this loading cycle (Figure 4.40-b).

During the push sequence of the 1.40 mm displacement (0.16% drift) cycle,

less displacement was recorded by the top dial gauge compared to the next lower

one which can be due to plastic shear sliding of the fractured bed joint along the

uppermost course of the wall. Since the remainder of the lateral displacement

(a) Pull   (b) Push
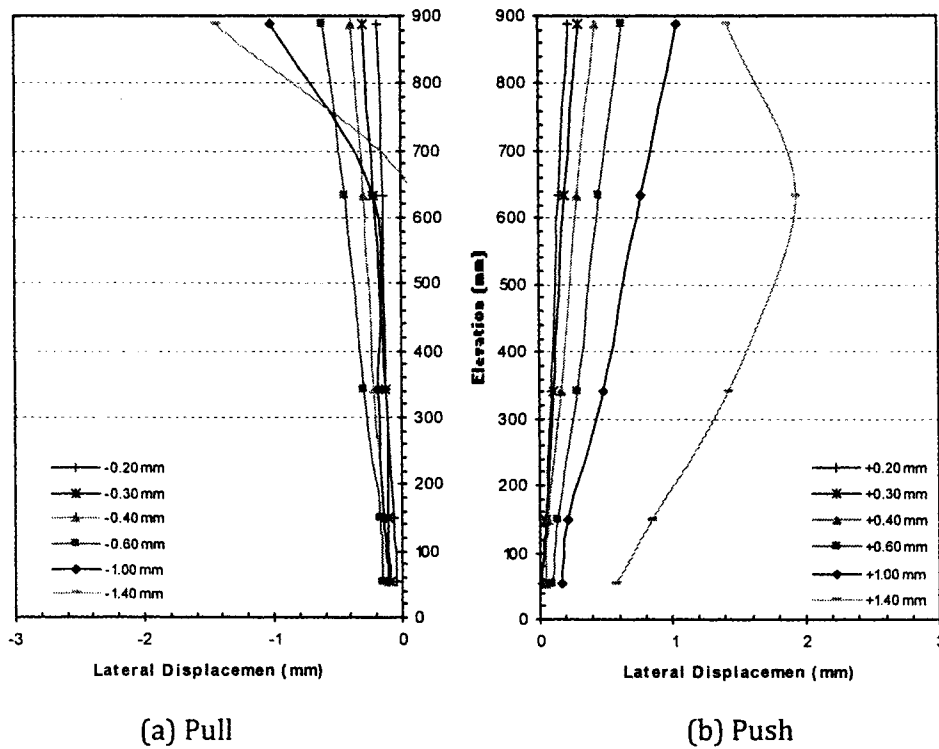
Figure 4.46 - *Lateral displacement profiles for Wall 4 at selected displacement levels*

readings showed very erratic changes and are thought to be locally affected by opening and closing of cracks, these data were not used in the analysis of results.

4.3.4.4 Wall Curvature

Average curvature was measured at four elevations using five Demec points over the height of the wall based on the method explained in Appendix E. Average curvatures at the end of the second sequence of loading for low displacement levels are presented in Figure 4.47. At higher displacements, due to opening and closing of existing cracks, results were highly affected by the local cracks in the vicinity of or

(a) Pull   (b) Push
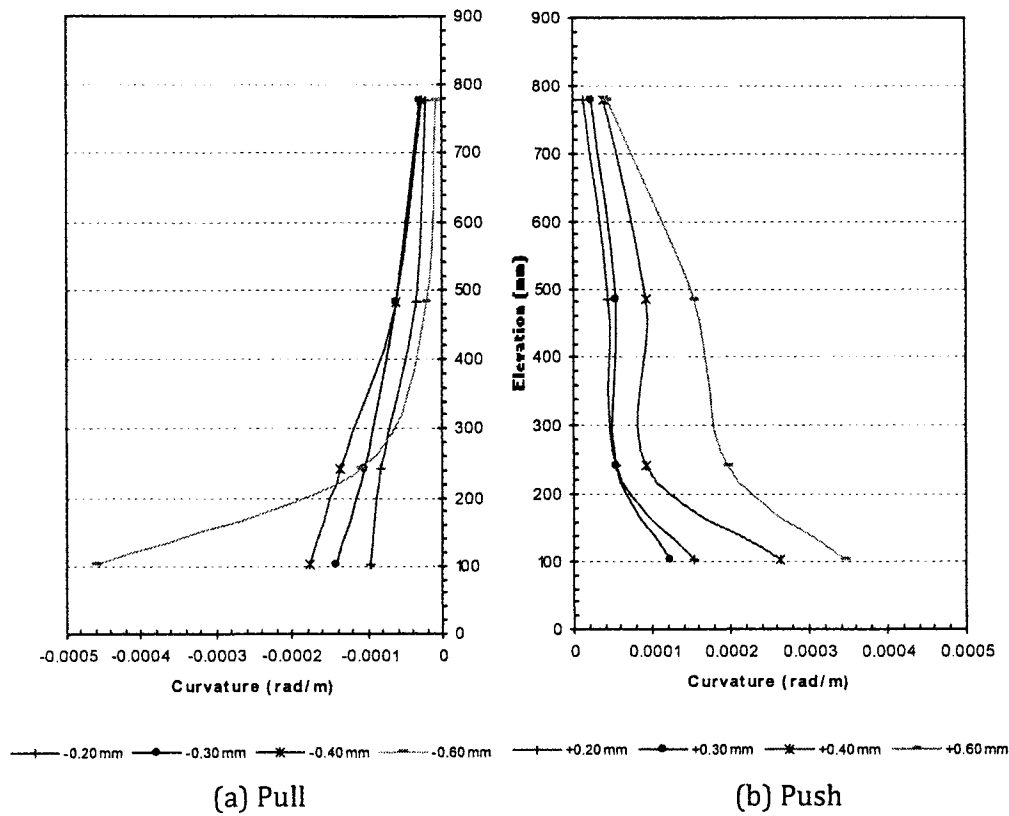
Figure 4.47 - *Average curvature profiles for Wall 4 at selected displacement levels*

between Demec points. This led to abrupt changes in measured curvature values and, therefore, it is believed that the resulting curves are not useful evidence of differences in behaviour over the wall height. Accordingly, these data points were not included in the figure. The curvature profile of the wall at low displacement levels, in both the pull and push directions essentially indicate larger flexural deformation at the bottom of the wall compared to the top which may be attributed to opening of horizontal and diagonal stepped-pattern cracks. In general, very limited flexural deformation was observed for Wall 4 indicating domination of shear deformation in the overall behaviour of the wall.

4.3.5   Wall 5

Wall 5 was 1800 mm long and 2655 mm high with average 5.7 mm thick mortar bed joints (Figure 4.48). The wall was reinforced vertically using three No. 10 bars (A_s =100 mm^2) with 855 mm spacing (ρ_v =0.19%) located at the ends and midlength of the wall. Four D4 deformed wires (A_s =25.8 mm^2) were used as horizontal reinforcement with 855 mm spacing (ρ_h =0.05%) at the top, third points and bottom of the wall. Each horizontal reinforcing bar was anchored around the extreme vertical bars with a 180° hook. The wall was subjected to a superimposed axial load of 120 kN resulting a compressive stress of 0.75 MPa based on gross area.

4.3.5.1   General Observations

The load-displacement hysteresis loops for Wall 5 are presented in Figure 4.49 for the full loading history. Top displacement was monitored using two dial

gauges attached to the reference frame and touching the top-left and the top-right corner of the wall. Fairly consistent readings were observed between the dial gauges throughout the test. For the purpose of presentation, the readings from the dial gauge touching the wall's top-left corner were employed in this report. Loading started with ±0.20 mm displacement cycles corresponding to 0.01% drift and then the amplitudes of the cycles were increased to ±0.40, ±0.80, ±1.00, ±1.25, ±1.50, ±2.00, ±2.50, ±3.00, ±4.00, ±5.00, ±6.50, ±8.00, ±11.0 and +13.0/-16.0 mm. Each cycle was repeated twice throughout the test.
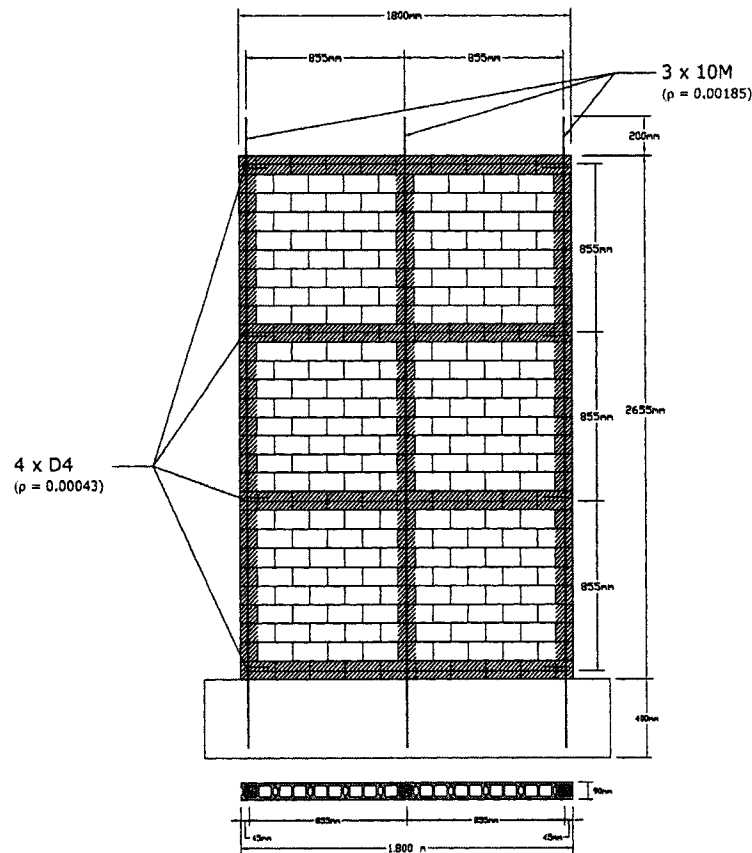
Figure 4.48 - *Schematic view of Wall 5*
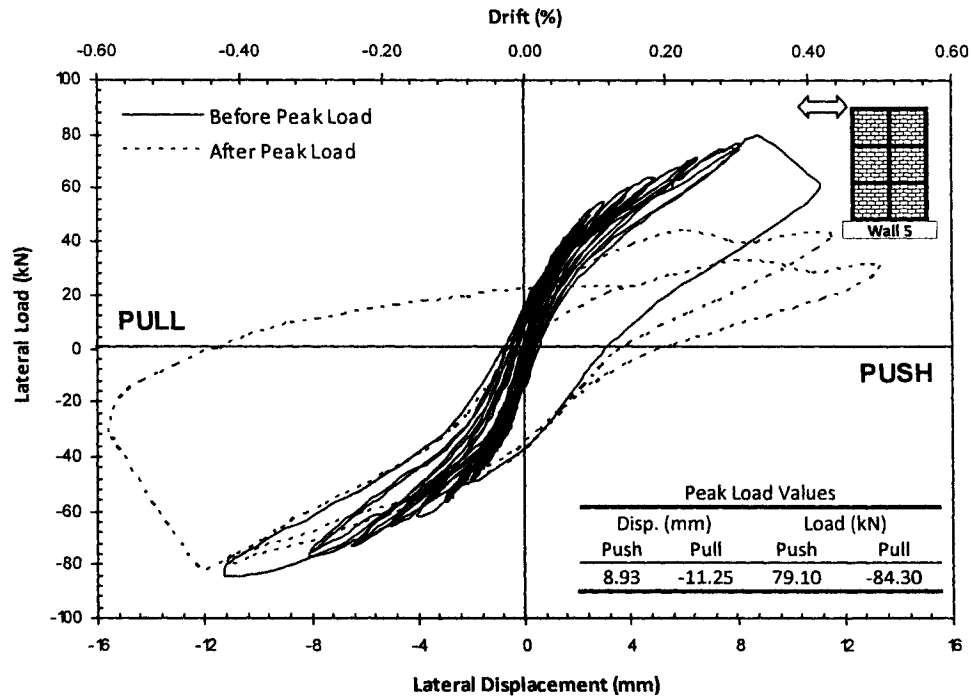
Figure 4.49 *- Hysteresis loops for Wall 5*

The first cracks appeared on the wall during the 1.50 mm displacement

(0.06% drift) loading cycle in the form of horizontal bed joint cracks on both the

right and left ends of the wall. The number of horizontal cracks increased and the

existing cracks extended to midlength of the wall during the next cycles up to

2.50 mm top-displacement (0.09% drift - Figure 4.50-a).

The first stepped-pattern cracks were observed during the 3.00 mm

displacement (0.11% drift) cycle on the left part of the wall starting from midheight

of the wall. During the 4.00 mm displacement (0.15% drift) cycle, fairly symmetric

cracking occurred on the wall's right end, as shown in Figure 4.50-b. At this point,

the horizontal cracks at the fifth and sixth courses covered the full length of the wall

(a) New cracks during 1.50 mm,
2.00 mm and 2.50 mm disp. cycle
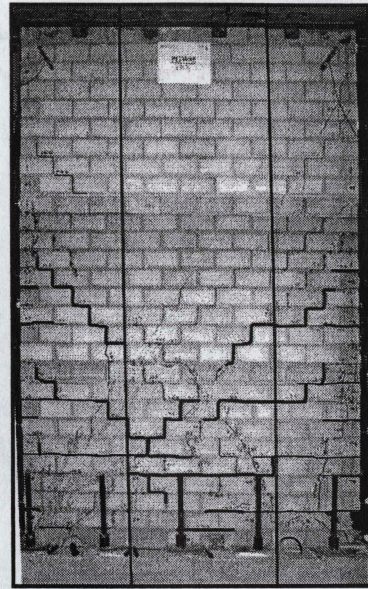
(b) New cracks during 3.00 mm,
and 4.00 mm displacement cycle
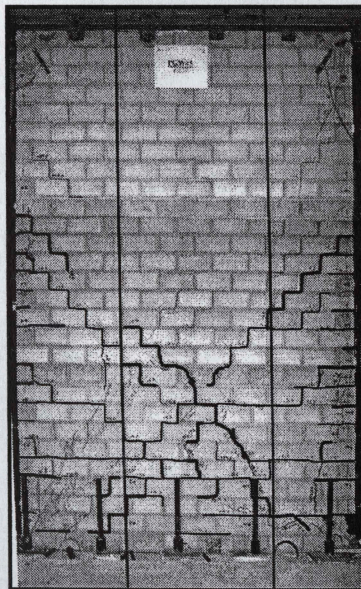
(c) New cracks during 5.00 mm,
6.50 mm and 8.00 mm disp. cycle
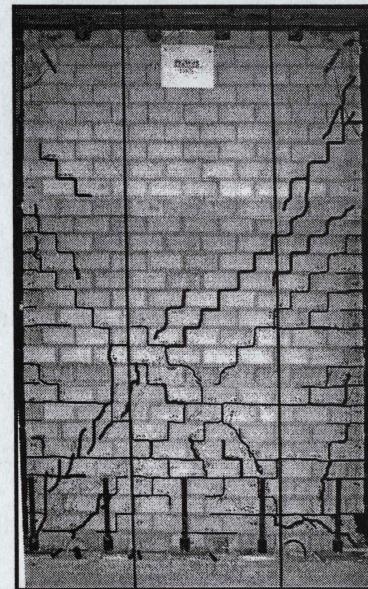
(d) New cracks during
11.0 mm displacement cycle

Figure 4.50 *– Crack pattern for Wall 1 at selected displacement levels (Photos enhanced for crack pattern - darker lines indicate new cracks during the specified displacement cycle)*

and the diagonal stepped-pattern cracks formed a cone shape for the uncracked portion of the wall above the existing cracks.

During the 5.00 mm displacement cycle corresponding to 0.19% drift, new stepped-pattern cracks, parallel to the diagonal stepped-cracks observed in the previous cycle, appeared on the wall. Some new cracks were also observed on the lower half of the wall and the existing cracks widened.

The behaviour of Wall 5 became distinct from other test walls by exhibiting outermost vertical steel bar yielded at 70.6 kN in the push direction and 73.23 kN in the pull direction during the 6.50 mm top wall displacement (0.24% drift) cycle. The first diagonal cracks also penetrated into the lower right-half of the wall at the end of this cycle.

During the next loading cycle with 8.00 mm (0.30% drift) displacement, a few diagonal stepped-cracks extended and the existing cracks visibly widened as shown in Figure 4.50-c. No other major damage developed during this cycle.

Severe crushing around the right toe of the wall was observed during the first push sequence of the 11.0 mm displacement (0.41% drift) cycle and the wall reached its maximum lateral load carrying capacity of 79.10 kN at 8.93 mm displacement (0.33% drift). The toe crushing extended up to three courses from the base and extended one block from the end of the wall. Spalling occurred in the face shells and outer web of the affected blocks (see Figure 4.51). After removing the loose portion of the blocks and interior grouting, it was observed that the vertical steel reinforcement embedded in the grouted cells had also buckled. Some parts of

the grout around the vertical bar were observed to be poorly compacted near the bottom course of the wall. A large diagonal crack propagated from the top right to the centre of the wall during the pull sequence of the 11.0 mm displacement (0.41% drift) cycle (Figure 4.50-d). Maximum lateral load carrying capacity of the wall in the pull direction was 84.30 kN at 11.25 mm top displacement (0.41% storey drift). However, no sign of toe crushing was observed at the left end of the wall.

During the second cycle of the 11.0 mm displacement, several diagonal cracks penetrated into the blocks in the bottom left half of the wall but a lower level of damage was observed compared to the right toe (Figure 4.50-d). A strength degradation of approximately 50% occurred in this loading cycle in the push direction whereas the resistance was unchanged in the pull direction. This was believed to be due to the better grout compaction that was observed near the left toe compared to the right toe after dismantling the wall at the end of the test.

During the next loading cycle in the pull direction, when the wall was pulled to 12.2 mm (0.45% drift), diagonal cracks suddenly formed near the left toe of the wall.
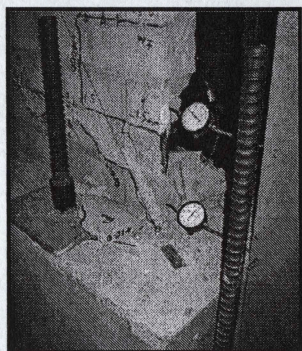
Figure 4.51 – *Toe crushing at the right toe of Wall 5 at 11.0 mm displacement (push)*
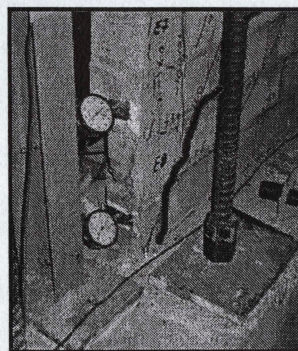
Figure 4.52 – *Toe crushing at the left toe of Wall 5 at 12.2 mm displacement (pull)*

Onset of cracking was audible and the two surface of the crack visibly slid along each other (see Figure 4.52). At this point, the lateral load rapidly dropped to approximately 35% of the maximum strength of the wall in the pull direction and the top displacement overshot to 15.6 mm top displacement (0.58% drift) instead of the intended 13.0 mm. Some head joint cracks widened to approximately 5 mm.

Due to significant strength degradation (about 70% of the peak load) and safely considerations, loading were terminated at this point. The final crack pattern of the wall is presented in Figure 4.53.

4.3.5.2 Load-Displacement Response

Wall 5 showed fairly symmetric load-displacement hysteresis loops prior to reaching the ultimate lateral load resistance of the wall in the push and pull directions (Figure 4.49). Linear behaviour was observed up to 1.5 mm top displacement (0.06% drift) corresponding to development of the first horizontal cracks. Afterwards, a bilinear pattern with narrow loading-unloading curves was observed up to the ultimate load. This indicated opening and closing of existing cracks with only a small amount of energy dissipation.

The ultimate lateral loads resisted in the push and pull directions were within 5% of each other. The strength degradation in the pull direction was more gradual compared to the push direction which was believed to be due to poor compaction of grout near the base at the right end of the wall.

The strain profile recorded by three strain gauges attached to the vertical reinforcing steel bars indicated that the vertical reinforcement yielded at both the
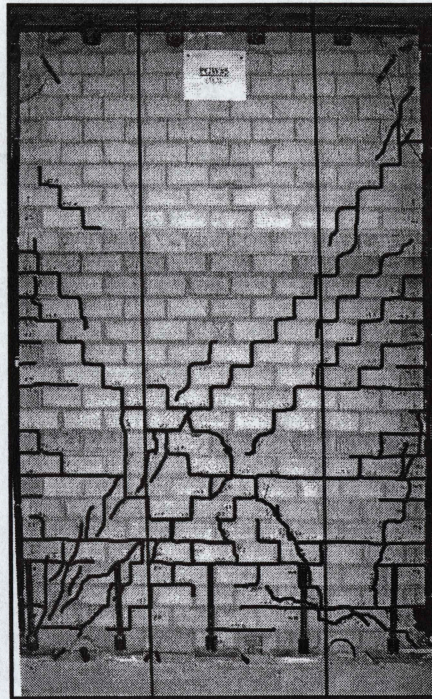
Figure 4.53 – *Crack pattern of Wall 5 at the end of the test*
(Photo enhanced for crack pattern)

left and right ends of the wall. Yielding of the flexural reinforcement along with the
wide diagonal cracks, observed in Wall 5 indicated domination of a mixed shear-
flexure failure mode for the wall's behaviour.

4.3.5.3   Wall Deformation and Drift

The in-plane lateral displacement of the wall was monitored using eight dial
gauges mounted on a reference frame at various levels over the height of the wall at
both the left and right ends. Figure 4.54 shows the lateral displacement profiles of
the wall at the end of the second sequence of loading for selected loading cycles. For
comparison purposes, deformations at both the left and right end of the wall are
shown in the same plot. The displacement profiles over the height of the wall

showed an essentially linear response throughout the test. Hence, despite the

relatively high aspect ratio ($h/\ell = 1.5$) for Wall 5, it appears that deflection

continued to be shear dominated. Due to the crushing of the right toe, the

displacement readings close to the base were affected by opening of the cracks after

reaching the ultimate resistance of the wall. That is, the recorded deflection changes

depending on which side of the crack the deflection instrumentation is attached.

Therefore, the data corresponding to the base do not represent sliding of the wall.

(a) Pull   (b) Push
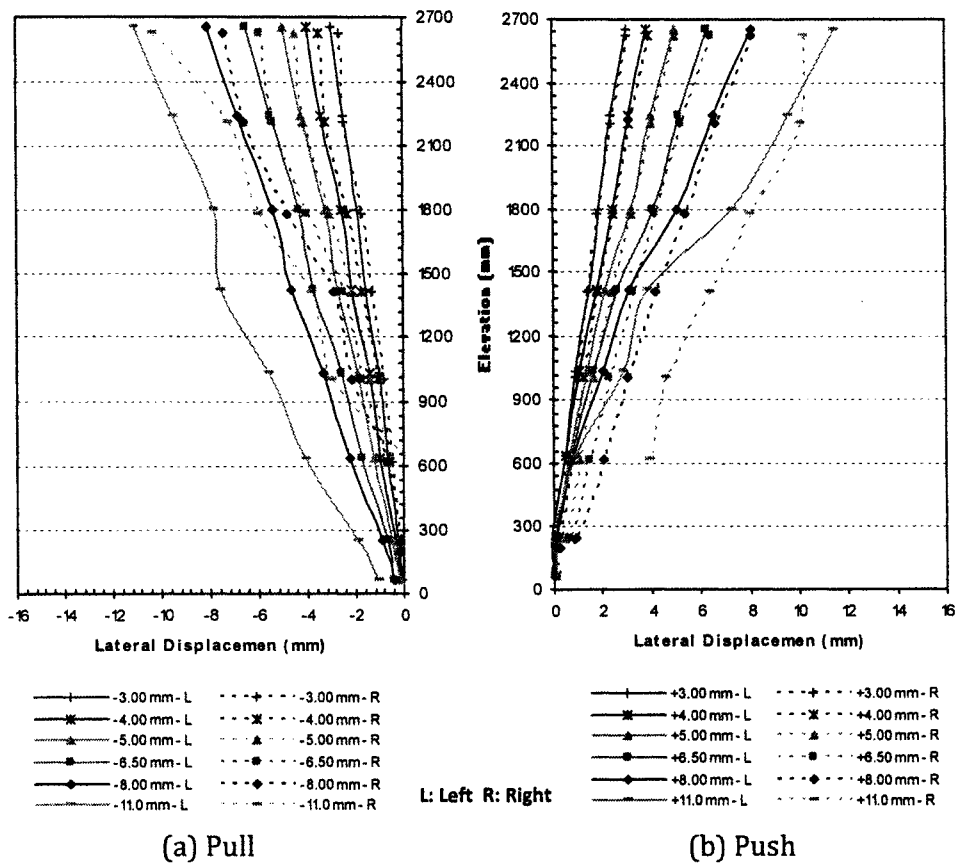
Figure 4.54 - *Lateral displacement profiles for Wall 5 at selected*
displacement level

4.3.5.4 Wall Curvature

Average curvature was measured at eight elevations over the height of the

wall as explained in Appendix E. Curvature profiles of the wall at the end of selected

loading cycles are presented in Figure 4.55. Curvature values are likely to be

affected by the cracking in the vicinity of the Demec points. The obtained profiles

indicate relatively limited rotation along the height of the wall with slightly higher

curvature near the base. This, along with the linear lateral deformation profiles

discussed in the previous section, is another sign of shear dominated deflection.
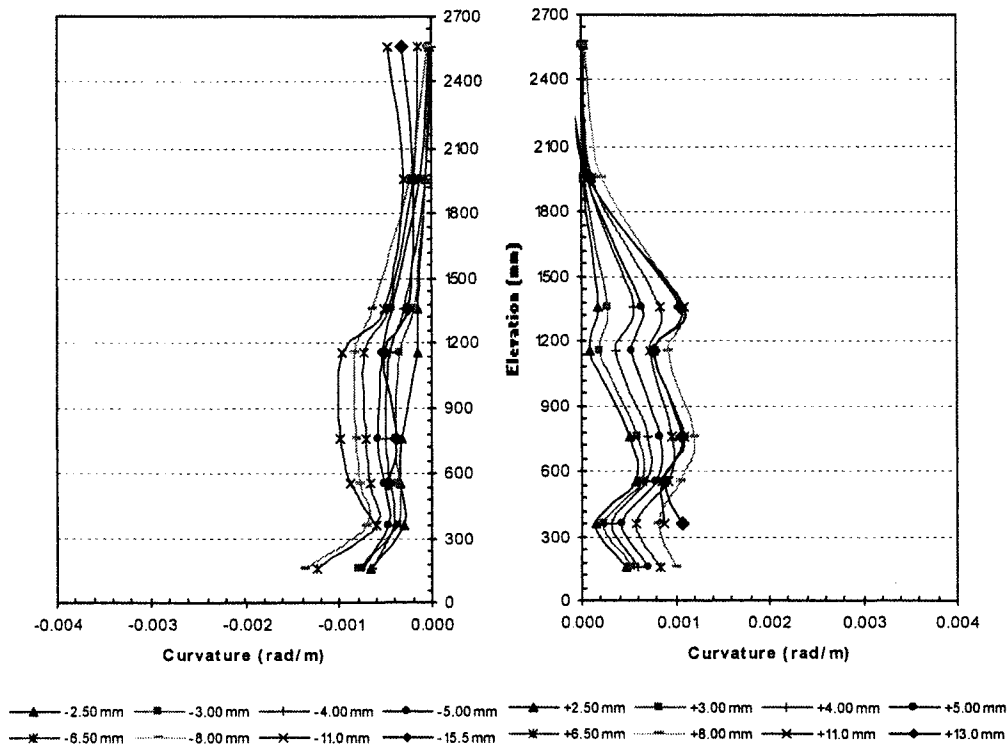
(a) Pull   (b) Push

Figure 4.55 - *Average curvature profiles for Wall 5 at selected displacement levels*

4.4 Overall Analysis of the Shear Wall Test Results

4.4.1 General Load-Displacement Response of the Test Walls

The overall responses of shear walls are compared in Figure 4.56 using the envelopes of the load-displacement hysteresis loops recorded during the test. It should be noted that the envelopes are not considered to be significantly affected by the sequence of increasing cycles of displacement or small variation of axial load during the test (Abram 1987). The vertical and horizontal steel ratios were almost the same in all test walls except Wall 3 (with 1710 mm bar spacing at half scale) which had 85% of the vertical steel ratio compared to the other walls.

As can be seen in Figure 4.56-a, Walls 1, 2 and 3, having the same aspect ratio and amount of vertical and horizontal steel with bar spacing of 855 mm (1.71 m at full scale), 570mm (1.14 m at full scale), and 1710 mm (3.42 m at full scale), respectively, showed fairly similar behaviour under the imposed lateral loading cycles. This indicates that the global response of the test walls is not very sensitive to the reinforcement pattern. In contrast, shown in Figure 4.56-b, Walls 4, 1 and 5 with aspect ratios of 0.5, 1.0 and 1.5, respectively, experienced significantly distinct reduction in maximum load carrying capacity and stiffness. However, the maximum base moments reached at the peak load increased significantly but not proportionally with the increase in aspect ratio. This indicates shear rather than flexure dominated capacity.

4.4.2 Capacity

The maximum lateral load resisted by each wall during the test is defined as
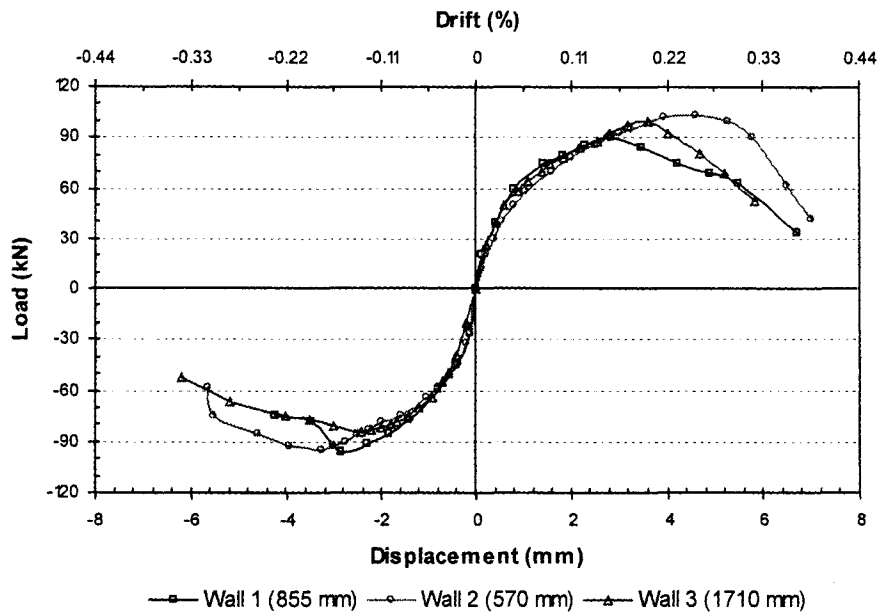
(a) Walls with an aspect ratio of one and different bar spacing
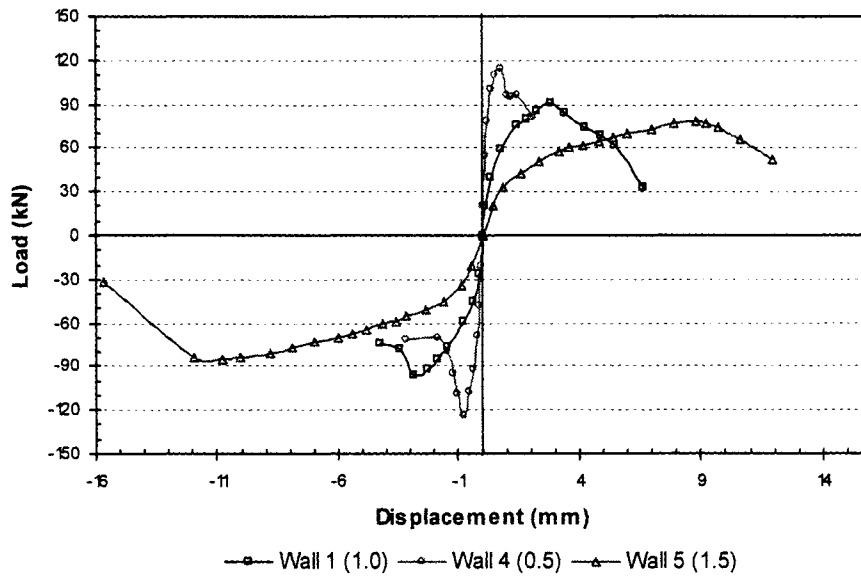
(b) Walls with different aspect ratios and similar bar spacing

Figure 4.56 – *Load-displacement envelope of the test walls*

the capacity of the wall. A summary of the predicted and measured capacities for the test walls are presented in Table 4.3. The flexural and shear capacities of the walls estimated in the design phase of the experiments were adjusted for the actual material properties measured via auxiliary tests. The average compressive strength for masonry, f'_m for all test walls was taken 12.2 MPa for the grouted masonry and 21.1 MPa for the hollow sections as determined based on the masonry prism test results presented in Section 3.3.5.5. The mechanical properties of vertical and horizontal steel bars were also adjusted according to the results of the tensile test reported in Section 3.3.5.4.

As can be seen in Table 4.3, two sets of calculations were conducted for shear capacity of the walls; one assuming 100% involvement of horizontal reinforcement and the other one assuming 60% contribution from horizontal reinforcement as

Table 4.3 – Predicted and measured values for the ultimate load

Specimen No. Bar Spacing (Aspect Ratio)	Ultimate Load				
	Predicted (kN)		Measured (kN)		Predicted / Measured*
	Flexural Strength	Shear Strength 60% Hor. Steel (100% Hor. Steel)	Push (Drift)	Pull (Drift)	
Wall 1 855 mm (1.0)	121.1	88.3 (102.9)	91.2 (0.16%)	96.9 (0.17%)	0.94 – SH 60%** 1.09 – SH 100%
Wall 2 570 mm (1.0)	115.9	97.6 (115.3)	103.7 (0.22%)	93.2 (0.20%)	0.99 – SH 60% 1.17 – SH 100%
Wall 3 1710 mm (1.0)	122.2	79.4 (91.2)	96.7 (0.21%)	84.4 (0.13%)	0.88 – SH 60% 1.01 – SH 100%
Wall 4 855 mm (0.5)	230.6	103.8 (115.7)	114.2 (0.10%)	122.9 (0.09%)	0.88 – SH 60% 0.98 – SH 100%
Wall 5 855 mm (1.5)	80.7	88.3 (102.9)	79.1 (0.33%)	84.3 (0.42%)	0.99 – F

Average strength of the wall in the push and pull directions was considered.

** *SH 60/100%: Shear dominated failure mode assuming 60/100% effectiveness for horizontal steel, F: Flexural dominated failure mode*

recommended by CSA (2004). Sample calculations for flexural and shear strength of the test walls are presented in Appendices B and C. Differences relative to using the American masonry design standards (MSJC 2008) are also addressed in Appendix D.

Shear strength predicted to be lower than the flexural strength for Walls 1, 2, 3 and 4 indicates domination of shear failure mode in the tests. This is consistent with the test observations where, except for Wall 5, none of the test walls experienced vertical bar yielding before reaching ultimate (peak) load. Wall 5 could be characterized as having a mixed shear-flexure failure mode because both tensile yielding of vertical reinforcement, and diagonal cracking and failure through the compression zone were clearly observed during the test (Section 4.3.5.1). Comparisons between calculated shear strengths and measured ultimate loads indicated very close agreement between predicted and measured strength values. This agreement for Walls 1, 2, 3 and 4 governed by shear failure mode, falls within -12% and on average within -8% where 60% contribution is considered from horizontal reinforcement and within +17% and on average within +6% where horizontal reinforcement is assumed to be 100% effective in ultimate shear resistance of the walls. This implies that the Canadian masonry design standard provides acceptable accuracy for shear predictions for this type of masonry shear wall. Wall 5, with yielding of flexural steel, also shows very close agreement with the strength prediction using CSA (2004) provisions.

The calculated first yield strengths of the test walls are presented in Table 4.4. Only Walls 2 and 5 showed tensile yielding prior to reaching ultimate load during the test. This is consistent with the higher yielding capacity which was predicted for

Table 4.4 – Predicted and measured values for the first yield load

Specimen No. Bar Spacing (Aspect Ratio)	Ultimate Load Measured (kN) Push (Pull)	First Yield Load		
		Predicted (kN) Yield Strength	Measured (kN) Push (Pull)	Predicted / Measured*
Wall 1 855 mm (1.0)	91.2 (96.9)	102.6	---**	---
Wall 2 570 mm (1.0)	103.7 (93.2)	96.6	102.7 (92.4)	0.99
Wall 3 1710 mm (1.0)	96.7 (84.4)	115.5	---	---
Wall 4 855 mm (0.5)	114.2 (122.9)	205.2	---	---
Wall 5 855 mm (1.5)	79.1 (84.3)	68.4	70.6 (73.2)	0.95

*Average strength of the wall in the push and pull directions was considered.
** No tensile bar yielding was recorded before ultimate load.

Walls 1, 3 and 4 compared to their shear strength. Wall 2 showed slightly lower first yield strength compared with its shear strength predicted assuming 60% contribution from the horizontal reinforcement. Very good agreement can be seen between the predicted and measured yield strengths for both Wall 2 and Wall 5 which confirms the accuracy of simple beam theory used for yield strength calculation at the base of the walls.

The measured lateral load resistances for Walls 1, 2 and 3, with an aspect ratio of one and reinforcement spacing of 855 mm, 570 mm, and 1710 mm, respectively, are presented in Figure 4.57-a. It can be seen from the figure that the shear capacity of the walls is not very sensitive to the spacing of the bars. This is consistent with the design code provisions for shear resistance of a masonry wall in the Canadian masonry standard CSA S304.1 (2004) where only total amount of horizontal steel bars is incorporated.

(a) Effect of bar spacing on wall capacity

(b) Effect of aspect ratio on wall capacity
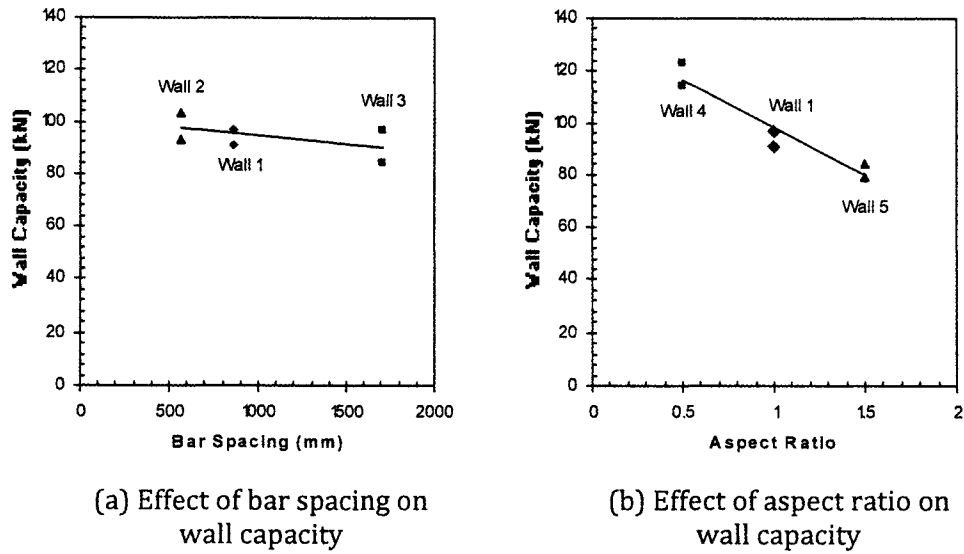
Figure 4.57 – Effect of bar spacing and aspect ratio on lateral load capacity of tests walls

Figure 4.57-b contains the ultimate capacities of Wall 1, 4 and 5 having different aspect ratios of 1.0, 0.5 and 1.5, respectively, but the same amount and distribution of vertical and horizontal reinforcement. It can be seen that the ultimate load is very sensitive to the aspect ratio of the wall with almost a linear but not proportional trend line. This can be simply explained where a given lateral load produces higher bending moment at the base of the wall with larger aspect ratio. This in turn leads to higher participation from flexural deformation.

4.4.3 Stiffness

The secant stiffnesses of the test walls under increasing top displacement are presented in Figure 4.58 with initial stiffness shown as the first data point for each wall. The stiffnesses of the test walls were nearly identical in both the push and pull
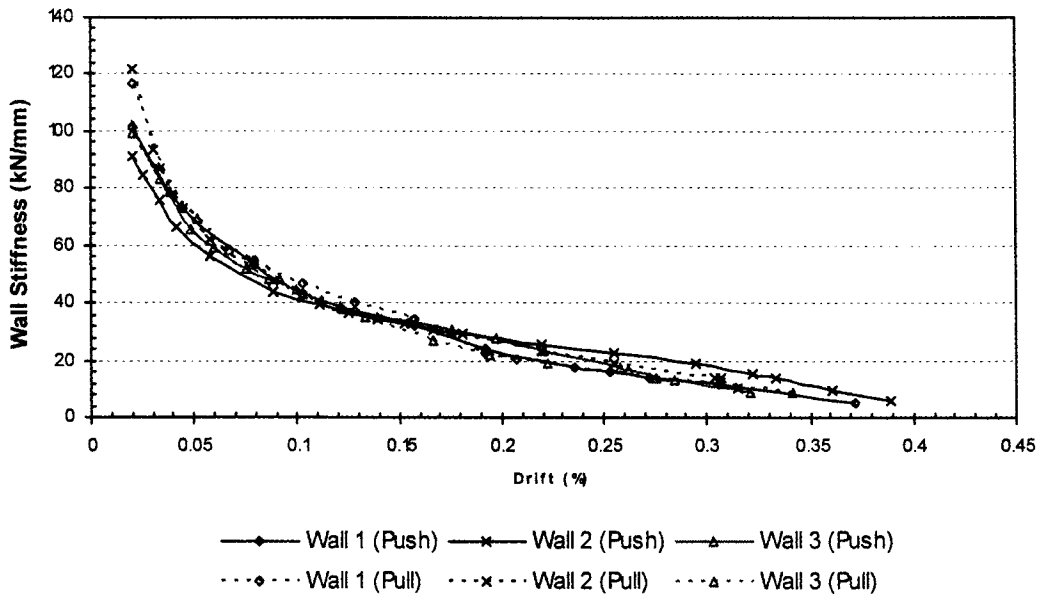
(a) Effect of bar spacing on secant stiffness
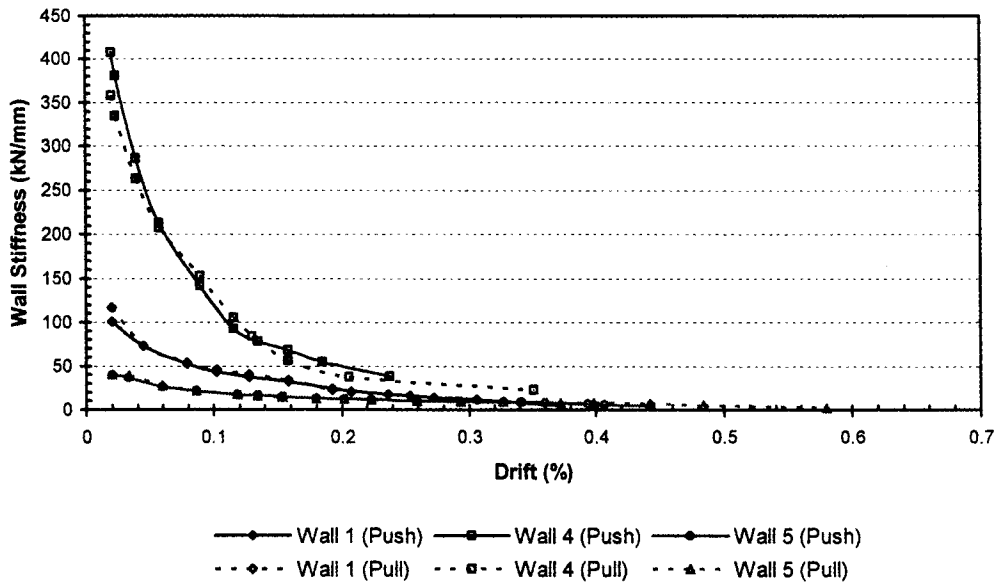
(b) Effect of aspect ratio on secant stiffness

Figure 4.58 – Secant stiffness versus lateral drift for the test walls

loading directions except for Wall 2 where, as can be seen in Figure 4.59, lower initial stiffness was observed in the push direction compared to the pull direction at low displacement levels. This was found to be odd since, as described in Section 4.3.2.1, the cracks due to accidental impact before testing were mainly in the areas effective in the pull direction indicating that the wall's load resistance and consequently its stiffness should be lower in the pull direction rather than the push direction. However, the stiffnesses for Wall 2 became identical in both directions above about 0.1% drift (1.8 mm displacement).
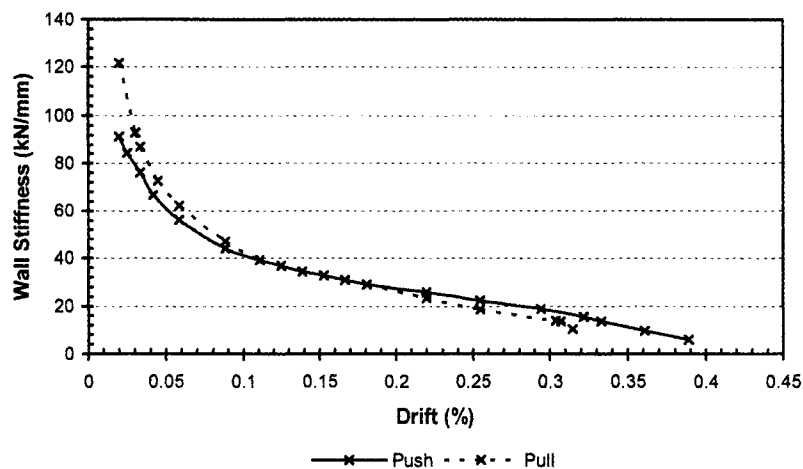
Figure 4.59 – Secant stiffness for Wall 2 in the push and pull direction of loading

As shown in Figure 4.58-a, Walls 1, 2 and 3, having different bar spacing equal to 855 mm, 570 mm and 1710 mm, respectively, showed fairly similar degradation in stiffness during the test. However, it can be seen in Figure 4.58-b that stiffness significantly increased in walls with lower aspect ratios. The increase in initial stiffnesses for Walls 4 and 1 with aspect ratios of 0.5 and 1.0, respectively, were about 9.0 times and 2.5 times, respectively, compared to Wall 5 (aspect ratio of 1.5).

These increases deviate from the expected third order flexure-based relation between aspect ratio and initial stiffness of a shear wall indicating high involvement of shear deformation in overall stiffness of this type of masonry walls.

The initial (uncracked) stiffness of the test walls, presented in Table 4.5, were estimated based on the commonly used equation in the context of design of shear walls taking into account both flexural and shear deformation. This equation is defined by:

$$K = \left(\frac{h^3}{3E_m I} + \frac{1.2h}{G_m A} \right)^{-1}$$
(4.1)

where h represents the height of wall, E_m is modulus of elasticity and G_m is modulus of rigidity (shear modulus) and is considered to be equal to $0.4E_m$. The factor 1.2 is a shape factor assuming a rectangular section for the test walls and A is the area of the wall's cross section. The modulus of elasticity for masonry was assumed to be equal to $850f_m'$ throughout the calculations in which f_m' is the

Table 4.5 – Predicted and measured values for initial (uncracked) wall stiffness

Specimen No. Bar Spacing (Aspect Ratio)	Predicted Stiffness* (kN/mm)	Measured Stiffness** (kN/mm)	Predicted Stiff. Measured Stiff.
Wall 1 855 mm (1.0)	102.4	104.0	0.98
Wall 2 570 mm (1.0)	104.4	106.6	0.98
Wall 3 1710 mm (1.0)	100.2	102.2	0.98
Wall 4 855 mm (0.5)	358.6	383.1	0.94
Wall 5 855 mm (1.5)	39.8	39.7	1.00

* *Elastic beam theory with a linear strain profile is used for calculations.*
** *The average value from the push and pulls direction is used.*

uniaxial compressive strength for masonry determined based on masonry prism test results as described in Section 3.3.5.5. Considering the different thickness and uniaxial compressive strength for grouted and hollow sections along the length of a partially grouted reinforced masonry shear wall, a transformed section based on the ratio of the moduli of elasticity was used for calculation of the moment of inertia and cross section area at both the initial and cracked loading levels. A linear strain profile along the length of the wall was assumed and the section properties were considered to be constant over the wall height.

The comparison between initial stiffness calculated using Equation (4.1) and the average secant stiffness from the push and pull loading cycles was found to be at its closest at a top displacement level corresponding to 0.02% storey drift (see Table 4.6). Excluding the accidental cracks from Wall 2, none of the test walls had shown any sign of cracking at this level of displacement.

The secant stiffnesses for the test walls were normalized with respect to the corresponding initial stiffness. The normalized stiffnesses of the walls with respect to different drift levels are presented in Figure 4.60. For a better presentation, the figure only includes the results of the push direction of loading. The point at which ultimate (peak) load was reached is also indicated in this figure. In general, all test walls showed a similar trend of stiffness degradation. Comparing similarly reinforced Walls 4, 1 and 5 with different aspect ratios of 0.5, 1.0 and 1.5, respectively, indicates a lower degradation rate for walls with higher aspect ratios which can be simply explained by more contribution from flexural deformation due

Table 4.6 – Predicted initial stiffness and the corresponding drift level measured in the test

Specimen No. Bar Spacing (Aspect Ratio)	Predicted Initial Stiffness (kN/mm)	Drift Level (%)
Wall 1 855 mm (1.0)	102.4	0.019
Wall 2 570 mm (1.0)	104.4	0.016
Wall 3 1710 mm (1.0)	100.2	0.019
Wall 4 855 mm (0.5)	358.6	0.026
Wall 5 855 mm (1.5)	39.8	0.018
Average =		0.020
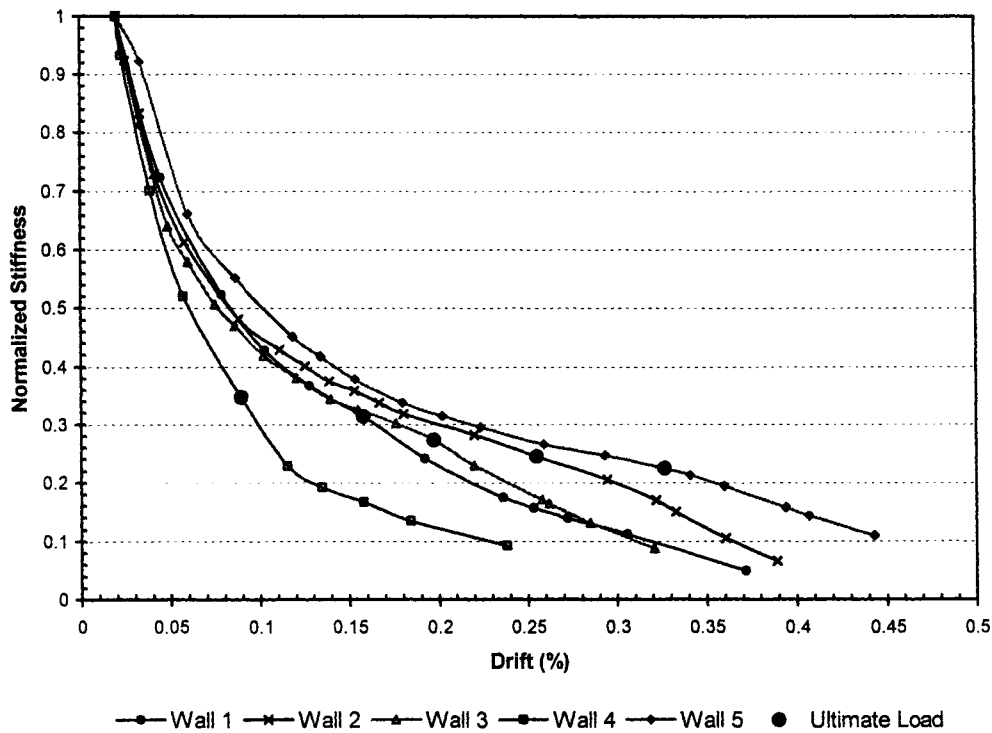
Figure 4.60 – Normalized secant stiffness versus lateral drift

to the increase in the height of the wall. It can be seen from Figure 4.60 that the stiffness for all walls decreased rapidly to about 25% - 35% of the initial stiffness at their ultimate load and to about 10% - 30% at 0.2% drift.

4.4.4 Pseudo Displacement Ductility and Load Reduction Factor

Ductility is defined as the ability of an individual structural member or a structure as a whole to provide inelastic deformation beyond the maximum lateral load carrying capacity without significant loss in strength and post-peak stiffness which leads to dissipation of the energy stored in the structure through applied loads (Drysdale et al. 1999). As a result of the energy dissipation capacity, there is usually no need for a structure to be designed for strength corresponding to expected elastic seismic load and a load modification factor is considered to reduce the seismic demands. The conceptual definition of ductility involving a well defined yield point and plastic post-yield behaviour is readily applied. However, lack of perfectly elastic-plastic behaviour has led to different methods being used to quantify this structural characteristic. Displacement ductility, μ_Δ, is considered to be one of the most commonly used measures which is defined by:

$$\mu_\Delta = \frac{d_u}{d_y} \tag{4.2}$$

where d_u is the lateral deflection at the end of the post-elastic range and d_y is the lateral deflection at yielding point where the structural member exhibits a clear plastic behaviour. Although the yielding point usually coincides with yielding of the extreme tensile reinforcements in flexural walls, the yielding point is not expected

to be well defined particularly for squat partially grouted reinforced masonry shear walls (as shown in Section 4.4.2,). Therefore, in order to evaluate the inelastic performance of the test walls, pseudo displacement ductility is introduced by representing the hysteretic behaviour of the walls with an idealised bilinear resistance envelope suggested by Tomazevic (1999). This approach and associated parameters are defined in Figure 4.61-b.

The ultimate resistance, H_u, in this method does not represent the actual but the idealised maximum experimental value. An average value of 0.9, suggested by Tomazevic (1999), is considered for H_u / H_{max} ratio. The ultimate idealised displacement, d_u, is an arbitrarily chosen displacement level and was defined where 20% strength degradation has occurred in the experimental load-displacement curve.

The initial slope of the idealised envelope (see Figure 4.61-b) is called, herein, effective elastic stiffness of the wall, K_e. An equal energy approach was used to determine the effective stiffness such that the energy dissipated based on the area
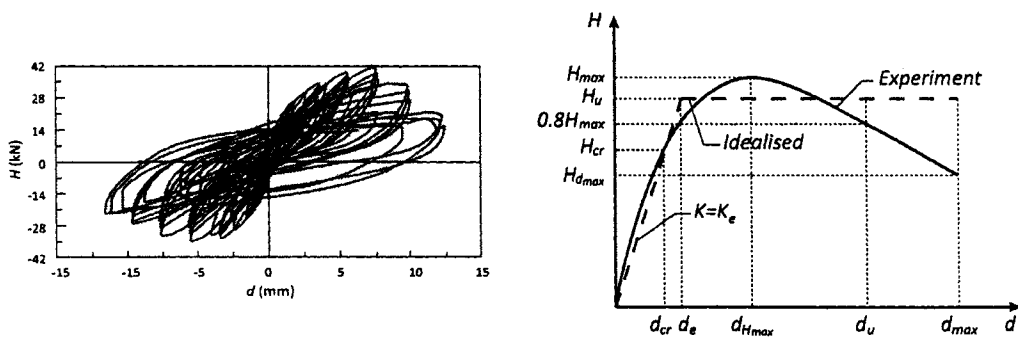
| (a) Typical load-deflection hysteresis loops | (b) Idealisation of experimental hysteresis envelope with bilinear relationship |

Figure 4.61 – Idealised bilinear envelope (from Tomazevic 1999)

under the idealised bilinear envelope gives the same amount of energy dissipated as

calculated using the area under envelope of the experimental hysteresis loops at

20% degradation in strength of the test walls.

Consequently, in the absence of a clear bilinear perfectly elastic-plastic

behaviour, the pseudo displacement ductility factor, μ_{Δ}, is defined as a ratio of:

$$\mu_{\Delta} = \frac{d_u}{d_e} \qquad (4.3)$$

where d_e is the displacement at the idealised elastic limit. The measured values of

pseudo displacement ductility and corresponding idealised effective stiffness are

presented in Table 4.7 with details of calculation presented in Appendix F. The table

also includes lateral load reduction factors calculated based on the equal energy

concept (Drysdale et al. 1999, and Paulay and Priestley 1992) defined by:

$$R = \sqrt{2\mu_{\Delta} - 1} \qquad (4.4)$$

where μ_{Δ} is displacement ductility of the structure (see Appendix F for more

details). This method is mainly used for relatively rigid structures such as masonry

buildings with a fundamental period between 0.4 and 0.8 second which is close to

the period for the peak elastic acceleration response (i.e. about 0.5 seconds for the

El-Centro Earthquake 1940). For more rare cases where structures have longer

fundamental periods, the maximum displacement that would be experienced is very

similar to that experienced by an elastic system with the same initial elastic

stiffness. Therefore, the equal maximum displacement approach is used instead

(Paulay and Priestley 1992).

Table 4.7 – Measured values for displacement ductility and load reduction factor

Specimen No. Bar Spacing (Aspect Ratio)	$\overline{K_e}$ * (Elastic Limit Drift %)	Displacement Ductility (μ_Δ)		Load Reduction Factor*** (R)	
		Push (Ult. Drift %)**	Pull (Ult. Drift %)**	Push	Pull
Wall 1 855 mm (1.0)	77.7 (0.06)	4.4 (0.25)	3.3 (0.21)	2.8	2.4
Wall 2 570 mm (1.0)	68.0 (0.07)	3.8 (0.33)	5.0 (0.30)	2.6	3.0
Wall 3 1710 mm (1.0)	76.5 (0.06)	3.4 (0.26)	5.7 (0.28)	2.4	3.2
Wall 4 855 mm (0.5)	368.8 (0.03)	6.4 (0.18)	3.6 (0.13)	3.4	2.5
Wall 5 855 mm (1.5)	22.9 (0.12)	3.8 (0.41)	3.6 (0.48)	2.6	2.5

* *Effective stiffness of the idealised bilinear envelope based on equal energy approach.*
** *Drift at ultimate displacement corresponding to 20% strength degradation.*
*** *Load reduction factor determined based on equal energy approach.*

The displacement ductilities of the test walls, presented in Table 4.7, indicate reasonably consistent values for the push and pull direction given the accuracy of displacement measurements. It can be seen from the table that all load reduction factors are greater than 2.0 which is the maximum R value currently specified in CSA S304.1 (2004) for masonry shear walls (moderately ductile masonry shear walls). This indicates that the seismic load reduction factor, R, suggested by the Canadian masonry design standard, underestimates the energy dissipation ability of partially grouted reinforced masonry shear walls despite large reinforcement spacing and generally no yielding of the tension reinforcement.

The variations of R factor with respect to wall aspect ratio including Walls 1, 4 and 5 and with respect to bar spacing including Walls 1, 2 and 3 are presented in Figure 4.62. As shown in Figure 4.62-a, the load reduction factor tends to decrease with increase of aspect ratio of the walls considering average R value of the push
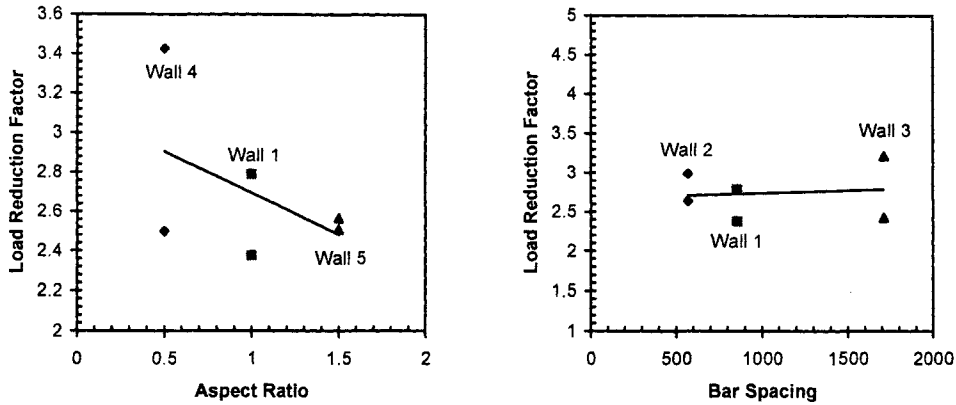
(a) Effect of aspect ratio on
load reduction factor

(b) Effect of bar spacing on
load reduction factor

Figure 4.62 – *Effect of bar spacing and aspect ratio on the seismic
load reduction factor*

and pull direction for each wall. Although tall walls would normally be expected to

have higher ductilities, the observed results may be explained by increased

possibility of shear sliding along the horizontal bed joints in the unreinforced areas

of the more squat walls. This type of failure was clearly observed during the

1.00 mm loading cycle (0.11% drift) of Wall 4 having an aspect ratio of 0.5 as

described in Section 4.3.4.1. A typical hysteresis loop for a shear sliding failure along

a single bed joint is shown in Figure 4.63. Sliding along the cracked joint, as can be

seen in the figure, provides high ability for inelastic deformation in the post-peak

regime indicating high energy dissipation capacity.

The test data presented in Figure 4.62-b shows that the load reduction factor

for the test walls slightly increased with increase in the reinforcement spacing.

Similarly, higher potential for shear sliding along the cracked bed joints with

increase in bar spacing may provide a reasonable explanation for this behaviour.
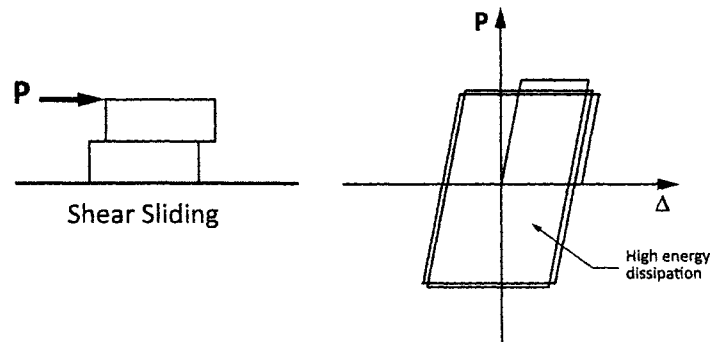
Figure 4.63 *– Shear sliding failure*

4.5   Closing remarks and Conclusion

The diagonal behaviours of masonry panels (wallettes) with and without peripheral reinforcement along the four sides of the panel and with different extents of grouting were investigated. The post-peak responses of the partially grouted wallette specimens showed two peak points in the load-deformation curves; this divided the behaviour of this type of panel into two stages. The first stage was up to initiation of the post-peak hardening behaviour and contained the first peak point which corresponded to the cracking strength. The second stage showed a reserved strength after cracking which resulted in a more ductile failure. The failure of hollow and fully grouted reinforced specimens was characterized by a sudden drop in the load with increased deformation. The shear-sliding failure mode for hollow specimens suggests that the test method may not be suitable for large unreinforced wallettes. The ultimate shear stress (calculated based on the method specified in ASTM E519 (ASTM 2002b)) decreased as the extent of grout decreased from fully grouted to partially grouted and then to hollow. Reinforcement spacing exceeding

the current Canadian masonry code limitation for seismic reinforcement (1200 mm) was also tested in this study using 1400 mm spacing. The fairly stable and ductile post-initial cracking response of the partially grouted specimens indicated potential applications of larger reinforcement spacing in so called partially grouted reinforced masonry shear walls.

The cyclic responses of the partially grouted reinforced masonry shear walls under in-plane axial and lateral loading were also documented with the main focus on the effect of reinforcement spacing and aspect ratio. The experimental data recorded during testing were analyzed and discussed with regard to key characteristics of a shear wall behaviour comprising load-displacement hysteresis loops, lateral load carrying capacity, wall stiffness and ductility. Comparisons between predicted and measured values were also presented. The following outcomes may be highlighted from the analysis of the partially grouted reinforced masonry shear wall tests:

1. The global response of the test walls is not sensitive to the reinforcement pattern whereas it is highly sensitive to the aspect ratio of the wall.

2. The behaviour of the partially grouted reinforced masonry shear walls with aspect ratio of 1.0 or less was dominated by shear failure. A mixed shear-flexure failure was observed for the wall with as aspect ratio of 1.5. Additional data is required to determine effects of axial load and steel ratio on this behaviour.

3. Close agreement was observed between the shear strengths calculated using

the Canadian masonry standard and the experimental results of the partially grouted reinforced masonry shear walls.

4. Wall capacities (resistance to lateral load) are highly dependent on the aspect ratio whereas little sensitivity was observed with respect to the reinforcement spacing.

5. The secant stiffness for all walls decreased rapidly to about 25% – 35% of the initial stiffness at the ultimate load and to about 10% - 30% at 0.2% drift.

6. The seismic load reduction factor, R, suggested in the Canadian masonry design standard, CSA S304.1 (2004), underestimates the energy dissipation ability of partially grouted reinforced masonry shear walls despite large reinforcement spacing.

7. Pseudo displacement ductility was used to replace the common definition of displacement ductility where the walls showed no clear bilinear perfectly elastic-plastic behaviour. This included the squat shear walls having an aspect ratio equal to or less than one. In general, displacement ductility increased when the aspect ratio (height to length ratio) decreased, whereas, it was not very sensitive with respect to the reinforcement spacing. Again, the extension of these findings to cover other combinations of reinforcing and axial load requires an additional evaluation.

CHAPTER 5

PREDICTION OF SHEAR WALL BEHAVIOUR USING THE TWO-PHASE MATERIAL MODEL FOR MASONRY

5.1 INTRODUCTION

The two-phase material model, proposed in Chapter 2, is evaluated in this chapter by direct comparison between the numerical and the experimental results obtained from the diagonal compression tests and the shear wall tests of this study. One of the two main purposes of this chapter is to demonstrate the ability of the model to predict the behaviour of partially grouted reinforced masonry assemblages and shear walls in terms of strength characteristics, crack pattern and load-deflection/displacement curves considering both the pre- and post-peak response. Given the high complexity existing in a masonry structure which results from the presence of a variety of constituent components and their highly nonlinear stress-strain relationships, the main focus is to verify the consistency between the numerical and experimental results.

Since none of the experiments performed in this investigation were designed to study either the effect of axial load or the amount of reinforcement in the vertical and horizontal direction, the second purpose of this chapter is to use the two phase material model to predict the behaviour of a typical partially grouted reinforced masonry shear wall under the influence of these key parameters. In addition, the effect of reinforcing two cells at the ends of a partially grouted reinforced masonry shear wall is also simulated.

5.2 GENERAL APPROACH

In numerical modelling dealing with a large number of material parameters without enough experimental evidence to evaluate them, it is common to adopt a limited set of parameters capable of providing results that closely fit the experimental load-displacement data and other behaviours. However this process is not implemented here. Instead, the parameters concerning grouted and ungrouted masonry are mostly determined based on the auxiliary tests conducted on masonry assemblages. Concerning the parameters associated with the unit-mortar interface, in the light of the previous studies by Lotfi and Shing (1994), Pluijm (1993), and Lourenco (1994 and 1996), initial values are assumed and the key parameters are calibrated based on the results of the diagonal compression tests described in Chapter 3 and Chapter 4. Then the calibrated parameters are directly used to analyze the partially grouted reinforced masonry shear walls which were constructed with the same material and technique as the diagonal compression test specimens.

For the numerical analysis, masonry units are represented by eight-noded plane stress isoparametric elements using two rectangular elements for each masonry block. Six-noded contact elements with zero thickness are used to represent the unit-mortar interface (line interface element). The constitutive relations of the elements involved in the finite element model were described previously in Chapter 2. The interface between units and mortar head joints and bed joints are modelled separately with different strength characteristics. This is because vertical head joint usually do not experiences any normal compression load after construction compared to horizontal bed joint. The lack of compression or even the presence of some tension due to shrinkage results in weaker bond between masonry and mortar along the head joint (Hamid and Drysdale, 1988). Elastic behaviour of mortar is assumed in the stiffness matrix of the interface elements.

The nonlinear constitutive relations of the materials, described in Chapter 2, are implemented in a displacement-driven finite element code developed in Visual FORTRAN Compiler as part of this study. The analyses are carried out with an indirect displacement controlled scheme, the so-called arc-length method (Crisfield 1997). The convergence criterion is based on the ratio between the norm of the displacement vector of each iteration to the norm of the total displacement vector obtained in the corresponding load increment. To achieve adequate accuracy, the ratio of convergence tolerance is set to 0.001 as recommended by other researchers (Lotfi and Shing 1991, and Hegemier and Arya 1982) and a maximum of 200 iterations is used.

5.3   MODELLING OF DIAGONAL COMPRESSION TEST (WALLETTES)

5.3.1   Finite Element Model

The wallette specimens were modeled along a global (x, y) coordinate system using 64 (8×8) eight-node elements for masonry and 84 six-node interface elements for the unit-mortar interface. Figure 5.1 shows the finite element mesh used for the partially grouted reinforced wallette specimens. Due to the continuity provided by rows and columns of grout, the effect of mortar joints between elements representing grouted masonry was eliminated by assigning a dummy stiffness with relatively high modulus of elasticity (i.e., 100 times higher than regular joints). The thickness used for masonry elements was set equal to the 90-mm-thick half-scale blocks for elements representing grouted areas and 31.2 mm for elements representing ungrouted areas. The latter indicates the total thickness of the face shells of the half-scale masonry units used in the wall construction.
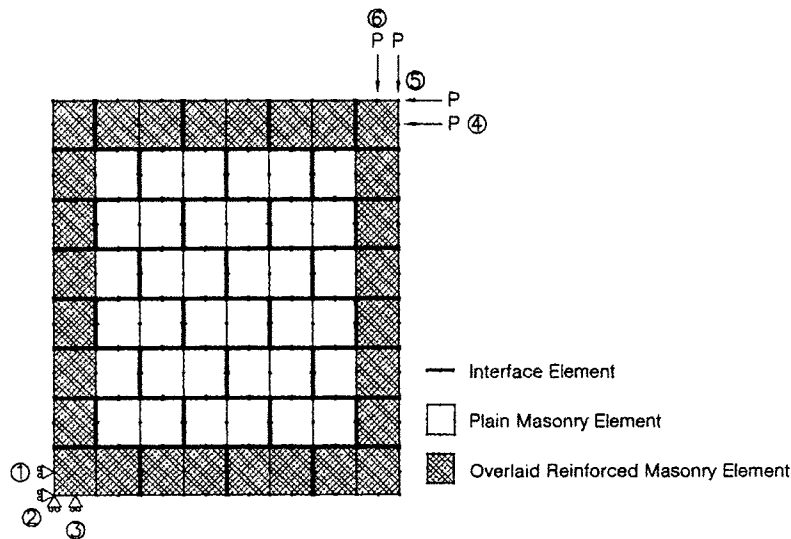
Figure 5.1 – *Finite element model for partially grouted reinforced wallettes*

In order to simulate the boundary conditions and apply the external load along the diagonal of the finite element model, three adjacent nodes (nodes 1, 2 and 3, as shown in Figure 5.1) were restrained in the x- and y-directions. The pairs of nodes 4 and 5 and nodes 5 and 6 were also constrained to have the same deformations in the x- and y- directions, respectively, with equal horizontal and vertical loads, respectively applied on each pair.

5.3.2 Material Properties

The material properties used for the masonry elements are presented in Table 5.1. The uniaxial compressive strength (f_m') and the corresponding masonry strain (ε_m) were chosen based on the results of the uniaxial compressive tests on masonry

Table 5.1 – *Material properties for masonry*
(Diagonal Compression Analysis)

Material Properties	Hollow	Grouted
f_m' (N/mm^2)	26.3	14.1
ε_m (mm/mm)	0.0013	0.0014
f_{cr} (N/mm^2)	2.65	1.4
E_m (N/mm^2)	20000	20000
v	0.16	0.16
α	0.5	0.2
β	0.1	0.1
A_o	3.65	3.65
A_1	2.0	2.0
A_2	2.0	2.0
A_3	0.1	0.1
A_4	0.6	0.6

prisms as described in Section 3.2.4.5. The tensile cracking strength of ungrouted

masonry units (f_{cr}) was determined based on the splitting tensile test carried out

by Long (2006) on the face shells of the half-scale masonry blocks similar to the

ones used in this study. This was consistent with a typical $f_{cr} = 0.1 f_{m}'$ recommended

for masonry materials (Drysdale et al. 1999). Consequently, in the absence of

splitting test results for grouted masonry units, the tensile cracking strength of

grouted masonry was assumed equal to 10% of the compressive strength observed

in uniaxial compression test of grouted masonry prisms. The constitutive

parameters concerning the stress-strain relationship and biaxial strength envelope

of masonry (A_0 , A_1 , A_2 , A_3 , A_4 , α , and β) were adopted from other similar studies

(Ewing et al. 1990, Maleki et al. 2005).

A thorough investigation of the bond characteristics at the masonry unit-

mortar interface along with the related parameters involves a more comprehensive

experimental program than was feasible in the limited timeframe of this study.

Therefore, the properties of the mortar joints were calibrated based on previous

studies (see Table 5.2) on bond properties of mortar joints and masonry units.

Accordingly, both the initial tensile strength, s_0 , and cohesive strength, r_0 , of the

unit-mortar interface elements were chosen to be 0.8 MPa for bed joint and 0.6 MPa

for head joints. Initial shear friction coefficients of 0.95 and 0.75 were also used for

bed joint and head joints, respectively, with post-slip residual values equal to 0.60

and 0.45, respectively. The chosen values are not the best fit of the experimental

results but, as indicated in Table 5.2, they are in the vicinity of the bond properties

Table 5.2 – *Mortar joint properties from experimental studies on mortar bed joint shear strength (from Atkinson et al. 1989)*

Source	Unit	Mortar Mix*	Cohesion (MPa)	Friction Coeff.	Tensile Bond Strength (MPa)	Normal Stress Range (MPa)
Atkinson & Amadei	New Clay Units	1:1.5:4.5	0.811 0.037(R)**	0.745 0.747(R)	-	0-4
Hegemier et al.	Concrete Block	Type S	0.25	0.89	-	0-2.75
Stockl and Hofmann	Clay Brick	1:0.68:15	0.95	0.7	-	0-2.4
Pook et al.	Concrete Block	Type S	0.76	0.7	-	0-1.6
Nuss et al.	New Clay Units	1:2:9	1.10	0.77	-	0.7-6.3
Pieper	Clay	1:2:8	0.20	0.84	-	0-1.2
Drysdale et al.	Clay Brick	1:0.5:4	0.57	0.90	-	0-14
Rob van der Pluijm	Wire Cut Brick	1:0.5:4.5	1.85	0.97	1.43	0.1-1
	Red Mud Brick	1:0.5:4.5	0.85	1.22	0.35	0.1-1

* *cement:lime:sand by volume*
** *(R): Residual value*

obtained for Type S mortar joint and concrete block units which were used in this

study as well. The remainder of the parameters, defining the shape of the yield and

plastic potential surfaces along with the softening rules, were adopted from Lotfi

and Shing (1994). Similar to other studies (Lourenco and Rots 1997, Mehrabi and

Shing 1997), the elastic properties of the mortar were adjusted to reproduce the

initial stiffness results of the wallette tests. A summary of the parameters used in

the numerical model is presented in Table 5.3.

Table 5.3 – Material properties for mortar joints

Joint Properties	Bed Joints	Head Joints
D_{nn} (N/mm²/mm)	400	400
D_{tt} (N/mm²/mm)	200	200
s_0 (N/mm²)	0.8	0.6
r_0 (N/mm²)	0.8	0.6
r_r (N/mm²)	0.035	0.035
μ_0	0.95	0.75
μ_r	0.60	0.45
α, β (mm/N)	11.4	11.4
η	0.1	0.2
$G^f_{min} \times 10^{-3}$ (N.mm/mm²)	0.8	0.45
$G^f_I \times 10^{-3}$ (N.mm/mm²)	4.0	2.25
$G^f_{II} \times 10^{-3}$ (N.mm/mm²)	40	22.5

For reinforcing steel bars, the yield stress and corresponding strain as well as

elastic modulus, presented in Table 5.4, were based on the tensile test results

previously reported in Section 3.2.4.4. The effect of buckling of steel bars due to

axial compression was neglected for modelling of diagonal compression tests.

Table 5.4 – *Geometric and mechanical properties used for steel elements (wallette tests)*

Bar Type	Area (mm²)	E_s (GPa)	f_y (MPa)	ε_y (mm/mm)
No. 3 (USA Size)	71	201	485	0.0024

5.3.3   Comparison of Numerical vs. Experimental Results

A comparison between numerical and experimental load-deformation curves for diagonal compression testing of the masonry wallettes is shown in Figure 5.2. Except for the hollow specimens, the experimental behaviour is satisfactorily simulated and the maximum load carrying capacity of the wallettes is estimated within a 5% range of the experimental results. The failure load for hollow specimens is overestimated by 40% in the numerical model. As will be discussed later in this section, this discrepancy may be associated with a different failure mode observed in the numerical analysis compared to the tests. The post-peak response of fully grouted reinforced samples and especially the hardening behaviour in the partially grouted reinforced specimens are distinctly reproduced by the finite element model.

The crack patterns predicted by the numerical model together with the observed crack patterns are presented in Figure 5.3. The numerical results include the tensile cracking in masonry units, bond failure in interface elements and crushing of masonry. Crushing was assumed to occur when the principal compressive strain at integration points of an element reached the strain at peak compressive stress of the masonry. According to the numerical results, the failure mode of the fully grouted reinforced model was distinctly initiated by vertical

cracking and crushing of masonry blocks along the full length of the compressive

diagonal which is consistent with the experimental crack pattern. Under increasing

deformation, crushing started and progressed in the direction of the loading path

(compressive diagonal) until maximum resistance of the specimen was reached. A

collapse mechanism then rapidly formed with propagation of crushing along the full

length of the vertical diagonal followed by numerical instability in the finite element

(a) W-G Series (Grouted)   (b) W-PG Series(Partially Grouted)

(c) W-H Series (Hollow)
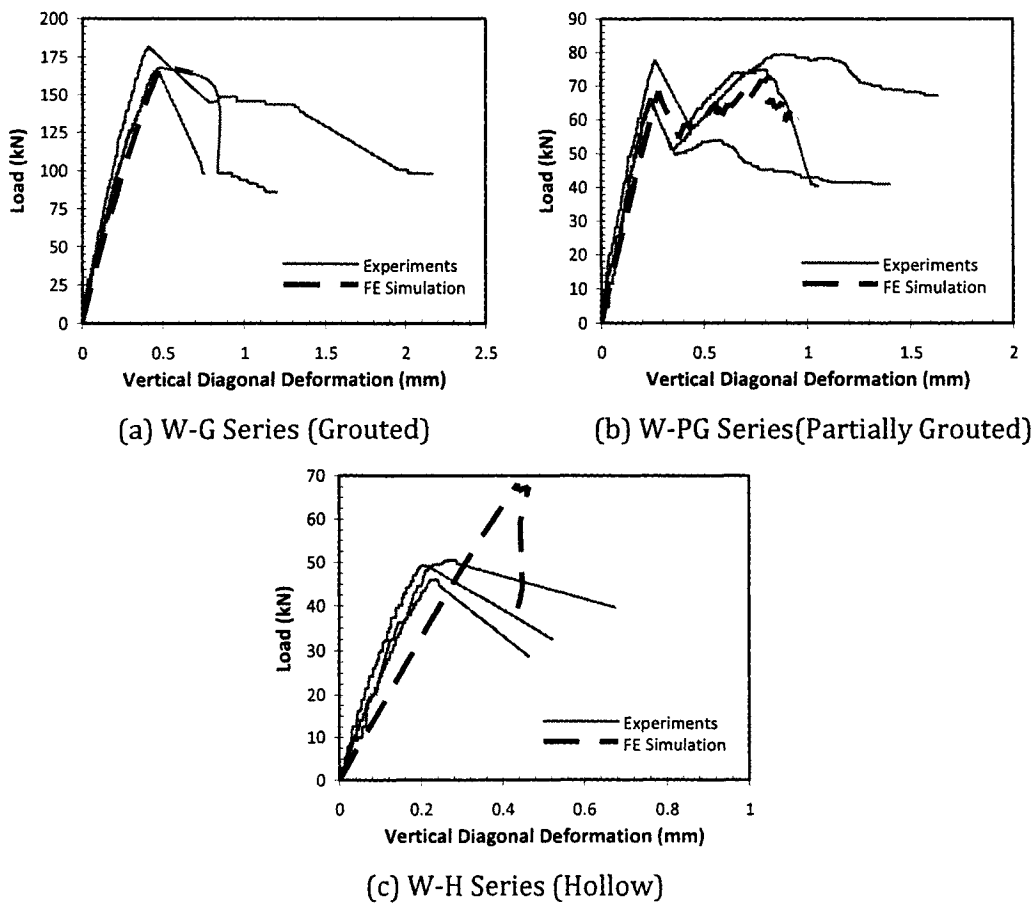
Figure 5.2 – *Finite element simulation vs. experimental load-deformation
responses of masonry wallettes*
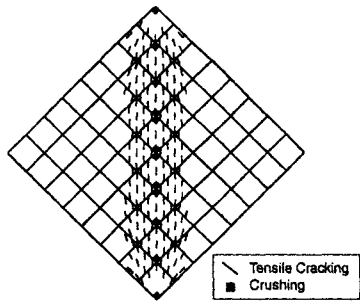
(a) W-G Series (FE Simulation)
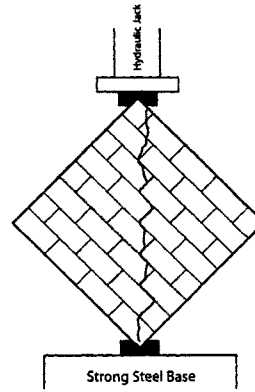
(b) W-G Series (Experiment)
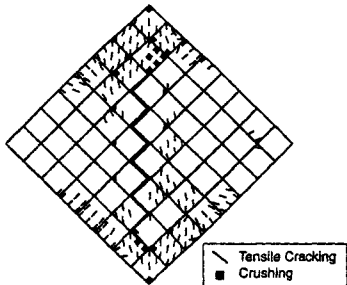
(c) W-PG Series (FE Simulation)
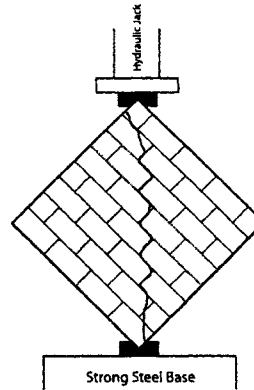
(d) W-PG Series (Experiment)
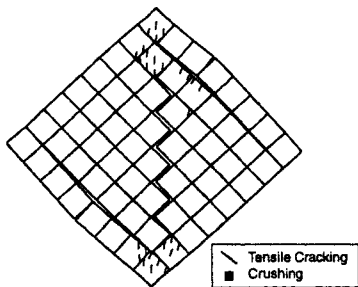
(e) W-H Series (FE Simulation)
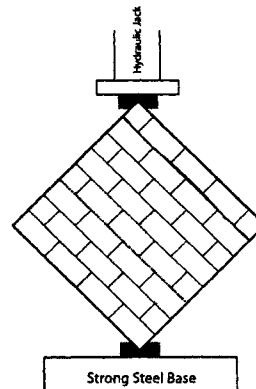
(f) W-H Series (Experiment)

Figure 5.3 – *Finite element simulation vs. experimental crack pattern (wallette tests)*

solution. This explains why the load-deflection curve for the fully grouted reinforced

wallette terminated shortly after reaching the peak load in Figure 5.2-a.

The first peak load in the predicted load-deflection curve in Figure 5.2-b for

the partially grouted reinforced specimen corresponds to the formation and

opening of the stepped pattern crack along the vertical diagonal and the second

peak load coincides with crushing of the loading corners. Despite the significant

variability in the post peak response of the tested wallettes, this behaviour agrees

very well with the overall trend in the experimental observations.

The failure of the hollow specimens in the finite element model started by

shear sliding along the mortar bed joints closest to the loading corners followed by

initiation and opening of the stepped pattern cracks along the compression

diagonal. However, no diagonal stepped cracking was observed in the test

specimens after failure. The observed experimental behaviour might be considered

odd since, despite the expected weaker failure path along the compression diagonal,

a crack developed along the top bed joint. Absence of perimeter confinement and

weaker joints on the top due to less overhead weight during construction could be

an explanation of this preferential failure location.

5.3.4   Effect of Reinforcing Steel

The effect of reinforcing steel bars on the behaviour of partially grouted

reinforced specimens was evaluated using the developed numerical model. Figure

5.4 contains a comparison of the same partially grouted reinforced specimen used in

the experiment with an unreinforced model and a model with double the amount of

reinforcement. No significant contribution of the reinforcement was observed

before onset of diagonal cracking. However, after cracking, the steel bars serve as

the main confining elements and provide resistance against diagonal deformation.

Furthermore, as shown in Figure 5.4, the resulting post-peak strength is highly

dependent on the amount of reinforcing steel.
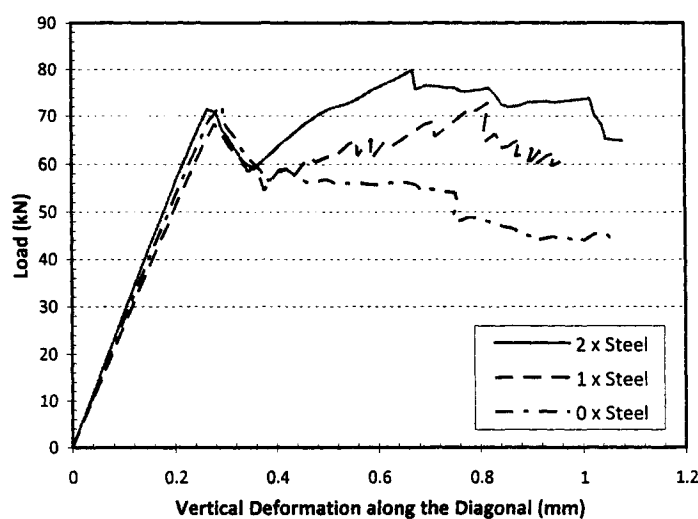
Figure 5.4 – Effect of amount of steel on behaviour of partially grouted wallettes

5.4 MODELLING OF SHEAR WALL TESTS

5.4.1 Finite Element Model

The finite element model for Wall 1, as a typical model used to simulate the

behaviour of partially grouted reinforced masonry shear walls with aspect ratio of

one, is illustrated in Figure 5.5. Walls 1, 2 and 3 were modelled using 380 (20×19)

eight-node elements for the masonry and 541 six-node interface elements for

mortar head and bed joints. Walls 4 and 5 were modelled using 209 (11×19) and

551 (29×19) masonry elements and 289 and 793 six-node interface elements,

respectively. Consistent with the previous studies (Lotfi and Shing 1991 and 1994,

and Lourenco 1996), each masonry block was modelled using two identical

rectangular elements. Further analysis for the sensitivity of numerical results with

respect to the element size is provided is Section 5.5.6. As can be seen, the top row

of elements follows the pattern of masonry elements. However, the properties of the

top row of elements for each wall together with the "mortar head joints" between

these elements were modified to represent the effect of the relatively rigid loading

beam actually utilized in the experiments. These loading beam elements were

assumed to behave in a linear elastic manner with a relatively high dummy value for

the elastic moduli (i.e. 100 times higher than masonry elements). The top nodes

were also programmed to have equal displacement in the x-direction. The lateral

and axial loads were applied to the top of the masonry elements representing the

last course of the shear wall's finite element model. Perfect contact between the

shear wall and the concrete base was assumed in the model. Accordingly, all of the

nodes at the bottom of the finite element model at the bottom of concrete base were

restrained against displacements in both the x- and y-directions.

—— Interface Element

☐ Plain Masonry Element

▦ Overlaid Reinforced Masonry Element

■ Relatively Rigid Element
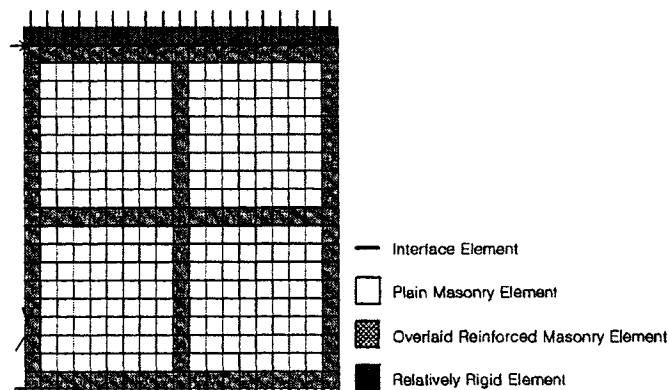
Figure 5.5 - Finite element model for Wall 1

The first load increment of the analysis was set only to account for the initial deformation due to superimposed axial compression. Subsequently, the total axial load was maintained constant and lateral load were applied incrementally.

5.4.2 Material Properties

The same material properties and constitutive parameters used for the simulation of the diagonal compression tests were used for the shear wall tests. Only the uniaxial compressive strength and corresponding strain, masonry tensile cracking strength and reinforcement properties were modified according to the auxiliary test described in Sections 3.3.5.4 and 3.3.5.5. The parameters related to the effect of bucking of reinforcing steel bars in the compression zone were also determined based on the uniaxial compression tests on reinforced masonry prisms reported in Section 2.4. According to the test results (Figure 2.13), a value of $\varepsilon_b = -2.5\varepsilon_y$ was used as the initial buckling strain and the degradation rate was set to $A_s = -640$ MPa. The buckling was also assumed to be completed in a strain interval of $\Delta_b = 2.5|\varepsilon_b|$. The material parameters used for the masonry are summarized in Table 5.5. The geometric and mechanical properties of steel bars obtained from the tensile tests presented in Section 3.3.5.4 are listed in Table 5.6.

5.4.3 Numerical vs. Experimental Results

5.4.3.1 Shear Walls 1, 2, and 3 (aspect ratio $h/\ell = 1$)

The ultimate load carrying capacity and corresponding lateral top displacement of Walls 1, 2 and 3 predicted by the numerical model along with the values measured during the tests are presented in Table 5.7. The numerical and

Table 5.5 – *Material properties for masonry in the shear wall tests*

Material Property	Hollow	Grouted
f_m' (N/mm²)	21.1	12.0
ε_m (mm/mm)	0.0013	0.0013
f_{cr} (N/mm²)	2.65	1.2
E_m (N/mm²)	20000	20000
v	0.16	0.16
α	0.5	0.2
β	0.1	0.1
A_o	3.65	3.65
A_1	2.0	2.0
A_2	2.0	2.0
A_3	0.1	0.1
A_4	0.6	0.6
A_5	-	-640
ε_b	-	$2.5\varepsilon_y$
Δ_b	-	$2.5\varepsilon_y$

Table 5.6 – *Geometric and mechanical properties used for steel elements in the shear wall tests*

Bar Type	Area (mm²)	E_s (GPa)	f_y (MPa)	ε_y (mm/mm)
No. 10 (CND Size)	100	201.6	491.7	0.0024
No. 3 (USA Size)	71	201.0	485.0	0.0024
No. 4 (USA Size)	126	201.8	564.7	0.0028
D3 (USA Size)	19.4	183.6	743.7	0.0041
D4 (USA Size)	25.8	198.2	690.7	0.0035

Table 5.7 – *Numerical and experimental results for Walls 1, 2 and 3*

Shear Wall (Bar Spacing)	Property	Numerical	Experiment		Num. / Exp.	
			Push	Pull	Push	Pull
Wall 1 (855 mm)	Ultimate Load	94.71 kN	91.2 kN	96.9 kN	1.04	0.98
	Top Disp.	2.42 mm	2.88 mm	2.88 mm	0.84	0.84
Wall 2 (570 mm)	Ultimate Load	96.73 kN	103.7 kN	93.2 kN	0.93	1.04
	Top Disp.	2.40 mm	4.50 mm	3.24 mm	0.53	0.74
Wall 3 (1710 mm)	Ultimate Load	91.53 kN	96.7 kN	84.4 kN	0.95	1.08
	Top Disp.	3.49 mm	3.60 mm	2.34 mm	0.97	1.49

experimental load-displacement curves for the walls having an aspect ratio (h/ℓ) of one are shown in Figure 5.6. The envelopes of the hysteresis cycles have been implemented as the experimental load-displacement curves.

As can be seen in Figure 5.6, satisfactory agreement exists between the simulated load-displacement responses of Walls 1, 2 and 3 and the actual behaviours during the tests. The ultimate strengths of the walls, presented in Table 5.7, indicate that wider bar spacing corresponds with slightly lower wall strength. It can also be seen that less than 10% difference exists between the numerical estimations and the measured values. A stiffer pre-peak numerical model response is observed in the load-displacement curve for Wall 2 (Figure 5.6-b) compared to the test results. This is believed to have been caused mainly by the accidental damage of this wall prior to testing. Details of the accidental loading and the resulting cracks were reported in Section 4.3.2.1.

(a) Wall 1

(b) Wall 2

(c) Wall 3
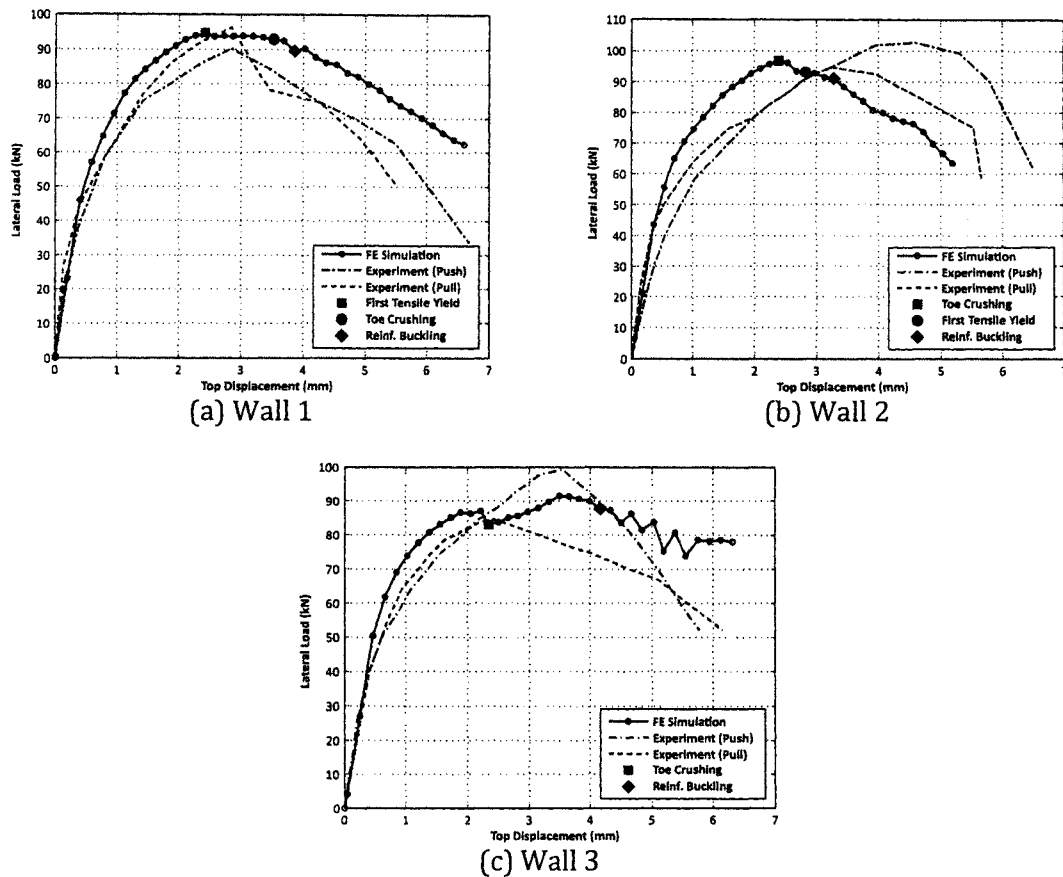
Figure 5.6 – *Experimental and finite element load-displacement responses for the shear walls having aspect ratios* $h/\ell = 1.0$

The simulated post-peak crack patterns at 80% of the peak load (after failure) along with the experimental observations are shown in Figure 5.7. Crushing of masonry and yielding and buckling of steel bars are also shown in the figures. It should be pointed out that the deformations are highly exaggerated for better presentation. The virtual discontinuity along the horizontal cracks at the bottom of the wall is due to using relatively rigid interface elements representing mortar bed joints in the grouted-reinforced areas. However, the effect of horizontal cracks is reflected in the vertical deformation of the involved masonry elements.
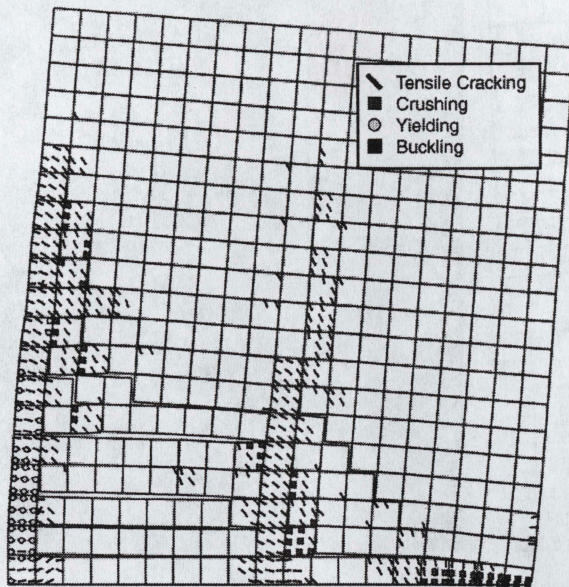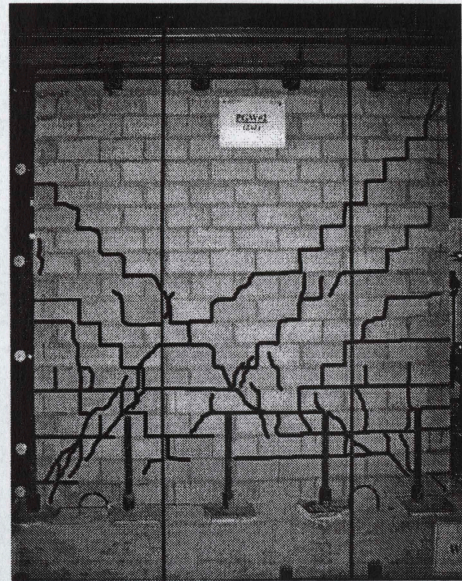
Finite Element Results · Experiment

(a) Wall 1
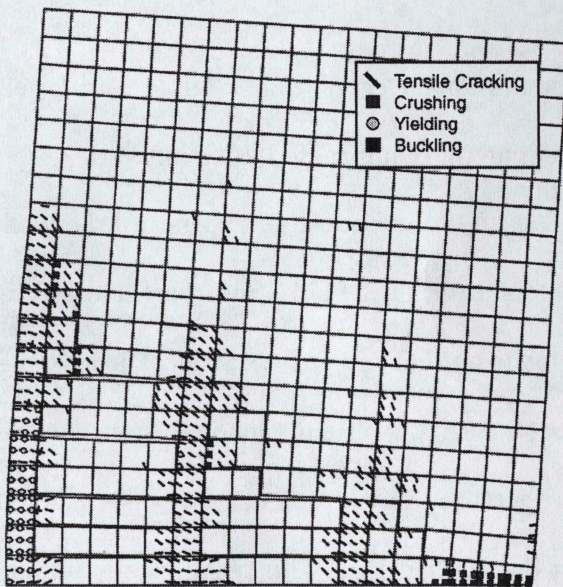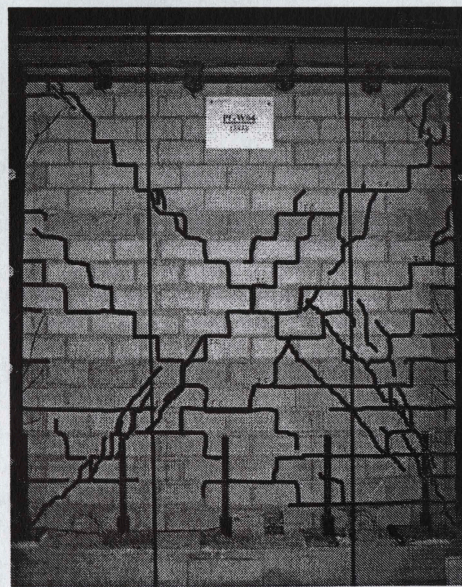
Finite Element Results · Experiment

(b) Wall 2

Figure 5.7 – *Numerical and experimental post-peak cracking and other deformations at approximately 80% of peak load (to be continued)*

| Finite Element Results | Experiment |
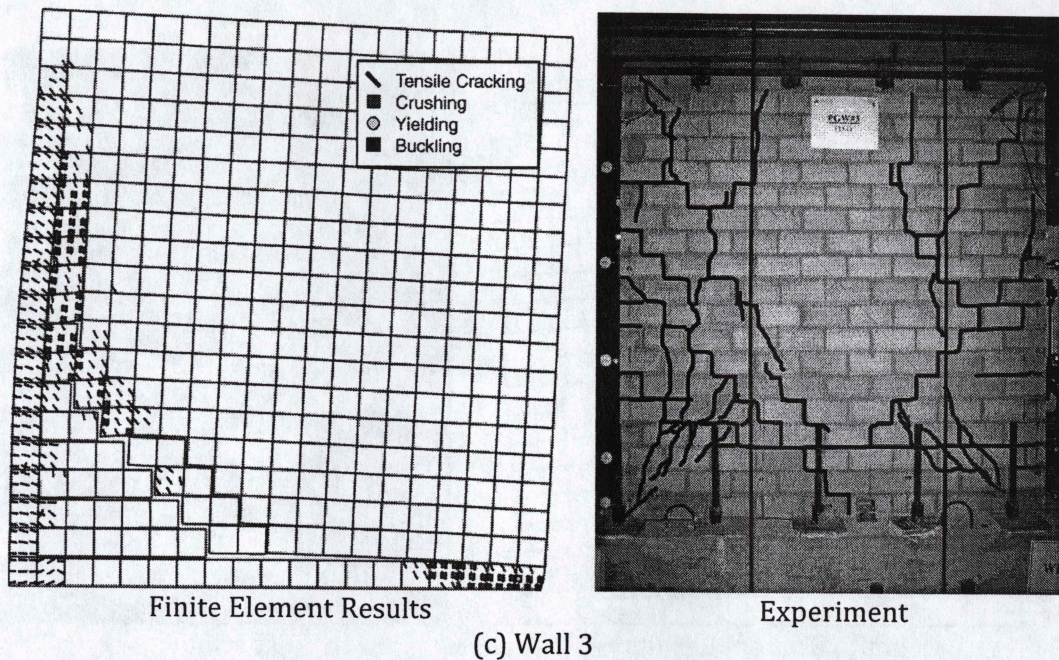
(c) Wall 3

Figure 5.7 – *(Continued)*

The numerically predicted diagonal stepped cracks for Walls 1 and 2 fell inside the unreinforced portion containing the compressed toe. In Wall 3, the stepped-cracks initiated and progressed close to the bottom left corner of the wall. Due to the large spacing of reinforcement in Wall 3 (1710 mm bar spacing), a sudden widening of the stepped-cracks led to a predicted post-peak local drop in the lateral load resistance of the wall to about 94% of the ultimate load resistance of the wall (see Figure 5.6-c). However, with increased displacement, the wall regained this resistance and continued resisting the applied load. The resistance gradually increased to a slightly higher value than the previously predicted peak resistance. Then resistance decreased as the compressive toe of the wall crushed and the embedded vertical reinforcement buckled as a result of high compressive strain.

The simulated crack patterns for Walls 1, 2 and 3 (having an aspect ratio of one) may appear to be very limited compared to the extensive pattern of stepped cracks observed in the tests. This may be caused by overestimation of the bond strength characteristics of the masonry unit and mortar joints in the finite element model. Further sensitivity analysis concerning this parameter is presented in Section 5.3.3.4.

In the finite element simulation of the Wall 1 test, buckling of the compressive steel bar, located in the bottom right corner masonry element, started shortly after reaching the maximum load resistance of the wall (after approximately 5% load degradation). At approximately 4 mm top displacement, crushing covered the bottom 2/3 of integration points of the bottom right corner masonry elements (Figure 5.7). This agrees fairly well with the average top displacement at which the same level of damage was observed at both toes of the actual test wall (see Figures 4.8 and 4.9). Similar agreement was also observed for Wall 2 and Wall 3.

The finite element analyses of Walls 1, 2 and 3 predicted fairly similar failure modes for each wall. Horizontal tensile cracking started to propagate at the bottom courses of the walls at about 50% of the ultimate load. The failure modes of the walls were characterized by crushing of the compression toes and buckling of compressive reinforcing steel bars followed by widening of joint cracks.

5.4.3.2   Shear Wall 4 (aspect ratio $h/\ell = 0.5$)

The numerical and experimental load-displacement curves for Wall 4, having an aspect ratio of 0.5, are presented in Figure 5.8. In general, the experimental

behaviour up to the peak load is reasonably simulated by the finite element model.

Better agreement in terms of overall response of the wall was observed for the push

direction compared to the pull direction. It should be mentioned that, as previously

discussed in Section 4.3.4.1, due to some problems associated with displacement

monitoring during the pull direction of loading, the experimental results associated

with the post-peak regime are more reliable in the push direction than in the pull

direction. As can be seen, much more rapid post-peak degradation of strength was

observed in the test results. Possible causes will be discussed when reviewing the

predicted crack pattern. In terms of ultimate load, Table 5.8 indicates very close

agreement between the numerical prediction and experimental measurements for

Wall 4.
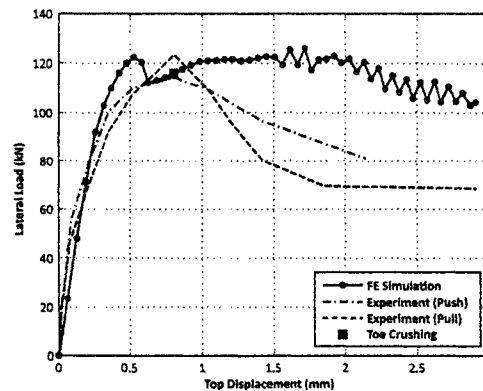
Figure 5.8 – *Experimental and finite element load-displacement
response for Wall 4 (aspect ratio h/ℓ = 0.5)*

Table 5.8 – *Numerical and experimental results for Wall 4*

Shear Wall (Bar Spacing)	Property	Numerical	Experiment		Num. / Exp.	
			Push	Pull	Push	Pull
Wall 4	Ultimate Load	122.3 kN	114.2 kN	122.9 kN	1.07	1.00
(855 mm)	Top Disp.	0.52 mm	0.80 mm	0.81 mm	0.65	0.64

The post-peak cracking pattern and other damage simulated by the numerical model at a residual (post-peak) strength of 90% of the peak load along with experimental observations are illustrated in Figure 5.9. The predicted first sudden drop in load (at 0.52 mm top displacement) corresponds to the onset of the predicted crack pattern of the wall consisting of fairly symmetric shear-slip failure at the top-left and the bottom-right corners and a stepped-pattern crack intersecting the middle grouted reinforced section of the wall. Predicted failure of the wall occurred as a result of the crushing of top-left and bottom-right corners at a large displacement level. Progression of shear-slip failure combined with widening of diagonal stepped cracks resulted in larger inelastic deformation after the peak point and delayed complete failure of the wall. However, the significant amount of shear-slip predicted in the numerical simulation was not observed in the actual test. This could be explained by the fact that the transverse shear resistance due to clamping action of the vertical reinforcing steel bars were neglected in the numerical model. Thus, bars did not provide resistance against progression of shear-slip failure along the fractured bed joints leading to prediction of large displacements during the post-peak loading.

No major yielding or buckling of steel bars was detected in the finite element model of the wall which is consistent with experimental observations and the shear dominated failure mode for this wall.
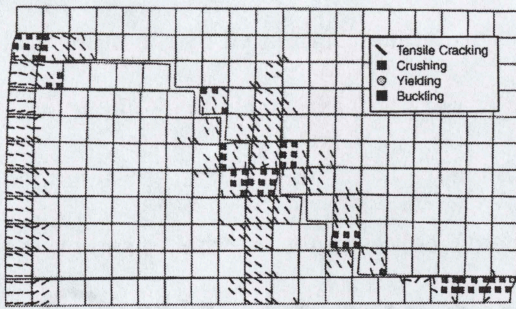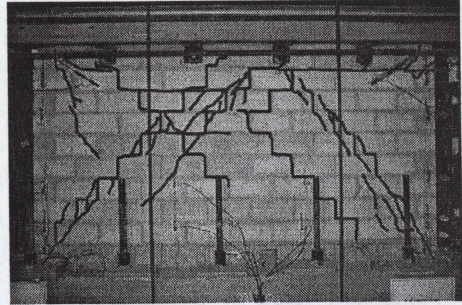
Finite Element Results   Experiment

Figure 5.9 – *Numerical and experimental post-peak cracking and other deformations at approximately 80% of the peak load for Wall 4 (aspect ratio $h/\ell = 0.5$)*

5.4.3.3 Shear Wall 5 (aspect ratio $h/\ell = 1.5$)

The numerical and the experimental load-displacement responses for Wall 5 having an aspect ratio of 1.5 are presented in Figure 5.10. The post-peak cracking pattern and other damage simulated by the numerical model at 80% of the peak load (after failure) along with experimental observations are presented in Figure 5.11. A comparison between the numerical and experimental results for Wall 5 in terms of onset of the first horizontal crack, first yield and ultimate load is presented
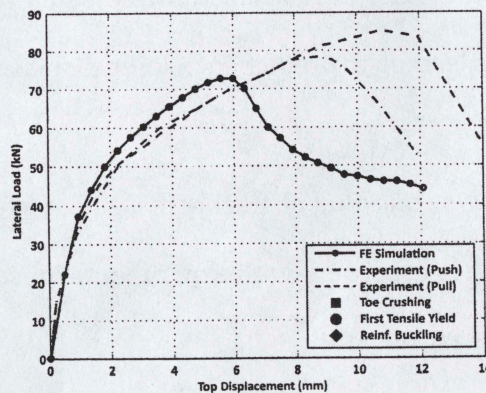
Figure 5.10 – *Experimental and finite element load-displacement response for Wall 5 (aspect ratio $h/\ell = 1.5$ - Experimental curves coincide in the push and pull directions)*

<center>Finite Element Results   Experiment</center>
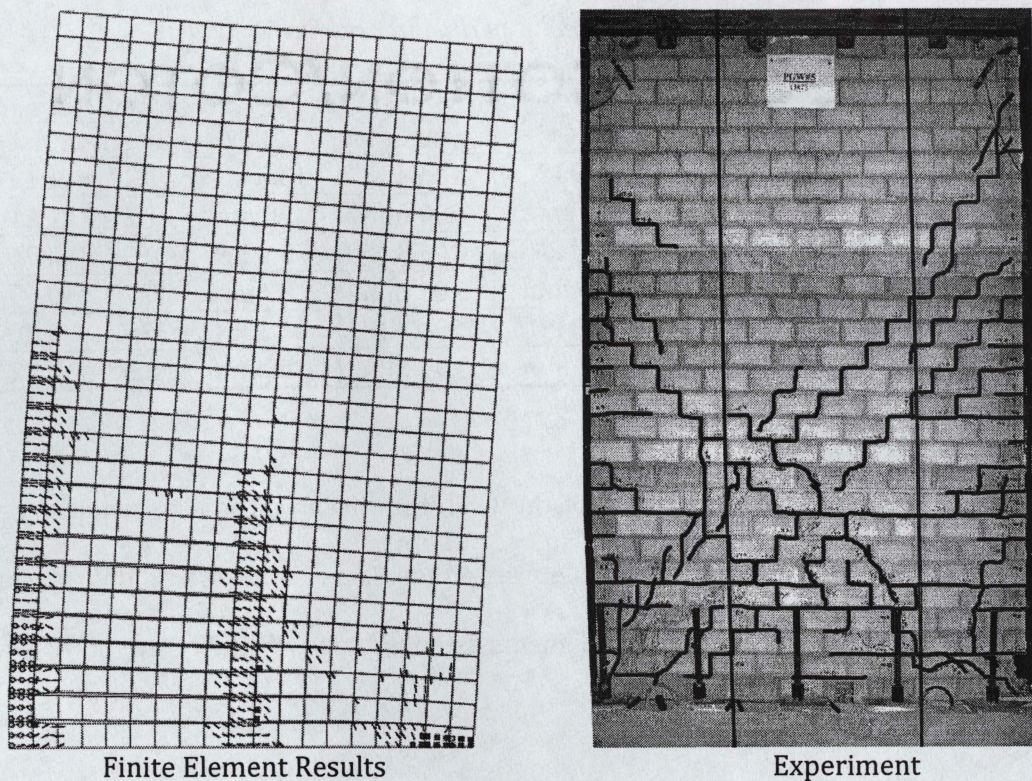
Figure 5.11 – *Numerical and experimental post-peak cracking and other deformations at approximately 80% of peak load for Wall 5 aspect ratio h/ℓ = 1.5)*

in Table 5.9. Overall, the trends of the experimental and numerical responses are fairly similar. The load-displacement, obtained from the finite element simulation, shows better agreement with experimental results in the push direction compared to the pull direction. As can be seen, the numerical results indicate an average of 11% lower ultimate load carrying capacity. Given the variability in the properties of constituent materials, this difference is considered to be acceptable. It is also important to recognize that the numerical analysis does not include the effects of either reversed loading or cumulative damage due to many cycles of loading.

Table 5.9 – *Numerical and experimental results for Walls 5*

Properties for Wall 5		Numerical	Experiment		Exp./Num.	
			Push	Pull	Push	Pull
First Hor. Crack	Load	49.9 kN	40.9 kN	43.5 kN	1.22	1.15
	Top Disp.	1.81 mm	1.50 mm	1.50 mm	1.21	1.21
First Yield	Load	70.0 kN	70.5 kN	73.2 kN	0.99	0.96
	Disp.	4.76 mm	6.03 mm	6.87 mm	0.79	0.69
Ultimate Load	Load	72.8 kN	79.1 kN	84.3 kN	0.92	0.86
	Disp.	5.58 mm	8.91 mm	10.8 mm	0.63	0.52

In the finite element model of the wall, the maximum load resistance was reached just before crushing of the compressed toe. The existing cracks then started to widen and crushing of masonry elements extended towards the centre of the wall along the bottom course.

5.5 Sensitivity Analysis

Due to the uncertainty and to lack of experimental data regarding some of the key constitutive parameters used in the proposed numerical model, it is necessary to assess the sensitivity of the simulation results to the employed values. Only Wall 1, with an aspect ratio of one and 855 mm bar spacing, is considered for the sensitivity analysis with respect to the following parameters.

5.5.1 Elastic Moduli of Mortar Joints

Among the key parameters, the elastic modulus of the mortar joints is one of the material properties which could affect the displacement characteristics of a partially grouted masonry shear wall. Figure 5.12 shows the load-displacement
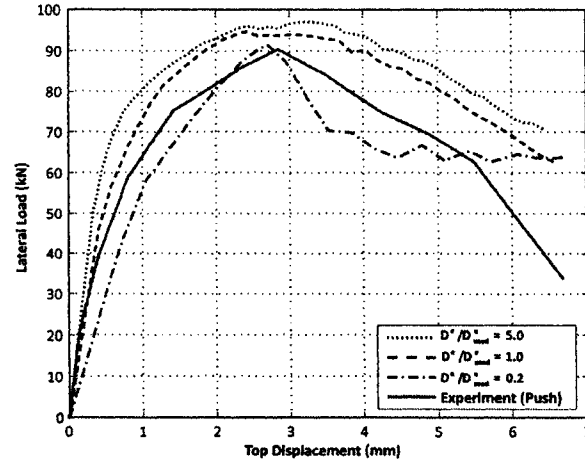
Figure 5.12 – *Sensitivity analysis for elastic modulus of mortar joints*

curves for Wall 1 for D^e / D^e_{used} = 0.2, 1.0 and 5.0 where D^e is the altered stiffness

matrix of the mortar joints and D^e_{used} is the one used in the finite element

simulations of this study. Although the pre-peak part of the load-displacement curve

shows significant dependency on the factor of five changes to elastic properties of

the mortar joints, the ultimate strength is not significantly affected. More rapid

degradation of strength was observed in the wall with lowest modulus of elasticity

which caused by greater localization of deformation at the toe of the wall. A similar

trend was observed for the numerical analyses of other test walls. It is thought that

the possible differences between the assumed and the actual modulus of elasticity

values would be much less than the range employed here.

5.5.2   Tensile and Shear Bond Strength of the Unit-Mortar Interface

To study the sensitivity of the numerical results to the chosen tensile and shear

bond strengths of the unit-mortar interface elements, the associated parameters, s_0

and r_0, Equation (2.20), were altered to be double and to be half of the values used

in the finite element analysis of the tested shear walls. Figure 5.13 shows the load-

displacement responses for Wall 1 after applying the changes. In addition, the post-

peak crack patterns and other damage for the new bond strength values are

illustrated in Figure 5.14. The post-peak crack patterns correspond to a residual
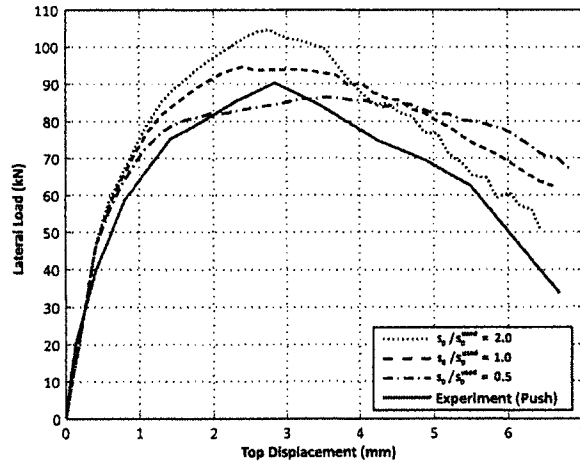
Figure 5.13 – *Sensitivity analysis for tensile and shear bond strength of mortar joint*

(a) $s_0 / s_0^{used} = 2.0$ (b) $s_0 / s_0^{used} = 0.5$
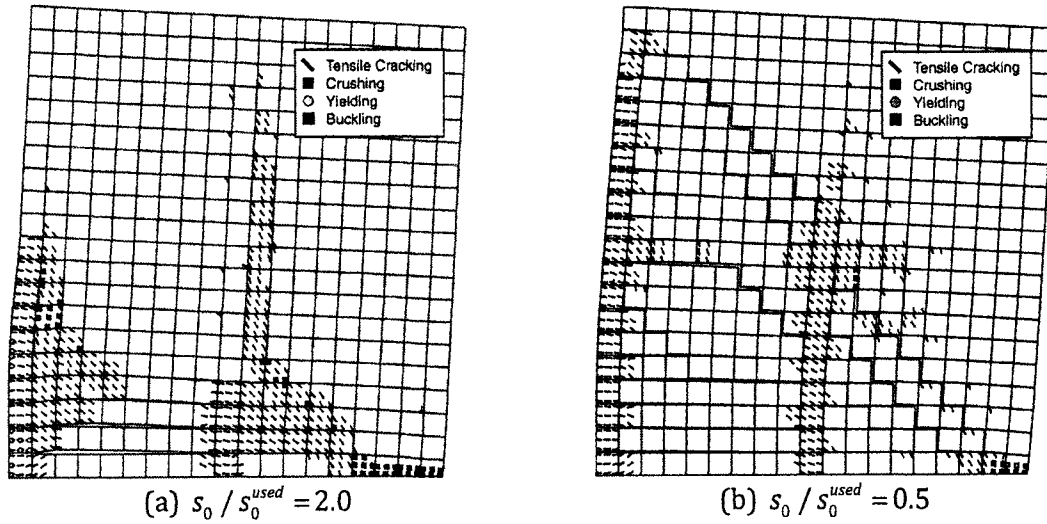
Figure 5.14 – *Post-peak cracking and other deformations at 80% of the peak load for the modified tensile and shear bond strengths of the mortar joints*

strength of approximately 80% of the peak-load. As expected, higher ultimate load carrying capacity was obtained for the wall with higher tensile and shear bond strength. The comparisons between initial lateral displacements indicate no effect due to changing the tensile and shear bond strength. More rapid post-peak strength degradation occurs in the wall with higher bond strength. This could be explained by more pronounced crushing and cracking of masonry units associated with higher bond whereas development of diagonal stepped-pattern cracking in the finite element model of the wall with weakest joints (see Figure 5.14-b) results in higher drift of the wall due to shear slip along the joints without as much strength degradation.

The pattern of the stepped-cracking in Figure 5.14-b, predicted for the weakest tensile and shear bond strengths exhibits a closer match to the crack pattern observed in the test. This indicates that tensile bond strength might have been over estimated in the analysis of the shear walls.

5.5.3   Shear-Friction Coefficient of Unit-Mortar Interface

Wall 1 was re-analysed with the finite element model to study the sensitivity of the numerical results to the shear-friction coefficients at the unit-mortar interface. The initial and residual shear-friction coefficient parameters, μ_0 and μ_r, were reduced to half of the values used in the shear wall's finite element models. The resulting load-displacement curve is presented in Figure 5.15. As shown, the load-displacement curve shows significant reduction in the wall strength while increasing the ductility by maintaining the load carrying capacity of the wall over a large displacement range in the post-peak response.
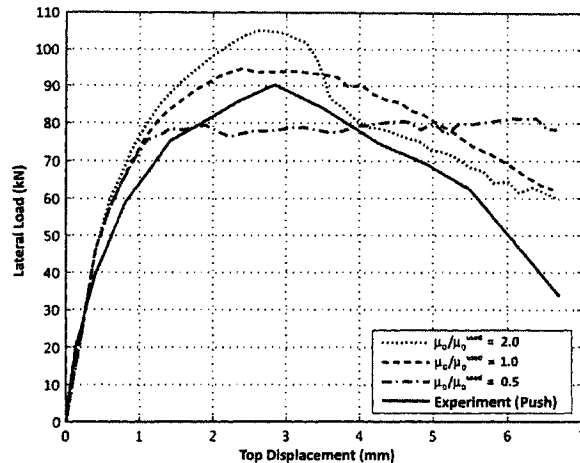
Figure 5.15 – Sensitivity analysis for shear-friction coefficient of mortar joint

The initial and residual shear-friction coefficients were also increased to double the values used in the original numerical analysis. This, as shown in Figure 5.15, led to an increase in the ultimate load carrying capacity of the wall. This along with the previous observation emphasizes the significance of an accurate estimation of shear-friction coefficient representing the conditions of the actual wall.

5.5.4   Buckling of Vertical Reinforcing Bar

As shown in Figure 5.16, the post-peak response of the finite element analysis of Wall 1 is noticeably affected by the effect of buckling of the vertical steel bar in the compression zone. As also shown in Figure 5.16, ignoring this effect eliminates one of the major characteristics of the failure mode in partially grouted reinforced masonry shear walls and leads to a spurious resistance resulting in the unrealistically ductile response for the wall.

In masonry shear walls with widely spaced reinforcement, once the extreme compression bar buckles, partial grouting and large spacing between reinforcing bars result in significant strength degradation. However, this effect is significantly
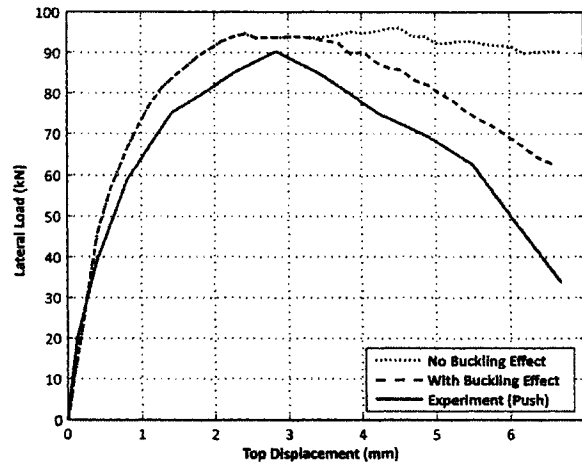
Figure 5.16 – Sensitivity analysis for buckling of vertical reinforcing bar

alleviated in closely spaced reinforcement and fully grouted masonry shear walls

where crushing of the end compression zone and buckling of the embedded vertical

reinforcing bar represent a small fraction of the available strength.

5.5.5   Tension Stiffening Effect

To study the sensitivity of the numerical results to the slope of the descending

curve of the stress-strain relation of masonry in tension between cracks (so-called

tension stiffening effect), the associated parameter, α, Equation (2.12), for the

reinforced masonry elements was altered to $\alpha = 0.02$ and 0.5 as upper and lower

extremes, respectively. The value of 0.02 for α indicates little strength degradation

for masonry after tensile debonding which is commonly observed for closely spaced

reinforcement in masonry shear walls; it delays failure of masonry in tension. On

the other hand, $\alpha = 0.50$ indicates almost no residual strength for masonry after

reaching the cracking strength such as unreinforced masonry components.

The load-displacement curves for $\alpha = 0.02$ and 0.50 together with the one for

$\alpha = 0.20$ used in the finite element analysis of the tested shear walls are shown in
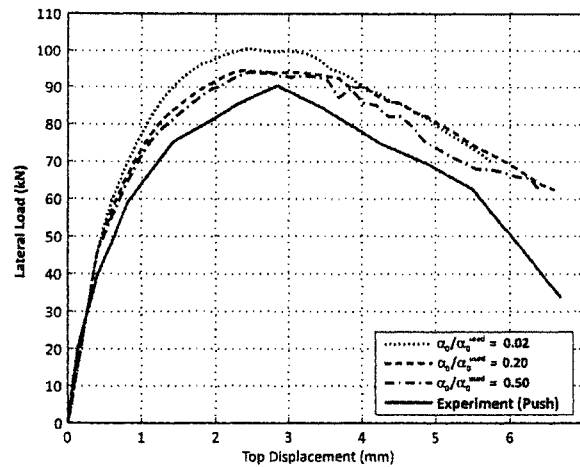
Figure 5.17 – *Sensitivity analysis for tension stiffening effect*

Figure 5.17. As expected, the ultimate strength of the wall decreased with increasing

α values whereas the post-peak response follows nearly the same pattern. The very

small difference associated with more rapid strength degradation (higher α),

indicating negligible sensitivity of the results to this parameter, could be attributed

to the high reinforcement ratio in the grouted reinforced region of the masonry

model. This could counteract and reduce the effect of extra stiffness provided by the

tension-stiffening model.

5.5.6   Mesh-Size Sensitivity

As discussed in the technical literature (Lotfi and Shing 1991, Bazant and Oh

1983), the presence of softening behaviour in constitutive relations merely based on

the material's strength characteristics can affect the finite element results by

mesh-size dependency and deformation localization. As a remedy, incorporating a

crack width limiter or enforcing constant energy per volume of fracture zone are

suggested (Bazant and Oh 1983, Borst 2002).

Since the softening behaviour of the unit-mortar interface is governed by preserving the Mode-I (pure tensile) and Mode-II (pure shear) fracture energies per unit length during strength degradation, the interface element used in the model is essentially independent of the size of the selected mesh. However, in the material model proposed for masonry, neither tension nor compression softening regimes employs fracture energy based equations for the constitutive relations. Thus, it is necessary to evaluate the dependency of the numerical results to the mesh-size.

Figure 5.18 shows the predicted load-displacement curves of Wall 1 for a finer mesh containing double the number of elements in both the x- and y-directions. Up to the peak-load, despite tensile cracking and joint debonding, the load-displacement responses are nearly identical and there is no indication of mesh sensitivity. This implies that no strain localization occurs in the tension zone.

It is believed that, close to the reinforcing bars, the overall behaviour of the masonry elements in tension is stabilized by the overlaid steel elements and the much higher stiffness provided by the steel bars prevents localization of tensile deformation into a narrow zone of elements. Furthermore, in the unreinforced parts of the wall, the failure is governed mostly by tensile debonding and shear failure of mortar joints (see Figure 5.7-a), which are insensitive to the size of elements. Hence, as also discussed by Lotfi and Shing (1991), the mesh-size sensitivity observed is the result of compressive softening, which is always localized in the elements at the bottom row (i.e., the first elements fail in compression) irrespective of the mesh size. As shown in Figure 5.19, in the post-peak region at 80% of the ultimate
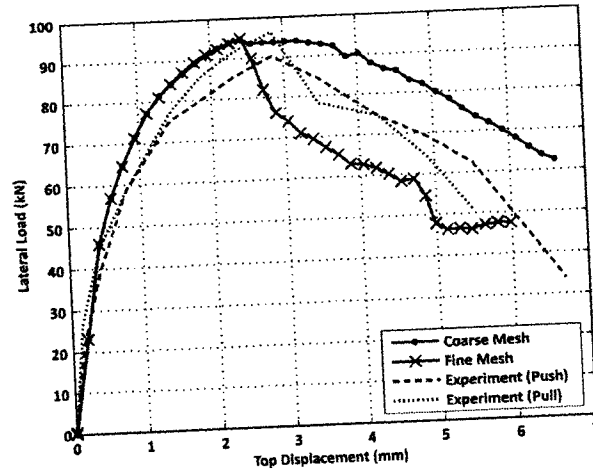
Figure 5.18 – *Sensitivity analysis for size of elements*

(a) Coarse Mesh

(b) Fine Mesh
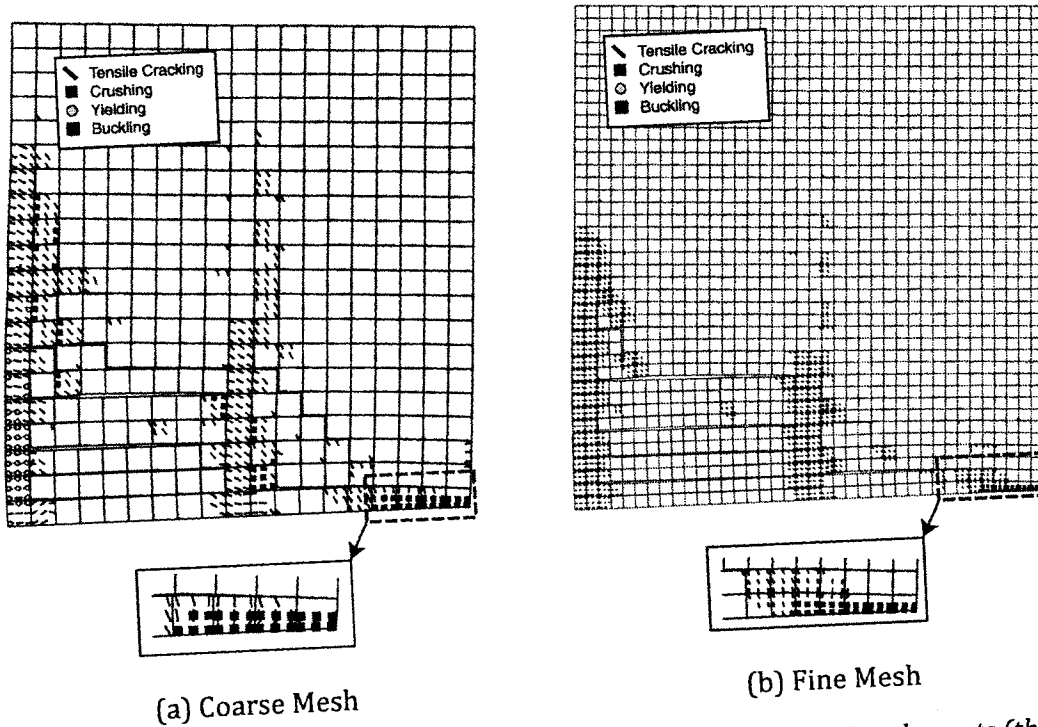
Figure 5.19 – *Localization of compressive softening in the smaller size elements (the post-peak crack pattern corresponds to 80% of the peak load after failure)*

resistance of the wall, localization of compression failure in the smaller size elements is clearly observed. Finer mesh leads to more rapid propagation of the softening zone along the bottom layer due to more severe stress concentration which, in turn, increases the degradation rate of the wall.

According to a model suggested by Borst (2002), the problem of mesh-size dependency of the results in quasi-brittle materials such as concrete and masonry could be eliminated by using a continuum damage-based approach. However, to experimentally capture the fracture energy of highly brittle materials, very accurate servo-controlled loading equipments are required which are rarely found in typical research institutes and were not available in the McMaster University's laboratory.

In this study, consistent with previous research by Lotfi and Shing (1991, 1994), Lourenco (1996), and Maleki et al. (2005 and 2007), the size of masonry elements was chosen to be equal to a half masonry block (two elements per masonry block). This element size is compatible with the size of the experimentally observed compressive fracture zone at the toe of a masonry shear wall. As discussed above, the proposed element size provides acceptable agreement between numerical and experimental results.

5.6   Parametric Study

As discussed earlier in Section 3.3.1, due to realistic limits on budget and time, providing experimental evidence concerning the effect of all of the key parameters on the behavioural characteristics of partially grouted reinforced masonry shear walls was not feasible. Hence, to increase the value of this research, the two phase

material model was developed to predict the effect of axial stress and amounts of

the vertical and horizontal reinforcement on the behaviour of a typical partially

grouted reinforced masonry shear wall. In addition, the effect of using two adjacent

reinforced cells at the ends of a partially grouted reinforced masonry shear wall was

also simulated. For the purpose of this parametric study, Wall 1 from the

experimental program (having an aspect ratio $h/\ell = 1.0$ and bar spacing equal to

855 mm at half-scale corresponding to 1710 mm spacing at full-scale) was selected

for numerical simulations as representative of a typical partially grouted reinforced

masonry shear wall.

5.6.1   Level of Axial Stress

The effect of level of axial stress on the load-displacement response of Wall 1

is presented in Figure 5.20. Five different levels of axial stresses, 0.00 MPa, 0.38

MPa, 0.75 MPa, 1.13 MPa, and 1.5 MPa based on gross area, were considered for

simulations corresponding to 0.0 kN, 60.0 kN, 120.0 kN, 150.0 kN, and 240.0 kN,
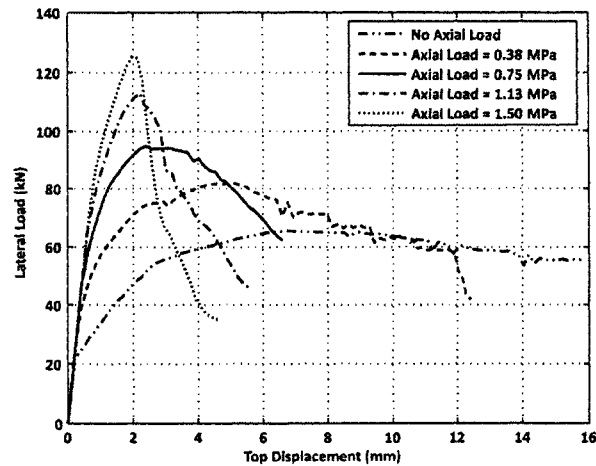
Figure 5.20 – Effect of axial stress on the load-displacmeent response of Wall 1

respectively. As can be seen, increases in axial stress result in increases in wall

stiffness as well as the ultimate lateral load capacity. A summary of the ultimate

(peak) lateral loads and the corresponding displacements at the top of the wall at

the peak loads along with the pseudo displacement ductilities and lateral load

reduction factors is presented in Table 5.10. Displacement ductilities and load

reduction factors were calculated using the idealized bilinear envelope suggested by

Tomazevic (1999) and described in Section 4.4.4.

Table 5.10 – *Parametric study results for the effect of axial load for Walls 1*

Axial Stress (MPa)	Peak Load (kN)	Displacement (mm)	Displacement Ductility (μ_Δ)	Load Reduction Factor** (R)
0.00	65.4	8.47	14.8	5.3
0.38	81.8	4.88	10.1	4.4
0.75	94.7	2.41	8.4	4.0
0.113	113.2	2.21	3.4	2.4
1.50	125.1	1.97	2.4	1.9

* *Idealised bilinear envelope based on equal energy approach suggested by*
  Tomazevic (1999) was used

** *Load reduction factors determined based on equal energy approach*

Increased axial stress leads to increased maximum load resistance of the wall.

However, the corresponding more rapid loss of strength after reaching the peak

load significantly affects the post-peak response of the wall and leads to reduce

displacement ductility and energy dissipation capacity. Ductilities of the walls with

different levels of axial stresses are plotted against the axial stress in Figure 5.21. As

can be seen, the pseudo displacement ductility varies almost linearly with respect to

increase in the level of superimposed axial compressive stress. Similar behaviour for

a partially grouted reinforced masonry shear wall under different level of axial load

was also reported by Ghanem et al. (1993). The substantial difference in
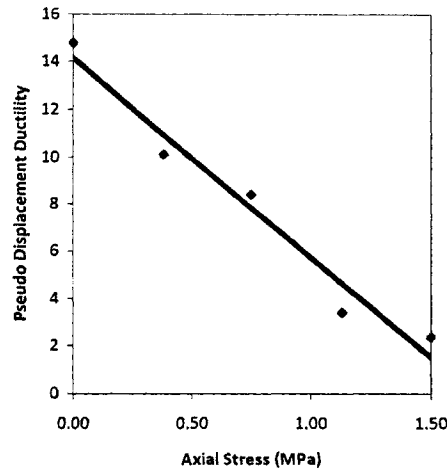
Figure 5.21 – Axial stress vesus pseduo-displacmenrt ductility for Wall 1

displacement ductility value and load reduction factor between the wall with no

axial compression and the wall with 1.50 MPa axial compressive stress is related to

the different post-peak crack patterns observed in the walls. Figure 5.22 shows the

post-peak crack patterns of the wall models with 0.00 MPa and 1.50 MPa axial

stresses at 80% of the maximum lateral load resistance after reaching the peak load.

As can be seen in Figure 5.22-a, absence of axial compression leads to extensive

yielding of the tensile bar and formation and propagation of bed joint debonding at

multiple courses of the wall which, in turn, permits significant lateral deformation

with a limited amount of strength degradation. However, applying high levels of

compressive stress prevents yielding of the vertical tensile bar and reduces the

amount of the horizontal bed joint cracking and diagonal stepped-pattern cracking

(see Figure 5.22-b).

5.6.2   Amount of the Vertical and Horizontal Steel Reinforcement

The effect of the amount of vertical reinforcement on the behaviour of Wall 1

| (a) No Axial Stress | (b) 1.50 MPa Axial Stress |
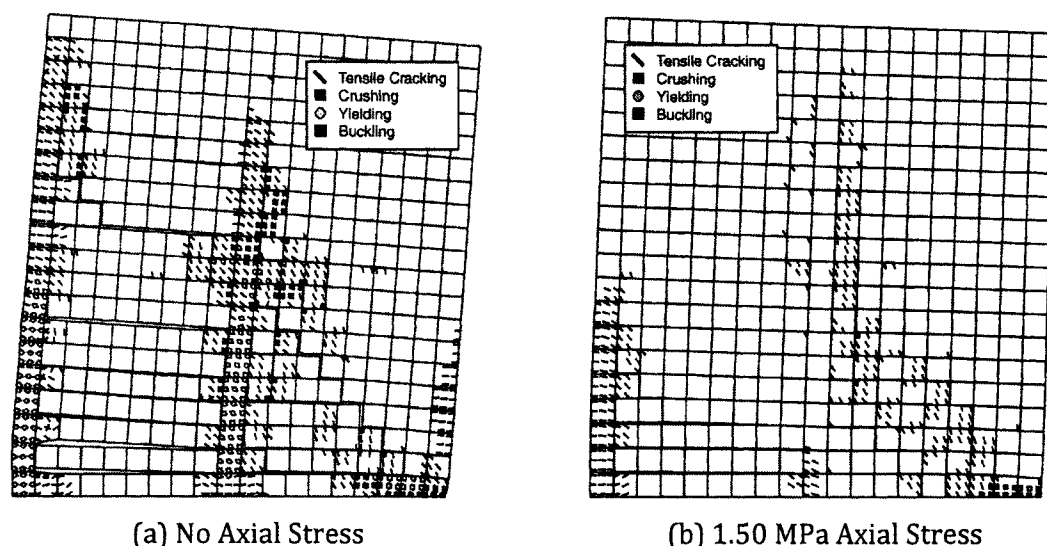
Figure 5.22 – *Crack pattern for Wall 1 subjected to 0.00 MPa and 1.50 MPa axial stress at 80% of the ultimate laod after failure*

was predicted using the developed two-phase material model which maintaining the same reinforcing pattern and bar spacing. Figure 5.23 shows the load-displacement responses of Wall 1 after changing the total area of the vertical reinforcement to half and then to double the amount used in this study. As can be seen, similar trends are observed in the overall pre- and post-peak responses of the walls. The lateral load capacity of the wall increases with the increase in amount of vertical reinforcement. Reducing the vertical reinforcement ratio to half leads to changing the failure mode from shear to flexural characterized by yielding of the tension bar at the peak load. No tension bar yielding is observed for the other two reinforcing ratios.

As shown in Figure 5.24, changing the total area of horizontal steel to half and then to double the total amount used in Wall 1 had almost no effect on the load-displacement response of the wall. This could be attributed to the fact that, due to
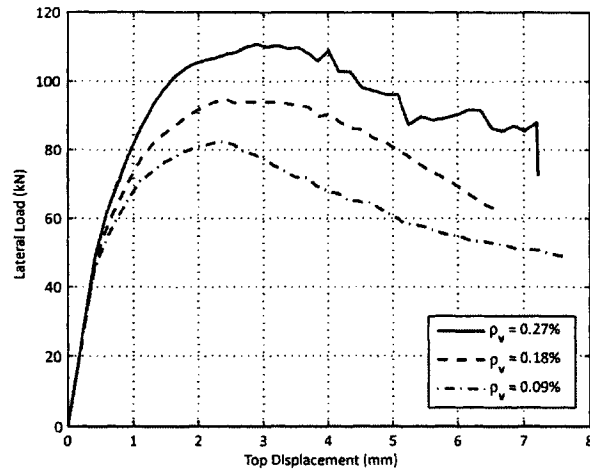
Figure 5.23 – *Effect of amount of vertical steel on the load-displacmeent response of Wall 1*
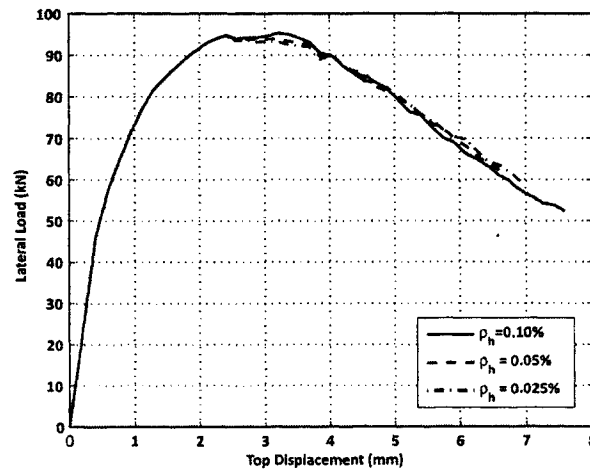
Figure 5.24 – *Effect of amount of horizontal steel on the load-displacmeent response of Wall 1*

large spacing between horizontal and vertical steel bars, diagonal cracks could easily widen inside the unreinforced areas surrounded by the horizontal and vertical steel bars. A more efficient contribution of shear reinforcement is expected in masonry shear walls with closely spaced horizontal or vertical reinforcement.

5.6.3   Using Two Adjacent Reinforced Cells at the End of a PG-RM Wall

The effect of using two adjacent reinforced cells grouted and reinforced at both the left and right ends of a typical partially grouted reinforced masonry shear wall was predicted using the two-phase material model developed in this study. As shown in Figure 5.25-a, Wall 1, as a typical PG-RM shear wall, was reanalyzed using the two columns of reinforced masonry at each end while maintaining the same total amount of steel as existed with only one cell grouted and reinforced at the ends of the wall. The load-displacement responses of Wall 1 for the two different reinforcement pattern are presented in Figure 5.25-b. As can be seen, a slightly higher strength degradation rate was observed in the post-peak regime of the wall with two grouted reinforced cells at the ends. This could be explained by assuming a linear strain profile at the bottom of the wall. In the wall model in which compression steel bars were equally distributed in the last two cells, a deeper compression block for masonry was required to satisfy equilibrium requirements compared to the wall model where equivalent compression steel bar was positioned inside the end cell. Consequently, at the same magnitude of lateral load, higher compressive strain could be imposed to the extreme compression bar in the wall model with two grouted cells at the end. This, in turn, could result in initiation of
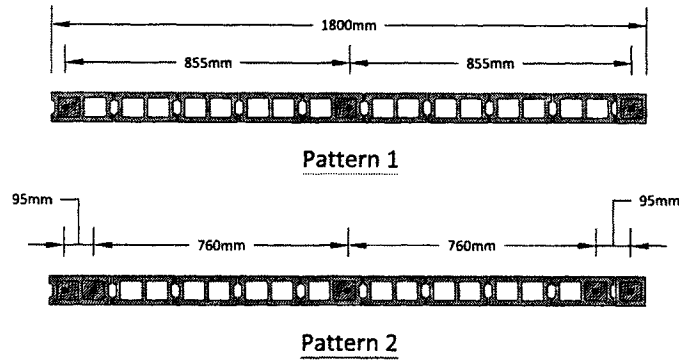
Pattern 1

Pattern 2

(a) Reinforcement Patterns for Wall 1
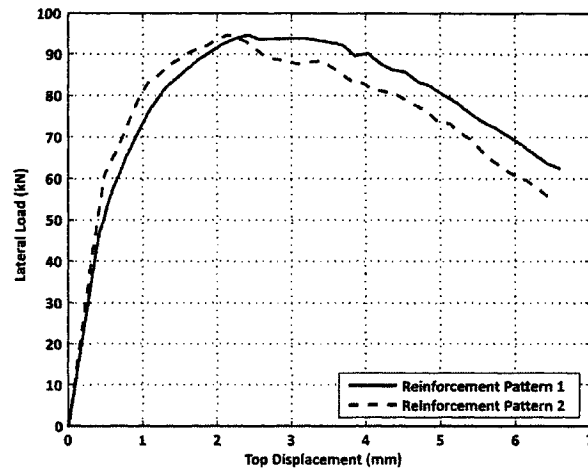
(b) Load-displacement Curves for Wall 1

Figure 5.25 – *Effect of having two adjacent cells reinfroced at both ends of the
wall versus having only the end cell reinfroced for Wall 1*

buckling of the outermost compression steel bar and eventually failure of the wall at

a lower displacement level compared to the wall reinforced only in the end cell.

5.7 CLOSING REMARKS AND CONCLUSION

This chapter provides validation of the ability of the finite element model as a

numerical tool to predict the behaviour of partially grouted reinforced masonry

shear walls. In general, in terms of maximum lateral load carrying capacity, post-

peak response and damage pattern, satisfactory agreement was achieved between the results of the finite element model and actual test observations. The comparison between walls with different aspect ratios revealed that the model provides most accurate load-displacement and crack-pattern prediction for walls with an aspect ratio of one.

The sensitivity of the numerical results to the key material parameters was also studied. Among the parameters, the elastic modulus, initial tensile bond strength and shear friction coefficient of the interface model showed considerable influence on the load-displacement response and the crack pattern for Wall 1. The significance of the bond strength characteristics of mortar joints on the overall behaviour of a partially grouted-reinforced masonry shear wall is especially emphasized.

The effects of level of axial load, amount of horizontal and vertical reinforcement, and of having two adjacent cells reinforced at both ends were also investigated using the developed numerical model. Wall 1 was used as a typical partially grouted reinforced masonry shear wall. Increasing the level of superimposed compressive stress led to significantly increased ultimate lateral load resistance of the wall. On the other hand, it changed the behaviour of the wall from a ductile flexural failure mode to a more brittle shear failure. Reducing the vertical reinforcement ratio also resulted in changing the failure mode from shear to flexure characterized by yielding of the tension bar at the peak load. However, altering the total area of the horizontal steel showed almost no change in the load-displacement response of the wall. A slightly higher strength degradation rate was observed in the post-peak regime of the wall with two grouted reinforced cells at the ends.

CHAPTER 6

CONCLUSIONS

6.1 SUMMARY

The main objective of this research project was to evaluate the performance of partially grouted reinforced masonry (PG-RM) shear walls subjected to superimposed axial stress and in-plane lateral cyclic loading. The behaviour of PG-RM shear walls was investigated to examine the possibility of using less than the commonly used amount of steel as the minimum amount for reinforcement or larger spacing than specified in the current Canadian masonry standard (CSA 2004).

The experimental program of this research study focused on documenting the effects of reinforcement spacing and aspect ratio on the response of PG-RM shear wall under cyclic reversed loading. Direct small scale modelling using half-scale model concrete masonry units was chosen for the experiments. This was necessary because of the large sized specimens needed to accommodate wide bar spacing and also because of the limited capacity of the actuators available in the laboratory.

Two stages of testing were conducted in the experimental program of this research. The first stage was designed to investigate the performance of masonry panels (wallettes) under the action of diagonal compression loading. Various patterns of grouting and reinforcing were studied by testing nine diagonal compression specimens made of half-scale model units. Visual observations, loading and corresponding displacements, and crack pattern were recorded throughout the tests.

The second stage of the experimental research, pursuing the primary goal of this research program, focused on the response of partially grouted reinforced masonry shear walls under constant axial load and fully reversed cyclic lateral loading. The test matrix consisted of five masonry shear walls with nearly the same reinforcement ratios. The walls included three aspect ratios and three reinforcement spacings.

Visual observations, general load-displacement response, crack pattern, wall deformation and drift, and reinforcement strains were recorded throughout the tests. The test results were analyzed and discussed with regard to key characteristics of a shear wall behaviour including load-displacement hysteresis loops, lateral load carrying capacity, wall stiffness and energy dissipation properties which were quantified using calculated displacement ductility and lateral load reduction factors.

A computationally efficient finite element program was developed as part of this study to numerically simulate the response of partially grouted reinforced

masonry shear walls under in-plane loading. An orthotropic rotating smeared crack model was adopted for the concrete masonry and the steel was represented by a separate overlaid element connected to the masonry elements at each node. The interface between the mortar joints and masonry units, as the planes of weakness in a masonry shear wall, was modeled in a plasticity framework. The proposed model was implemented in a displacement driven finite element code.

The performance of the numerical model was evaluated by simulating available shear wall tests from other studies as well as this work. In general, acceptable accuracy was observed in numerical predicting both the pre- and post-peak behaviours. The model was shown to be a reliable tool for further studies.

The developed numerical model was used to expand the scope of the study to include the effects of level of axial load and amounts of horizontal and vertical reinforcement on the behaviour of partially grouted reinforced masonry shear walls. In addition, the effect of reinforcing two cells at the ends of a partially grouted reinforced masonry shear wall was also simulated using the developed numerical model.

6.2 CONCLUSIONS

6.2.1 Diagonal Compression Test – Wallette Tests

The post-peak response of the wallette specimens that were partially grouted and reinforced along the four sides of the masonry panel (wallette) showed two peak points in the load-deformation curves indicating a reserved strength after cracking which resulted in a more ductile failure. The failure of the hollow and fully

grouted reinforced specimens was characterized by a sudden drop in the load with increased deformation. The ultimate shear strength, calculated based on the method specified in ASTM E519 (ASTM 2002b), decreased as the extent of grouting decreased from fully grouted to partially grouted and then to hollow.

6.2.2   Partially Grouted Reinforced Masonry Shear Wall Tests

6.2.2.1   General Wall Response

The test results indicate that the behaviour of partially grouted reinforced masonry shear walls with aspect ratio (height to length ratio) of 1.0 or less is dominated by shear failure characterised by formation of wide diagonal cracks followed by complete toe crushing. A mixed shear-flexure failure occurred for Wall 5 having an aspect ratio of 1.5 since both tensile yielding of flexural reinforcement and diagonal cracking were observed during the test.

The behaviour of all walls upon reaching the peak load coincided with sudden opening of existing cracks and subsequent development of toe crushing leading to eventual instability in the hysteresis loops in the post-peak loading range. Nevertheless, the load-displacement responses of the walls showed relatively fat loops after the maximum resistance which provided a high level of displacement ductility and energy dissipation comparable to other reinforced masonry shear wall tests done by Shedid (2006). This implies that partially grouted reinforced masonry shear walls could be used even in areas with high seismic demand.

From the test results, it was concluded that the global response of the test walls was not sensitive to the reinforcement pattern; however, walls with higher

aspect ratio (height to length ratio) experienced significantly distinct reduction in maximum load carrying capacity and stiffness.

6.2.2.2 Lateral Load Capacity

Close agreement was observed between the shear resistance estimated based on the current Canadian masonry standard CSA S304.1 (2004) and the experimental results of the partially grouted reinforced masonry shear walls dominated by shear failure mode. Wall 5 was dominated by a mixed shear-flexure failure mode and also showed a very close agreement with the flexural resistance prediction of the Canadian masonry standard (CSA 2004).

Wall capacities were shown to be highly dependent on the aspect ratio whereas little sensitivity was observed with respect to the reinforcement spacing.

6.2.2.3 Seismic Load Reduction Factor (R)

Based on the method described in Section 4.4.4, a value greater than or equal to 2.4 was calculated for the seismic load reduction factor, R, of all test walls. This indicates that the R value, suggested by the Canadian masonry standard (maximum R=2.0 for shear walls with moderately ductile behaviour - CSA 2004), underestimates the energy dissipation ability of partially grouted reinforced masonry shear walls despite the shear dominated behaviour observed for the test walls.

6.2.2.4 Initial stiffness

The comparison between initial stiffness estimated based on plane section

theory and the average secant stiffness from the push and pull loading cycles of the test walls was found to be closest at a small top displacement level corresponding to 0.02% storey drift.

The secant stiffness for all walls decreased rapidly to about 25% – 35% of the initial stiffness at the ultimate load and to about 10% - 30% of the initial stiffness at 0.2% drift.

6.2.2.5   Level of Axial Stress

The effect of axial stress on the behaviour of partially grouted reinforced masonry shear walls was investigated using the developed numerical tool. Based on the finite element simulation of a typical partially grouted reinforced masonry shear wall, it was observed that increasing the level of axial load significantly increased the ultimate lateral load resistance of the wall and changed the behaviour of the wall from a ductile flexural failure mode (for wall with no axial stress) to a brittle shear failure mode (for a wall with 1.50 MPa axial stress).

6.2.2.6   Amounts of Vertical and Horizontal Reinforcement

Based on the results of the parametric study using the numerical model, reducing the vertical reinforcement ratio resulted in changing the failure mode of a typical partially grouted reinforced masonry shear wall from shear to flexure characterized by significant yielding of the extreme tension bar at the peak load. However, altering the total area of the horizontal steel showed no major change in the load-displacement response of the wall.

6.2.3 Predictions using the Numerical Model

6.2.3.1 Effect of Buckling of Vertical Reinforcement

It was concluded that, for an accurate simulation of post-peak behaviour of a partially grouted reinforced masonry shear wall, the effect of buckling of the compressive steel reinforcement needs to be taken into account. This effect was added to the material model of the grouted masonry and reinforcing steel bar combination and the associated parameters were calibrated through a series of uniaxial compressive tests on reinforced and unreinforced masonry prisms. These represented the compression behaviour of the toe of a partially grouted reinforced masonry shear wall.

6.2.3.2 Mesh Size Sensitivity

While the pre-peak load-displacement response and ultimate load carrying capacity of simulated shear wall tests always indicated very good agreement with the experimental data, the post-peak behaviour was shown to be very sensitive to selection of the size of masonry elements. Consistent with previous research done by Lotfi and Shing (1991, 1994), Lourenco (1996), and Maleki et al. (2005 and 2007) using two rectangular elements per masonry block provided acceptable agreement with experimental results.

6.2.3.3 Simulated Crack Patterns

The predicted crack pattern of a partially grouted reinforced masonry shear wall predicted using the numerical model was shown to be dependent on the initial

tensile bond strength and shear friction coefficient of the unit-mortar interface. This emphasizes the significance of correct estimation of bond properties of mortar joints for an accurate prediction of crack pattern using the proposed numerical model.

6.3 RECOMMENDATIONS FOR FUTURE RESEARCH

The following research areas, mainly related to the scope of this work, are recommended to be further investigated in order to provide a better understanding of the behavioural characteristics of partially grouted reinforced masonry shear walls:

1. More tests on partially grouted reinforced masonry shear walls are suggested in order to provide experimental evidence concerning the effect of level of axial load, amount of the horizontal and vertical reinforcement on the ultimate lateral load resistance of the wall and on the level of energy dissipation as well as load reduction factor.

2. According to the numerical results presented in Section 5.4.4.1, it would be worthwhile to study the effect of modulus of elasticity of mortar joints on the initial stiffness of partially grouted reinforced masonry shear walls.

3. More research is essential in order to better understand the effect of buckling of vertical compression steel bar on the rate of post-peak strength degradation of a partially grouted reinforced masonry. The outcomes will help to improve the stress-strain relation of grouted masonry and steel in the compression zone.

4. Development of a constitutive model in a framework of plasticity technique is recommended in order to enforce constant energy per volume in the compression fracture zone in order to alleviate the mesh-size dependency observed in this study.

5. More tests are recommended to be undertaken to provide experimental evidence related to bond properties between concrete masonry block and mortar joint. The key parameters such as type of mortar, rate of absorption of masonry units, effect of normal compressive stress, and boundary conditions are suggested to be considered for future studies.

6.4 CONCLUSIONS

Based on the findings of this research study, partially grouted reinforced masonry shear walls having larger spacing than the minimum seismic requirements specified in the current Canadian masonry design standard, CSA S304.1 (2004), were shown to provide relatively ductile behaviour with satisfactory energy dissipation capability under superimposed axial load and reversed cyclic loading. This indicates potential application of this type of masonry construction as a more cost-efficient alternative in areas with low or moderate seismic activity. Therefore, it is recommended that partially grouted reinforced masonry shear walls be included in a future edition of the Canadian masonry standard with a load reduction factor greater than 1.0 (a value of 1.5 would be conservative). This implies that the current R values, 1.5 and 2.0, for reinforced masonry shear walls specified in the current masonry code (CSA S304.1 2004) should be re-examined.

The results of this study along with the developed numerical tool can help in future efforts to introduce a new intermediate category between unreinforced and reinforced masonry structures namely Partially (or Nominally) Reinforced Masonry which can offer some relief from the current code's limitation (CSA S304.1, 2004).

REFERENCES

Abboud, B. E., Hamid, A. A., Harris, H. G. (1990), "Small-scale modeling of concrete block masonry structures", Structural Journal, ACI, vol. 87, no. 2, pp. 145-155

ASTM International (2002a), "Standard Test Method for Compressive Strength of Hydraulic Cement Mortars (Using 2-in. or 50-mm Cube Specimens)", ASTM C109/C109M-02, West Conshohocken, Pennsylvania, www.astm.org

ASTM International (2002b), "Standard Test Method for Diagonal Tension (Shear) in Masonry Assemblages", ASTM E519-02, West Conshohocken, Pennsylvania, www.astm.org

ASTM International (2003a), "Standard Test Method for Sampling and Testing Grout", ASTM C1019-03, West Conshohocken, Pennsylvania, www.astm.org

ASTM International (2003b), "Standard Test Method for Compressive Strength of Masonry Prisms", ASTM C1314-03b, West Conshohocken, Pennsylvania, www.astm.org

ASTM International (2005), "Standard Specification for Steel Wire, Deformed, For Concrete Reinforcement", ASTM A496/A496M-05, West Conshohocken, Pennsylvania, www.astm.org

ASTM International (2007), "Standard Test Method for Flow of Hydraulic Cement Mortar", ASTM C1437-07, West Conshohocken, Pennsylvania, www.astm.org

Atkinson, R. H., Amadei, B. P., Saeb, S., and Sture, S. (1989), "Response of Masonry Bed Joints in Direct Shear", Journal of Structural Engineering, vol. 115, no. 9, pp. 2276-2296

Bae, S., Mieses, A. M., and Bayrak, O. (2005), "Inelastic Buckling of Reinforcing Bars", Journal of Structural Engineering, ASCE, vol. 131, no. 2, pp. 314-321

Bazant, Z. O., and Oh, B., H. (1983), "Crack Band Theory for Fracture of Concrete", Materials and Construction, vol. 16, no. 93, pp. 155-177

Bazant, Z. P., and Chen, E. (1997), "Scaling of Structural Failure", Applied Mechanics Review, vol. 50, no. 10, pp. 593-627

Bazant, Z. P., and Sener, S. (1988), "Size Effect in Pull-out Tests", Material Journal, ACI, vol. 85, no. 5, pp. 347-351

Borst, R. (2002), "Fracture in Quasi-Brittle Materials: A Review of Continuum Damage-Based Approaches", Engineering Fracture Mechanics, vol. 69, no. 2, pp. 95-112

Brunner, J. D., and Shing, P. B. (1996), "Shear Strength of Reinforced Masonry Walls", TMS Journal, vol. 14, no. 1, pp. 65-77

Canadian Standard Association (CSA) (2004), CSA S304.1-04, "Design of Masonry Structures, Mississauga, Ontario

Cerioni R., and Donida, G. (1994), "A Finite Element Model for the Nonlinear Analysis of Reinforced and Prestressed Masonry Walls", Computers and Structures, vol. 53, no. 6, pp. 1291-1306

Chopra, A. K. (1995), "Dynamics of Structures", Prentice Hall

Criesfield, M. A., and Wills, J. (1989), "Analysis of RC Panels using Different Concrete Models", Journal of Engineering Mechanics, ASCE, vol. 115, no. 3, pp. 578-597

Crisfield, M. (1997), "Nonlinear Finite Element Analysis of Solids and Structures", John Wiely & Sons, Inc., New York, New York

Darwin, D., Pecknold, D. A. (1977), "Nonlinear Biaxial Stress-Strain Law for Concrete", Journal of Engineering Mechanics, vol. 103, pp. 229-241

Drysdale, R. Hamid, A. A., and Baker, L. (1999), "Masonry Structures: Behaviour and Design", 2nd edition, The Masonry Society, Boulder, Colorado

El-Dakhakhni, W., Drysdale R.G., and Khattab, M. (2006), "Multi-Laminate Macromodel for Concrete Masonry: Formulation and Verification", Journal of Structural Engineering, ASCE, vol. 132, no. 12, pp. 1984-1996

Elshafie, H., Hamid, A. A., and Nasr, E. (2002), "Strength and Stiffness of Masonry Shear Walls with Openings", TMS Journal, December, vol. 20, no. 1, pp. 49-60

Ewing, R. D., El-Mustapha, A. M., and Kariotis, J.C. (1988), "A Finite Element Computer Program for the Non-Linear Static Analysis of Reinforced Masonry Walls", In Proceedings, 8th International Brick/Block Masonry Conference, Dublin, Ireland, vol. 2, pp.1119-1130

Ewing, R. D., El-Mustapha, A. M., Kariotis, J. C. (1987 – Revised 1990), "FEM/I – A Finite Element Computer Program for the Non-Linear Static Analysis of Reinforced Masonry Building Components", U.S.-Japan Coordinated Program for Masonry Building Research, Report no. 2.2-1

Fattal, S. G. (1993a), "Strength of Partially Grouted Shear Walls under Lateral Loads", U. S. Department of Commerce, NISTIR 5147, National Institute of Standards and Technology, Gaithersburg, Maryland

Fattal, S. G. (1993b), "The Effect of Critical Parameters on the Behaviour of Partially Grouted Masonry Shear Walls under Lateral Loads", U. S. Department of Commerce, NISTIR 5116, National Institute of Standards and Technology, Gaithersburg, Maryland

Fattal, S. G., and Todd, D. R. (1993), "Ultimate Strength of Masonry Shear Walls: Predictions versus Test Results", U. S. Department of Commerce, NISTIR 4633, National Institute of Standards and Technology, Gaithersburg, Maryland

Ghanem G. M. (1992), "Behaviour Characteristics of Partially Reinforced Loadbearing Masonry Wall Structures", Ph.D. Thesis, Department of Civil Engineering, Helwan Univeristy, Egypt

Ghanem G. M., Salama, A. E., Elmagd, S. A., and Hamid A. A. (1993), "Effect of Axial Compression on the Behaviour of Partially Reinforced Masonry Shear Walls", In Proceedings, 6th North American Masonry Conference, Philadelphia, Pennsylvania, pp. 1145-1157

Giambanco, G., Rizzo, S., and Spallino, R. (2001), "Numerical Analysis of Masonry Structures via Interface Models", Computer Methods in Applied Mechanics and Engineering, vol. 190 (2001), pp. 6493-6511

Halucha, J. A. (2002), "In-Plane Shear Behaviour of Reinforced Concrete Masonry Panels Under Biaxial Loading", M.A.Sc. Thesis, Department of Civil Engineering, McMaster University, Hamilton, Ontario

Hamid, A. A. (1978), "Behaviour Characteristics of Concrete Masonry", Department of Civil Engineering, McMaster University, Hamilton, Ontario

Hamid, A. A., Abboud, B. E. (1986), "Direct Modeling of Concrete Block Masonry under Shear and In-Plane Tension", Journal of Testing & Evaluation, vol. 14, no. 2, pp. 112-121

Hamid, A. A., and Chandrakeerthy, S. R. De S. (1992), "Compressive Strength of Partially Grouted Concrete Masonry using Small-Scale Wall Element", TMS Journal, vol. 11, no. 1, pp. 75-85

Hamid, A. A., and Drysdale, R. G. (1988), "Flexural Tensile Strength of Concrete Block Masonry", Journal of the structural Division, Proceedings of ASCE, vol. 114, no. 1, pp. 50-66

Harris, H. G., and Becica I. J. (1978), "Behaviour of Concrete Masonry Structures and Joint Details using Small-Scale Direct Models", In Proceedings, North American Masonry Conference, University of Colorado, Boulder, Colorado, pp.10.1-10.18

Harris, H. G., and Sabnis, G. M. (1999), "Structural Modelling and Experimental Techniques", Second Edition, Boca Raton: CRC Press

Hegemier, G. A., and Arya, S. K. (1982), "Finite Element Method for Interface Problems", Journal of Structural Division, ASCE, vol. 108 (ST2), pp. 327-342

Ingham, J. M., Davidson, B. J., Brammer, D. R., and Voon, K. C. (2001), "Testing and Codification of Partially Grout Filled Nominally Reinforced Concrete Masonry Subjected to In-Plane Cyclic Loads", TMS Journal, September, vol. 19, no. 1, pp. 83-96

Khattab, M. (1993), "In-Plane behaviour of Grouted Concrete Masonry under Biaxial States of Stress", Ph.D. Thesis, Department of Civil Engineering, McMaster University, Hamilton, Ontario, Canada

Kupfer, H. B., Hilsdorf, H. K., and Rusch, H. (1969), "Behaviour of Concrete under Biaxial Stresses", ACI Journal, vol. 66, no. 8, pp. 656-666

Kwak, H. G., Kim, D. Y. (2004a), "Material Nonlinear Analysis of RC Shear Walls Subjected to Cyclic Loadings", Engineering Structures, vol. 26, no. 10, pp. 1423-1436

Kwak, H. G., Kim, D. Y. (2004b), "Material Nonlinear Analysis of RC Shear Walls Subjected to Monotonic Loadings", Engineering Structures, vol. 26, no. 11, pp. 1517-1533

Long, L. (2006), "Behaviour of Half-Scale Masonry Shear Walls", M.A.Sc. Thesis, Department of Civil Engineering, McMaster University, Hamilton, Ontario

Long, L., Hamid, A. A., and Drysdale, R. G. (2005), "Small-Scale Modelling of Concrete Masonry using Half-Scale Units: A Preliminary Study", In Proceedings, 10th Canadian Masonry Symposium, Banff, Alberta

Lotfi, H. R., and Shing, P. B. (1991), "An Appraisal of Smeared Crack Models for masonry Shear Wall Analysis", Computers and Structures, vol. 41, no. 3, pp. 413-425

Lotfi, H. R., and Shing, P. B. (1994), "Interface Model Applied to Fracture of Masonry Structures", Journal of Structural Engineering, vol. 120, no. 1, pp. 63-80

Lourenco, P. B., and Rots, J. G. (1997), "Multisurface Interface Model for Analysis of Masonry Structures", Journal of Engineering Mechanics, ASCE, vol. 123, no. 7, pp. 660-668

Lourenco, P., B. (1994), "Analysis of Masonry Structures with Interface Elements; Theory and Applications", Report No. 03-21-22-0-01, Department of Civil and Environmental Engineering, Delft University of Technology

Lourenco, P., B. (1996), "Computational Strategies for Masonry Structures", Ph.D. Thesis, Department of Civil and Environmental Engineering, Delft University of Technology

Lubell, A., Sherwood, T., Bentz, E., and Collins, M. P. (2004), "Safe Shear Design of Large, Wide Beams", Concrete International, ACI, vol. 26, no. 1, pp. 66-78

Maleki, M., A. A. El-Damatty, A. A. Hamid and R. G. Drysdale (2005), "Finite Element Analysis of Reinforced Masonry Sear Walls Using Seared Crack Model", In Proceedings, 10th Canadian Masonry Symposium, Banff, Alberta

Maleki, M., A. A. Hamid, A. A. El-Damatty, and R. G. Drysdale (2007), "Behaviour of Partially Grouted Reinforced Concrete Masonry Panels under In-Plane Diagonal Loading", In Proceedings, 10th North American Masonry Conference, St. John, Missouri

Manos G. C., Soulis, V., Thawabteh, J. (2003), "Numerical Investigation of Mortar-Joint Models of In-Plane Failure Utilizing Unreinforced Masonry Assemblages", In Proceedings, 9th North American Masonry Conference, Clemson, South Carolina

Matsumura, A. (1985), "Effect of Shear Strength in Concrete Masonry Walls", The first meeting of Joint Technical Coordinating Committee on Masonry Research (TCCMAR) – U.S.-Japan Coordinated Program for Masonry Building Research, Tokyo, Japan

Matsumura, A. (1987), "Shear Strength of Reinforced Hollow Unit Masonry Walls". In Proceedings, 4th North American Masonry Conference, Los Angeles, California, pp. 50.1-50.16

Matsumura, A. (1990), "Planar Shear Loading Test on Reinforced Fully Grouted Hollow Clay Masonry Walls", In Proceedings, 5th North American Masonry Conference, Urbana, Illinois, pp. 347-358

Mehrabi, A. B., and Shing, P. B. (1997), "Finite Element Modeling of Masonry-Infilled RC Frames", Journal of Structural Engineering, vol. 123, no. 5, pp. 604-613

Miller, S. C., El-Dakhakhni, W., and Drysdale, R. G. (2005), "Experimental Evaluation of the Shear Capacity of Reinforced Masonry Shear Walls", In Proceedings, 10th Canadian Masonry Symposium, Banff, Alberta

Montgomery, D. C., and Runger, G. C. (1994), "Applied Statistics and Probability for Engineers", Third Edition, John Wiley & Sons, Inc., New York

Moon, F. L. (2004), "Seismic Strengthening of Low-rise Unreinforced Masonry Structures with Flexible Diaphragms", Ph.D. Thesis, Volume I and II, Department of Civil and Environmental Engineering, Georgia Institute of Technology

Moon, F. L., Yi, T., Leon, R. T., and Kahn, L. F. (2003a), "Structural Analysis of a Prototype Unreinforced Masonry Low-Rise Building", In Proceedings, 9th North American Masonry Conference, Clemson, South Carolina

Moon, F. L., Yi, T., Leon, R. T., and Kahn, L. F. (2003b), "Large-scale tests of an unreinforced masonry low-rise building,", In Proceedings, 9th North American Masonry Conference, Clemson, South Carolina

Masonry Standards Joint Committee - MSJC (2008), "Building Code Requirements for Masonry Structures", TMS 402-08/ACI 530-08/ASCE 5-08, American Concrete Institute, American Society of Civil Engineers, and The Masonry Society, Detroit, New York, and Boulder

NZS 4230:1990 (1990), "Code of Practice for the Design of Masonry Structures", Standards Association of New Zealand, Wellington, p. 71

Ortiz, M., and Popov, E. P. (1985), "Accuracy and Stability of Integration Algorithms for Elasto-Plastic Constitutive Relations", International Journal of Numerical Methods in Engineering, vol. 21, no. 9, pp. 1561-1576

Page, A. W. (1978), "Finite Element Model for Masonry", Journal of Structural Division, ASCE, vol. 104 (ST8), pp. 1267-1285

Paulay, T., and Priestley, M. J. N. (1992), "Seismic Design of Reinforced Concrete and Masonry Buildings", John Wiley & Sons, New York, New York

Pluijm, R. (1993), "Shear Behaviour of Bed Joints", In Proceedings, 6th North American Masonry Conference, Philadelphia, Pennsylvania

Rosenhaupt, S., Sokal, Y. (1965), "Masonry Walls on Continuous Beams", Journal of Structural Division, ASCE, vol. 91, n. ST1, 1965, pp. 155-171

Saadeghvaziri, M. A., and Mehta, S. (1993). "An Analytical Model for URM Structures", In Proceedings, 6th North American Masonry Conference, Philadelphia, Pennsylvania, pp. 409-418

Schneider, R. (1959), "Tests on Reinforced Grouted Brick Masonry Shear Walls", Report issued by California State Division of Architecture, Los Angeles

Scrivener, J. (1966), "Concrete Masonry Wall Panel Tests – Stati Cracking Tests with Predominant Flexural Effects", New Zealand Concrete Construction

Seible, F., Hegemier, G., Igarashi, A., and Kingsley, G. (1994b), "Seismic Response of Full-Scale Five-Story Reinforced-Masonry Building", Journal of Structural Engineering, ASCE, vol. 120, no. 3, pp. 925-946

Seible, F., Hegemier, G., Priestley, M., Kingsley, G., Igarashi, A., and Kurkchubasche, A. (1993), "Preliminary Results from the TCCMAR Five-Storey Full-Scale Reinforced Masonry Research Building Test", TMS Journal, vol. 12, no. 1

Seible, F., La-Rovere, H. L., and Kingsley, G. R. (1990), "Nonlinear Analysis of Reinforced Concrete Masonry Shear Wall Structures-Cyclic Loading", TMS Journal, vol. 9, no. 1, pp. 70-77

Seible, F., Priestley, M., Kingsley, and Kurkchubasche, A. (1994a), "Simulated Seismic-Load Tests on Full-Scale Five-Story Masonry Building" Journal of Structural Engineering, ASCE, vol. 120, no. 3, pp. 903-924

Shedid, M. (2006), "Ductility of Reinforced Masonry Shear Walls", M.A.Sc. Thesis, Department of Civil Engineering, McMaster Univeristy, Hamilton, Ontario

Shedid, M., Hamid, A. A., and Drysdale, R. G. (2005), "Ductility of Reinforced Masonry Shear Walls and Impact of Incomplete Grouting", In Proceedings, 10th Canadian Masonry Symposium, Banff, Alberta

Shing, P. B., and Cao, L. (1997), "Analysis of Partially Grouted Masonry Shear Walls", U. S. Department of Commerce, National Institute of Standards and Technology, NISTIR GCR 97-710, Gaithersburg, Maryland

Shing, P. B., Brunner, J. D., and Lotfi, H. R. (1993a), "Evaluation of Shear Strength of Reinforced Masonry Walls", TMS Journal, vol.2, no. 1, pp. 61-75

Shing, P. B., Brunner, J. D., and Lotfi, H. R. (1993b), "Analysis of Shear Strength of Reinforced Masonry Walls", In Proceedings, 6th North American Masonry Conference, Philadelphia, Pennsylvania, pp. 1133-1143

Shing, P. B., Noland, J., Klamerus, E., and Spaeh, H. (1989), "Inelastic Behaviour of Concrete Masonry Shear Walls", Journal of Structural Engineering, ASCE, vol. 115, no. 9, pp. 2204-2225

Shing, P. B., Schuller, M. and Hoskere, V. S. (1990a), "In-Plane Resistance of Reinforced Masonry Shear Walls", Journal of Structural Engineering, ASCE vol. 116, no. 3, pp. 619-640

Shing, P. B., Schuller, M. and Hoskere, V. S. (1990b), "Flexural and Shear Response of Reinforced Masonry Walls", ACI Structural Journal, vol. 87, no. 6, pp. 646-656

Shing, P. B., Schuller, M. and Hoskere, V. S. (1990c), "Strength and Ductility of Reinforced Masonry Shear Walls", In Proceedings, 5th North American Masonry Conference, Urbana, Illinois, pp.309-321

Shultz, A. E. (1996), "Minimum Horizontal Reinforcement Requirements for Seismic Design of Masonry Walls", TMS Journal, vol. 14, no. 1, pp. 49-64

Stankowski, T. (1992), "Numerical Simulation of Failure in Particle Composite", Computers and Structures, Vol. 44, No. 1-2, pp. 459-468

Swamy, N., and Qureshi, A. (1971), "Strength, Cracking and Deformation Similitude in Reinforced T-Beams under Bending and Shear", ACI Journal, vol. 68, no. 3, pp. 187-195

Timoshenko, S., Goodier, J. N. (1970), "Theory of Elasticity", Third Edition, McGraw-Hill, New York, New York

Tomaževič, M. (1999), "Earthquake-Resistance Design of Masonry Buildings", Imperial College Press, London

UBC (1988), "Uniform Building Code", International Conference of Building Officials, Whittier, pp. 926

Vecchio, F. J., Collins, M. P. (1986), "The Modified Compression-Filed Theory for Reinforced Concrete Elements Subjected to Shear", Structural Journal, ACI, vol. 83, no. 2, pp. 219-231

Voon, K. C. (2007), "In-plane Seismic Design of Concrete Masonry Structures", Ph.D. Thesis, Department of Civil and Environmental Engineering, The University of Auckland, Auckland, New Zealand

Voon, K. C., and Ingham, J. M. (2005), "Experimental Study of Partially Grouted Concrete Masonry Walls with Openings", In Proceedings, 10th Canadian Masonry Symposium, Banff, Alberta

Warner, R. F., Rangan, B. V., and Hall, A. S. (1999), "Concrete Structures", Addison-Wesley Longman Pty. Ltd., Australia, pp. 752-780

Yankelevsky, D. Z., and Reinhardt, H. W., "Model for Cyclic Compressive Behaviour of Concrete", Journal of Structural Engineering, ASCE, vol. 113, no. 2, pp. 228-240

APPENDICES

Appendix A: Control Test Results

Mortar Cube Test Results for Diagonal Compression Tests (Wallette Tests)

Three 50mm mortar cubes were cast before using each batch of mortar in the construction of wallette specimens. The cubes were air cured for at least 28 days under the same laboratory conditions as the wallette specimens and were tested under uniaxial compression in accordance with ASTM C109/C109M-02 method (ASTM 2002a). Detail of the test results are as presented in Table A.1.

Table A.1 – Mortar cube test results for diagonal compression tests (wallette tests)

Type	Sample No.	Cube Strength (MPa)
Mortar Cube*	Batch 1	22.7
		22.1
		22.7
	Batch 2	23.4
		22.4
		21.6
	Batch 3	25.0
		26.0
		24.5
	Batch 4	25.3
		24.2
		25.5
	Average (C.O.V.)	23.8 (6.3%)

Dimensions: 50mm × 50mm × 50mm

Grout Sample Test Results for Diagonal Compression Tests (Wallette Tests)

Three grout samples were cast for each batch of grout at the same time as wallettes was grouted. The samples were block-moulded prisms with the approximate dimensions 90×90×185 mm prepared using the full scale blocks according to the method specified in ASTM C1019. All samples were hard capped using hydrostone and were tested under uniaxial compression. Detail of the test results are as presented in Table A.2.

Table A.2 –*Grout sample test results for diagonal compression tests (wallette tests)*

Type	Sample No.	Prism Strength (MPa)
Block-Moulded Prism*	Batch 1	32.2
		33.2
		46.2
	Batch 2	41.2
		45.6
		45.7
	Average (C.O.V.)	40.7 (15.9%)

Cross sectional area = 8100 mm²

Initial Flow and Mortar Cube Test Results for Shear Wall Tests

The initial mortar flow was measured before using each batch of mortar in the construction of shear walls in accordance with ASTM C1437-07 (2007). Three 50-mm mortar cubes were also cast before using each batch of mortar. The cubes were air cured in the laboratory under the same conditions as the wall specimens. The mortar cubes were tested in compression in accordance with ASTM C109/C109M-02 (ASTM 2002a). Detail of the test results are as presented in Table A.3.

Table A.3 – *Initial flow and mortar cube test results for shear wall tests (to be Cont'd)*

Batch No.	Initial Flow (mm)	Cube Strength (MPa)	Batch No.	Initial Flow (mm)	Cube Strength (MPa)
1	127.5	41.7	4	129	45.9
		54.6			48.2
		47.4			47.7
2	128.5	47.1	5	130	37.6
		52.6			46.2
		51.3			51.6
3	127	53.2	6	133	49.2
		49.1			45.6
		42.8			49.4

Table A.3 – (Continued)

Batch No.	Flow (mm)	Strength (MPa)	Batch No.	Flow (mm)	Strength (MPa)
		47.0			48.0
		39.7			48.4
7	125.25	40.4	18	127	N/A
		53.0			N/A
		64.4			62.0
8	126.5	66.8	19	129	62.8
		56.6			61.2
		54.6			71.2
9	124	57.3	20	127	60.0
		57.0			64.8
		64.7			67.4
10	129.6	66.6	21	129	47.7
		58.4			70.7
		44.6			58.8
11	126	42.9	22	127	57.6
		57.0			63.8
		52.0			55.8
12	127.75	59.4	23	129.5	51.4
		42.1			60.7
		42.7			57.3
13	128	67.6	24	126.5	45.7
		61.6			48.0
		64.2			61.6
14	126.5	56.0	25	127.5	59.8
		68.0			46.1
		65.3			47.4
15	123	73.6	26	129.5	47.8
		53.4			58.0
		57.8			54.6
16	127.5	45.2	27	122.5	61.0
		69.8			51.3
		63.8			64.1
17	131	N/A*	28	125	54.1
			Average (C.O.V.)	127.5 (1.8%)	21.3 (15.7%)

* *Data are not available due to Damaged or lost sample*

Appendix B: Calculation Method for Flexural and First Yield Capacity of the Test Walls

The flexural capacity for the test walls were predicted based on the following equations specified in Canadian Masonry Standard, CSA S304.1 (2004). Material resistance factors are ignored in the design of the test walls.

$$P = C_m + C_s - T_s$$

Solve for c where:

$$C_m = 0.85 f'_m t (0.8c)$$

$$C_s = \sum A'_s f'_s \quad \text{and} \quad f'_s = \frac{c - d_i}{c} \times 0.003 E_s \leq f_y \quad \text{(Compression Reinforcement)}$$

$$T_s = \sum A_s f_s \quad \text{and} \quad f_s = \frac{d_i - c}{c} \times 0.003 E_s \leq f_y \quad \text{(Tension Reinforcement)}$$

And calculate:

$$M_u = C_m \left(\frac{\ell_w - 0.8c}{2} \right) + \sum A_s f_s \left(d_i - \frac{\ell_w}{2} \right) + \sum A'_s f'_s \left(\frac{\ell_w}{2} - d_i \right)$$

The lateral load carrying capacity for the test walls at the onset of the first flexural bar yielding were predicted based on simple beam theory and assuming a linear strain profile along the length of the wall. Material resistance factors are ignored in the design of the test walls.

$$P = C_m + C_s - T_s$$

Solve for kd where:

$$C_m = \left(\frac{kd}{d_1 - kd} \right) \varepsilon_y E_m \frac{bkd}{2}$$

$$C_s = \sum A'_s f'_s \quad \text{and} \quad f'_s = \frac{kd - d'_i}{d_1 - kd} \varepsilon_y E_s A'_s \quad \text{(Compression Reinforcement)}$$

$$T_s = \sum A_s f_s \quad \text{and} \quad f_s = \frac{d_i - kd}{d_1 - kd} \varepsilon_y E_s A_s \quad \text{(Tension Reinforcement)}$$

$$T_s = T_y = A_s f_y \qquad \text{for the extreme tension bar}$$

And calculate:

$$M_y = C_m \left(\frac{\ell_w}{2} - \frac{kd}{3} \right) + \sum A_s f_s \left(d_i - \frac{\ell_w}{2} \right) + \sum A_s' f_s' \left(\frac{\ell_w}{2} - d_i \right)$$

Index of notations:

P = Axial compressive load

C_m = Compressive resistance of masonry

C_s = Total compressive resistance of the vertical reinforcements

T_s = Total tensile resistance of the vertical reinforcements

M_u = Moment resistance at maximum strain in masonry

ℓ_w = Length of wall

c = Distance from the extreme compression fibre to the neutral axis of wall

kd = Depth of the neutral axis in the compression zone of wall

f_m' = Compressive strength of masonry

t = Actual wall thickness (full thickness for grouted sections and total of face-shell thicknesses for ungrouted sections)

d_i = Distance from extreme compression fibre to the centre of the vertical reinforcement

A_s = Area of the vertical tensile reinforcement in wall

f_s = Tensile stress in the vertical reinforcement

A_s' = Area of the vertical compressive reinforcement in wall

f_s' = Compressive stress in the vertical reinforcement

E_s = Modulus of elasticity for steel reinforcement

f_y = Yield strength in the vertical reinforcement

Appendix C: Calculation Method for Shear Capacity of the Test Walls

The shear capacity for the test walls were predicted based on the following equations specified in Canadian Masonry Standard, CSA S304.1 (2004). Material resistance factors are ignored in the design of the test walls.

$$V_u = \left(0.16\sqrt{f'_m} \times 0.8\ell_w b_w + 0.25P\right)\gamma_g + \left(0.60A_v f_y \frac{0.8\ell_w}{s}\right)$$

But not greater than

$$0.4\sqrt{f'_m} b_w d_v \gamma_g$$

Index of notations:

V_u = Shear resistance of wall

f'_m = Compressive strength of masonry

ℓ_w = Length of wall

b_w = Overall width of wall

P = Axial compressive load

γ_g = A_e / A_g not greater than 0.5; where, A_e and A_g are the effective and gross cross-sectional area of masonry, respectively

A_v = Area of shear reinforcement in wall

f_y = Yield strength in the vertical reinforcement

s = Spacing of shear reinforcement

Appendix D: Flexural and Shear Capacity of the Test walls based on the Requirements of the Masonry Standards Joint Committee (MSJC 2008)

The flexural and shear capacity for the test walls were calculated based on the Masonry Standards Joint Committee (MSJC 2008) provisions. Similar methodology as described in Appendix B is used for flexural capacity calculations. According to the code requirements, the maximum usable strain, ε_{mu}, at the extreme masonry fibre is assumed to be 0.0025 which is different compared to 0.003 as specified in the requirements of the Canadian standard (CSA 2004). Masonry stress of $0.80\,f'_m$ (compared to $0.85\,f'_m$ as specified in CSA 2004) is also assumed to be uniformly distributed over an equivalent rectangular compression stress block bounded by edges of the cross section and a straight line located parallel to the neutral axis and located at a distance $a = 0.80\,c$ from the fibre of maximum compressive strain where c is the distance of the neutral axis from the fibre of maximum compressive strain. The results of lateral load resistance of the test walls based on flexural capacity calculations are presented in Table D.1.

The shear capacity for the test walls were predicted based on the shear strength requirements specified in the Masonry Standards Joint Committee code (MSJC 2008). Material resistance factors are ignored in the calculations. According to the code requirements, the following equation is used in the prediction of shear capacity of the tests walls.

$$V_u = 0.19 A_n \sqrt{f'_m} + 0.25 P + 0.50 A_v f_y \frac{d_v}{s} \leq 0.33 A_n \sqrt{f'_m}$$

where A_n is the net cross-sectional area of a wall. The other parameters are described in Appendix C. In comparison to the CSA (2004) shear equation used in Appendix C, in the MSJC code (2008), slightly higher shear strength is predicted for masonry. However, the contribution of shear reinforcement is reduced to 50% compared to the 60% horizontal steel effectiveness assumed in CSA 2004. The lateral load resistances of the test walls based on shear capacity calculations are presented in Table D.1.

Table D.1 – *Measured versus predicted lateral load carrying capacity of the test walls based on CSA (2004) and MSJC (2008) codes*

Specimen No. Bar Spacing (Aspect Ratio)	Measured Strength*	CSA (2004)		MSJC (2008)	
		Flexure (kN)	Shear (kN)	Flexure (kN)	Shear (kN)
Wall 1 855 mm (1.0)	94.1	121.1	**88.3****	119.5	**93.4**
Wall 2 570 mm (1.0)	98.5	115.9	**97.6**	112.6	**102.6**
Wall 3 1710 mm (1.0)	90.6	122.2	**79.4**	121.0	**84.6**
Wall 4 855 mm (0.5)	118.6	230.6	**103.8**	227.6	**120.7**
Wall 5 855 mm (1.5)	81.7	**80.7**	88.3	**79.7**	93.4

* *Average strength of the wall in the push and pull directions was considered*
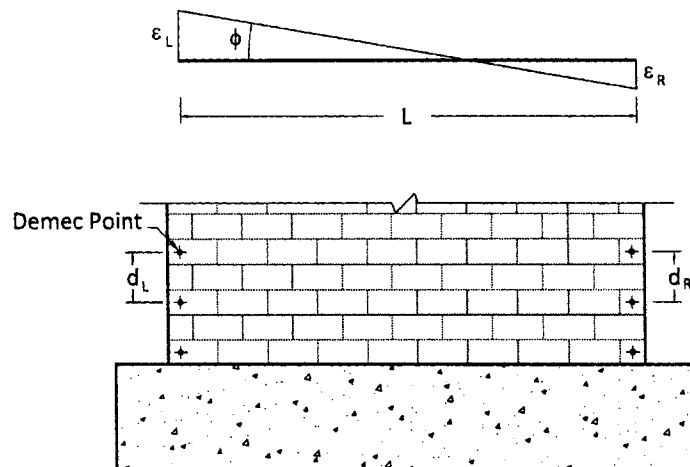** *Bold numbers indicate governing design strength.*

Appendix E: Calculation Method for Average Curvature

Average curvature over wall height is calculated using the deformation readings from pair of Demec gauges (Figure E.1) based on the following equation:

$$\phi = \frac{|\varepsilon_L| + |\varepsilon_R|}{L}$$

where ε_L and ε_R are the average strains over d_L and d_R calculated by:

$$\varepsilon_L = \frac{\Delta d_L}{d_L} \quad \text{and} \quad \varepsilon_R = \frac{\Delta d_R}{d_R}$$

Figure E.1 – *Strain profile used for curvature calculation*

Appendix F: Calculation Method for Pseudo-Displacement Ductility and Lateral Load Reduction Factor

Pseudo-Displacement Ductility

The inelastic performance of the test walls without a definite yielding point can be evaluated by a pseudo displacement ductility capacity suggested by Tomazevic (1999). In this approach the hysteretic behaviour of the wall is represented by an idealised bilinear resistance envelope as shown in Figure F.1. In this method, H_u is not the actual but the idealised maximum experimental value with an average ratio of $H_u / H_{max} = 0.9$. The ultimate idealised displacement, d_u, is assumed where 20% strength degradation has occurred in the experimental load-displacement curve (Tomazevic 1999).

The initial slope of the idealised envelope which is called, herein, effective elastic stiffness of the wall, K_e, is determined by an equal energy approach such that the energy dissipated based on the area under the idealised bilinear envelope gives the same amount of energy dissipated based on the area under envelope of the experimental hysteresis loops at 20% degradation in strength of the test walls. For example, details of pseudo-displacement ductility calculation for Wall 1 are as presented here.
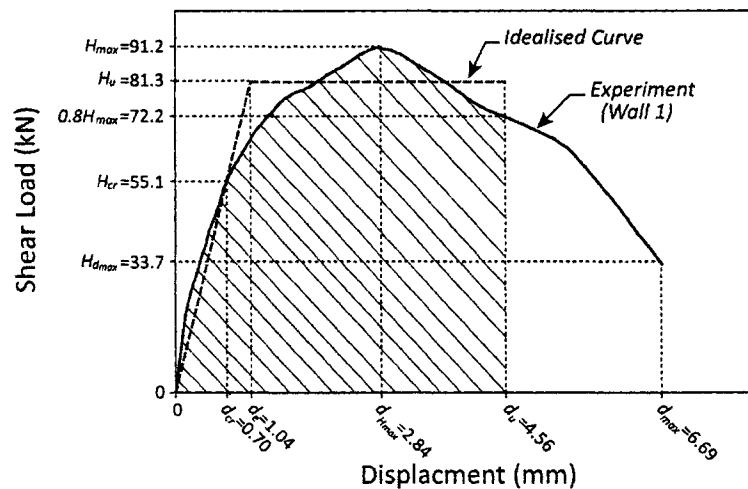

Figure F.1 – *Idealisation of experimental hysteresis envelope with bilinear relationship*

For Wall 1:

$$H_{max} = 91.2 \text{ kN}$$

$$0.8H_{max} = 72.2 \text{ kN} \quad \rightarrow \quad d_u = 4.56 \text{ mm}$$

$$H_u = 0.9H_{max} = 81.3 \text{ kN}$$

Equating the two areas under actual envelope and idealized bilinear envelope of hysteresis loops:

$$d_e = 1.04 \text{ mm} \quad \rightarrow \quad K_e = 78.3 \text{ kN/mm}$$

Therefore:

$$\therefore \mu_\Delta = \frac{d_u}{d_e} = 4.4 \quad \text{(for Wall 1)}$$

Lateral Load Reduction Factor

For relatively rigid structures such as masonry buildings with a fundamental period between 0.4 to 0.8 seconds which is close to the period for peak elastic acceleration response (i.e. about 0.5 seconds for El-Centro 1940 – Figure F.2), the relation between displacement ductility, μ_Δ, and load reduction factor, R, can be rationally obtained by establishing the equivalence of the energy between the elastic and idealized elastic-perfectly plastic systems (Pauley and Priestly 1992). This is illustrated in Figure F.3 where R is the ratio of the equivalent elastic load P_e to the
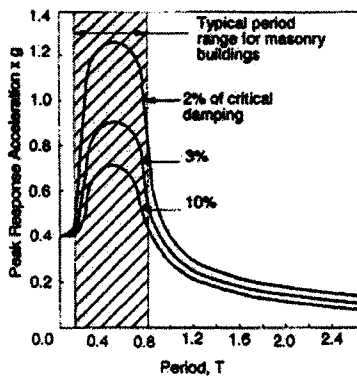
Figure F.2 – *Elastic Response Spectra for El-Centro (1940) (from Drysdale et al. 1999)*
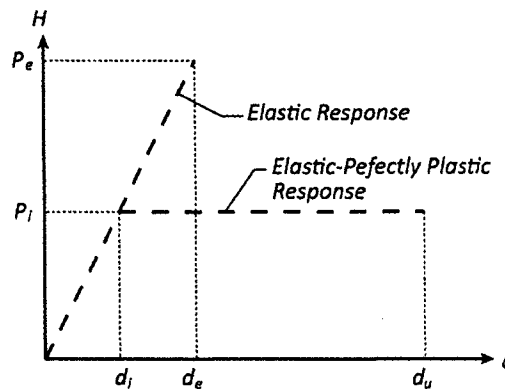
Figure F.3 –*Elastic and elastic-perfectly plastic response*

inelastic load, P_i. Equating the two areas under the elastic and elastic-perfectly plastic curves:

$$Area\ under\ the\ elastic\ response = \frac{P_i d_i}{2} + \left(\frac{P_i + P_e}{2}\right) \times (d_e - d_i)$$

$$Area\ under\ the\ elastic\text{-}perfectly\ plastic\ response = \frac{P_i d_i}{2} + P_i \times (d_u - d_i)$$

$$\frac{P_i d_i}{2} + \left(\frac{P_i + P_e}{2}\right) \times (d_e - d_i) = \frac{P_i d_i}{2} + P_i \times (d_u - d_i)$$

Knowing that $R = P_e / P_i = d_e / d_i$, and $\mu_\Delta = d_u / d_i$:

$$\left(\frac{1+R}{2}\right) P_i \times (R-1) d_i = P_i \times (\mu_\Delta - 1) d_i \quad \rightarrow \quad (R^2 - 1)/2 = \mu_\Delta - 1$$

$$\therefore R = \sqrt{2\mu_\Delta - 1}$$

So for Wall 1:

$$\mu_\Delta = 4.4 \quad \rightarrow \quad \therefore R = \sqrt{2 \times 4.4 - 1} = 2.8$$

9371   10